

# A fibre optic and machine learning based health monitoring system for superconducting power applications in modern supergrids

Présentée le 17 juin 2022

Faculté informatique et communications  
Groupe SCI IC BD  
Programme doctoral en génie électrique

pour l'obtention du grade de Docteur ès Sciences

par

## Arooj AKBAR

Acceptée sur proposition du jury

Prof. D. Dujic, président du jury  
Dr. B. Dutoit, Prof. M. Paolone, directeurs de thèse  
Dr A. Chiuchiolo, rapporteuse  
Dr S. Ishmael, rapporteuse  
Dr K. Sedlak, rapporteur



To my Mama, my Baba and Hira, whose love and support for me know no limits  
To my loving husband Henry, for crossing oceans and continents to be there for me

# Acknowledgments

As I make my way towards the finish line of my doctoral studies, I must express my gratitude to the people who helped me along the way and without whom this work would not have been possible.

First and foremost is my PhD supervisor, Dr. Bertrand Dutoit, for giving me the valuable opportunity to pursue a PhD under his supervision. I am truly honored to have had the chance of working with a wonderful boss and a remarkable experimentalist. Bertrand introduced me to a vast dimension of hands-on work in the laboratory and made me believe anything was possible to achieve inside the playground that was our lab. Thank you, Bertrand, for your unwavering support and for encouraging me to be in command of the reigns of my PhD, to define my horizons and to charge freely towards them. Thank you for the enjoyable and insightful discussions throughout my PhD that have served as a guiding light for my professional and personal growth. Thank you, for showing me the inspiring summits of Mont Blanc and Allalin, the intriguing depths of Mer de Glace, the incredible thunderstorms in the valley of Chamonix and inculcating the Swiss passion for mountains and nature in me. Thank you, for making my PhD experience profound inside and outside of the lab. It has been a great pleasure. *Merci beaucoup!*

I would also like to extend my sincere gratitude to my thesis co-advisor Prof. Mario Paolone, for supporting my work. Thank you, Mario, for teaching me valuable mathematical modelling tools during your course, that have helped me on my journey to learn and apply machine learning methods to my research.

I would also like to express my thanks to the head of the Group of Fibre Optics (GFO) at EPFL, Dr. Luc Thevanaz for providing his expert advice on fibre optic sensing. I would also like to thank Dr. Zhisheng Yang (former post-doctoral fellow at GFO), for helping me work with optical setups when I was new and unfamiliar to the domain of fibre optics. Thank you to Sheng Wang (former PhD student at GFO), for helping me gain expertise in building and debugging optical sensors in the lab.

This thesis would not have been possible without the help and support of the FastGrid project partners. Thank you to Dr. Pascal Tixador from CNRS, Grenoble, for skillfully overseeing the FastGrid project and ensuring target milestones were met. Thank you to Markus Bauer, from Theva, for kindly collaborating with EPFL to provide HTS tape samples for testing and for the SFCL pancake. Thank you, to Pierre Legendre, Christophe Creusot and Amélie Berthe from SuperGrid Institue (SGI), Lyon, for welcoming me to SGI for my first experience of testing large scale superconducting setups, to test my technique with the FastGrid pancake. Thank you to SGI, for also kindly winding a SFCL pancake for long term testing at EPFL. Thank you to Dr. Marcela Pekarcikova, from Slovak University of Technology in Bratislava (STU), for promptly providing me data on material properties in cryogenic temperatures, whenever I needed them for my finite element models.

I would also like to thank, the following people from SCI-consulting in Lausanne: Pierre-Alain Probst whose excellent electronics acumen and extensive experience helped guide me in designing the required circuitry for my experiments. Thank you to Adrien Alain, Vincent Berseth and Gabriel Safar for always making time when needed, to assist me in working with the digital current pulser.

I would also like to thank Marta Bajko from CERN, for always being extremely kind and supportive of my endeavours. Thank you for making it possible for me to present my work at CERN and for sharing your insightful experience with fibre optic sensors for superconductors with me; your work and advice were of immense help throughout the course of my PhD.

Thank you to Nicolo, who added joy and laughter to my time spent in the office. Thank you, for giving me the best tutorial to COMSOL, as I embarked on my journey of finite element modelling. Thank you, for showing me the beautiful night sky of Baceno and introducing me to the warmth that is your family.

Thank you to my little sister, Hira, who endured all my setbacks with me and celebrated all my victories with me. Thank you for being the best support system and embodying: when the going gets tough, the tough get going.

Thank you to my husband Henry, for always sticking by my side through thick and thin. Thank you for adding love, joy and light to my life everyday.

Finally, thank you to the ones who are the reason why I am where I am today: my parents. Thank you, Mama and Baba, for putting in all the love and effort despite all the hardships, to fulfill the dream that you dreamt with me.



# TABLE OF CONTENTS

Abstract.....	x
---------------	---

## Chapter One

Climate change, renewable energy and superconductivity.....	1
1.1 The inevitable HVDC Supergrids.....	1
1.1.1 HVDC grid protection .....	2
1.2 Superconducting applications for generating and transmitting renewable energy.....	3
1.2.1 Superconducting fault current limiters for Supergrids .....	4
1.2.2 HTS cables.....	5
1.2.3 High temperature superconductors (HTS) in fusion technologies.....	7
1.3 The need for health monitoring of high temperature superconductors in power applications.....	7
Conclusion and thesis motivation.....	9

## Chapter Two

The European Union project FastGrid.....	10
2.1 FastGrid: Building an optimized Superconducting Fault Current Limiter.....	10
2.2 Existing protection mechanisms for Superconducting Fault Current Limiters.....	15
2.3 Thesis motivation and aspirations.....	16
Summary.....	18

## Chapter Three

An innovative fibre optic based health monitoring system for superconductors.....	20
3.1 Why fibre optic sensors?.....	20
3.1.1 Strain and temperature monitoring using fibre optic sensors.....	21
3.1.2 Fibre optic sensors for cryogenic temperatures.....	23
3.2 The Mach-Zehnder method.....	24
3.2.1 MZI working principle .....	24
3.3 Comparative feasibility and cost analysis of the Mach-Zehnder Interferometer.....	25
Summary.....	27

## Chapter Four

Experiment Setup.....	29
4.1 Building the Mach-Zehnder Interferometer.....	29
4.2 The MZI plug and play box.....	33

4.2.1 Cost of the MZI setup .....	34
4.3 Building the current pulser.....	35
4.4 The experiment setup for 10cm-30cm superconductor tapes.....	37
4.4.1 Building the sample holder .....	37
4.4.2 Integrating the fibre on a linear sample.....	37
4.4.3 Placing voltage measurement contacts on HTS sample.....	39
4.4.4 The complete assembled setup and data acquisition.....	40
4.4.5 Setup for 1 m linear HTS samples.....	42
4.4.6 Building a sample holder to avoid Lorentz force .....	42
4.5 The experiment setup for the FastGrid Superconducting Fault Current Limiter pancake.....	43
4.5.1 Integrating optical fibres on long lengths of HTS tape for the FastGrid SFCL pancakes.....	43
4.5.2 Fully assembled setup for the FastGrid project pancake .....	44
4.5.3 Fully assembled setup for the Petite SFCL Pancake .....	47
Summary.....	48
 <b>Chapter Five</b>	
<b>Experiment Results and Discussion.....</b>	<b>51</b>
5.1 1 m long SCS4050-AP sample.....	52
5.1.1 Sample specifications .....	52
5.1.2 Experiment results.....	52
5.1.3 Discussion for the 1 m SCS4050-AP sample .....	55
5.2 65 cm long Theva TPL5121 HTS sample.....	56
5.2.1 Sample specifications .....	56
5.2.2 Experiment results.....	57
5.2.3 Discussion for the 65 cm TPL5121 sample .....	59
5.3 30 cm OFE-HTS sample with soldered optical fibre.....	61
5.3.1 Sample specifications .....	61
5.3.2 Experiment results.....	62
5.3.3 Discussion for the 30 cm OFE-HTS sample.....	64
5.4 Petite SFCL Pancake.....	66
5.4.1 Sample specifications .....	66
5.4.2 Experiment results.....	67
5.4.3 Discussion for the Petite SFCL Pancake.....	69
5.5 The FastGrid pancake.....	70
5.5.1 Sample specifications .....	70
5.5.2 Experiment results.....	70

5.5.3 Discussions for the FastGrid pancake .....	72
5.6 Challenges faced with the MZI method.....	73
5.6.1 High sensitivity to noise.....	73
5.6.2 Birefringence .....	73
Summary.....	74
 <b>Chapter Six</b>	
Using finite element modelling to understand the Mach- Zehnder Sensitivity.....	77
6.1 Optical fibre sensitivity in cryogenic temperatures.....	77
6.2 Building a thermal model.....	79
6.3 Simulation results and discussion.....	80
6.4 The importance of optical fibre integration quality with the superconducting power devices....	83
Summary.....	84
 <b>Chapter Seven</b>	
Using Machine Learning with the Mach-Zehnder Method.....	85
7.1 Feature extraction using discrete wavelet transform.....	86
7.2 Machine learning based classification.....	88
7.2.1 k-Nearest Neighbours – KNN .....	90
7.2.2 Artificial Neural Networks – ANN .....	90
7.2.3 Support Vector Machines – SVM.....	92
7.2.4 Goals of the machine learning analysis.....	93
7.3 Results and Discussion.....	94
7.3.1 Classification results for OFE-HTS tape 30 cm .....	95
Distribution of OFE-HTS tape dataset.....	95
Classification performance for different wavelets .....	96
Misclassified data for highest performing classifier .....	97
7.3.2 Classification results for TPL5121 65 cm sample .....	98
Distribution of TPL5121 dataset .....	98
Classification results.....	99
Misclassified data for highest performing classifier .....	100
7.3.3 Classification results for the Petite SFCL Pancake .....	101
Distribution of Petite Pancake dataset .....	101
Classification results.....	102
Misclassified data for highest performing classifier .....	103
7.4 Understanding classification results based on class separability.....	104

7.5	Dependence of classifiers performance on size of the feature vector.....	105
7.6	Classification accuracy dependence on training dataset size.....	106
	Concluding remarks.....	107
 Chapter Eight		
	Milestones and future outlook.....	111
	Milestones.....	112
	Future work.....	113
	Thesis impact.....	114
	 Appendix.....	 116
A.1	Working of the digital current pulser.....	116
A.2	Differential amplifier to interface voltage measurement to DAQ.....	121
A.3	Low pass filter design for low noise DAQ measurements.....	123
	 <b>ACRONYMS</b> .....	 126
	<b>LIST OF FIGURES</b> .....	128
	<b>LIST OF TABLES</b> .....	134
	<b>BIBLIOGRAPHY</b> .....	135
	 CURRICULUM VITAE.....	 144



# Abstract

The concerns for climate change and the transition to renewables is increasing the relevance of superconducting applications: High Temperature Superconductor (HTS) cables for efficient power transmission, superconducting magnets for nuclear fusion, superconducting fault current limiters (SFCLs) for HVDC grid protection and superconducting compact generators for wind turbines, to name a few. However, to tap into the full potential of HTS applications, the main problem of hotspots needs to be addressed. Hotspots are localized points of heating, which can arise in HTS devices mainly due to the intrinsic inhomogeneity of critical current along the superconductor length. The motivation behind this thesis, was to develop a health monitoring technique for a SFCL device under the European union project FastGrid. This device required a fast hotspot detection time of 10 ms in order to timely open the DC breaker in order to protect the device. During the course of this thesis an extremely fast and economical optical fibre sensing based hotspot detection technique has been developed and patented. The technique uses the Mach-Zehnder Interferometer (MZI) and is an efficient and economical way to detect hotspots in HTS applications. Due to the MZI sensitivity being a composite of strain sensitive and temperature sensitive contributions, the MZI gives an instantaneous response to a hotspot (within 10 ms), because of the quick strain transfer to the optical fibre. The research carried out under this thesis has involved experimentation on HTS tapes (10 cm to 1 m in length). The technique has also been integrated and tested with a SFCL pancake prototype with long lengths of conductor (12 m and 17 m). The thesis has also focused on finite element modelling to better understand the MZI sensitivity. The experimentation and modelling together, has enabled a better understanding of the MZI response to hotspots and the challenges of using MZI for HTS health monitoring. Due to the extremely high sensitivity of the MZI, the MZI output signal can also manifest the environmental noise caused by mechanical vibrations, bubbling in the cryostat and temperature variations, along with the response to heating in the sample. This presents the problems of false alarms and indiscernible response to hotspots. The work done for this thesis has also focused substantially on finding a suitable data analysis technique to supplement the MZI method. A discrete wavelet transform (DWT) based feature extraction together with a machine learning based classification for reliable quench detection has been developed in the course of this work with very encouraging results. This is an important development for the MZI technique as it significantly impacts and improves the MZI reliability and practicality for HTS applications. Additionally, this is also of substantial importance to the progress of HTS applications in the industry, especially the power sector which continues to evolve with the shift towards renewables and will rely more on HTS applications like SFCLs and HTS cables. With a reliable hotspot detection technique like the MZI, we can facilitate mass adoption of such HTS applications.

# 1

## Climate change, renewable energy and superconductivity

Climate change, two words that have been uttered with urgency by scientists and scoffed at by skeptics for a long time, have now almost found their rightful place in a growing global consensus: that climate change is an undeniable phenomena and the world needs to collectively act in order to quell an imminent catastrophe. Net zero emissions by 2050, is the mission that is being undertaken by an increasing number of countries, and the stage is being set for a total reformation of how energy will be generated, transmitted and distributed in what some politicians have termed as the *century of decarbonization*.

### 1.1 The inevitable HVDC Supergrids

To achieve net zero emissions, a transition to renewable energy generation is of paramount importance. Electricity production alone contributes to 25% of the greenhouse emissions, the second largest contribution after transportation[1]. This is explained by how 62% of the electricity that is currently being generated is sourced from the burning of fossil fuels, namely coal and natural gas. The switch to renewable energy generation therefore becomes imperative, in order to achieve substantial cuts in carbon dioxide emissions. The Sustainable Development Goals (SDGs) that were set in 2015 by the United Nations have heralded that the share of renewable energy generation will increase to 63% in the primary energy supply, and to 85% in the power sector by 2050 [2]. These projected trends are shown in Fig. 1 taken from the International Energy Agency (IEA) report. Doing the math shows that a six-fold acceleration of renewable energy growth rate is needed to realize the numbers projected by the SDGs. This together with the Paris Agreement, will have a profound impact on the energy sector that is not equipped (for now) to handle a full transition to renewables. Renewable energy generation comes with the challenges of variability and unpredictability, while its transmission becomes problematic due to the locality. Unlike fossil fuel powered generation sites, humans cannot pick where to set up a renewable generation site; it is nature and the landscape that determine the energy generation location. Often, these generation sites (for example for wind, hydro power, geo-thermal and waves) are far from the consumption sites and irregularly distributed, making transmission an equally important aspect for renewable energy as generation. Supergrids thus become an inescapable solution for a transition to green energy [3]. Supergrids are large networks that can transmit electricity over long distances enabling the connection of resource rich renewable energy generation sites to distant consumer sites. Such a largescale, cross border, interconnected grid facilitates the connection of remotely located renewable energy sources over a large area overcoming the erratic nature of the supply. It also increases energy reliability and enables better

integration and sharing of resources [4]. To transmit power over long distances in supergrids, High Voltage Direct Current (HVDC) lines are the key enabling technology. HVDC is preferred over High Voltage Alternating Current lines (HVAC) due to their lower cost and higher efficiency of transmitting over long distances; HVDC becomes more economical than HVAC after 800-1000 km. In addition, HVAC presents a higher line cost (more copper required) than HVDC and requires more reactive support. While HVDC supergrids have plenty of social, economical and environmental benefits to offer, their deployment comes with the added technical challenge of network protection.

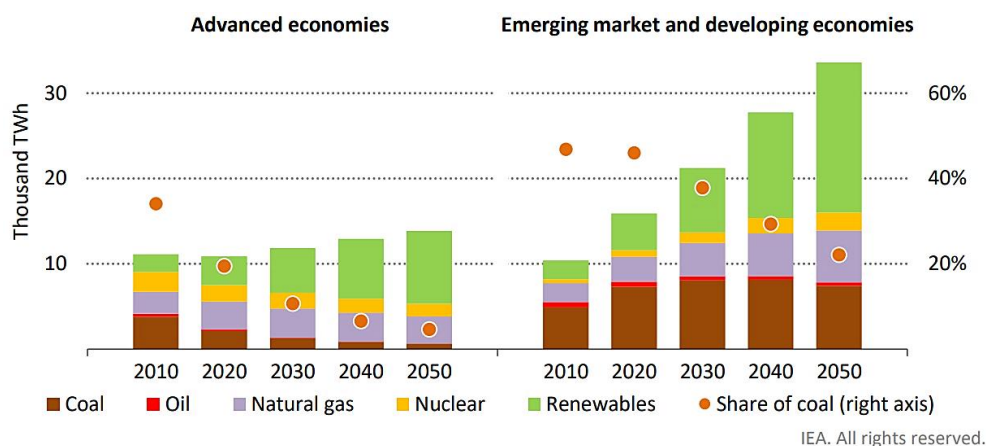


Figure 1. Projected trends for renewable energy contribution by the International Energy Agency [2]

### 1.1.1 HVDC grid protection

To this day, HVDC is mostly being used for point-to-point connections with converters on either ends. The motivation behind these links can be either long distance transmission, connection of asynchronous grids or submarine cables. The converter stations in such links can operate as rectifiers converting AC to DC or as inverters converting DC to AC. However, by interconnecting several HVDC links, a multi-terminal DC (MTDC) grid arises, which reduces total asset cost and increases system reliability by adding redundancy. This meshed DC grid can be embedded into an existing AC grid or be used to link multiple asynchronous AC systems.

For a MTDC system, fault handling is a crucial issue that needs to be resolved[5]. The fact that no current zero crossing are present in DC grids means that HVDC grids are vulnerable to a sharp rise of fault currents. Fault detection and quick isolation is a necessity for MTDC grids to prevent destructive current levels, damage to the converters and fall of voltage levels. The fault must be detected, isolated and cleared in an order of 5-10 ms according to scientific data, which is significantly faster than AC grids[5,6]. The AC grid protection mechanisms therefore fail for MTDC systems. The report by the International Energy Agency (IEA) predicts that due to the need for enabling technologies, the largest share of the investment for net zero by 2050 will be in the grid infrastructure and end use sector [7]. Even though the MTDC grid situation differs from AC grids in all respects, their viability in the energy sector is measured by the comparison of their protection system to the existing “well designed” AC system. This viability for HVDC grids is currently deemed to be lacking. In AC grids fault handling is done by transformers, switching elements and DC breakers; the propositions for MTDC grid protection usually involve similar elements despite the evident dissimilarity in fault handling criteria for the two systems [8]. Existing protection mechanisms being proposed for MTDC systems range



from non-selective to selective strategies which either are relatively new with insufficient data on feasibility or fall short of the MTDC grid fault detection requirements[9]. These requirements include speed, selectivity and stability (during and after fault handling)[10]. It is also necessary that the protection system is robust and feasible for redundancy.

The non-selective fault handling deals with faults using the AC side breakers. In point to point HVDC links, fault handling is done conveniently on the AC side. However, if such an approach is taken for a MTDC grid, all of the DC grid must be de-energized for fault isolation followed by the re-energization of the non-faulty part[11]. This is an inefficient and non-selective way of fault handling that causes unacceptably large losses in the grid infeed.

The selective fault handling strategies include the circuit breakers. Circuit breakers for current interruption while easy to use for AC due to zero crossings, remains challenging for DC. In DC due to the lack of zero crossings, circuit breakers must perform the task of forcing the current to zero. This is done in resonant circuit breakers for example, using the capacitor discharge to create a current zero crossing, however, their operation time ranges from 30 to 100 ms which is too slow for DC grid protection [8,12]. Another kind of circuit breaker, the hybrid solid state circuit breaker uses the semiconductor technology. The circuit breaker comprises a fast switch in parallel to IGBTs that redirect the fault current and enable the opening of the mechanical switch. Such a circuit breaker has been commercially introduced by ABB in 2019 which has an operation time of 2 ms; the device is a recent breakthrough with limited data available on its suitability for MTDC grids [13]. Literature shows that while their fault clearing time is extremely feasible for MTDC systems, hybrid DC circuit breakers come with the drawback of high on-state losses in high voltage and high current applications, which need to be minimized through the addition of the faster mechanical switches [8]. Scientific studies also show that hybrid DC circuit breaker is a cost effective solution for simple HVDC grids but requires a daunting communication system in the case of complex HVDC systems[14].

The fault handling for MTDC systems is therefore, still being explored and the quest for the best protection system continues. There is still a need to investigate new technologies to handle the high fault currents. HVDC and renewable energy form a playing field that needs one key player, which has a game changing potential for such futuristic yet inescapable supergrids. That key player being: superconductivity.

## 1.2 Superconducting applications for generating and transmitting renewable energy

The year 2021 marked 110 years of superconductivity. Superconductivity is still young and has seen its share of struggle in garnering acceptance in the industrial market. Currently, most superconducting applications in the industry or in scientific laboratories use low temperature superconductors (LTS) for example for particle physics, fusion experiments and magnetic resonance imaging (MRI), that operate at liquid Helium temperatures. The discovery of high temperature superconductors (HTS) in 1987 has introduced new materials that have the potential to transform the industrial applications, especially in the sector of energy generation and transmission. The energy sector is in a crucial era of change. As discussed in section 1.1 the climate change debacle and urgent need for a switch to clean energy are a harbinger of a complete transfiguration of the energy generation and transmission mechanisms. Consequently, HTS power applications like cables, transformers, fault current limiters (FCL) and fusion magnets are now finding use in

niche situations where conventional solutions are proving to be inadequate. It will not be wrong to say that the power sector is poised for progress by means of HTS applications.

### 1.2.1 Superconducting fault current limiters for Supergrids

Since the key player superconductivity was introduced in the context of MTDC grid protection, it is only appropriate to start the list of HTS power applications by talking about Superconducting Fault Current Limiters (SFCLs). SFCLs are promising candidates for MTDC grid protection that meet majority of the protection criteria outlined in 1.1.1:

- Minimum impedance during normal operation.
- Fast fault current mitigation.
- Quick recovery.

There are three different kinds of SFCLs that are being developed industrially or investigated in scientific laboratories around the world. These types are namely resistive, shielded core, and saturated core FCLs. The shielded core and saturated core are often collectively referred to as inductive type FCLs. Literature finds resistive SFCLs to be more suitable than inductive SFCL for protection of HVDC grids [15,16]. Therefore, this section will focus only on resistive SFCLs.

A resistive SFCL exploits the intrinsic property of superconductors to quench at current levels at and beyond the critical current. A quench is a sudden, unexpected and unrecoverable transition to the normal state of the superconductor in the device, which causes the conversion of the stored energy into mostly heat, which can lead to destruction of the device when not properly controlled [17]. Critical current  $I_c$  is the current at which the superconductor transitions from superconducting state of negligible resistance to a resistive state. During normal grid operation, resistive SFCLs remain *invisible* with negligible resistance but quenches at high current levels, using the highly resistive state for current limiting within few milliseconds. Resistive SFCLs constitute the simplest and compact kind of SFCL and can be installed in series with the power line or in busbar couplings. A schematic of the resistive SFCL circuit is shown in Fig.2.

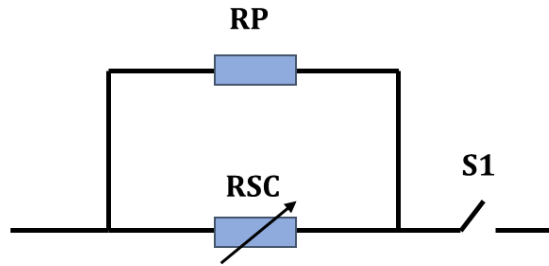


Figure 2. Schematic of a resistive SFCL showing the superconductor as a variable resistance adapted from [18]

The superconducting element  $R_{SC}$  is placed in parallel to a normal impedance  $R_p$  which can be in physical contact with the superconductor or placed separately in a parallel circuit pathway. During normal operation the superconductor has negligible resistance and voltage drop and hence carries the entire operating current. In the case of a fault, the resistance  $R_{SC}$  increases by many orders of magnitude in a small amount of time, redirecting majority of the current in  $R_p$ . The opening and closing of switch  $S1$  depends upon the recovery of the SFCL after a quench. The recovery of the SFCL back to superconducting state is achieved through cooling of the superconductor. This recovery time depends upon the device specifications and is usually in the order of

seconds. If the SFCL can recover under load, then S1 stays closed. However, if the SFCL requires recovery time then S1 is opened until the device is ready to operate again.

Nexans SuperConductors GmbH (NSC) was the first company to develop and commercially install the resistive SFCL device in 2009 (pictured in Fig. 3.) [19]. Since then, there have been several integrations by Nexans of SFCL devices [20]. There have also been successful development and testing of resistive SFCL devices by the cooperation of American Superconductor and Siemens one phase of 115 kV device [21]. Korean Electric Power Corporation also successfully implemented one phase of 154 kV device [22,23]. More recently, there has been successful commercial installation of resistive SFCL device in the Moscow city grid (pictured in Fig. 4) [24]. The device is installed at a 220 kV-class substation with high fault current level of above 50 kA. The SFCL is installed in series with 12 km long 220 kV cable line and has been in operation since 2019. The device has a fault clearing time of 60-80 ms and a recovery time of 15 s. After the satisfactory performance, Moscow city grid is set to continue installations of SFCL devices, with more challenging device specifications.

However, all these SFCL installations have been in AC power networks and while SFCLs are being tested experimentally for DC systems, there has been no installation in an HVDC system to date [25][26].

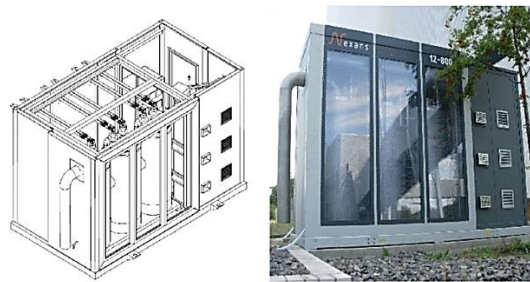


**Figure 3.** The first resistive SFCL installed in a thermal power plant by Nexans in Germany in 2009: A picture of the drawing and complete 3-phase system after installation with the three cryostats [19]



**Figure 4.** Front (left) and top view (right) of the 220 kV SFCL installed at the substation in Moscow [24]

## 1.2.2 HTS cables

The need for efficient transmission over long distances to utilize offshore renewable energy increases the relevance of another HTS application: HTS cables. The situation is analogous to how optical fibre constituted an *information superhighway*. HTS materials have the potential to replace copper conductors to form an *energy superhighway* by offering higher capacity and lower resistive losses [27].

Medium voltage HTS systems connected in series with a HTS fault current limiter (SFCL) is an attractive alternative to conventional systems, due to their numerous benefits [28]. They offer the same power rating

with lower voltage transmission and since they are more compact than conventional cables they can be installed easily in existing places dedicated to electrical wiring or sewage for example. High power distribution is possible at voltages lower than 4 kV and the cable diameter can be as low as 60 mm for a bifilar superconducting cable rated 66 MW 10 kA/3,3 kV. Fig. 5 shows how HTS cables compare to conventional cables in their power transfer capability.

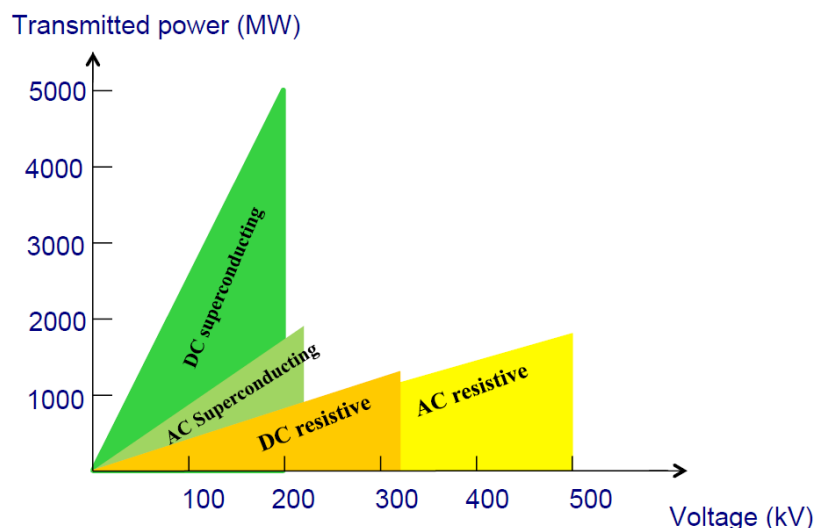


Figure 5. Comparison of HTS power transmission with conventional systems, taken from C. E. Bruzek, “Introduction to superconducting power cable systems“, ESAS Summer School, 2017

The losses in a conventional copper cable amount to 20 W/kA.m. In comparison, losses in HTS cables are up to ten times lower, as summarized in Table 1.

Table 1 Losses in HTS cables adapted from C. E. Bruzek, “Introduction to superconducting power cable systems“, ESAS Summer School, 2017

	Dependence	Losses at 65-77 K	Impact
<b>Cryogenic envelope losses</b>	None	0.5 to 2 W/m	HTS DC and HTS AC cables
<b>HTS AC losses</b>	Transported current and magnetic field distribution	0.05 to 1 W/kA.m	HTS AC cable
<b>Dielectric AC losses</b>	Voltage level	Up to 1 W/m	HTS AC cable
<b>Eddy current AC losses</b>	Magnetic field distribution	0.05 to 0.1 W/kA.m	HTS AC cable

There have been successful demonstrations of HTS cable installations in the grid around the world, the first one being a 30 kV and 104 MVA HTS cable, installed and operated in the electric grid of Copenhagen Energy in 2001[29]. Since then there have been numerous integration of HTS cables, for example the AmpaCity project in Essen, the Shingal project in Korea and HTS power cable in Long Island, USA, to name a few [30–32]. These installations have demonstrated, the ease of operability and the reliability of HTS cables. The main

reason for a lack of wider scale usage of HTS cable is the high cost of fabrication. HTS cables offer economic benefits by their reduced footprint, ease of installation, by cutting down the required substation equipment and decreasing losses. There is a need for acceptance by the utility companies around the world to overlook the initial cost estimate for long term economic, social and environmental benefits. The enhanced performance of HTS cables can in the right situation offset initial development costs which will enable an acceleration of their adoption.

### 1.2.3 High temperature superconductors (HTS) in fusion technologies

Very recently, on Sept. 5, 2021, there was a major breakthrough for high temperature superconductivity. For the first time, a large HTS electromagnet (10 feet tall) was ramped up to a field strength of 20 tesla. This successful demonstration is a big step in the efforts to building the world's first fusion power plant that can produce more power than it consumes, according to the project's leaders at MIT and startup company Commonwealth Fusion Systems (CFS)[33]. Superconducting magnets are necessary for future fusion reactors. Resistive magnets are not an option for fusion reactors because the magnets would consume more power than that generated by the reactor itself. The International Thermonuclear Experimental Reactor (ITER) is still a pulsed machine, but the electrical power needed to energize the magnet system with resistive magnets would be a massive 2 GW for 500 s which cannot be realistically obtained from the electrical grid [34]. With HTS magnets, it is possible to achieve substantial savings in cryogenic power requirements as compared to LTS magnets at 5 K. Even though the cost (at present) of HTS is one order of magnitude higher than LTS, it has advantages over LTS magnets in their ability to operate at very high magnetic field, high cryogenic temperature and larger tensile stress compared to LTS [35]. HTS magnets for fusion have challenges to overcome like long length of HTS tape production, quench protection mechanisms and optimization of REBCO tapes. With the recent demonstration at MIT, HTS for fusion has garnered interest, funding and is a step closer to building future fusion devices using HTS magnets.

## 1.3 The need for health monitoring of high temperature superconductors in power applications

A major challenge when it comes to HTS applications, is their health monitoring. In contrast to their low temperature counterparts (LTS), HTS are characterized by a high heat capacity and a slow normal zone propagation velocity (NZPV). After a local transition in the superconductor to a resistive state (normal state), this normal spot enlarges with a velocity termed as the NZPV. This NZPV is low in HTS. Fig. 6 shows a comparison of the NZPV in LTS and HTS tapes, by signifying how a normal zone propagates at a higher rate in LTS due to a much higher NZPV while in HTS this normal zone propagates slowly leading to localized temperature rise [36].

As a consequence, HTS typically have an enthalpy margin that is two to three orders of magnitude larger than in LTS [36]. Another distinguishing characteristic between LTS and HTS is the  $n$ -value. This value can be defined as the exponent in E-J power law equation in equation (1), where  $J_c$  is the critical current density and is a function of temperature  $T$ ,  $E_c$  is the critical electric field.

$$E = E_c \left( \frac{J}{J_c(T)} \right)^n \quad (1)$$

For LTS the  $n$ -value is higher signifying a sharp *on-off* transition of the superconductor to resistive state at the current sharing temperature (which is the temperature at which current transported through the superconductor also starts to flow through the metal stabilizer). However, in HTS in liquid nitrogen temperatures this  $n$ -value is lower causing the transition to resistive state to be much more gradual and presenting an opportunity for current sharing between the superconductor and the metal stabilizer. This combined with the critical current inhomogeneity paves way for the formation of hotspots and local heat dissipation in the superconductor.

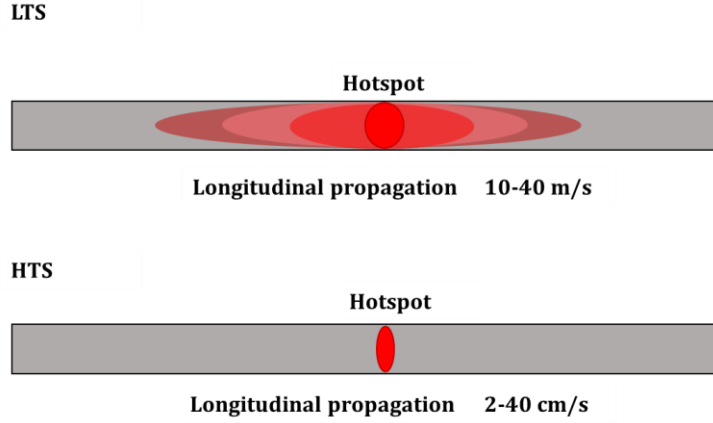


**Figure 6. A comparison of the normal zone propagation in HTS and LTS conductors**

The critical current  $I_c$  of HTS coated conductors (CC) can vary by 10-15% due to fabrication limitations. This material inhomogeneity produces an upper and lower bound on the local critical current ( $I_c$ ) along the HTS tape. This critical current, therefore, can be understood to lie in a band ranging from minimum critical current value ( $I_{c\_min}$ ) to the maximum critical current value ( $I_{c\_max}$ ), with different points along the superconductor transitioning to resistive state at different critical values. When a clear fault current develops, i.e., the operating current is beyond the highest  $I_c$  ( $I_o > I_{c\_max}$ ), the superconductor transitions uniformly from superconducting state to resistive state. It should be noted that the uniform transition may only occur if the electric field applied ( $E$ ) is greater than the critical electric field ( $E_c$ ), (i.e.  $E > E_c$ ), to ensure a homogenous quench as explained in Kraemer et al [37]. The problem of hotspots, however, can occur when the operating current level is in between the bounds  $I_{c\_min}$  and  $I_{c\_max}$ , so that only few points or even a singular point in the superconductor may transition to resistive state. Due to the normal zone propagating slowly, these hotspots in the superconductor can reach damagingly high temperatures causing thermal runaways [38]. The evolution of hotspot temperature with different  $n$ -values has been mathematically modelled in adiabatic conditions for HTS [36]. Fig. 7 shows the normal zone propagation for a REBCO conductor as a function of time. The plot shows the temperature evolution of hotspots for an operational current of 90%  $I_c$  and how the temperature of a 4 cm normal zone can reach 200 K within 0.4 s.

For LTS, the rapid expansion of the normal zone facilitates noticeable voltage measurements aiding quench detection. However, in HTS these voltage measurements would be the order of millivolts which are difficult to measure in accelerator magnet setups for example, due to the electromagnetic noise in the system and the connected power electronics. In addition, a main factor that makes LTS magnet quench detection techniques unfeasible for HTS is the time frame for energy extraction during a quench which is usually hundreds of milliseconds. This protection margin is too slow for the fast thermal runaways in HTS applications as established in this section. For HTS quench detection therefore, there is a need for more sensitive and faster

quench detection method. Different strategies are being explored to overcome this protection challenge in HTS applications: these range from conductor optimization, to increasing technique sensitivities to developing new methods.

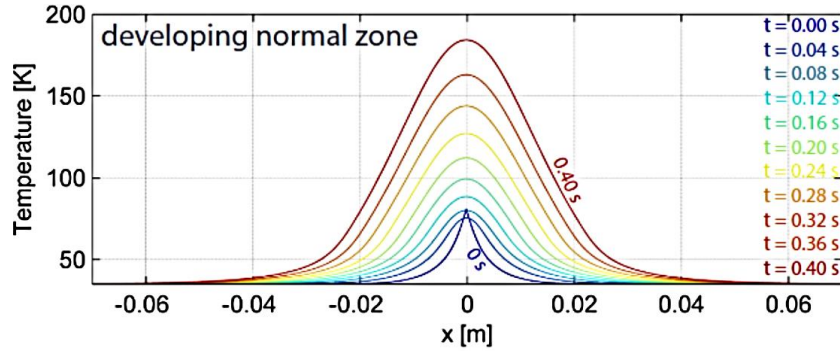


Figure 7. Demonstration of the transient solution of a 4 cm normal zone development inside of a ReBCO coated conductor at 35 K and 90% $I_c$  shows how the temperature can reach almost 200 K within 0.4 s [39]

## Conclusion and thesis motivation

This section highlighted the importance of HTS applications in the context of the changing energy trends. HTS applications provide attractive solutions to a lot of the energy needs like HVDC protection, low power fusion reactors and efficient long-distance power transmission from offshore renewable generation sites. However, there are four key challenges that HTS materials have to overcome before they can be deployed on a larger scale: cost, cooling, reliability and acceptance. The challenge this thesis will address is the challenge of reliability which arises due to the inhomogeneity of critical current along the length of the superconductor. Due to the slow NZPV and low  $n$ -value of HTS as compared to LTS, quench detection methods that are used at LTS are not usually feasible for HTS protection. This thesis will therefore cater to the need of quench detection methods in HTS and develop a fast and economical hotspot detection technique with a response time faster than existing quench detection methods to make HTS applications feasible and robust for large scale use in the power sector.



# 2

## The European Union project FastGrid

The FastGrid project overview mentioned in this chapter has been published in:

P.J. Tixador, A. Akbar, M. Bauer, M. Bocchi, A. Calleja, C. Creusot, G. Deutscher, F. Gomory, M. Noe, X. Obradors, M. Pekarcikova, F. Sirois, Some results of the EC project FASTGRID, IEEE Trans. Appl. Supercond. (2022) 1. ([Link to publication](#))

ECOFLOW project began in 2010, with the goals of developing and integrating a resistive SFCL in the electric grid [40]. The device that was developed was a YBCO based medium voltage AC device, which was successfully tested at Centro Elettrotecnico Sperimentale Italiano (CESI), Italy. While, the project was a demonstration of the operability of SFCLs in existing grids, the cost analysis gave a prohibitive number of 200 €/kA/m for the superconductor used to make the device. The device while suitable for fault current handling, was too expensive to be replicated and installed in multiple locations. It was also not a DC device, hence was not suited for HVDC grid protection. This together with the changing energy trends set the defining goals of the *European Union project FastGrid*.

### 2.1 FastGrid: Building an optimized Superconducting Fault Current Limiter

The FastGrid project commenced in 2017 with twelve international partners (three of which were industrial) from eight different countries. The goal of the project was to design a cost-effective high voltage (DC) resistive SFCL device that could be used for the future MTDC grids. A major contribution to the high cost of a SFCL device comes from the manufacturing of HTS tapes. Currently, most HTS tapes are manufactured with multiple layers around a thin superconducting layer which is a few micrometers thick as shown in Fig. 8. The superconducting material has the chemical formula  $(RE)Ba_2Cu_3O_7$ , where RE is any rare earth element. Hence, such conductors are often referred to as REBCO coated conductors. Additional layer of stabilizer can be added for electrical and thermal stabilization. The thickness of this stabilizer is determined according to the application and specification required from the HTS tape. In the case of SFCL for example, the tape architecture can determine the safety margins of the SFCL device and the recovery time.



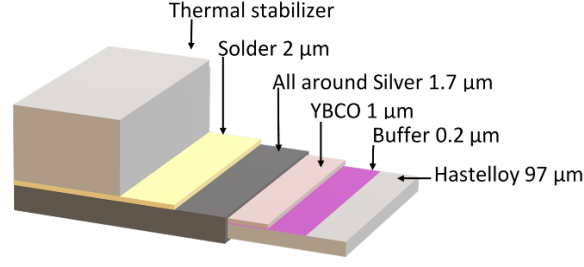


**Figure 8. The architecture of a thermally stabilized 2G HTS tape with all its layers**

The cost of the superconductor for a SFCL device is given by the equation (2) where  $C_{SC}$  is the cost of the superconductor per unit critical current and per unit length [41]. Expanding the equation by substituting for the length as the ratio of the voltage across the superconductor and the electric field under limitation ( $l_{sc} = \frac{V_{SC}}{E_{lim}}$ ) and substituting for the critical current ( $k_a = \frac{I_c}{I_a}$ ) gives equation (3) where  $k_a$  is the ratio of the rated current and critical current and is defined by the grid operators. From this equation (3), the two parameters that can be controlled to adjust the cost are  $C_{SC}$  and  $E_{lim}$ . Increasing the critical current can decrease  $C_{SC}$  and hence the cost, while enhancing the electric field under limitation is another way to decrease the cost.

$$Cost_{SC} = C_{SC} I_c l_{sc} \quad (2)$$

$$Cost_{SC} = C_{SC} k_a I_a \frac{V_{sc}}{E_{lim}} \quad (3)$$

The cost of HTS tapes is a big obstacle in the way of acceptance for superconductors in large scale power applications. The cheap competitor copper which costs only a few tens of \$/kAm, sets the bar one order of magnitude lower for HTS tapes (the price of YBCO conductor at present is around 400 \$/kAm) [42,43]. If sufficient demand is generated and HTS tapes are produced in bulk, the cost has the potential to go down to 50 \$/kAm according to experts, also illustrated in Fig. 9 [44].

The FastGrid project began with the goal of minimizing the conductor costs in order to build a cost effective SFCL device suitable for HVDC grid protection in terms of operability as well as economically. In order to minimize conductor costs, the superconducting tapes had to be optimized. In order to enhance the electric field under limitation, it is important to establish the relationship between the mean specific heat capacity per unit volume ( $C_p$ ) and the resistivity of the superconductor ( $\rho$ ), given in equation (4), where  $\Delta t$  is the fault clearing time of the SFCL device.

$$E_{lim} = \sqrt{\frac{\int_{T_c}^{T_{max}} \rho(T) C_p(T) dT}{\Delta t}} \quad (4)$$

It is apparent, that in order to achieve higher electric field under limitation, the specific heat capacity needs to be increased. This can be done by the addition of thicker thermal stabilizer layer which may favour the limitation field enhancement, but would increase recovery time of the SFCL device (a higher mass requiring more time to cool down) and would also lead to thicker conductors which are not suitable for winding SFCL pancakes. It should be noted here that higher electrical stabilization decreases the limitation electrical field which leads to increased cost hence the FastGrid conductor only had a thin layer of 1.7  $\mu m$  silver for electrical stabilization.

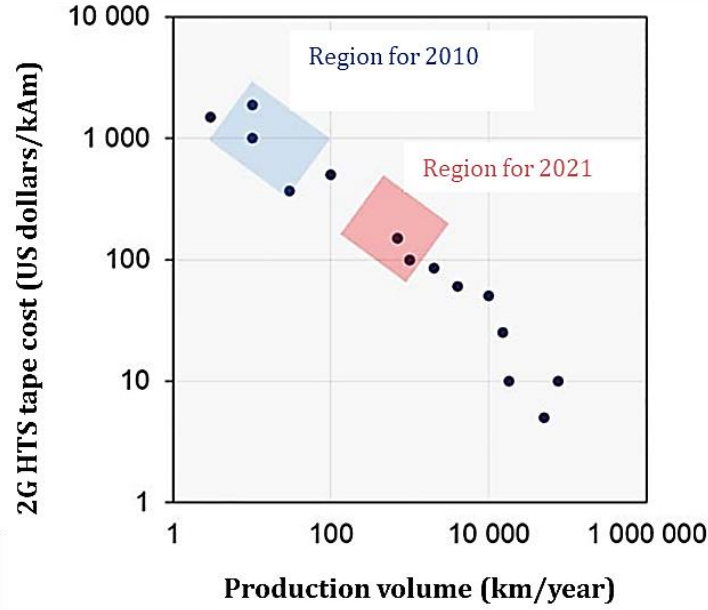


Figure 9. The projected costs of 2G HTS tapes compiled by the CEO of SuperOX from [45–47]

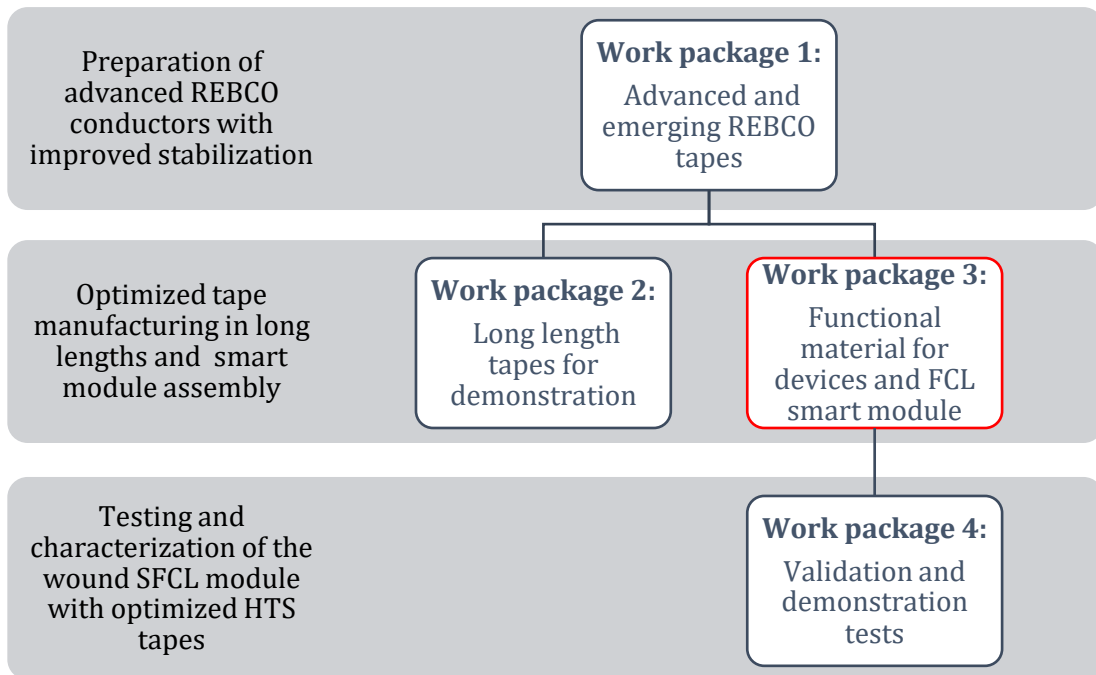


Figure 10. A break down of the work packages for the FastGrid project and the relevance of this thesis in the scheme outlined in red

The FastGrid project therefore aimed at improving the limitation field researching innovative ways without running into the aforementioned problems. The project was divided into multiple work packages (four of which are showcased in Fig. 10), where work package 1 aimed at exploring different techniques to optimize the HTS tapes. These included the approach of using a sapphire substrate capable of reaching high electric fields higher than 1000 V/m, optimizing the thermal stabilizer layer by using Hastelloy and exploring other suitable high heat capacity layers. The target limitation field that FastGrid aimed to achieve was twice that of the Eccoflow conductor: 100 V/m (clearing time of 30 ms). In order to increase the critical current, FastGrid opted

to operate at a liquid Nitrogen bath temperature of 67 K instead of 77 K as at lower temperature, the critical current increases. These specifications of the FastGrid SFCL device are mentioned in Table 2.

**Table 2. The specifications of the FastGrid SFCL device**

<b>Operating temperature</b>	67 K
<b>Bath pressure</b>	2.5 bar
<b>Pancake voltage</b>	5 kV
<b>Number of pancakes</b>	10
<b>Number of conductors</b>	2
<b>Operating current</b>	1.2 kA
<b>Critical current</b>	2-2.5 kA
<b>Clearing time</b>	30 ms
<b>Maximum temperature</b>	500 K
<b>Limitation electric field (target)</b>	100 V/m

The device is a high voltage DC device, comprising 10 pancakes (880 mm in diameter) rated 5kV each, with two conductors in each pancake wound in a non-inductive bifilar type winding shown in Fig. 11. The FastGrid pancake made use of a HTS tape produced by Theva, which was produced with a 500  $\mu\text{m}$  thermal stabilizer made of Hastelloy and a 50  $\mu\text{m}$  Hastelloy substrate. Each conductor was 34 m long giving a total of 68 m of HTS tape wound per pancake. The critical current as per Theva's TapeStar measurements was in the range of 600-800 A at 77 K which was also measured experimentally for each pancake at SuperGrid Institute Lyon (SGI) [48]. The TAPESTAR<sup>TM</sup> enables rapid, high-resolution, non-contact quality inspection of a superconducting tape [49]. The device can be used for all types of HTS tapes (1G or 2G) and gives continuous scans of the critical current along the tape length with millimeter resolution, which enables locating local weak points and non-uniformities in the superconductor critical current. An example of a TapeStar measurement for a 10 m long sample is shown in Fig. 12, where it can be seen how the critical current varies along the conductor length between 330 A and 700 A. Through these measurements, it is also possible to note the position of the weak points (with low critical current) along the length of the superconductor.

Conductor optimization therefore, is not complete without improving the fabrication process of HTS tapes to ensure a lower variation of critical current along the superconductor length. Another objective of the FastGrid project therefore, was to deal with the issue of critical current inhomogeneity across the superconductor length. Fig. 13 shows the distribution of tasks in order to deal with this issue. Industrial partner Theva, worked on improving this at the manufacturing level with the aim of reaching a critical current variation of less than five percent. Meanwhile, academic partners worked on exploring the Current Flow Diverter (CFD) concept to mitigate the effect of hotspots that arise due to the critical current inhomogeneity. CFD allows the enhancement of the NZPV which enables the homogenization of the quench thereby reducing the local temperature elevation. The goal was to manufacture the optimized HTS tapes in long lengths that

could be used to wind the SFCL pancake. However, since the problem of hotspots is unavoidable this SFCL device had to be functional with a proper hotspot detection technique in place to protect the device from damage. This was where the foundation of this thesis was laid.

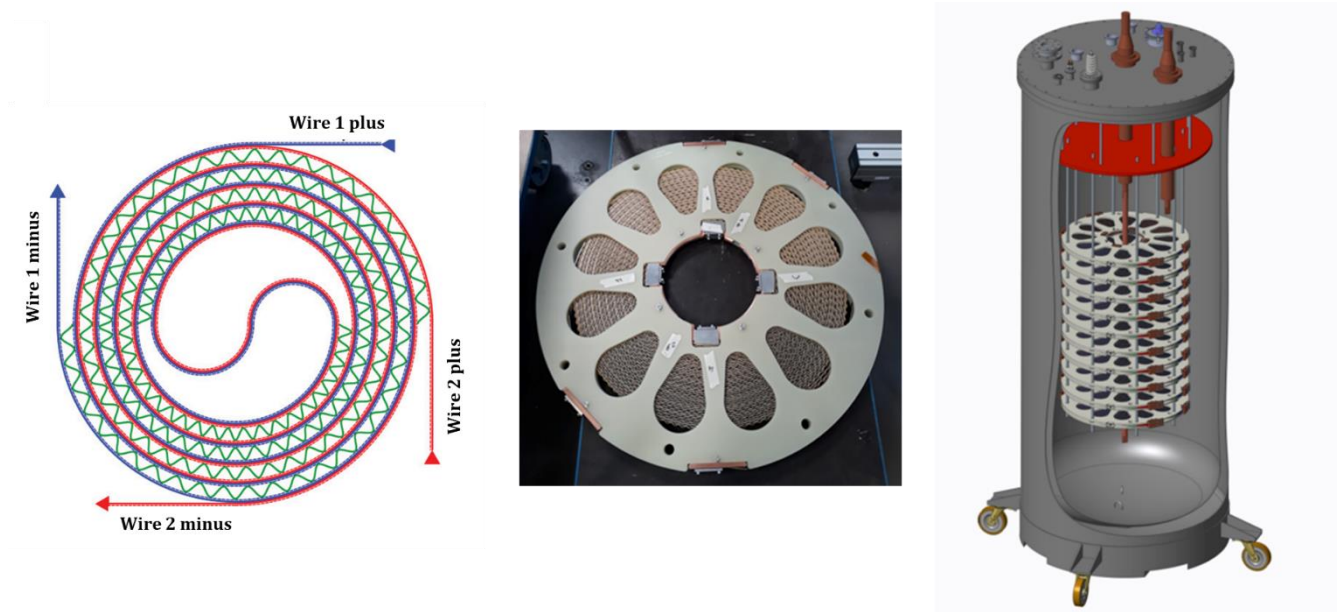


Figure 11. An illustration of the non-inductive bi-filar winding (left) for the winding of the pancake [21], a pancake, the building block of the SFCL device (center) and the illustration of the FastGrid device with ten pancakes each wound with a bifilar winding (right) courtesy SuperGrid Institute, Lyon

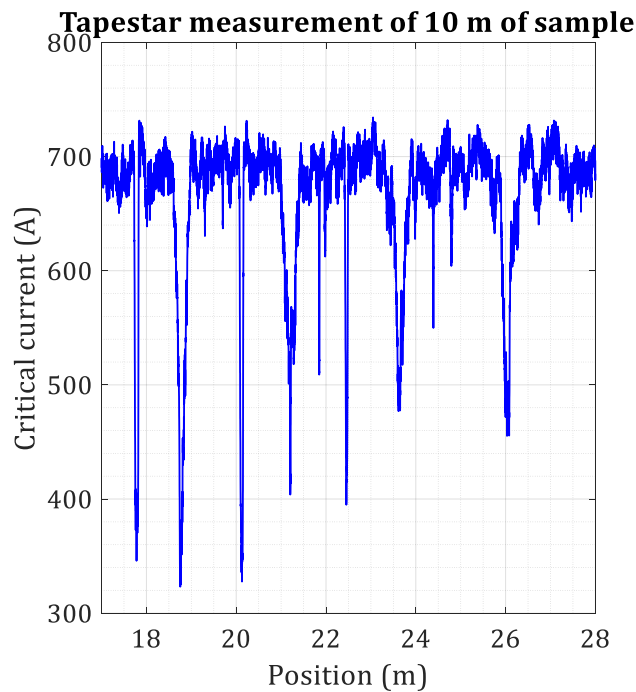


Figure 12. A Tapestar plot for 10 m long Theva tape (TPL5121) with critical current 330 A

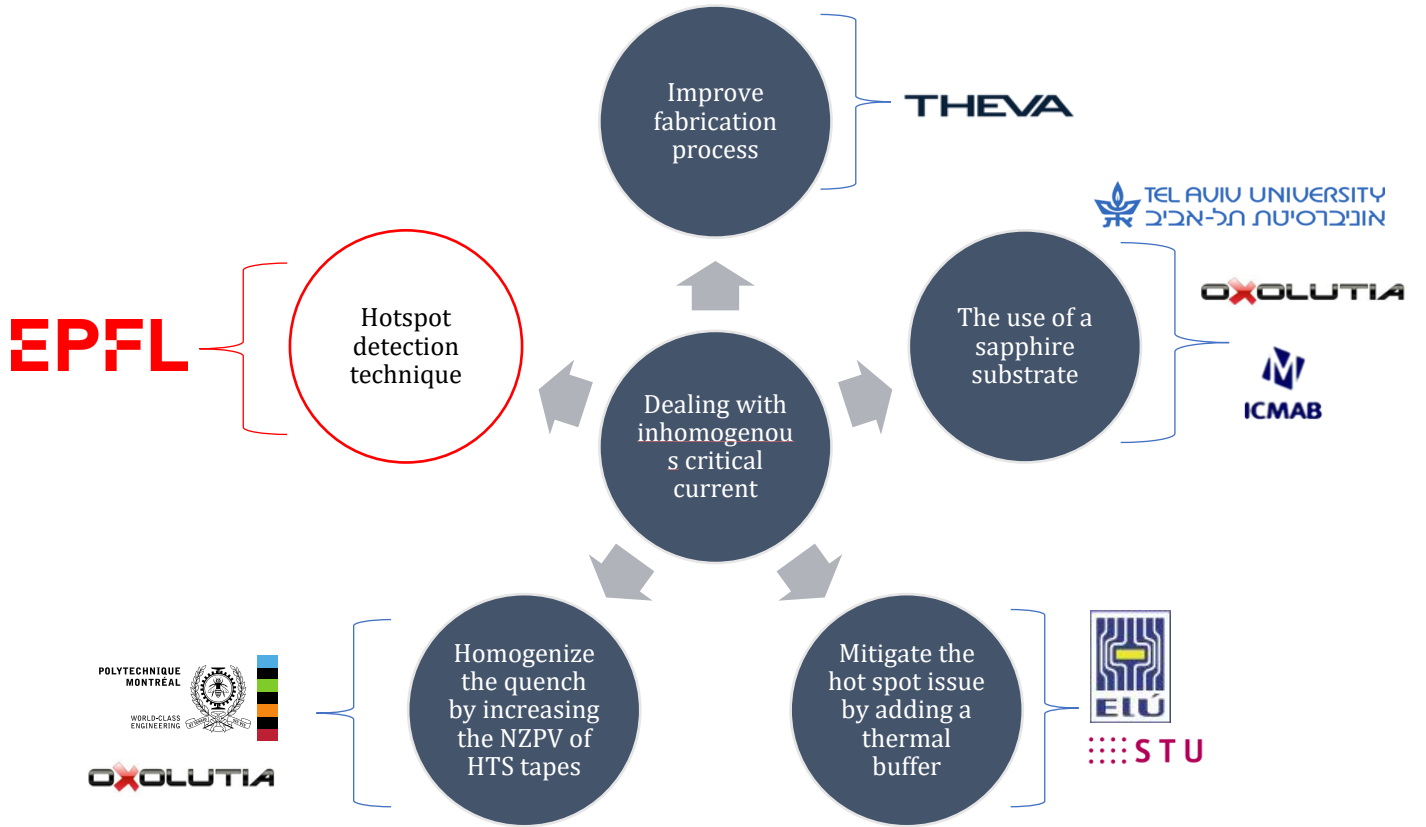
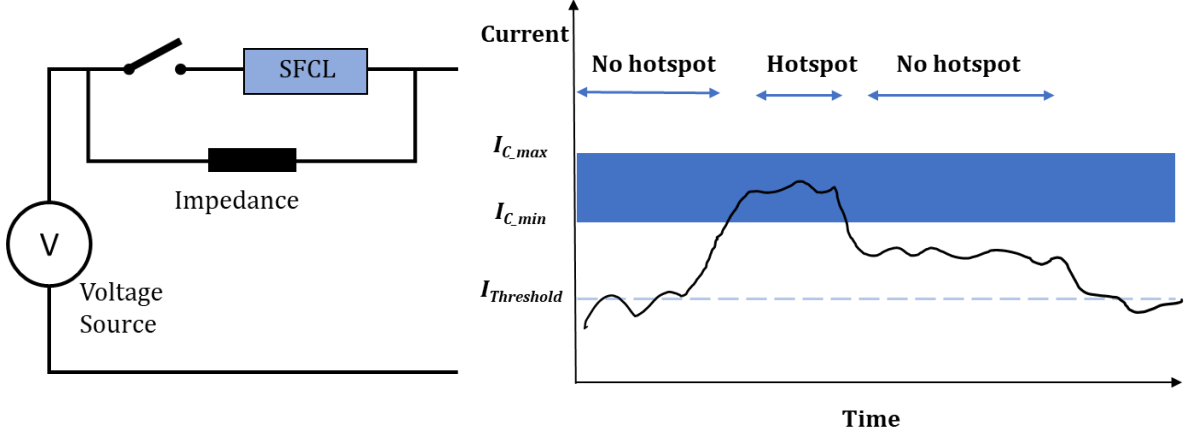


Figure 13. A break down of the FastGrid tasks to deal with critical current inhomogeneity in superconductors and the role of EPFL and this thesis in the project

## 2.2 Existing protection mechanisms for Superconducting Fault Current Limiters

It has been established in the previous chapter, how HTS are prone to hotspots due to the inherent inhomogeneity of critical current. This means that any power application using HTS tapes is in need of a proper health monitoring system. This applies to SFCLs as well. The current way to protect the SFCL device in the grid remains inefficient and infeasible. In order to use SFCLs in the grid, grid operators add a DC breaker in series with each SFCL device and define a current threshold which is usually a value below the critical current band of the superconductor. If the current in the line increases beyond this current value, the circuit breaker is opened even when there is no certainty about the SFCL device being in danger of damage. This is illustrated in Fig. 14 which shows the schematic of the SFCL device in series with the circuit breaker and in parallel with an impedance which is usually in the form of an Air Coil Reactor (ACR) for AC systems and a resistance in the case of DC systems. Fig. 14 also shows a hypothetical scenario of the operating current fluctuation (solid black line) and how it varies in reference to the defined threshold for SFCL protection (dotted blue). The graph also shows the critical current band of the superconductor (in blue). In this figure, the operating current crosses the threshold three times, but on only one occasion is it lying in the risky hotspot domain in the critical current band where only a few points in the superconductor have transitioned to a resistive state. Therefore, in such a situation, the circuit breaker would be opened three times but the SFCL device is at real risk of damage only

once. This technique to protect the SFCL is extremely inefficient leading to unnecessary shutdown of the device (and the load) even when there is no fault. Using current as the parameter to deal with the operating current fluctuation is an inefficient way leading to frequent opening of the DC breaker even when the SFCL device is in no danger of damage. It is also impossible to predict whether there is an actual hotspot within the superconductor using this technique.



**Figure 14.** A schematic of protecting the SFCL using current thresholds with a circuit breaker in series (left) and a hypothetical scenario of grid operating current variation and the inefficient opening of the circuit breaker even in the absence of hotspots (right)

In existing AC grid infrastructure, ACR are most commonly used for fault current limiting. They are coils with low ohmic resistance but high inductive reactance to limit short circuit current. While ACRs are easy to fabricate, require low maintenance and are low cost they come with the disadvantage: they introduce a constant impedance in the system and incur constant voltage losses. The ACRs also have stray magnetic fields which may introduce eddy currents in nearby grid elements. Currently, when a SFCL installation is made in a AC grid, the ACR is left in place in addition to the SFCL for redundancy in case of SFCL device damage. In this case, even though ACR is left in place, they do not incur voltage losses as they are in parallel to the SFCL device through which all the current flows. This is the case for the SFCL device installed in Moscow and also for the SFCL devices installed by Nexans [24,50]. While devices like the ones being tested by Korea Electric Power Corporation (KEPCO) use the overcurrent protection method described earlier. It is appropriate to say that both ways to protect the SFCL device is an indirect and inefficient way of health monitoring without any real information regarding the risk status of the device itself [22].

## 2.3 Thesis motivation and aspirations

The two main motivations behind this thesis are:

1. Need of a suitable fault current limiting technique for MTDC systems.
2. Need of a suitable protection mechanism for the SFCL device.

While SFCL is a solution to the motivation listed in bullet point number 1, the SFCL device feasibility is yet to be demonstrated for a MTDC system. Work needs be done for the SFCL device optimization, cost reduction and most importantly on its health monitoring. When the question of health monitoring comes in, a set of criteria and margins need to be established that have to be met with the proposed health monitoring method. In the case of this thesis, the hotspot detection time criteria were set by the specifications of the

FastGrid SFCL device, more importantly the FastGrid conductor. With the FastGrid conductor, the reaction time required to detect the hotspot plus open the circuit breaker was 30 ms, which meant that the hotspot had to be detected in under 15 ms. The other criteria stemmed from the need of an efficient shutdown of the SFCL device. The protection mechanism for SFCLs highlighted in section 2.2, is not an efficient way to protect the device, leading to device shutdown even in the absence of hotspots. This thesis aspired to develop a way for guaranteed hotspot detection so that the device is only disconnected in the case of a real risk situation. As for, the sensitivity of the hotspot detection technique, this thesis wanted to ensure that the hotspot detection technique developed should be able to detect a single hotspot. The different types of thermal runaway threats a SFCL device faces are shown in Fig. 15 which can range from a single hotspot to multiple hotspots to a clear fault.

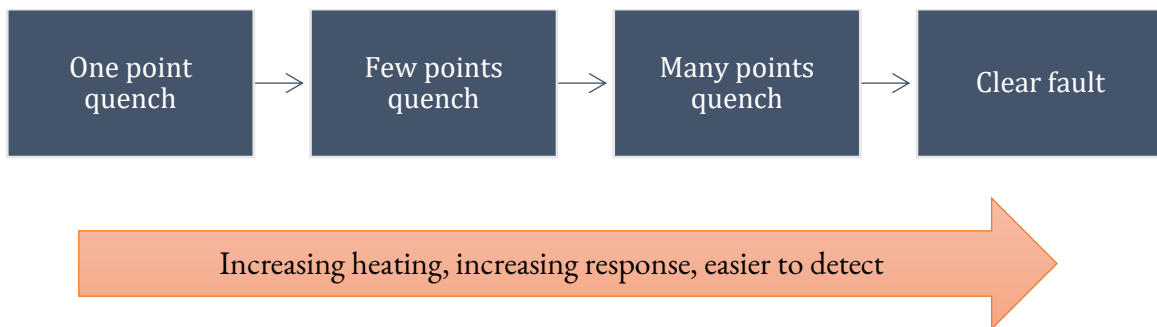


Figure 15. An illustration of the hotspot cases a SFCL device may experience ranging from a one point quench (hardest to detect) to many points quenching (easiest to detect) in a SFCL device

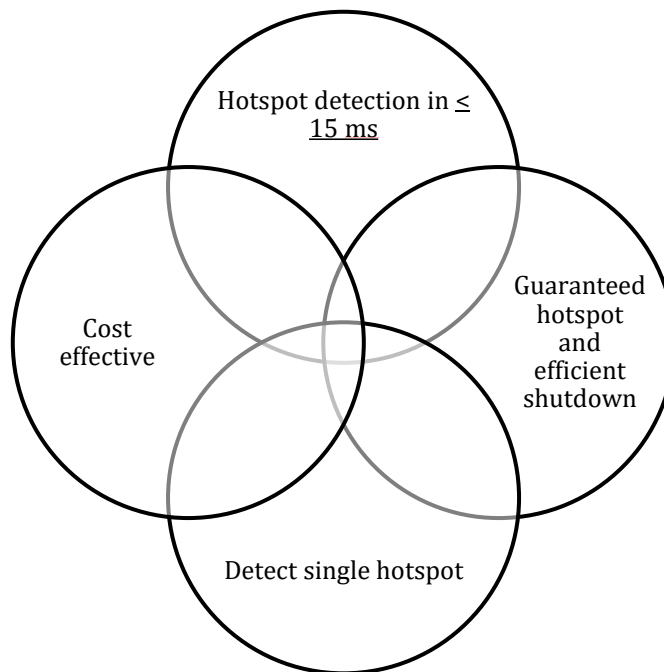


Figure 16. The requirements this thesis had to meet while developing and testing a hotspot detection technique for HTS power applications

A single point heating would produce the smallest response and hence would be the hardest case to detect. It should be noted that a clear fault is not a problem for the SFCL device as the entire superconductor transitions to normal state without any risk of local thermal runaways. The criteria that was set therefore, was to detect

the hardest case of a single hotspot to ensure that the detection technique would not miss the hardest cases and would for sure detect the easier cases of multiple hotspots. The last requirement was that of economical feasibility. The hotspot detection technique had to be economically feasible so that it would be suitable for large scale deployment. All these criteria are displayed in the diagram shown in Fig 16. The goal for this thesis was to full fill all these requirements and lie at the intersection of the diagram in Fig. 16.

## Summary

This chapter outlined the motivation and goals of the FastGrid project and set the goals and aspirations for this thesis. FastGrid aimed at optimizing REBCO tapes to build a cost effective HV SFCL device suitable for HVDC grid protection. Even though the project aimed at reducing the critical current variation in the REBCO tapes by improving the manufacturing process, the inherent critical current inhomogeneity still poses a risk of hotspots in the SFCL device. In order to protect the SFCL device from thermal runaways, a hotspot detection mechanism was needed that could meet the reaction time requirement of 30 ms set by the FastGrid device specifications. Currently, no hotspot detection technique that exists is capable of being this fast for hotspot detection in HTS applications. The goals of this thesis were to develop a fast and economical health monitoring technique that could detect hotspots within 10 ms, not only for the FastGrid device but also for HTS power applications in general, in order to make them robust against hotspots and increase their viability for use on a wider scale in large scale power systems.







# 3

## An innovative fibre optic based health monitoring system for superconductors

The MZI based hotspot detection technique introduced in this chapter has been patented:

Z. Yang, A. Akbar, Patent number: WO2021038505 (A1), Hotspot monitoring system for superconducting device, (2021). ([Link to patent](#))

Information superhighway was a term that was extensively used in the 1990s in research papers and news articles alike, referring to the ability of high speed transmission of large amount of data. Submarine fibre optic cables were (still are) a backbone of this superhighway, replacing 50 million digital phone channels with a single cable capable of high capacity and high speeds of data transmission [51]. Following extraordinary progress, the fibre optic technology since then has plateaued, a trend not foreign to technological inventions. However, there is another application for fibre optics that despite its huge potential has struggled in comparison to their information transmission application: *their use as sensors*.

### 3.1 Why fibre optic sensors?

An optical fibre is made of three elements: the core, the cladding and the coating. A cross section of an optical fibre is shown in Fig.17 with the thickness of each layer [52]. The core is the part of the optical fibre through which the light travels and is usually made of glass. In single mode fibres, the core provides a single pathway hence the thickness of the core is approximately 8  $\mu\text{m}$ . In multimode fibres, the core is thicker (up to 100  $\mu\text{m}$ ), providing multiple pathways for light to travel. The core is surrounded by a material with lower refractive index called the cladding which contains the light within the core and enables propagation via total internal reflection. The cladding is surrounded by the coating which cushions and protects the fibre. The coating is usually made from a hard and soft layer of acrylate, serving the purpose of protecting the fibre from the environment, humidity and external abrasion. There are a variety of coatings available for optical fibres commercially, including polyimide, polyurethane, polyethylene etc, each providing different kinds of protection to the fibre [53]. The diameter of the coating has traditionally been 250  $\mu\text{m}$ , but there are a variety of fibre diameters commercially available suited to a range of applications.

The research into optical fibres sensors began more than forty years ago. Optical fibres, are attractive as sensors due to their light weight, small size, immunity to electromagnetic interference (EMI) and high sensitivity.

Many fibre sensing techniques have been investigated for myriad of applications, however, in many cases these sensors have to compete with existing mature sensing methods like electronic detection [54]. In most cases, the advantage and feasibility of optical fibre sensors over conventional sensing mechanisms has to be demonstrated and has to be convincing enough for the user to opt for it. The main criteria of most users when it comes to sensors, is good performance, reasonable cost and ease of usability. Optical fibre sensors should therefore be available as complete system with the detection part and the signal processing part, in order to stand a chance against existing sensors.

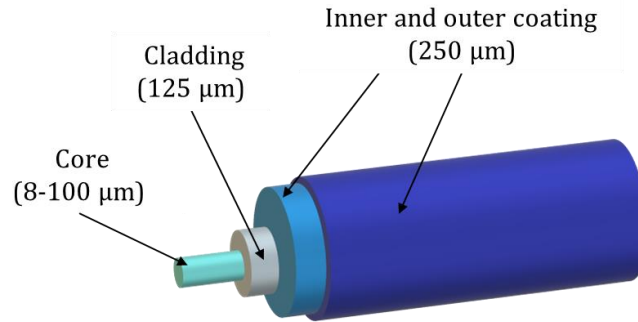


Figure 17. Cross section of an optical fibre

Fibre optic sensors have great potential for health monitoring applications due to the following reasons [55]:

1. **Distributed sensing:** Optical fibres are capable of performing distributed sensing and hence can enable the monitoring of the entire object without loss of information.
2. **High sensitivity:** Optical fibres are capable of measuring numerous quantities like strain, temperature, pressure, often simultaneously making them an attractive way for health monitoring.
3. **Flexibility:** Optical fibres are small and flexible enabling their integration on complex surfaces and in difficult-to-reach areas capable of both local (single point) and distributed measurements ranging to several tens of kilometers.
4. **Immunity to EMI:** Optical fibres can easily operate in electrically noisy environments and can transfer sensing data over a long distance without the problem of EMI contamination.
5. **Electrically insulating:** Optical fibres are non-conductive and hence suitable for integrating with a variety of hosts with minimal impact to the host structure.
6. **Economical:** Optical fibre costs per meter are extremely low and very feasible in comparison to conventional sensing techniques.
7. **Long lengths:** Continuous long lengths of optical fibre are easily available (typically 50 km) which makes them easy to use as sensors in large scale applications.
8. **Durability and long life:** Silica (the main component of optical fibres) is a very durable material with corrosion resistant properties and capability to withstand high tensile loading (up to 5% elongation).
9. **High temperature endurance:** Silica core fibres can measure temperature ranging from 70 K to 1100 K without damage.

### 3.1.1 Strain and temperature monitoring using fibre optic sensors

An optical fibre sensing system is composed of four elements: a light source, optical fibre, a sensing element or transducer and a detector shown in Fig. 18. The principle of operation of an optical fibre based sensor is that

the transducer modulates some parameter of the optical set up which can be intensity, wavelength, polarization or phase which gives rise to a change in the characteristics of the signal received at the detector.

Fibre optic sensors can be classified on three different basis [55]:

1. The light characteristic (intensity, wavelength, phase, or polarization) that is being modulated by the sensed parameter.
2. The location where the light is being modulated: outside the optical fibre (extrinsic) or inside the fibre (intrinsic). In the former, the light is modulated outside of the optical fibre while fibre itself remains unchanged. In the latter, however, environmental effects modulate the light as it propagates through the fibre,
3. The extent to which the object is being monitored: If the sensor is only sensing a local point it constitutes a local sensor, if multiple points are being sensed it's a quasi-distributed sensor and if the entire length is being sensed it is classified as a distributed sensor

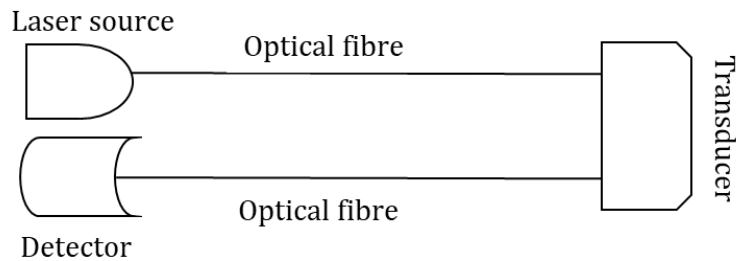


Figure 18. Basic components of a optical fibre based sensor system

Distributed fibre optic sensors allow sensing in long lengths and hence have been the sensor of choice for large structural applications. Distributed sensors make use of the modulation of light in the fibre due to external changes, making them intrinsic sensors. The external parameters that modulate the light can be strain, temperature and pressure for example. This makes fibre optic sensor a useful way to detect change in these external parameters. Strain and temperature are two parameters that are more commonly monitored using fibre optic sensors. Rayleigh backscattering and Brillouin scattering using Optical Time Domain Reflectometer (OTDR) are two well-known distributed fibre optic sensors that have been used in various applications to monitor strain and temperature changes.

Table 3. Fibre optic sensors for health monitoring

Sensor	Intrinsic/Extrinsic	Sensing type	Measurands	Modulated parameter
<b>Fabry–Perot</b>	Both	Local	Strain	Phase
<b>Fibre Bragg grating</b>	Intrinsic	Quasi-distributed / Local	Strain	Wavelength
<b>Raman/Rayleigh I</b>	Intrinsic	Distributed	Temperature / Strain	Intensity
<b>Brillouin</b>	Intrinsic	Distributed	Temperature / Strain	Intensity

Table 3 shows some common fibre optic sensors used for health monitoring and their classification based on the criteria explained before. Optical fibre sensors have found place for health monitoring in a range of applications: civil engineering, aviation industry, military vessels, wind turbines for example. There is another domain where optical fibre sensors are being considered and investigated as potentially superior sensors: superconductivity.

### 3.1.2 Fibre optic sensors for cryogenic temperatures

Superconductors operate at cryogenic temperatures, presenting a harsh and challenging environment for sensors. Fibre optic sensors for cryogenic environment have not been widely investigated. However, multiple fibre optic sensors have been explored for superconducting applications, especially in superconducting magnets for quench detection [56]. Resistive sensors, have remained the most common way of measuring temperature and strain in cryogenic and superconducting environments, however the problem of EMI, additional wires and power electronics has led to the use of optical fibre sensors, particularly Fibre Bragg Grating (FBG) sensors [57]. FBG sensors is a form of wavelength modulated sensor whereby the fibre core is exposed to an intense UV interference pattern to construct periodic changes in the refractive index along the core length. This refractive index variation forms an interference pattern which is referred to as a grating. As light propagates through the grating it only reflects a wavelength component at the Bragg wavelength. When the fibre is subject to strain or temperature changes, the grating pitch changes, resulting in a change in the reflected Bragg wavelength. FBG sensors have been successfully demonstrated for monitoring strain in superconducting accelerator magnets at 4 K in Nb<sub>3</sub>Sn magnet coils manufactured at CERN [58,59]. The use of FBGs is also being investigated for quench detection in fusion magnet cables [60]. The disadvantage for FBG sensors is the discrete nature of sensing, which means loss of information at the points that are not being sensed. This does not pair well the slow NZPV in HTS conductors and can be damaging to the HTS application.

Contrary to FBG sensors, distributed optical fibre sensing enables the measurement of temperature and strain continuously along the length of a single fibre. This is particularly interesting for monitoring large structures and in the case of superconductors: the entire conductor length. Rayleigh backscattering is a distributed sensing technique that has been patented for quench detection in HTS magnets [61]. Rayleigh backscattering works similar to FBG but in this case the refractive index varies continuously along the length of the fibre due to naturally occurring fluctuations and defects in the fibre. Each fibre is unique in terms of defects, giving each fibre a unique back scattered spectrum as light propagates through the fibre. When light of a known wavelength is shone into the fibre, some of this light back scatters containing the original Rayleigh wavelength and additional components that contain information about the local fibre properties (particularly strain and temperature). The Rayleigh backscattering spectrum is therefore first measured in a reference condition and then after with change in temperature or strain imposed on the fibre, these two spectra are compared to quantify the spatial distribution of the change in temperature and/or strain. With Rayleigh backscattering therefore, it is possible to detect hotspots along with the information about the location of the defect in HTS magnets. Experiments in HTS magnet coils have been able to detect hotspots as small as 5 mm using Rayleigh backscattering and the quench detection delay has been reported in the range of 30 ms to 100 ms [62,63]. The high spatial resolution, however, leads to a large amount of data which requires substantial computational power for real-time quench detection and hence reduces the temporal sampling resolution.

Other optical methods for continuous thermal sensing are being explored; for example, the use of Raman scattering to monitor temperature in solder impregnated HTS coils [64]. Typically for optical fibres the thermal sensitivity decreases at low temperatures due to the decrease in their thermo-optic coefficient (this will be discussed later on in Chapter 6). Their thermal sensitivity becomes more problematic at Liquid Helium temperatures. Therefore, techniques of recoating the optical fibres with materials that have a larger thermal expansion coefficient than silica are being explored to increase the thermal sensitivity of fibre optic sensors at lower temperatures [65].

## 3.2 The Mach-Zehnder method

The techniques mentioned in Section 3.1 showcase the developments and trend of fibre optic sensors for monitoring HTS magnets. However, these techniques did not fulfill the requirements for the health monitoring of the FastGrid SFCL device. FBG comes with the risk of not detecting hotspots that occur outside of the sensing points while Rayleigh backscattering does not meet the time and cost requirement for quench detection set in the FastGrid project. In this thesis therefore, a third kind of distributed sensor was investigated for HTS applications: the Mach-Zehnder Interferometer (MZI).

The MZI sensor works based on the modulation of the phase of the light by external influences. The use of fibre optic sensors using phase modulation was first investigated for LTS magnets in 1987 by Tsukamoto et al [66]. The quench detection was investigated for a small LTS magnet and the technique was deemed less feasible than the voltage measurement sensors due to the temperature fluctuations at the boundary of cryogenic and room temperature environments. In 1997 MZI based quench detection was experimentally investigated on a large-scale LTS magnet for fusion applications near operating conditions for the Quench Experiment on Long Length (QUELL) experiments in ITER. The optical fibres used were copper coated for operation at 4.2 K for temperature based sensing and the setup was able to detect a quench in 0.17 s [67,68]. While the results were encouraging, the technique was found to be challenging in terms of fibre integration during manufacturing of the coils and also in terms of reduced temperature sensitivity at 4.2 K which made the fibre unable to detect smaller temperature changes. The MZI method for HTS specifically, has therefore been in need of investigation and optimization before it can become a worthy competitor / candidate for the health monitoring of HTS applications. It is important to stress here that the MZI method is well suited for HTS applications because the optical fibre is still sensitive at these temperatures. As was mentioned in Section 3.1.2 the sensitivity of the optical fibre decreases dramatically at LTS temperatures (around 4 K), making it difficult to use them for sensing without recoating the fibres.

### 3.2.1 MZI working principle

The MZI technique requires a simple setup shown in Fig. 19 comprising a laser source, splitter, coupler, photo-detector and two single mode optical fibres [69]. One fibre is integrated with the sample while the other fibre constitutes the reference arm of the interferometer. A polarization controller is present on the reference arm to align the polarization of light in both arms to ensure maximum peak to peak amplitude in the output interference pattern. Light is split into the two optical fibres at the input via the splitter and recombined at the output via the coupler where interference occurs. The MZI output at the photo-detector (i.e. the interference pattern) can be expressed by equation (5):

$$\text{Interference Pattern} \propto [1 + \cos(\phi_{12} - \pi + \Delta\phi_H)] \quad (5)$$

$$\Delta\phi_H \propto (\{1 - \rho_a\}\Delta\varepsilon + [\alpha_o + \xi]\Delta T) \quad (6)$$

Where  $\phi_{12}$  is the initial phase shift between the two light paths and  $\Delta\phi_H$  is the phase shift due to hotspot plus ambient factors; as shown in equation (6)  $\Delta\phi_H$  depends on the change in strain ( $\Delta\varepsilon$ ) and temperature change ( $\Delta T$ ) experienced by the optical fibre [13], where  $\rho_a$ ,  $\alpha_o$  and  $\xi$ , are the photo-elastic coefficient, thermal expansion coefficient, and thermo-optic coefficient of the optical fibre respectively. Together the strain and temperature contribution (as apparent in equation (6)) define the MZI response sensitivity.

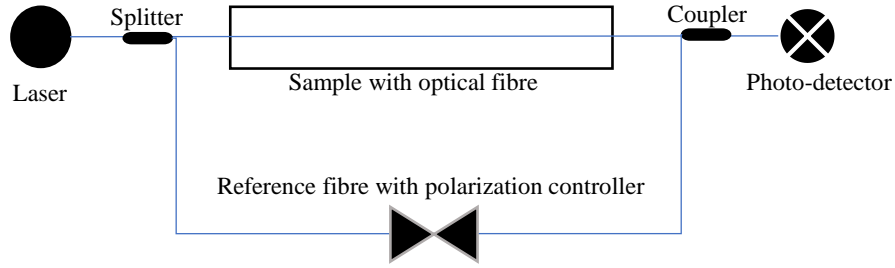


**Figure 19. The Mach-Zehnder Interferometer Schematic**

In the absence of a hotspot, both temperature and strain contributions arise due to environmental perturbations (like temperature, acoustic noise, and vibrations), which causes a slow variation of  $\Delta\phi_H$ . Hence, the MZI output in this case, exhibits slow fluctuations without any evident pattern. However, in the presence of a hotspot in the superconductor, the resulting temperature rise subjects the fibre to a temperature change while the thermal expansion of the Hastelloy imposes a strain change on the optical fibre. The two terms in equation (6) increase and  $\Delta\phi_H$  continuously increments from 0 to  $2\pi$ , within few ms, in response to the hotspot. The rapid change in  $\Delta\phi_H$  is visible at the MZI output as rapid, continuous periodic amplitude variations between 0 V and 1 V (normalized), which signals the presence of (at least) a single hotspot.

### 3.3 Comparative feasibility and cost analysis of the Mach-Zehnder Interferometer with other fibre optic sensing methods in superconducting applications

In order to select a suitable fibre optic sensor for the health monitoring of the FastGrid device, there were three criteria that had to be addressed: quench detection speed, cost and continuous sensing along the full length of the conductor. Considering the existing two main methods being investigated in superconductors (i.e. FBG and Rayleigh Backscattering), both fall short of meeting the full set of criteria. FBG is a discrete sensing technique with the risk of missing hotspots in the conductor lengths that are not being monitored. In addition, both Rayleigh backscattering and FBG do not meet the quick detection speed requirement for the FastGrid device. In terms of economic feasibility both FBG and Rayleigh backscattering require expensive hardware.

FBG sensors require a sophisticated readout unit to monitor the position of the Bragg wavelength with high accuracy. The two most common methods used are either, a broadband light source and a picometer-

resolution spectrometer, or a tunable laser and a suitable photodetector. Both these interrogation systems are bulky and costly, which makes FBG sensors an expensive option for health monitoring [70]. As a low-cost alternative to interrogate FBG sensors, compact, integrated read-units have been proposed but they are not at par in terms of performance.

Rayleigh backscattering meanwhile makes use of a commercial Optical Frequency Domain Reflectometry (OFDR) system from LUNA Tech Inc [71]. This system measures the reflected spectrum with a tunable scanning laser. The system acquires two measurements one from the reference and one from the measurement fibre. Fourier transform is used to extract temporal information from the signal. Thereafter strain and temperature can be recovered for any point along the fibre providing spatial information of the fault. The gap between the potential of this technique and its widescale use is the high hardware cost and the difficult calibration for users [72].

In this thesis, therefore, a third type of fibre optic sensor was investigated that was able to meet the FastGrid criteria. Using MZI as a sensor comes with the benefit of low cost and simple setup making it a more attractive option to use for the health monitoring the FastGrid SFCL, especially if the ultimate goal is to establish a sensor system that is economically feasible for large scale deployment in HTS applications. In the case of MZI sensors, the use of expensive hardware like tunable lasers and spectrum analyzers can be avoided [73]. In addition to cost, MZI sensor comes with the benefit of fast detection of hotspots and is able to meet the detection time criteria set by the FastGrid conductor. The drawback of using MZI for health monitoring is that the sensor, does not give information about the location of the hotspot, however that is not a bad bargain to make since the information that there is hotspot in the HTS device is sufficient to prompt the necessary protective mechanisms. Fig. 20 shows a comparison of MZI with FBG and Rayleigh backscattering sensors to signify the reason behind choosing the MZI technique for the health monitoring of the FastGrid SFCL device.

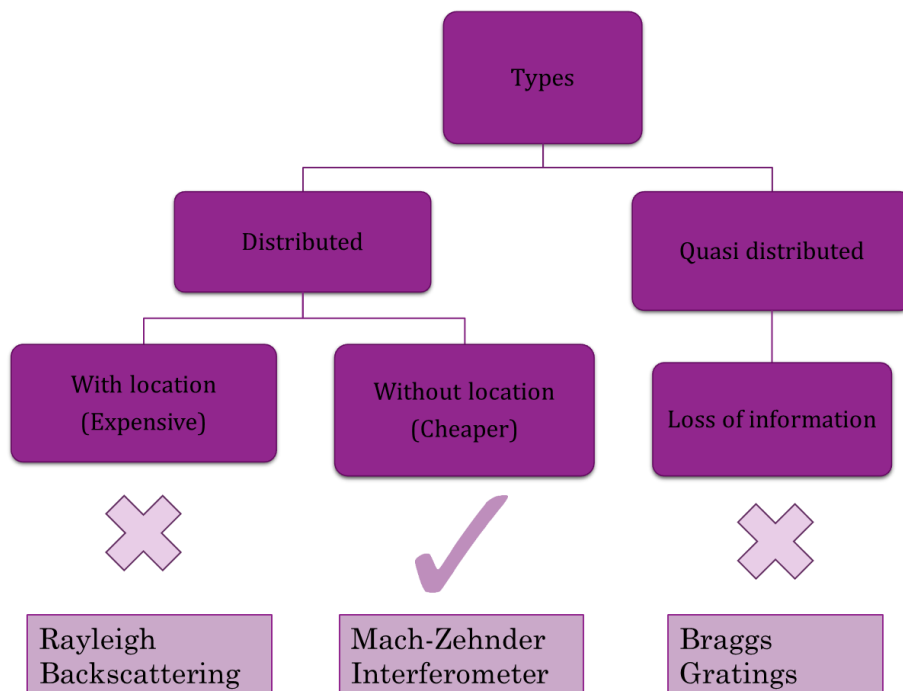


Figure 20. A decision tree showing the comparison between Rayleigh backscattering, MZI and FBG to show the reasoning behind selecting MZI



## Summary

This chapter gave an overview of fibre optic sensors and how they are being explored for quench detection in superconducting applications, especially superconducting magnets. Fibre optic sensors are attractive alternatives to electrical sensors, especially in high energy physics and superconducting power applications due to their inert nature, immunity to EMI and ease of integration. The ability of optical fibres to monitor temperature and strain changes makes them useful to monitor for hotspots in SFCLs. So far, no health monitoring technique has been developed that is capable for meeting the quick hotspot detection requirement of SFCLs. This chapter also presented a comparative analysis of existing fibre optic sensors being used for superconducting applications and the motivation behind selecting the MZI sensor for the FastGrid project and this thesis. This thesis will investigate and optimize the optical fibre based MZI sensor for HTS applications, which is capable for fast hotspot detection and requires a simple and cost-effective setup.





# 4

## Experiment Setup

Experimentation during the course of thesis was divided into two parts: testing on commercially available REBCO tapes 10 cm to 30 cm in length in linear configurations with integrated optical fibre. Once the MZI method was tested on short sample lengths, the technique was tested on a relatively longer length of 100 cm before testing it with a fault current limiter pancakes with 12 m and 17 m of conductor respectively. The experiment setup for these experiments can be broken down into the following steps:

1. Building the optical setup
2. Building the current source for pulsed current measurements
3. Preparing the sample holder to mount the HTS sample
4. Integrating the optical fibre on the HTS sample
5. Placing voltage contacts on the HTS sample
6. Data acquisition

### 4.1 Building the Mach-Zehnder Interferometer

The MZI setup requires two optical fibres, a polarization controller, a laser source, a splitter, a coupler and a photo-detector. In order to power the laser source, a laser driver is needed and a power supply is needed to power the photo-detector as well as the laser driver. Since one of the goals of the thesis was to build a simple and cost-effective hotspot detection suitable for commercial deployment, all the elements of the MZI were carefully chosen (in terms of cost and performance) and put together in the lab in the form of a compact plug and play box. This section will give a breakdown of all the elements that went into building that box.

#### A. The optical fibre

The optical fibres used during experimentation are single mode, with polymethyl acrylate coating and a diameter of 250  $\mu\text{m}$ . This type of fibre is the standard one commercially available at a low cost. One fibre constitutes the reference arm while the second fibre is integrated with the superconductor sample.

## B. Laser

The laser source is a Distributed Feedback (DFB) laser. DFB lasers are narrow-linewidth, single-frequency laser diodes that use a corrugated waveguide throughout the active region of the laser cavity [74]. A DFB laser's periodic structure acts as a distributed reflector, providing optical feedback and wavelength selection for the diode. This allows these lasers to achieve a 2 MHz or 0.1 nm typical linewidth with an excellent side mode suppression ratio. The laser used in the lab was LP1550-SAD2 from ThorLabs with a center wavelength at 1550 nm at room temperature and variation of 3 nm on each side; this spectrum is shown in Fig. 21. A DFB laser is important to ensure coherence in the MZI. Coherence length is the distance over which the laser beam can travel without experiencing a phase discontinuity. The linewidth  $\Delta\nu$  of the laser is related to its coherence length  $l_c$  by equation(7), where  $c$  is the speed of light in vacuum and  $n_g$  is the group refractive index of the propagation medium [75]. A narrow line width therefore leads to a high coherence length and hence DFB lasers are exclusively used for interferometers.

$$l_c = \frac{c}{\pi \cdot n_g \cdot \Delta\nu} \quad (7)$$

If a laser has a small coherence length, then the interference of a sample of the laser light with a time-delayed sample of the same laser light is not stable in time.

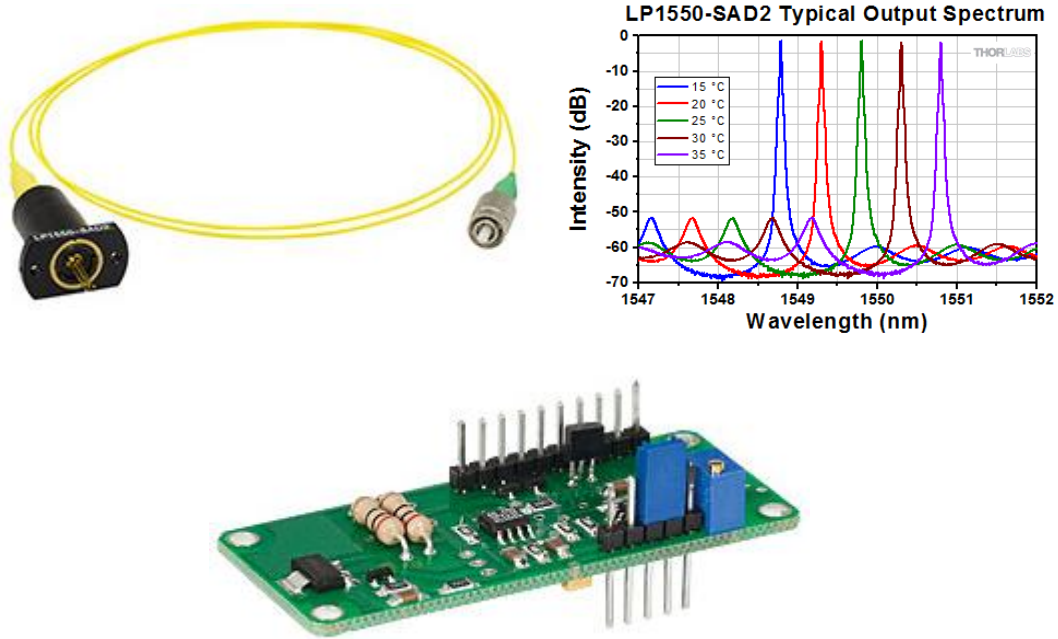


**Figure 21.** The DFB laser used to build the MZI (top left) and its wavelength spectrum (top right) [74], the laser driver used to power the laser diode with constant current (bottom) [76]

The laser operation is temperature sensitive and changes to temperature can cause wavelength shifts (also visible in the graph in Fig. 21). With the addition of a heavy heat sink coupled to the laser, this rate of temperature change in the laser is slow enough to not introduce a loss of coherence in the MZI. A heatsink was therefore coupled with the laser in the setup.

A laser driver was used to power the laser diode. The laser driver can be built from scratch on a small PCB and is also commercially available. For the MZI, a commercially available compact laser driver was used which has a tunable potentiometer that can be used to adjust the operating currenting of the laser diode [76]. The laser driver is shown in Fig. 21 and also comes with disable pin and diode protection circuitry to limit voltage transients produced by the power supply during start up, shut down, or by static shock.

### C. Polarization controller

In order for stable interference to occur the following conditions should be met [77]:

1. The two sources should be coherent.
2. The two sources should have similar amplitude.
3. The two sources should have similar polarization.

In order to ensure that the polarization is aligned at the coupler in the MZI, a manual polarization controller is connected in the reference arm of the MZI. The polarization controller used in the lab is FPC030 from ThorLabs shown in Fig. 22 which uses three waveplates (retarders) to alter the polarization state. It comprises a quarter-wave plate, half-wave plate, and quarter-wave plate in series to transform an arbitrary polarization state into any other polarization state.



Figure 22. The manual three paddle polarization controller placed on the reference arm of the MZI [78]

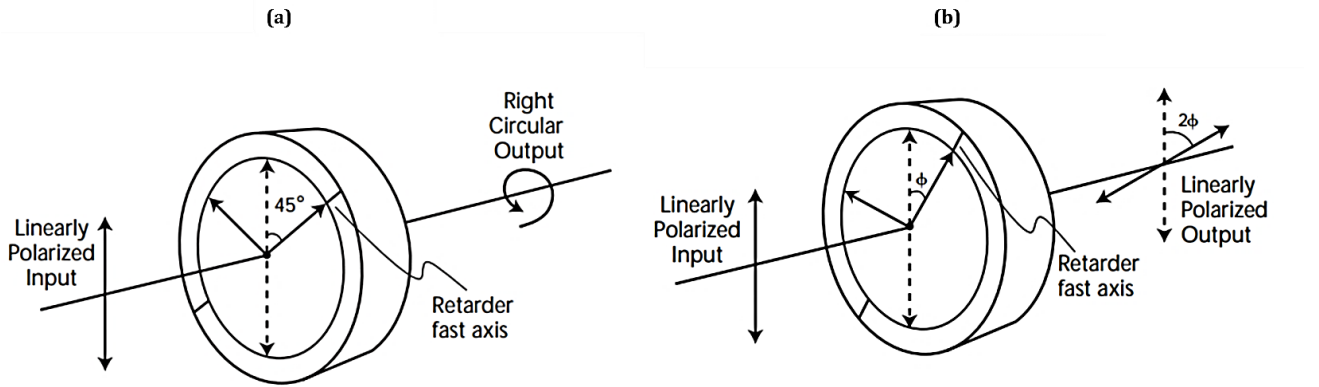


Figure 23. How the waveplates in the polarization controller change the polarization states by means of quarter-wave plate (a) and half-wave plate (b) [79]

The first quarter-wave plate transforms the input polarization state into a linear polarization state while the half-wave plate rotates the linear polarization state as shown in Fig. 23 [79]. A single mode fibre is looped

around each waveplate and as the paddles are turned the polarization of the light rotates accordingly. The goal in MZI is to align the polarization in the two arms of the interferometer to ensure a clear interference pattern.

#### D. Photo-detector

The interference pattern is observed by means of a photo-detector which converts the incident light intensity into a voltage. While commercially photo-detectors are easily available, for the MZI setup in the lab the photo-detector was made from scratch using a photo-diode to keep the setup economical and compact. This photo-diode shown in Fig. 24, converts incident light to electrical current as per equation (8) [80]. This current value depends on the responsivity ( $\mathfrak{R}$ ) of the photo-diode which is a function of the laser wavelength ( $\lambda$ ). The current can be converted to a voltage by placing a load resistor ( $R_L$ ) at the anode of the photo-diode. This voltage  $V_{PD}$  is observed at the photo detector. The circuit used to implement the photo-detector circuit is also shown in Fig. 24.

$$V_{PD} = P_{Light} \cdot \mathfrak{R}(\lambda) \cdot R_L \quad (8)$$

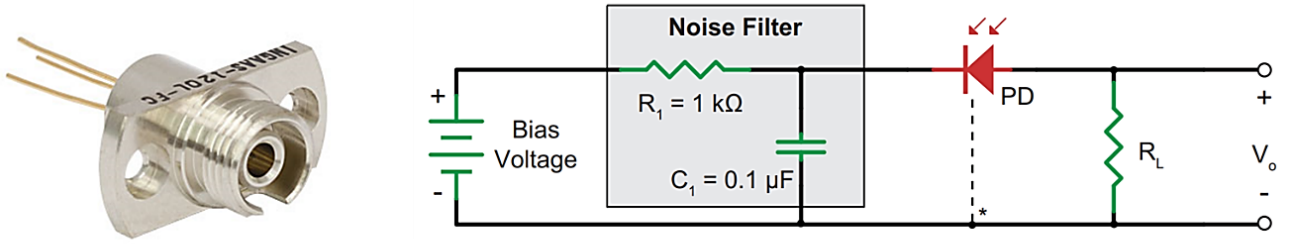


Figure 24. The InGaAs Photodiode (PD) used to build the photo-detector for the MZI (left), and the circuit used to build the photo-detector (right) [80]

#### E. Splitter and coupler

At the input of the MZI after the laser source, the light is split equally in the two fibre paths by means of a splitter. This light is then combined before the photodetector by means of a coupler. The same optical tool can be used as a coupler or splitter depending on how it is connected in the interferometer. In the case of MZI two wideband fibre optic couplers with a 50:50 ratio are used shown in Fig. 25, one is connected as a splitter and the other as a coupler.



Figure 25. Wideband Fibre Optic Splitter/Coupler [81]

### F. DC power supply for the laser driver and photo-diode

The laser driver requires a bipolar voltage supply of  $\pm 8\text{V}$  while the photo diode can operate at voltage up to  $20\text{ V}$ . Therefore a single DC power supply circuit was built to power both. The power supply was bipolar with an output voltage of  $8\text{ V}$ . The positive voltage of  $8\text{ V}$  was used to power the photo-diode while the positive and negative voltages powered the laser driver circuit. The compact linear DC power supply was built in the lab on a small PCB board, which stepped down the mains voltage and converted it to DC.

### G. Compensation lengths

It was explained earlier that DFB lasers are important for interferometers to ensure temporal coherence. DFB lasers have a narrow linewidth and hence longer coherence lengths. However, care should still be taken to ensure that both arms of the MZI are balanced in terms of lengths to ensure a clear interference pattern. In the case of experimentation, the length of the HTS sample being measured in most cases is longer than the length of optical fibre present on the reference arm of the MZI. Therefore, the remaining compensation length of optical fibre is added on the reference arm to make sure that the two optical path lengths are the same and avoid the risk of losing coherence.

### H. Attenuator

Another step that is taken to balance the two arms of the MZI in terms of light intensity, is to use an attenuator in the reference arm. The signal strength in the MZI arm with the sample is measured first and the attenuator is used to manually vary the attenuation of the signal in the reference fibre to match the light intensity in the sample arm of the MZI. The attenuator (shown in Fig. 26) allows the user to precisely balance the signal strengths in optical systems. The attenuation is changed by means of an adjustment screw. The maximum attenuation is achieved within 10 turns of the adjustment screw. The turning of the screw rotates the blocking window in the attenuator, causing a beam path deviation that changes the coupling efficiency (and hence the light intensity) in the output fibre as shown in Fig. 26.

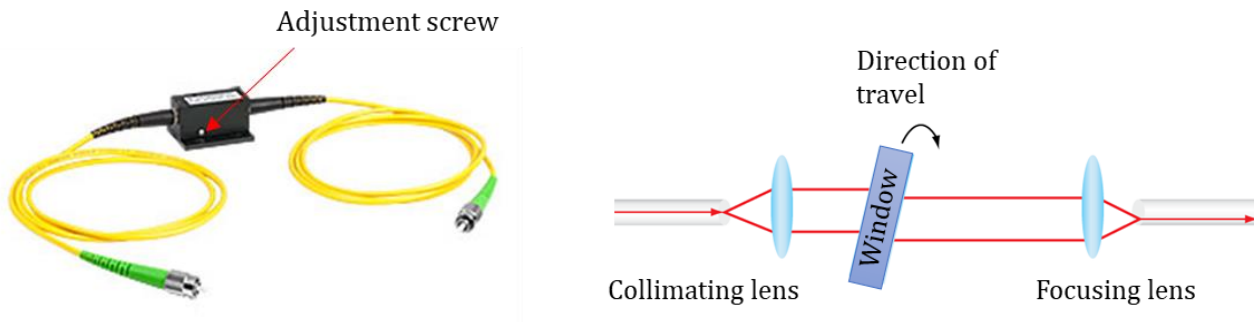


**Figure 26.** Variable attenuator used to balance the light intensity in the two optical paths of the MZI (left) and its working principle (right) [82]

## 4.2 The MZI plug and play box

All the above-mentioned components were assembled in a MZI configuration inside a compact  $20\text{ cm} \times 20\text{ cm} \times 12\text{ cm}$  box with connection points on the external side of the box for the fibre coming from the HTS sample. The connectors used in the optical setup are FC/APC connectors where APC stands for *angled physical contact* [83]. These connectors allow the surfaces of two connected fibres to be in direct contact

with each other and feature a low connector to connector loss of 0.25 dB and they prevent reflected light from travelling back into the fibre. Fig. 27 shows a schematic of how the components are connected within the box for ease of understanding while Fig. 28 shows the actual photograph of the assembled box with the lid open to show the components mentioned, and the lid closed to show the plug and play connections. The box has two FC/APC connections for the HTS sample that has to be monitored for hotspots. Connections are also present for the compensation length. The box is powered by the mains power supply and simply needs to be switched on once the HTS sample is connected. The output voltage of the photo-detector goes to a connector accessible on the outside of the box; a coaxial cable can be connected between this point and a data acquisition (DAQ) device or an oscilloscope to observe the MZI output interference pattern.

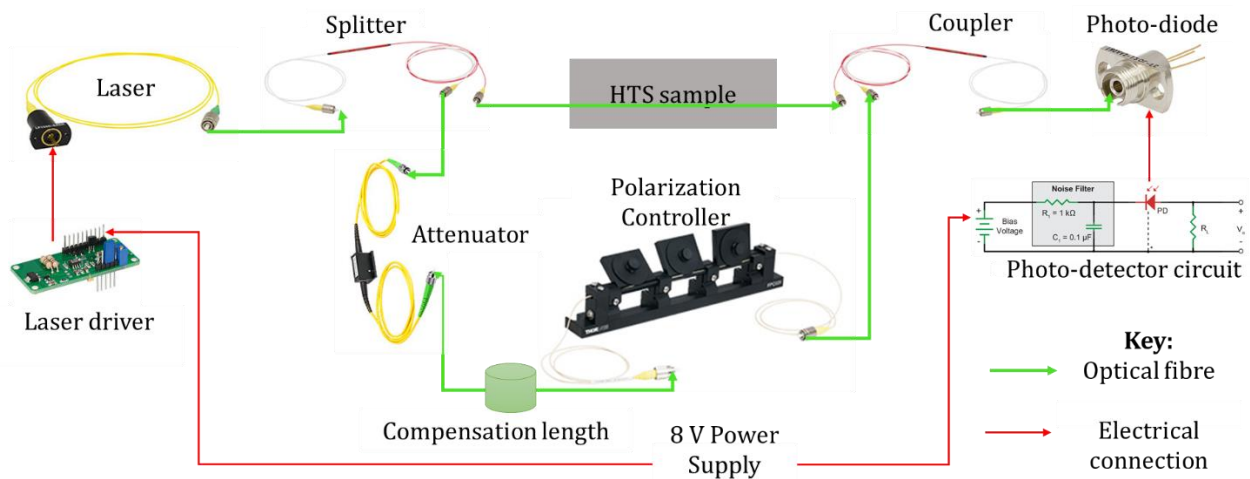


Figure 27. A schematic of the assembly of the MZI interferometer in the lab with the mentioned components

#### 4.2.1 Cost of the MZI setup

The cost breakdown of the MZI setup is given in Table 4.

Table 4. Cost break down of the MZI plug and play box

Component	Cost (CHF)
Laser	600
Photo-diode	150
Polarization controller	200
Splitter, coupler and optical fibre	50
Electronic equipment (power etc.)	250
Attenuator	250
<b>Total</b>	<b>1500</b>

The total cost of the setup comes to be around 1500 CHF. It is important to note that this does not include the optical fibre integration costs which will amount to a major portion of the total costs. Despite that, the



setup cost is very economical and low cost compared to other optical fibre sensing techniques which require high cost interrogating devices.

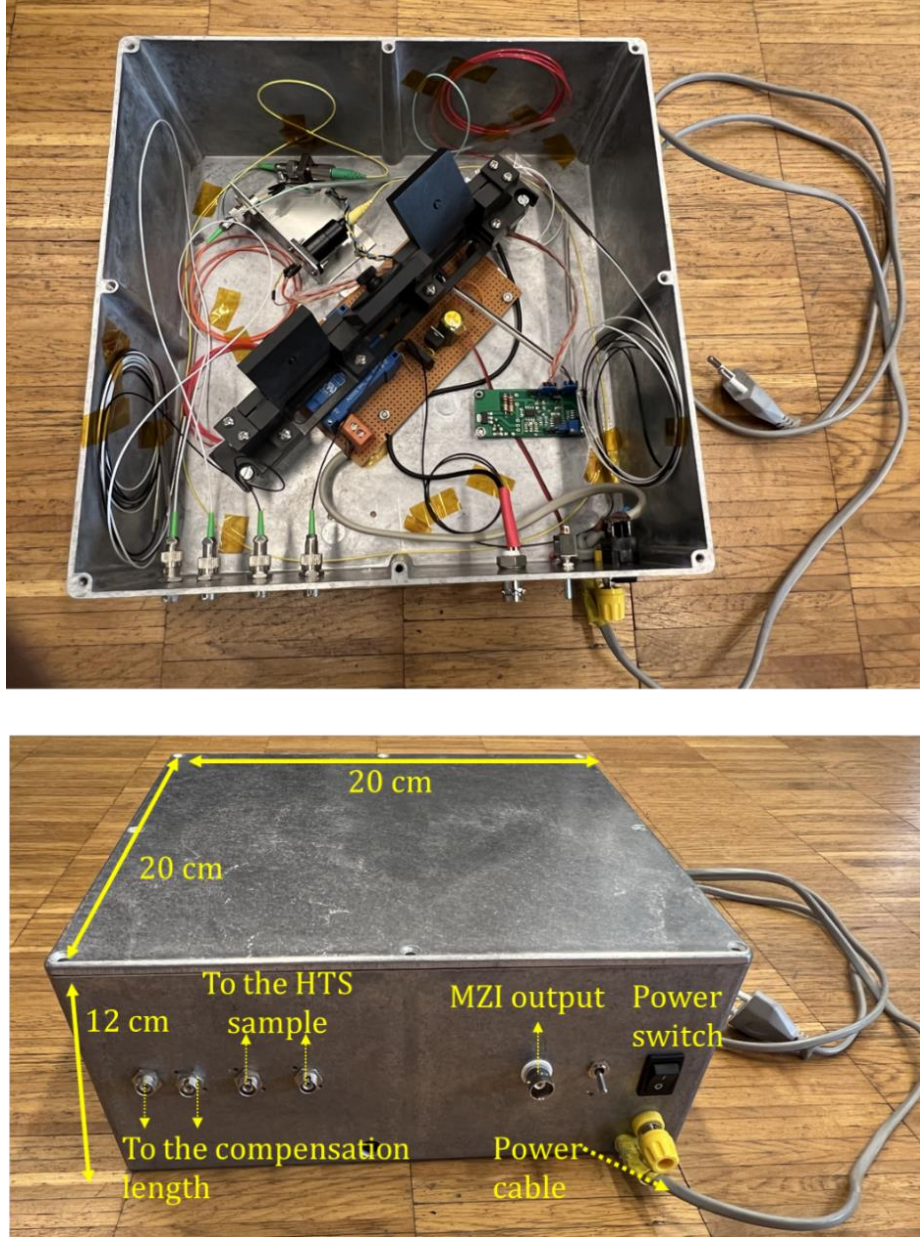
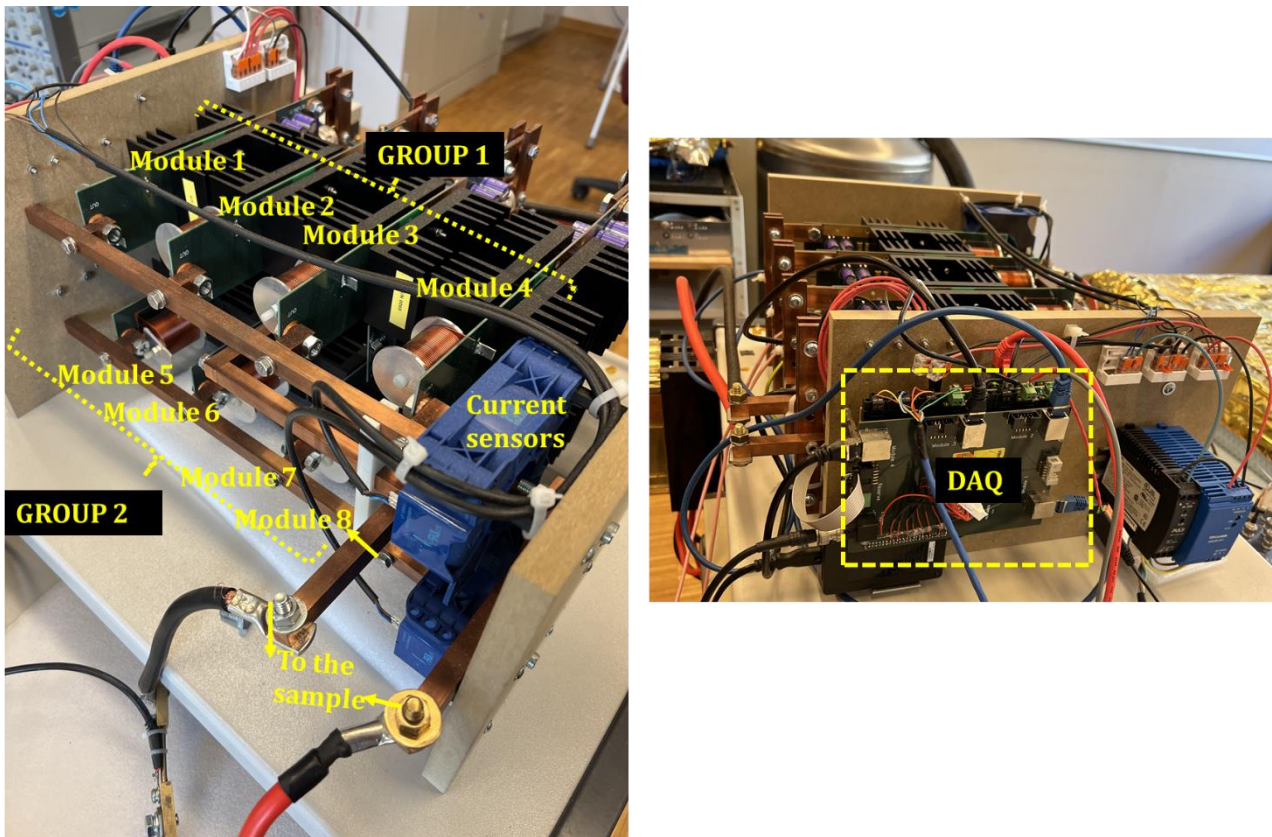


Figure 28. The inside of the MZI plug and play box (top) in a compact 20 cm x 20 cm x 12 box where the optical fibres from the HTS sample can simply be connected via FC/APC connectors (bottom)

### 4.3 Building the current pulser

Pulsed current measurement technique (PCM) has been used extensively for characterizing superconductors at current densities near or above their critical current [84]. PCM are used in order to minimize heating effects in the superconductor by applying large currents with short duration. Such measurements are important to better understand the superconductor behavior when they transition to resistive state; this helps in the optimization of applications like SFCLs which rely on this transition to work. In the case of the experiments done for this thesis however, PCM were performed in the order of tens of milliseconds (typically between 10 ms to 50 ms) in order to check the MZI output to heating in the HTS sample while preventing the sample

from burning. Superconductors have negligible resistance and transition to resistive state at currents higher than their critical current, this resistance changes rapidly during a quench. Therefore, the current source for superconductors face the challenge of not only driving stable current in a load with negligible resistance but also the challenge of driving current in a resistive load after the superconductor transitions. In addition, the current source should also track the rapidly changing resistance of the superconductor during a quench and maintain stable current in the sample. Initially for experiments for this thesis an analogue current pulser was used which had a charged capacitor as a voltage source and MOSFETs in their linear region of operation which behaved as gate voltage controlled current source. While this current pulser generated square pulses that were very well regulated in the plateau region without any inductive noise in the voltage measurements, it was difficult to pulse high currents in the HTS sample without damaging the current source. In such a current source, during superconducting state the voltage drop is in the MOSFETs while in the resistive state the voltage drop is in the sample. Therefore, when high currents are pulsed in the sample during superconducting state, greater amount of heat is dissipated inside the power semiconductors causing the MOSFETs to explode. To avoid this inconvenience and to achieve higher currents, a digital current pulser was designed and fabricated by SCI-consulting [85] for the experiments conducted during this thesis.



**Figure 29.** The digital current pulser designed by SCI-consulting for low impedance loads with a built in DAQ board

This digital current pulser was important to extend experimentation to long sample lengths which could not have been tested with the analogue current source. The current pulser made by SCI-consulting for EPFL has two groups, with a total of eight modules as shown in Fig. 29. One module generates 400 A therefore this pulsed current source is able to generate current pulses of up to 1600 A per group giving a deliverable maximum current of 3200 A. The source follows a multiphase buck converter design with each module in parallel. These modules are phase-shifted with respect to each other, so that ripple on the output current is minimized while the source maintains excellent efficiency as shown in Appendix A.1. Since the current pulser was equipped to



measure the current in each group for safety purpose, the DAQ board that was being used to measure this current was equipped with additional input channels that were used to acquire all the experiment measurements (sample voltage and MZI output) as shown in Fig. 29.

## 4.4 The experiment setup for 10cm-30cm superconductor tapes

Preparing the HTS tapes for experimentation requires two steps:

1. Mounting the sample on an appropriate sample holder.
2. Once the HTS sample is mounted, the fibre has to be integrated on the sample surface.

### 4.4.1 Building the sample holder

Customized sample holders have been prepared in the lab for experimentation which fit into the lab cryostat. The sample holders are made of copper and are tight u-shaped to minimize inductance as shown in Fig. 30. The 3-D figures drawn for the sample holder have a noticeable distance between the two current paths of the sample holder for ease of understanding, when in reality the two current paths were close together with negligible distance to minimize inductive noise. Current leads with screws are present at the ends to enable connection to the current source. Depending on the sample length to be tested, the sample holder used has either 10 cm or 30 cm length available for mounting the HTS tape. The HTS tape is fixed onto the sample holder by means of two thin copper plates on each end, with the help of screws. Current therefore goes through the sample and uses the bottom copper rod as the return path. As the sample holder is inserted vertically into a cryostat, a cryostat lid is fixed onto the sample holder with outlets drilled onto the lid for the optical fibre as well as the voltage measurement cable coming from the HTS sample.

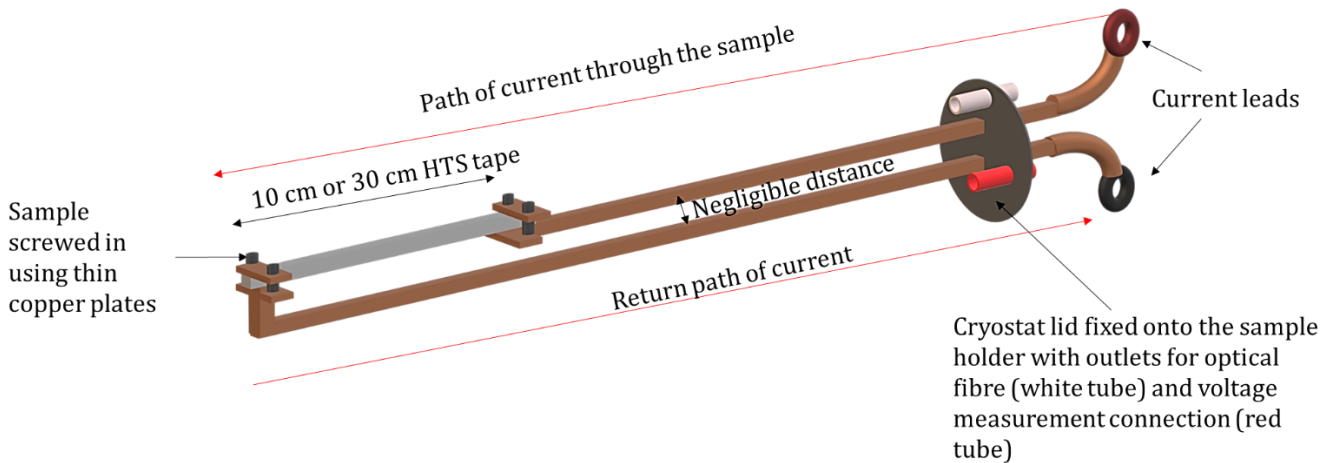
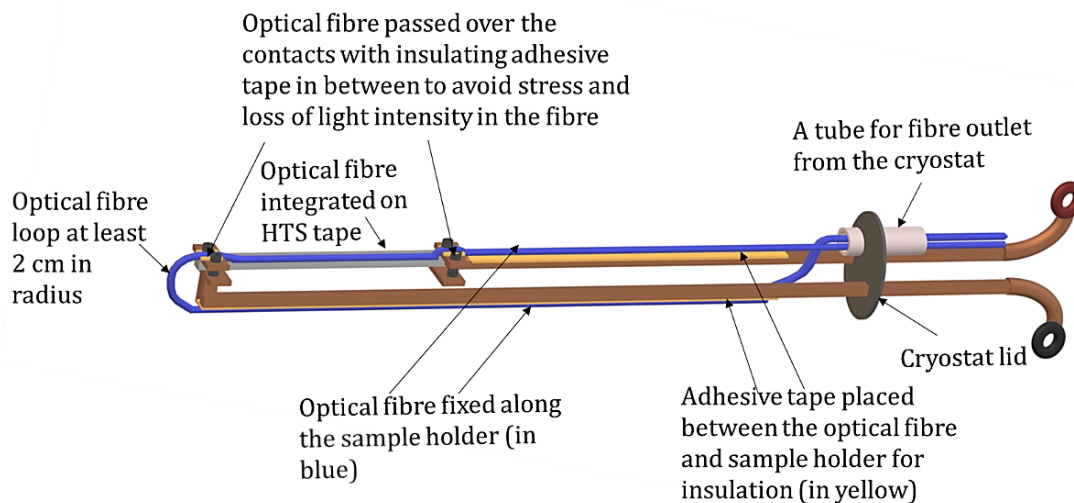


Figure 30. Sample holder used to mount linear samples of HTS tapes (not drawn to scale)

### 4.4.2 Integrating the fibre on a linear sample

Optical fibre is integrated on the HTS sample after it is mounted to avoid breakage of the optical fibre and also because the fibre is passed over the copper contacts that are screwed to fix the sample. This is to avoid stress on the optical fibre from the copper contacts that can lead to loss of light intensity in the optical fibre and hence a poor SNR in the MZI output. Two methods of integrating the optical fibre have been tried in the lab, one is

by means of using an epoxy (STYCAST®) and the other is by means of an adhesive tape (Kapton). Both methods of integration yield satisfactory MZI performance. The surface of the HTS sample is gently cleaned by means of alcohol to avoid poor integration quality due to dust or grease. In the case of using STYCAST®, the optical fibre is lightly covered with the epoxy and placed along the length of the HTS sample. The epoxy takes up to 24 hours to cure (with catalyst 9) and then the sample is ready to be used for experimentation. In the case of integration by means of Kapton however, the fibre is placed along the length of the HTS and the Kapton is placed on top of the optical fibre, fixing it in place. The sample in this case, is ready to use immediately for experimentation. In both cases however, care is taken that the fibre is not stretched when placing it on the HTS sample, to avoid a pre-strained optical fibre that can lead to low SNR in the MZI output. The fibre is integrated only on the HTS tape, but has extra length on either side to make it out of the cryostat to the optical setup present externally. This fibre therefore loops around the sample holder as shown in Fig. 31 and makes its way out of the cryostat through the fibre outlet tube in the cryostat lid. The optical fibre loop radius when the fibre turns around the sample holder should be at least 2 cm which is the minimum bending radius of an optical fibre. Care is taken to fix the extra length of the optical fibre along the sample holder. If this optical fibre is not fixed, it will be free to move in the cryostat leading to a noisy MZI output. However, before the optical fibre is fixed along the sample holder it is inserted into Teflon tubes. It is often possible to break the optical fibre at the copper contacts in such experiments. Therefore, to prevent optical fibre breakage in the experiments, bare fibre is only kept for the length of the HTS sample (10 cm or 30 cm) and the rest of the optical fibre is inserted into thin Teflon tubes. Fig. 32 marks the lengths of the fibre encased in Teflon tubes. Kapton is then placed along the length of the sample holder to insulate the optical fibre from any current heating in the copper. The fibre is then fixed on top of the Kapton as shown in Fig. 31. This minimizes noise in the MZI output that could arise if the optical fibre senses the current heating in the sample holder. Similarly, when the optical fibre is passed over the copper contacts fixing the HTS sample in place, Kapton is placed between the optical fibre and the copper plates for insulation.



**Figure 31.** Illustration of how the optical fibre is integrated with the HTS sample and fixed along the sample holder and making its way out of the cryostat to the optical setup (not drawn to scale)

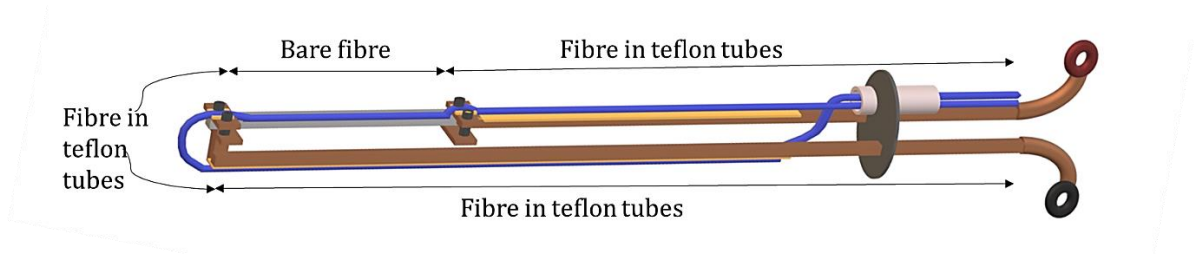


Figure 32. Optical fibre lengths outside of the HTS sample are encased in teflon tubes to avoid fibre breakage (not drawn to scale)

#### 4.4.3 Placing voltage measurement contacts on HTS sample

Voltage measurement in the sample are needed to understand and validate the MZI output. Voltage measurement in the sample and a corresponding MZI output will validate that the MZI signal is responding to heating in the HTS sample. In addition, voltage measurements also help identify the extent of heating in the sample that the MZI is responding to, this aids better understanding of the MZI output. To measure voltages in the HTS sample, voltage contacts are placed along the length of the sample as shown in Fig. 33. The voltage contacts measure voltage in the full sample, voltage around the magnet which is placed to artificially create a weak point that may become a hotspot. The sample length is between 10 cm to 1 m, while the magnet is 10 mm wide. Contacts can also be placed on sample segments adjacent to the magnet to better monitor the propagation of the normal zone or to monitor any hotspots that arise in areas aside of the magnet. These contacts can be clipped on the sample edge or soldered on the sample using low temperature solder. The contacts are connected to twisted wire pairs of a signal cable that plugs into the acquisition device. The signal cable is used due to its low twist pitch and high shielding. Twisted wire pairs minimize electromagnetic interference noise in measurements. Each twisted wire pair measures voltage in one segment of the HTS sample as shown in Fig. 33. The cable used for those signals makes its way along the sample and out of the cryostat by means of an outlet in the cryostat lid that was shown in Fig. 30.

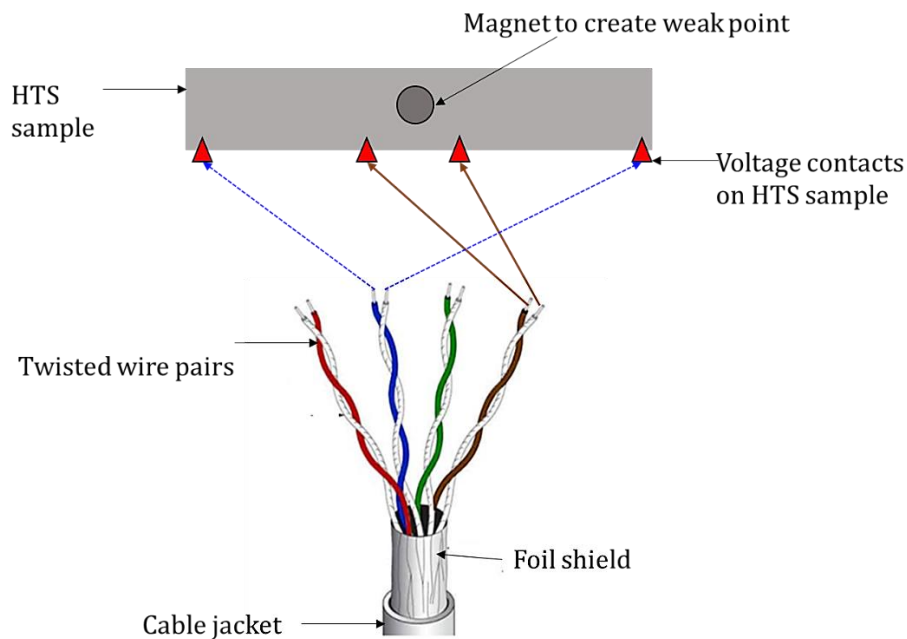
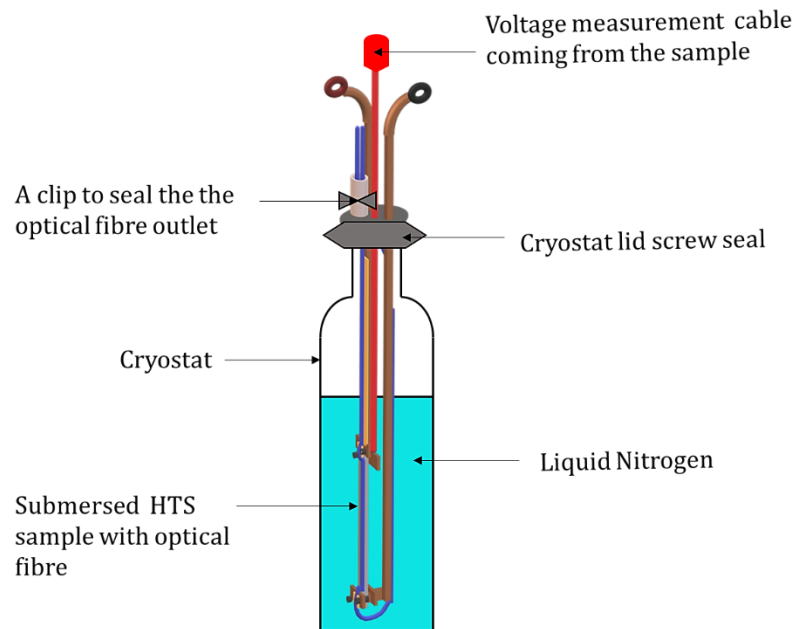


Figure 33. Voltage measurement contacts are placed on the HTS sample (top), voltage is acquired by means of a shielded signal cable (bottom) [86]

#### 4.4.4 The complete assembled setup and data acquisition

The prepared sample and sample holder is inserted vertically in a cryostat (diameter of 50 mm) with liquid Nitrogen at 77 K. The sample is fully immersed in liquid nitrogen. A screw ring goes around the cryostat lid and seals it in place as shown in Fig. 34. The outlet for the voltage is sealed by means of epoxy while a clip is used to loosely seal the fibre outlet taking care to avoid any stress on the fibre. Sealing any opening in the lid was done to have the possibility of decreasing the liquid nitrogen temperature by reducing pressure in the cryostat. It can also help avoid noise in the MZI output by ensuring lower temperature fluctuations in the ambient environment. The next steps include making connections to the current source, to the optical setup and to the acquisition device as shown in Fig. 35. In order to connect the optical fibre ends coming from the sample to the optical setup, the ends need to be spliced to optical fibre pigtails that terminate in FC/APC connectors that can connect to the MZI plug and play box. Splicing is the process by which two fibres are joined together. Each end of the fibre coming from the sample is spliced to an optical fibre pigtail by means of a fusion splicer as shown in Fig. 36. In order to splice an optical fibre, the fibre needs to be stripped off its coating and cleaved first. Cleaving is the process by which an optical fibre is “cut” precisely in order to create a perfectly flat end face, perpendicular to the longitudinal axis of the fibre for splicing. The cleaved fibre from the sample and the pigtail are placed in the fusion splicer (Fig. 36 (a) shows the two cleaved fibres) where they are thermally joined together by a process called arcing (Fig. 36(b)). Arcing is the production of an electric arc which melts the fibre ends and fuses them together. The fibre joint is placed in a protective sleeve and is then moved to the heating compartment of the fusion splicer which heats the protective sleeve, making it fit securely around the spliced joint (Fig. 36(c)). The two spliced fibres coming from the HTS samples are then connected to the FC/APC connections of the MZI plug and play box where they constitute the sample arm of the MZI.



**Figure 34. Placing the HTS sample in the cryostat and sealing the lid**

For the electrical connections, current leads at the end of the sample holder are connected to the DC current source with a current measuring resistor placed in series with the sample as shown in Fig. 35 in red. The resistance of this current measuring resistance is small (typically 1 m $\Omega$ ) and it enables the monitoring of the current that is pulsed through the sample.

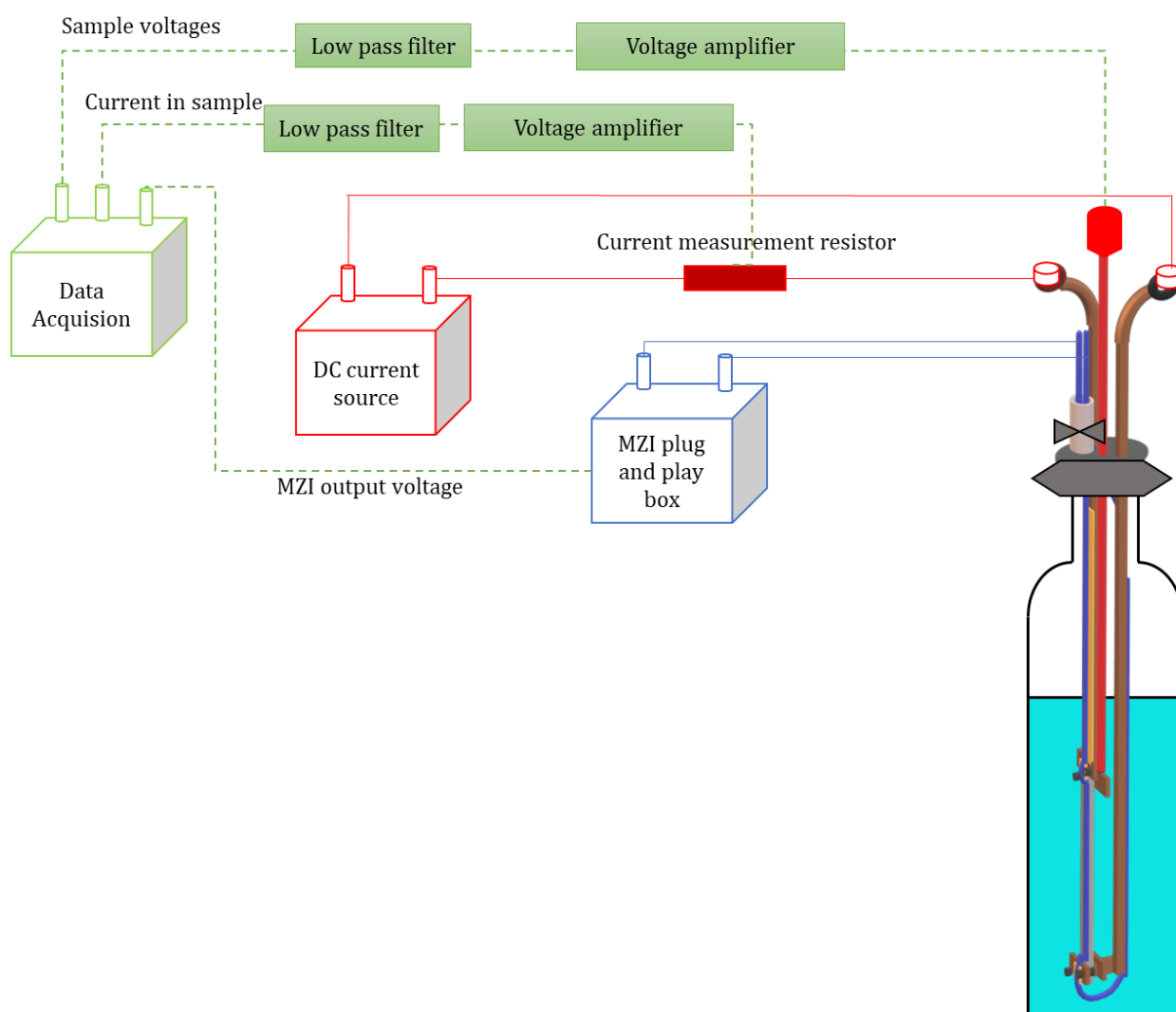


Figure 35. Making the optical, electrical and data acquisition connections after the sample is placed in the cryostat

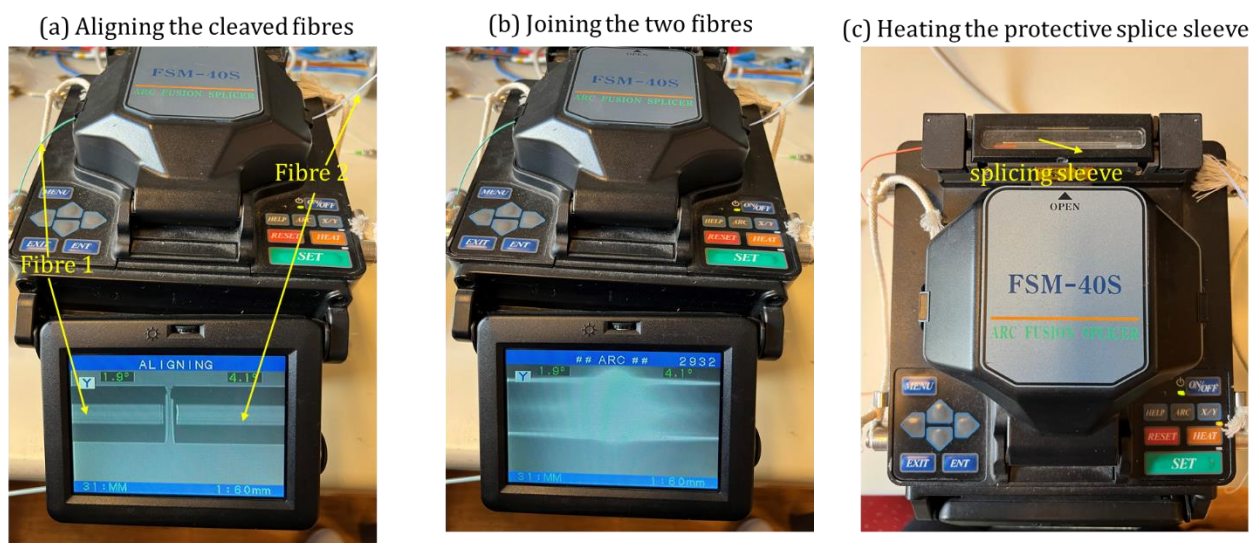


Figure 36. The process of splicing the optical fibres coming from the HTS sample

Voltage measurement in HTS samples in low heating scenarios can be in the order of microvolts, in the case of MZI experiments however, such a resolution was not implemented as the interests were the hotspots or normal zones which were measured in the 10 mV range of resolution. This necessitates the use of voltage amplifiers, as typically signals with voltage lower than 50 mV are too low to be applied directly to the data acquisition system inputs and need to be amplified. In the case of high voltages however, the data acquisition device needs to be protected because its inputs are typically limited to less than 30 V due to the presence of solid-state multiplexing circuits, which rapidly scan multiple input channels [87]. Therefore in the lab, two different amplifier circuits were designed (Appendix A.1), one with a high gain of 9 to amplify low sample voltages when low currents are pulsed through the sample and the second amplifier with a low gain of 0.25 for high voltages, to protect the data acquisition device which may be damaged when exposed to higher voltages that can occur in case of the superconducting sample burning, for example. The voltage measuring signal cable coming from the HTS sample as well as the voltage coming from the current measurement resistor are connected to these voltage amplifiers, the output of which is then connected to a low pass filter before going to the data acquisition device input channels.

Low pass filters (LPF) are placed on each input channel of the data acquisition device. These are important because the data acquisition device has a bandwidth (BW) of 250 kHz. In addition, the PWM frequency per module of the current source was 62.5 kHz which introduced noise at the frequency of 500kHz (for the eight modules of the current source) in the voltage measurements. Sampling at frequency of 100 kHz without LPF for example, would result in high noise. The filter designed therefore, had a cutoff of 80 kHz with a stopband and passband regions shown in Appendix A.2 for noise filtering and anti-aliasing. For better noise rejection, the same clock is used for controlling the current source and for the data acquisition.

#### 4.4.5 Setup for 1 m linear HTS samples

The setup for testing long samples (up to 100 cm in length) requires the exact same experiment setup which is outlined in section 4.4 except that the cryostat available is not big enough for a 100 cm sample therefore a different cryostat which is big enough for the sample holder is used. The sample holder, voltage contacts and optical fibre integration is done all in the same way. Care is taken, as mentioned before by adding compensation lengths of optical fibre to the reference arm of the MZI, in order to balance the two arms of the interferometer to maintain coherence.

#### 4.4.6 Building a sample holder to avoid Lorentz force

The linear sample holder shown in Fig. 30 is susceptible to Lorentz force. The in and out current paths cause a force on the HTS sample in the opposite direction, causing it to move during a current pulse. Since, the MZI is extremely sensitive to perturbations, the phenomena of Lorentz force can be minimized by designing a “cage” around the HTS sample to cancel out the magnetic fields of the two current paths for a net zero force on the HTS sample. Such a sample holder was also designed in the lab and tested with a 30 cm long HTS sample, the results of which will be showcased in the next chapter.



## 4.5 The experiment setup for the FastGrid Superconducting Fault Current Limiter pancake

### 4.5.1 Integrating optical fibres on long lengths of HTS tape for the FastGrid SFCL pancakes

The FastGrid pancakes were wound at SuperGrid Institute (SGI) Lyon, using HTS tapes manufactured by THEVA. There were two pancakes wound at SGI for the FastGrid project, one was wound along with the optical fibre while one was wound without it. The pancake co-wound with optical fibre was tested at EPFL with the MZI technique. A special device was purpose built at SGI to integrate three optical fibres to the HTS tape before the pancakes were wound. This device is pictured in Fig. 37, which shows the full device with three optical fibre spools being passed through grooves where they are adhered to the Kapton, before the Kapton is integrated to the surface of the HTS tape. Fig. 38 shows a picture of a HTS tape with three integrated optical fibres, done using this SGI device.

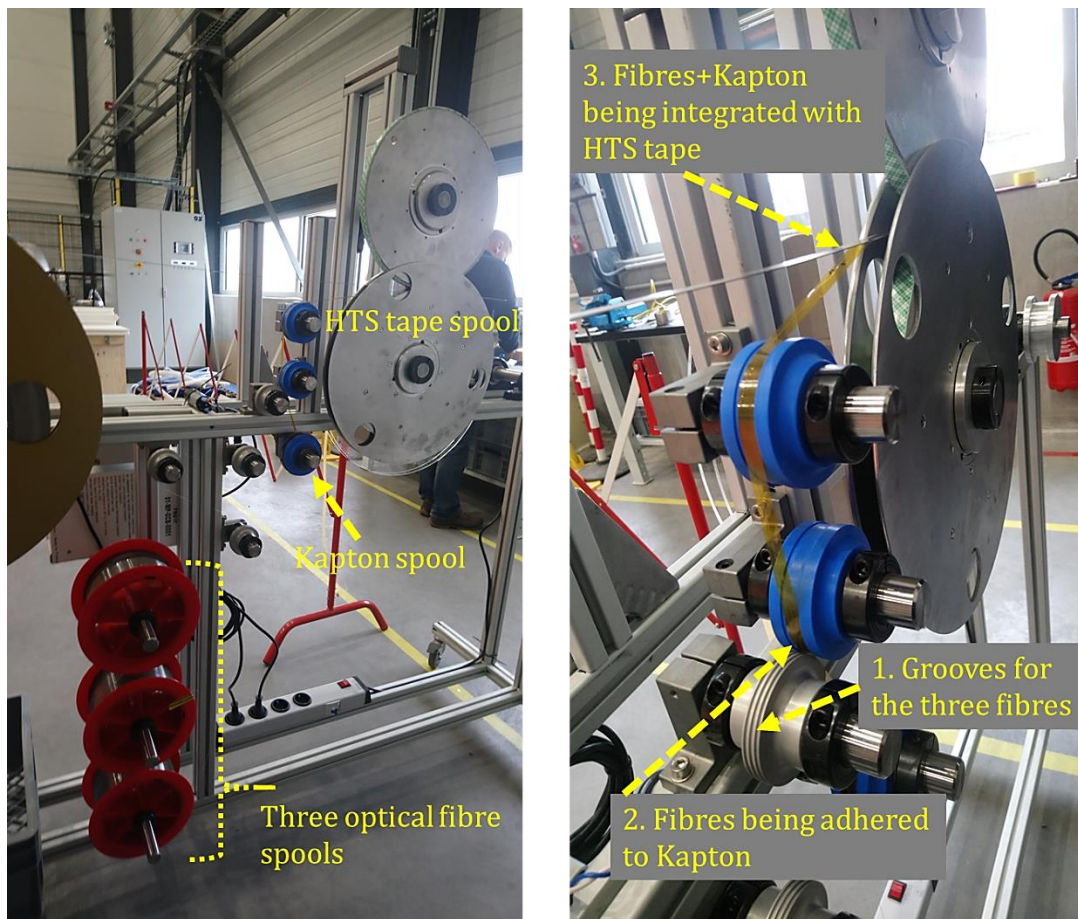
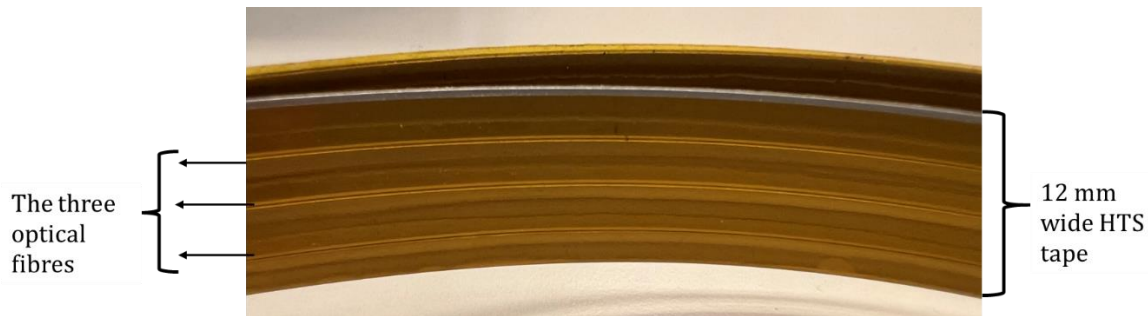


Figure 37. The purpose-built device at SGI for integrating three optical fibres on the surface of the HTS tape which was used to wind the FastGrid SFCL pancakes (left), the stepwise integration of the three optical fibres to the HTS tape by means of Kapton using this device

This FastGrid pancake was wound using two conductors. Each conductor was 34 m long giving a total of 68 m of HTS tape wound per pancake. Since this pancake could not be kept in the EPFL lab for a long period due to project timelines and commitments, another pancake was wound at SGI with optical fibre (the Petite SFCL

Pancake), especially for long time testing at EPFL. This pancake was more extensively tested with the MZI technique. This pancake had two conductors of 6 m, giving a total length of 12 m of HTS tape in the pancake.



**Figure 38.** Three optical fibres integrated with the HTS tape in the pancake by means of Kapton using the SGI device

When optical fibre was integrated along the length of the HTS tapes in the pancake, care was taken to leave at least 50 cm of extra optical fibre length outside of the pancake, to enable easy splicing to optical fibre pigtails. This optical fibre came out of the pancake through grooved current contacts manufactured at SGI as shown in Fig.39.

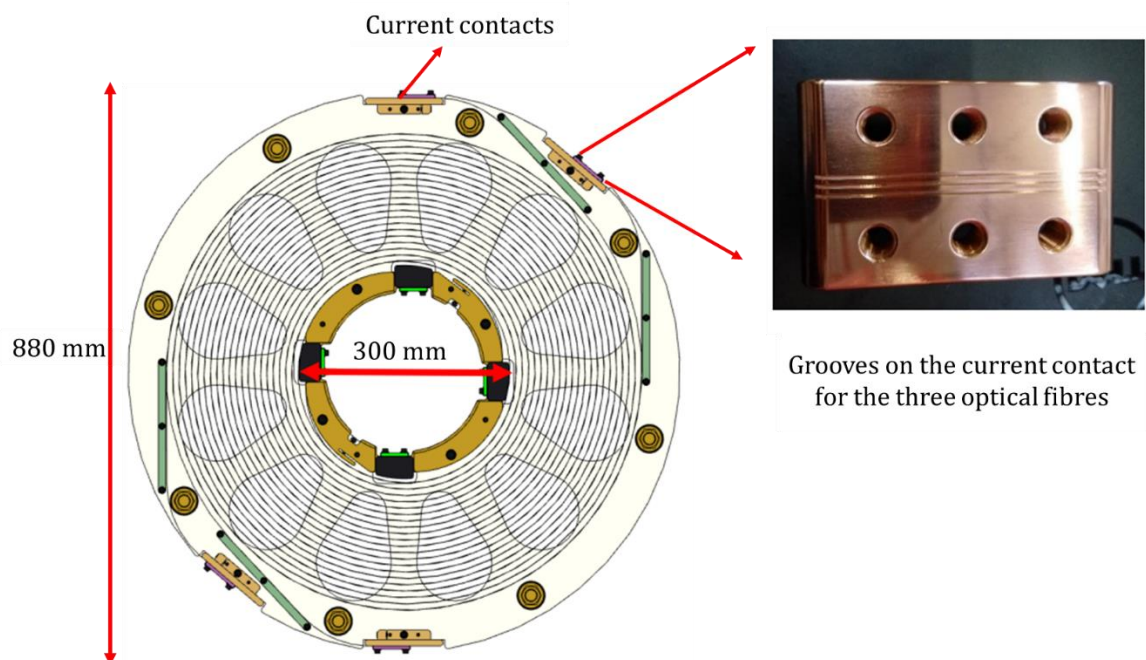


**Figure 39.** The CAD drawing of the FastGrid FCL pancake (left) and a picture of the grooved current contacts for safe passage of the optical fibre (right), both pictures are courtesy of SuperGrid Institute Lyon

#### 4.5.2 Fully assembled setup for the FastGrid project pancake

The diameter of the FastGrid pancake was 880 mm, therefore a customized cryostat was built in the lab which is shown in Fig. 40. Since the Petite SFCL Pancake was smaller in diameter than the main pancake mentioned, the same cryostat could be used to test both pancakes. This cryostat was covered in Mylar® which minimizes heat loss due to radiation because of its reflective properties. The cryostat lid was also covered in Mylar® and this lid was used to maintain the liquid Nitrogen bath temperature by minimizing convective heat exchange.

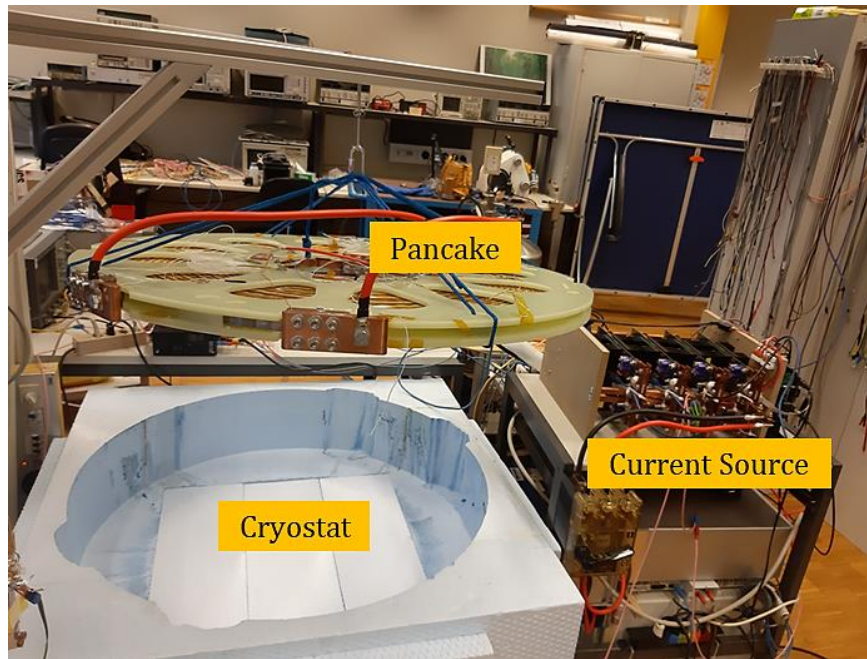


**Figure 40. A custom-made cryostat for the FastGrid pancake**

Later on, a tube was fixed on one side of the pancake to provide an outlet of the optical fibre, voltage measurement signal cable and the current cables from the cryostat.

One optical fibre per conductor was spliced to a fibre pigtail terminating in FC/APC connectors and these pigtails were connected to the MZI plug and play box. There are two ways to test the pancake, current could be pulsed in one conductor at a time in which case only the optical fibre from that conductor is connected to the box. In the case current is pulsed in both conductors, the two optical fibres (one from each conductor) can be connected in series and then connected to the MZI plug and play box.

The main FastGrid pancake has a total of two conductors named conductor A and conductor B. Each conductor is connected in parallel to achieve the target critical current, therefore conductor A is comprised of conductor A1 and A2 connected in parallel, similarly conductor B is conductor B1 and B2 connected in parallel. Fig. 41 shows the electrical connections made in order to connect the pancake to the current source. Current measuring resistors (resistance  $1\text{ m}\Omega$ ) are placed in series with each of these four conductors before connecting them to the current source. Voltage contacts are placed on the ends of the HTS tape for A1, A2, B1 and B2 to monitor the voltage in the full pancake, when current is pulsed in it. These voltage contacts are twisted wire pairs which are part of a shielded signal cable as was shown in section 4.4.

For the optical fibre, unfortunately some optical fibre ends broke during transportation and handling of the pancake therefore not all conductors had an optical fibre available to splice. Only one conductor could be monitored in the FastGrid pancake for hotspots using MZI and that was A2. The optical fibre from both ends of A2 were spliced to fibre pigtails which were then connected to the MZI plug and play box. A compensation length of optical fibre was also connected in the reference arm of the MZI.



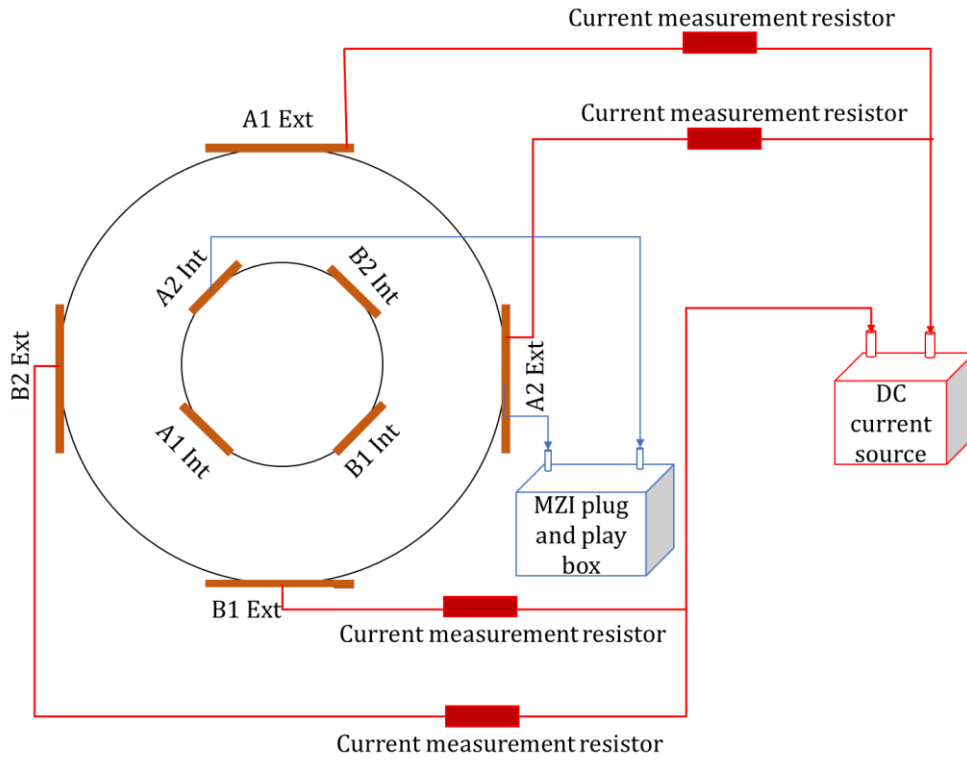


Figure 41. Connecting the FastGrid pancake to the current source and making the optical connections from fibres on conductor A2

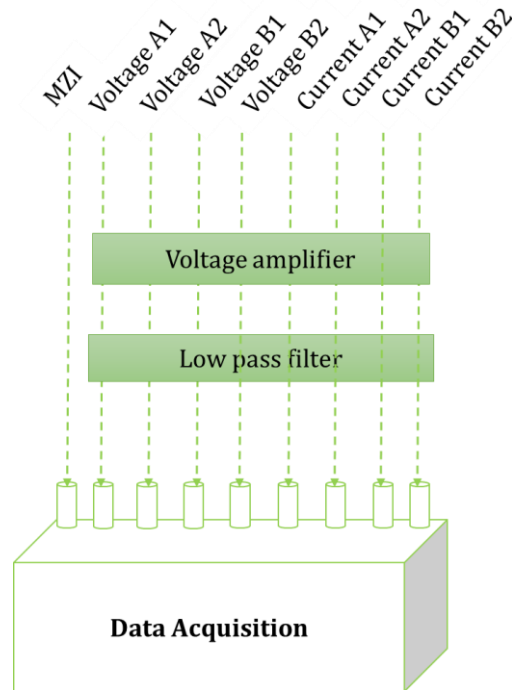


Figure 42. Acquired voltages for the FastGrid pancake measurements

The electrical connections of the FastGrid pancake and the optical connection from conductor A2 is shown in Fig. 41. To avoid complicating the image, data acquisition connections are separately illustrated in Fig. 42. The voltages in the full lengths of A1, A2, B1 and B2 as well as the voltages from all four current measuring resistors are connected to the same voltage amplifiers which were discussed in Section 4.4. The output of the amplifier is connected to a low pass filter before connecting to the data acquisition input channels, similar to

the setup explained for linear samples in Section 4.4. The MZI output from the plug and play box is also connected to one channel of the data acquisition board.

### 4.5.3 Fully assembled setup for the Petite SFCL Pancake

The small pancake wound by SGI had two conductors (6 m each) named conductor A and B respectively. Unlike the main project pancake discussed previously, conductor A and B were not made of two conductors in parallel but comprised single conductors. Three optical fibres were present on each conductor, with 50 cm of fibre length left outside of the pancake at the contacts, just like the main project pancake. Fig. 43 shows the Petite SFCL Pancake which was measured. One optical fibre on each conductor was spliced to optical fibre pigtails, these are visible in Fig. 43 in red and blue. The fibres from one end of conductor A and conductor B were connected together in series to monitor the entire 12 m of conductor length for hotspots. The other ends of optical fibres from conductor A and B were connected to the MZI plug and play box as shown in Fig. 44. The two conductors A and B were connected in series to the current source with a current measuring resistor present in series with the pancake to monitor the current injected into the pancake, as shown in Fig. 44. Voltage contacts were placed on the ends of each conductor and were connected to twisted wire pairs of a signal cable which was connected to the voltage amplifiers. The output of the amplifier was connected to the LPF before connecting to the input channels of the data acquisition device. The MZI output as well as the voltage from the current measuring resistor was acquired. Fig. 45 shows which signals were connected to the data acquisition board for the Petite SFCL Pancake.

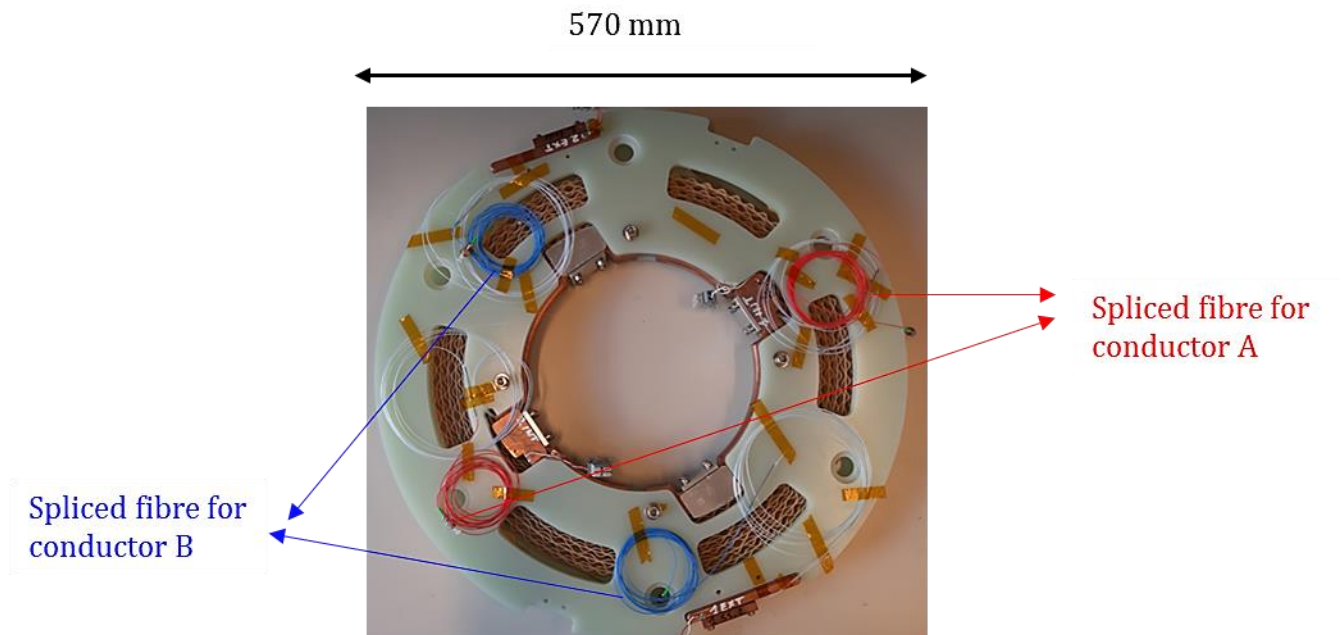
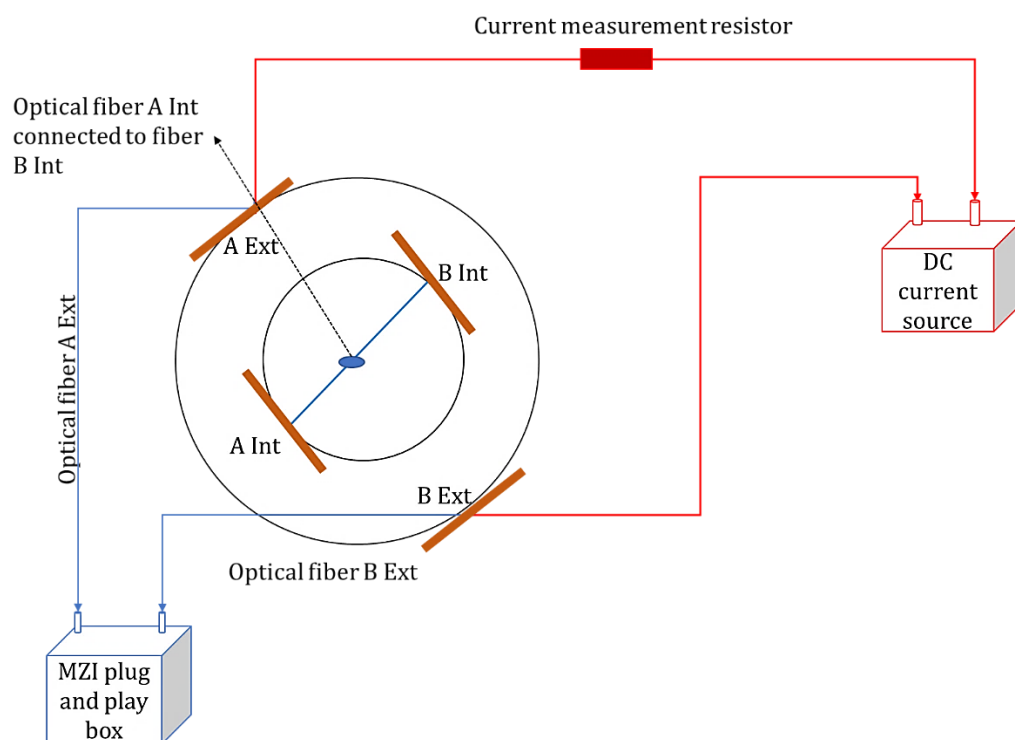
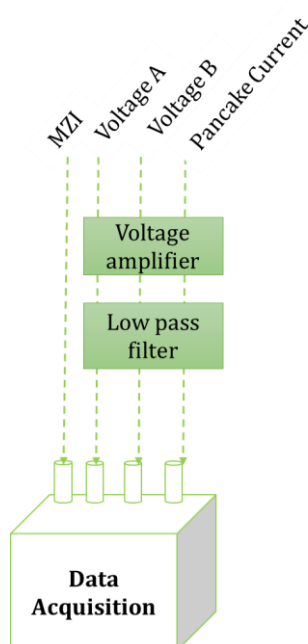


Figure 43. A picture of the Petite SFCL Pancake with the four spliced optical fibres visible in red and blue



**Figure 44.** The connections for the Petite SFCL Pancake



**Figure 45.** Acquired voltages for the Petite SFCL Pancake

## Summary

This chapter gave a detailed, step by step explanation of how the experiments were setup to investigate the MZI technique. The technique was tested with linear HTS tapes of lengths 10 cm, 30 cm upto 100 cm and also on the FastGrid SFCL pancakes with 12 m and 17 m of conductor. The description of the sample holder for linear samples and the integration process of optical fibre with these samples is also explained. Two different

pancakes were tested with the MZI pancake, one was the FastGrid project's main pancake while the other was a smaller prototype wound specifically for EPFL to test extensively with the MZI technique. The procedure for setting up the pancake for experimentation is also explained. The chapter also discusses the current pulser used for experimentation, the electrical and optical connections and how all the experiment measurements were interfaced with and acquired by means of a DAQ device. Most importantly, the chapter also showed how the MZI setup can be easily assembled by using a few components in a compact plug and play box which easily connects to the HTS sample that needs to be monitored for hotspots.







# 5

## Experiment Results and Discussion

Some of the experiment results showcased in this chapter have been published in:

- A. Akbar, Z. Yang, S. Wang, L. Thévenaz, B. Dutoit, Optical fibre sensing for fast hotspot detection in SFCLs, Superconductor Science and Technology journal 33 (2020) 115003. ([Link to publication](#))
- A. Akbar, B. Dutoit, Fast Quench Detection in SFCL Pancake Using Optical Fibre Sensing and Machine Learning, IEEE Transactions on Applied Superconductivity (2022) 1. ([Link to publication](#))

Experiment results will be shown and discussed for five samples in this chapter. These samples include:

- 1 m long and 4 mm wide HTS tape, stabilized with 10  $\mu\text{m}$  of copper, manufactured by SuperPower.
- 1 m long and 12 mm wide, HTS tape stabilized only with 2  $\mu\text{m}$  of silver, kindly provided by Theva.
- One 30 cm long HTS sample, kindly provided by the Shanghai Jiao Tong University (SJTU), China, with a unique integration of optical fibre by means of solder. This sample was mounted on a special sample holder so the sample was subject to zero Lorentz force during a current pulse.
- The Petite SFCL Pancake made with 12 m of bare HTS tape (stabilized with 2  $\mu\text{m}$  of silver), the entire conductor length of which was monitored using MZI.
- The FastGrid project pancake with 68 m of HTS tape thermally stabilized with 500  $\mu\text{m}$  of Hastelloy. 17 m of conductor was monitored using MZI in this pancake.

The 1m long samples were integrated with optical fibre in the lab by means of Kapton, while the 30 cm sample provided by SJTU came with integrated fibre which they manufacture in their laboratory. Both the SFCL pancakes tested were integrated with optical fibre and wound at SuperGrid Institute Lyon (SGI) using the conductor provided by Theva.

All experiments were conducted at 77 K.

## 5.1 1 m long SCS4050-AP sample

### 5.1.1 Sample specifications

Table 5. SCS4050-AP sample details

<b>Manufacturer</b>	SuperPower ( Sample name: SCS4050-AP)
<b>HTS tape length</b>	1 m
<b>HTS tape width</b>	4 mm
<b>HTS tape thickness</b>	0.1 mm
<b>Stabilization</b>	2 $\mu\text{m}$ silver + 10 $\mu\text{m}$ copper both sides
<b>Substrate thickness</b>	50 $\mu\text{m}$ Hastelloy
<b>Critical current</b>	125 A (at 77 K and self-field conditions)
<b>Fibre integration</b>	Taped along the sample length by means of Kapton
<b>Fibre diameter</b>	250 $\mu\text{m}$
<b>Magnet</b>	10 mm diameter placed at the center of the sample
<b>Sample holder</b>	Linear sample holder with the sample susceptible to movement due to Lorentz force during current pulse

This sample (SCS4050-AP) was a copper stabilized SuperPower tape with a critical current of 125 A at 77K and self-field conditions. A 10 mm magnet was placed at the center of the sample to artificially create a weak point of a known location. Voltage taps were placed around this weak point (1 cm apart) and voltage was also measured in the full sample length (1 m). The sample was tested at 77 K and current was pulsed in the sample for a duration of 25 ms every time. The experiment measurements are showcased in the subsequent plots with the two sample voltages (in blue), MZI output (in green) and the current in the sample (red). It should be noted that the MZI output voltage value is not important but the MZI output voltage variation is what helps determine heating in the sample. In the plots for this sample and subsequent samples, the MZI output voltage has been normalized by the maximum voltage. Data is acquired 50 ms before the current is pulsed as well, to properly observe the MZI response variation in the event of heating in the HTS tape. Data is also acquired 100 ms after the pulse has ended to observe the MZI response to sample cool down.

### 5.1.2 Experiment results

Fig. 46 shows the result for no heating in SCS4050-AP. 100 A of current is pulsed in the sample for 25 ms. The overall voltage (voltage in full sample length) as well as the hotspot voltage (voltage around the weak point) is zero signifying no heating in the sample. There are peaks in the two voltages due to the inductance in the experiment circuit. The MZI output is showing slow fluctuations with no identifiable pattern which indicates that there is no heating in the sample. These slow fluctuations arise due to variation in the temperature of the ambient environment.

In Fig. 47, the response of the MZI is shown for a single hotspot in the SCS4050-AP sample. 170 A of current is pulsed in the sample for 25 ms and the plot shows that the overall voltage and hotspot voltage are equal (with a peak value of 0.6 V), signifying that only the weak point around the magnet is heating and hence a single hotspot is present in the sample. It can be seen that the MZI response shows slow fluctuations before voltage is observed in the sample and transitions to an oscillatory response within 10 ms of the voltage rise observed in the sample, as can be seen clearly in the MZI output graph in Fig. 47. After the pulse has ended, lower frequency oscillation can be observed in the MZI response which is indicative of the sample cool down. Since the sample cool down happens at a slower rate than the heating event, the frequency of these oscillations is lower as compared to the ones observed during the hotspot event.

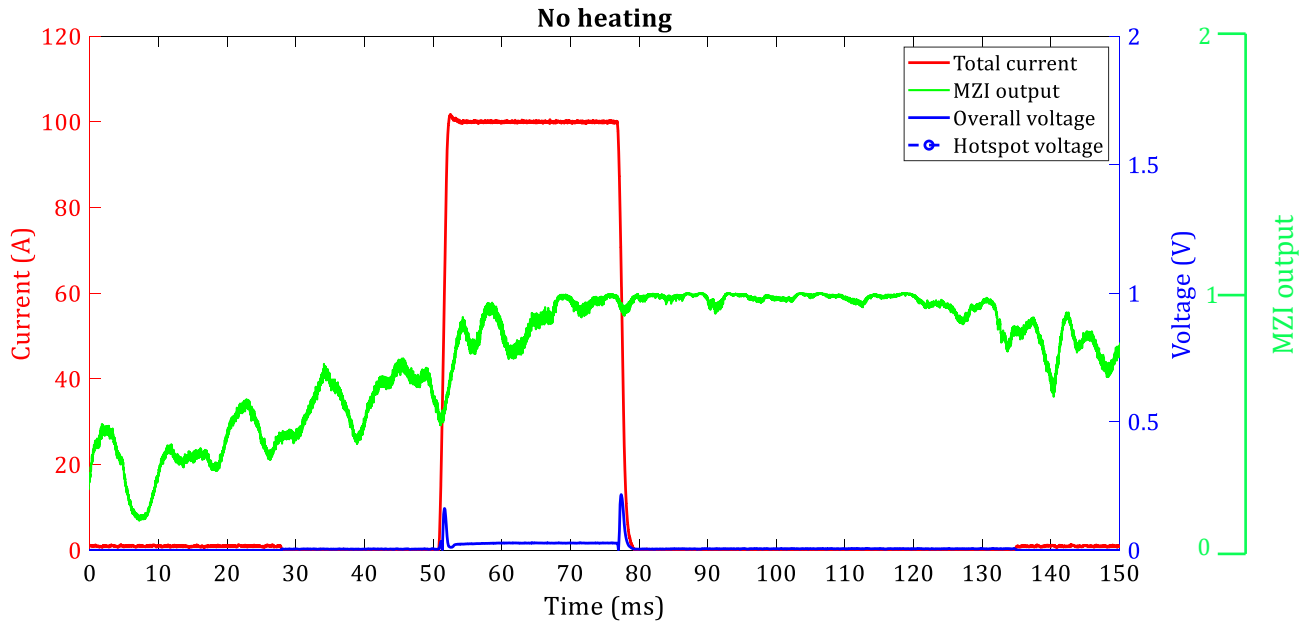


Figure 46. MZI response to no heating in the SCS4050-AP sample

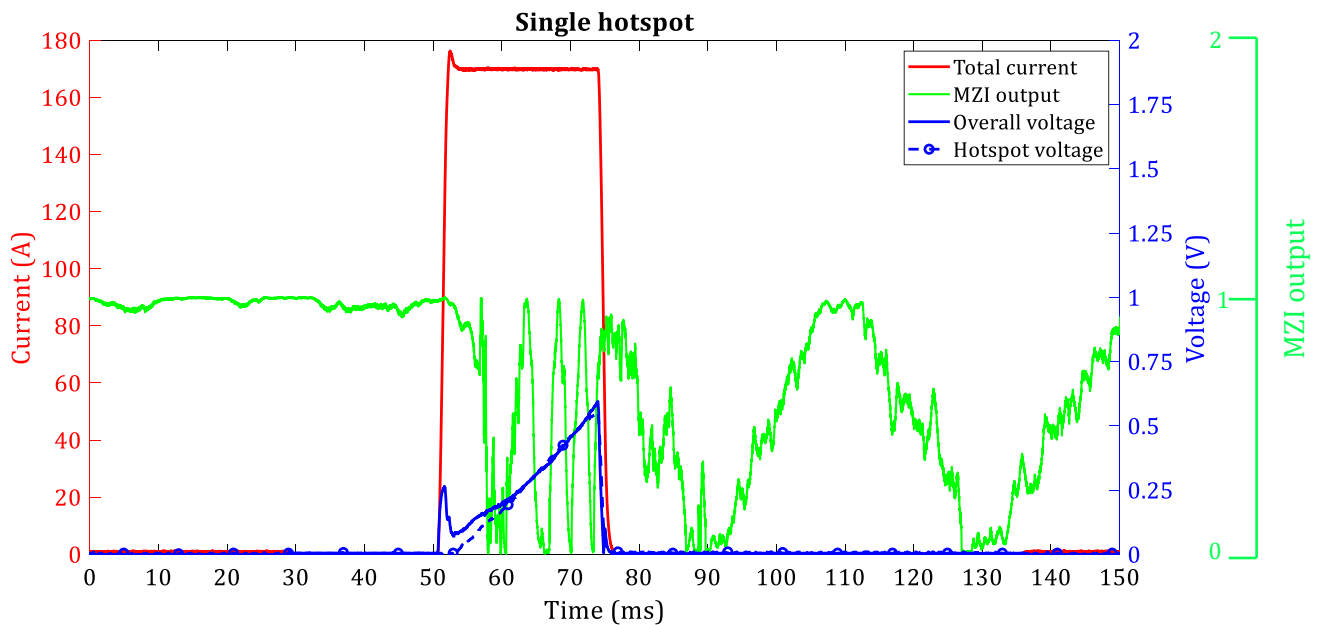


Figure 47. MZI response to single hotspot in the SCS4050-AP sample

Fig. 48 shows the MZI response to multiple hotspots in the SCS4050-AP sample. In this case 175 A of current is pulsed in the sample for 125 ms. The overall voltage is 1.6 V (peak value) while the peak hotspot voltage is 0.5 V. Since the total voltage in the sample is greater than the hotspot voltage, there are points in addition to the magnet region which are heating in the sample. The MZI therefore, is detecting multiple hotspots. The MZI voltage is slowly fluctuating (almost constant) before the heating event occurs and transitions to high frequency amplitude variations within 10 ms of the voltage rise in the sample, signifying heating in the sample. After the current pulse has ended a lower frequency oscillatory response can be observed in the MZI output in response to the sample cool down. The current can be seen to drop as the sample becomes resistive due to lack of voltage on the capacitor in the current pulser to sustain the current.

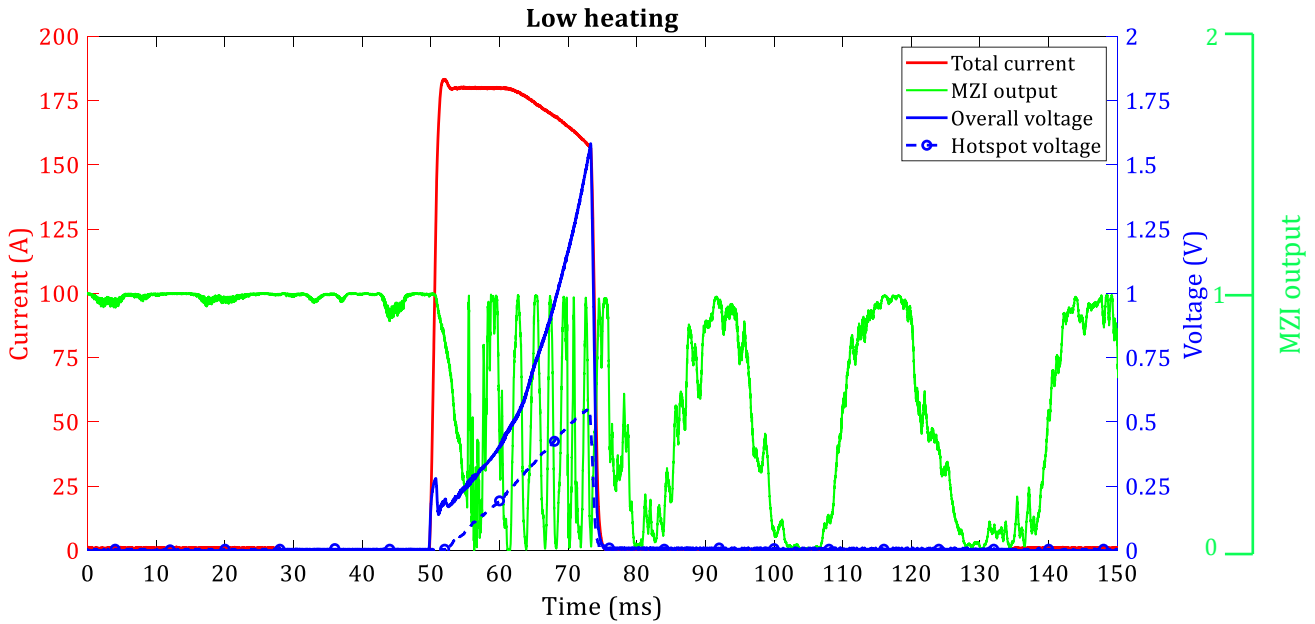


Figure 48. MZI response to multiple hotspots in the SCS4050-AP sample

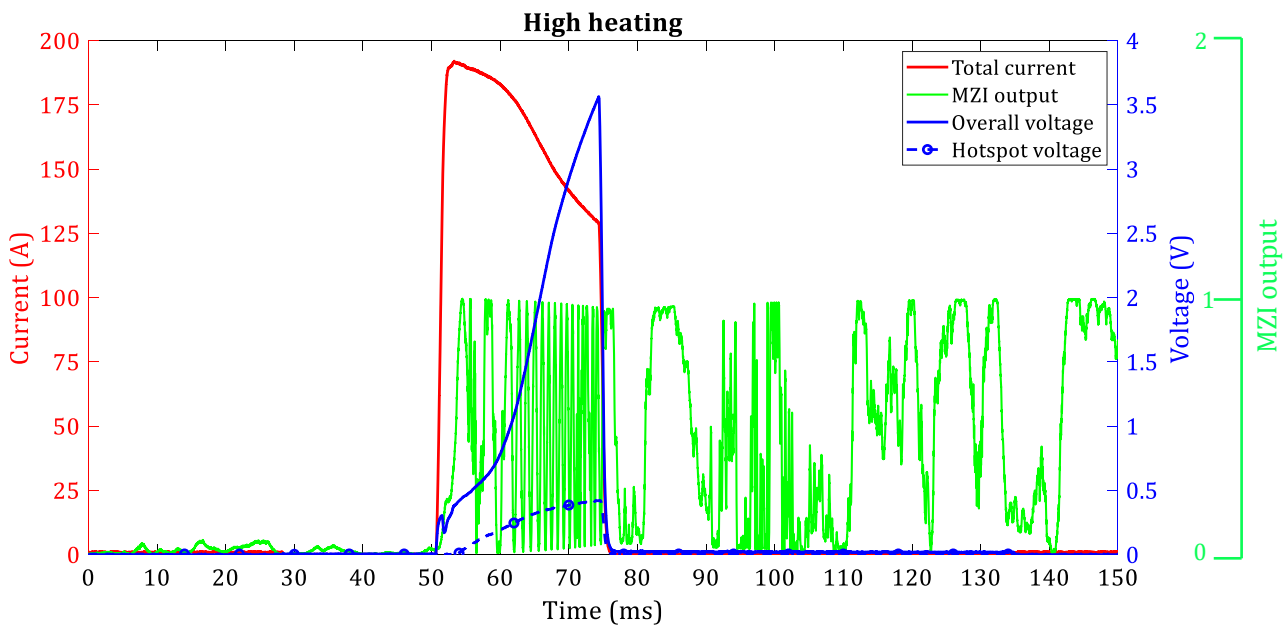


Figure 49. MZI response to high heating in the SCS4050-AP sample

Fig. 49 shows the MZI response to high heating (clear fault) in the SCS4050-AP sample. In this case 190 A of current is pulsed in the sample for 25 ms. The plot shows that the overall voltage is 3.6 V (peak value) while the hotspot voltage is 0.4 V (peak value) which is much lower than the total sample voltage; hence there are multiple heating locations in the sample causing a high heating fault. The MZI output can be seen to transition from a quiet slowly varying signal to high frequency oscillations within 10 ms of voltage rise in the sample.

### 5.1.3 Discussion for the 1 m SCS4050-AP sample

The MZI hotspot detection technique managed to detect a single hotspot in the sample within 10 ms which is an important demonstration of the high sensitivity and quick reaction time of the MZI method to hotspots in HTS samples. The critical current of the sample is specified by the manufacturer as 125 A, and should theoretically reduce further due to the addition of the magnet. However, the single hotspot was observed at 170 A which is much higher than 125 A. This could be due to the critical current inhomogeneity and the possibility of the sample being taken from a higher critical current variation part of the HTS tape reel. Response of the MZI to low heating and high heating in the sample are shown and it can be seen from Fig. 47 to Fig. 49 that the frequency of the oscillations in response to heating in the sample increases. This is because the sample is attaining a higher temperature change within the same duration (current pulse duration of 25 ms), meaning a higher rate of change of temperature. Therefore, in high heating case, according to the mathematical overview presented in Chapter 3, the phase is modulated at a higher rate leading to higher frequency oscillations. It is also interesting to note that the oscillatory response of the MZI to sample cool down is less noisy in the lower heating cases in Fig. 47 and Fig. 48 as compared to the case in Fig. 49. This could be due to multiple factors: higher acoustic noise when the sample quenches, higher Lorentz force or more bubbling in the cryostat due to higher sample temperature. Overall, however, the MZI performance for this sample was highly satisfactory with a good signal to noise ratio (SNR). The MZI response before the heating event in the sample was not noisy at all allowing easy identification of the MZI output variation in response to hotspots in the sample.

## 5.2 65 cm long Theva TPL5121 HTS sample

### 5.2.1 Sample specifications

Table 6. Theva TPL5121 details

<b>Manufacturer</b>	HTS tape provided by Theva (Sample name: TPL5121)
<b>HTS tape length</b>	0.65 m
<b>HTS tape width</b>	12 mm
<b>HTS tape thickness</b>	0.1 mm
<b>Stabilization</b>	All around 2 $\mu\text{m}$ of silver
<b>Substrate thickness</b>	50 $\mu\text{m}$ Hastelloy
<b>Critical current</b>	330 A (at 77 K and self-field conditions)
<b>Fibre integration</b>	Optical fibre taped along the conductor length by means of Kapton
<b>Fibre diameter</b>	250 $\mu\text{m}$
<b>Magnet</b>	Not used
<b>Sample holder</b>	Linear sample holder with the sample susceptible to movement due to Lorentz force during current pulse

This sample was a 65 cm long bare HTS tape sample that was taken from the 11 m TPL5121 reel between the position 27.202 m and 27.8502 m. The sample had a critical current of 330 A at 77 K and self-field conditions specified by Theva with the critical current distribution along the length given by the Tapestar measurements plotted in Fig. 50 [49].

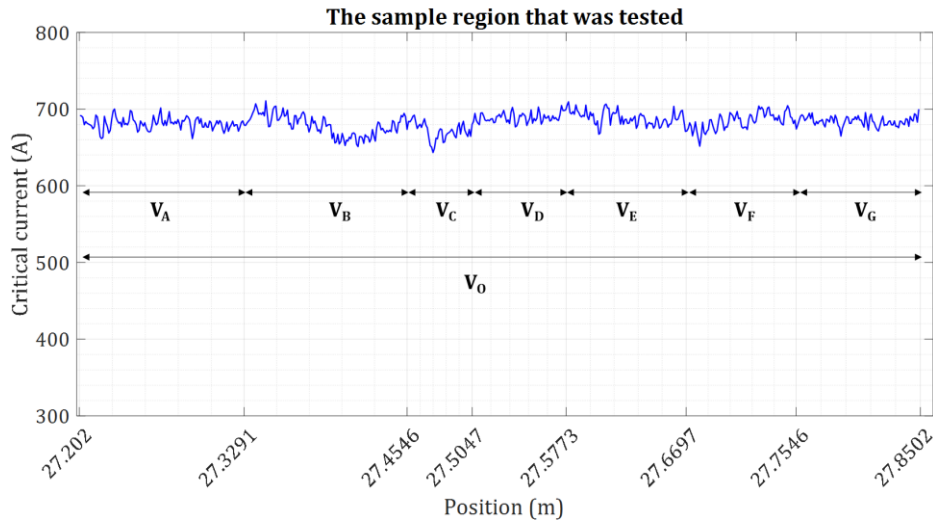


Figure 50. Tapestar measurements and voltage tap locations for the portion (27.202 m to 27.8502 m) of the Theva TPL5121 tape which was tested with the MZI

Since the TPL5121 reel had a high inherent critical inhomogeneity, this experiment did not make use of a magnet to artificially create a weak point. The weakest point in the 65 cm sample was at 620 A. Voltage taps

were placed 5.5 cm apart around this weak point (marked  $V_C$  on Fig. 50) and voltage taps were also placed in the adjacent segments on either side of  $V_C$  (marked  $V_A$ ,  $V_B$ ,  $V_D$ ,  $V_E$ ,  $V_F$ ,  $V_G$  on Fig. 50). The voltage in the full sample was also measured (marked  $V_O$  on Fig. 50). The sample was cooled to 77 K and current was pulsed in the sample for a duration of 50 ms each time.

## 5.2.2 Experiment results

Fig. 51 shows the MZI response for no heating in the sample.

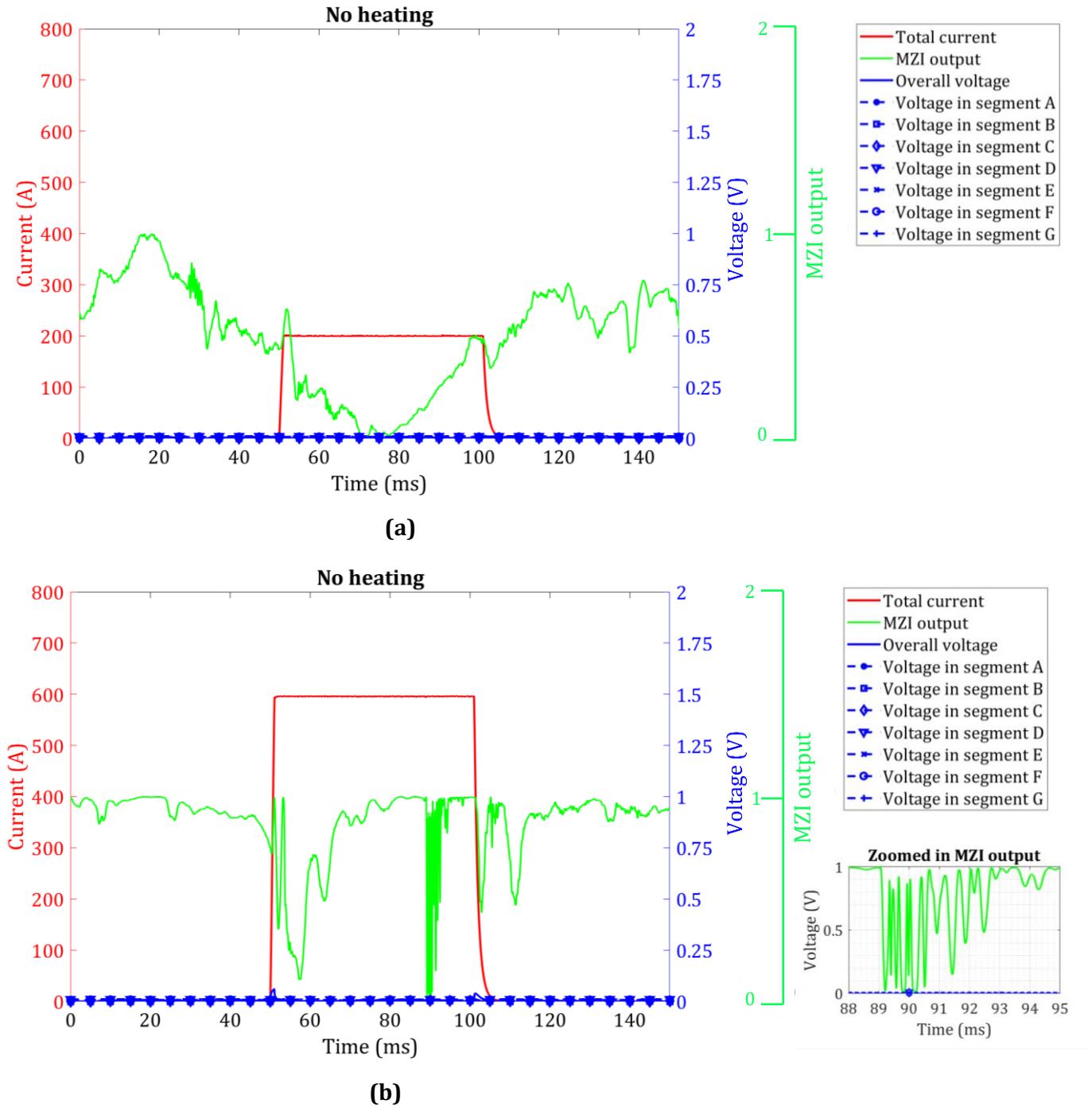


Figure 51. MZI response to no heating in TPL5121 sample with low current (a), with high current (b)

In Fig. 51(a) 200 A of current is pulsed in the sample and the voltage in all segments of the sample is zero. There is therefore no heating in the sample and the MZI output shows slow variations with no identifiable pattern. Fig. 51(b) shows a case where 650 A of current is pulsed in the sample and even though the voltage in the sample is zero, the MZI output is noisier as compared to that in Fig. 51 (a). This is due to higher Lorentz force at higher currents. Zooming in on the plot in Fig. 51 (b) shows that the Lorentz force is manifesting in the MZI interference pattern in the form of high frequency oscillations (this presents a difficulty in MZI response analysis as will be discussed in detail further in the thesis).

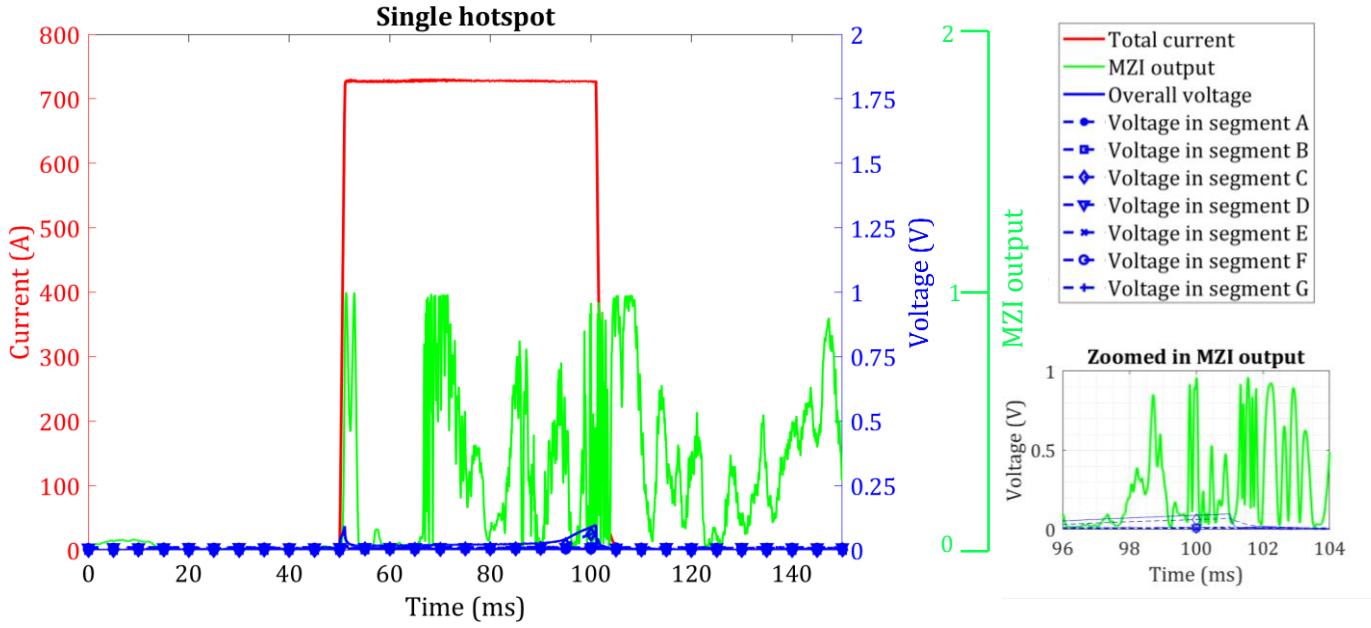


Figure 52. MZI response to single hotspot in TPL5121 sample

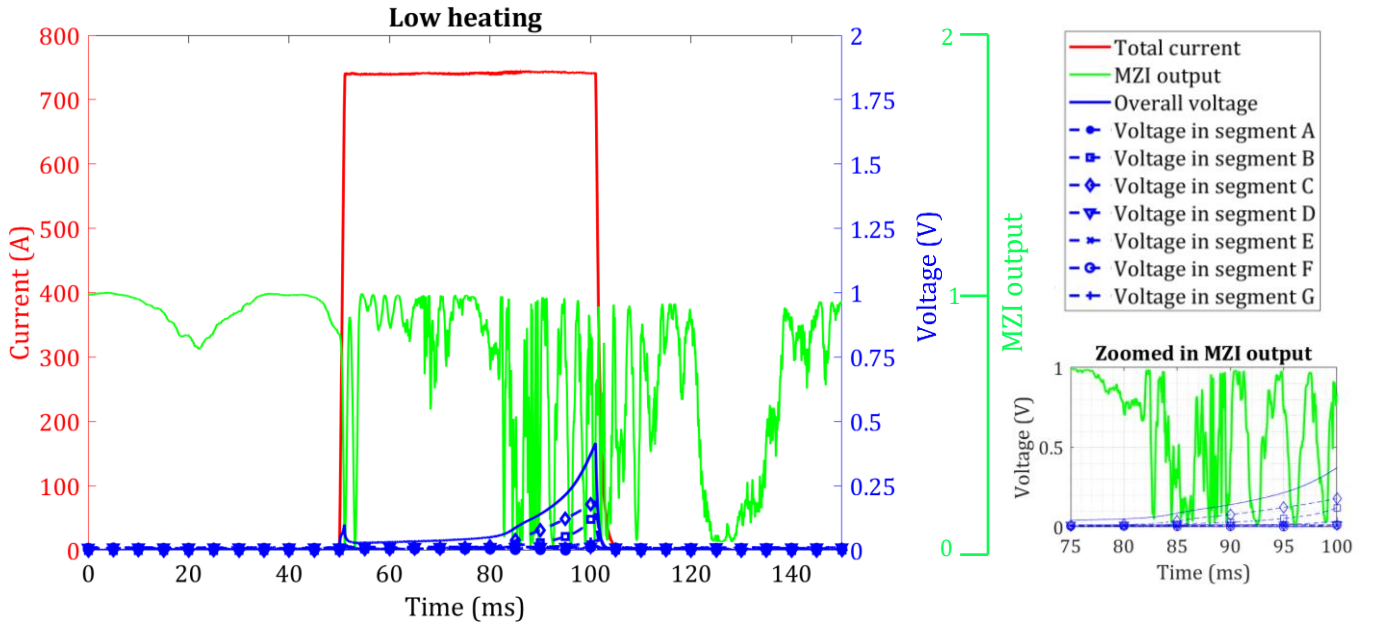
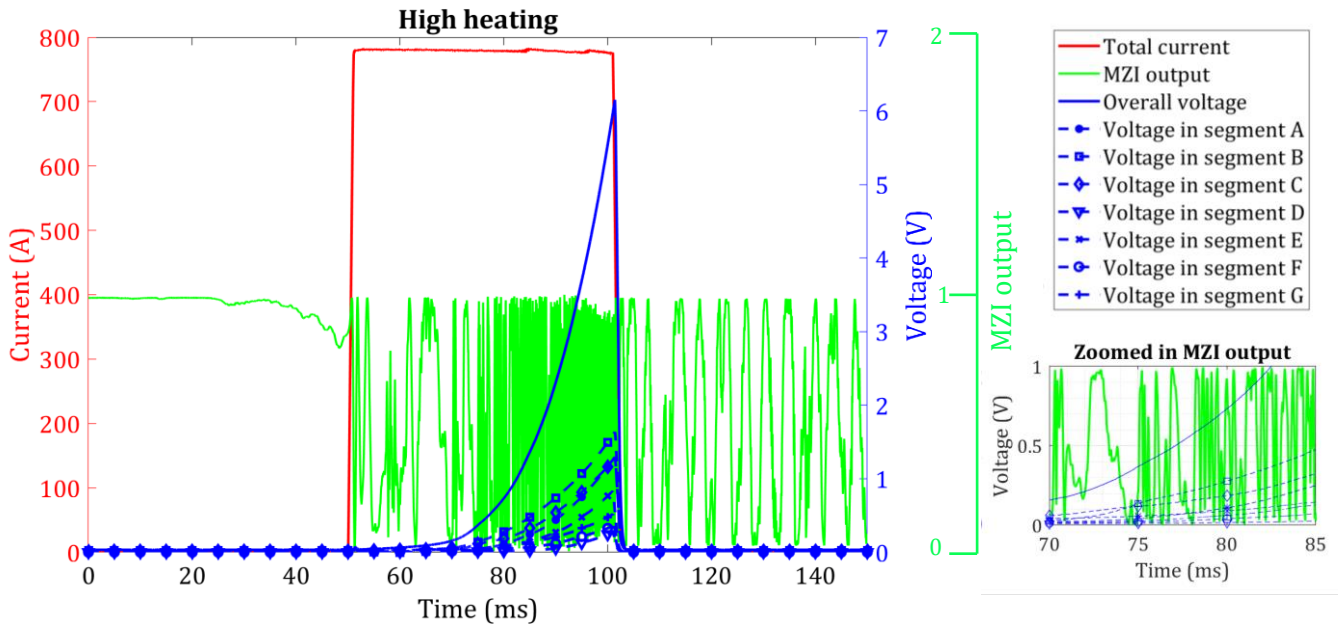


Figure 53. MZI response to low heating in TPL5121 sample



Fig. 52 shows the MZI response to a single hotspot in the sample. 720 A of current is pulsed in the sample and only voltage in segment C can be seen to rise to a voltage of 0.1 V which is the same as the overall voltage in the sample. The MZI output while quiet before the event of the current pulse shows some disturbance when current is injected in the sample even though the voltage in segment C is observed later. Zooming in on the MZI output, some oscillations are observed near the peak hotspot voltage, however, due to the very low heating and high Lorentz force noise, the oscillations are poor quality and do not sustain for long.

Fig. 53 shows the MZI response to relatively low heating in the TPL5121 sample. 740 A of current is pulsed in the sample, and in addition to the weak region of segment C, voltage rise is also observed for the adjacent segment B. The normal zone therefore has propagated from segment C to segment B. The total voltage in the sample is 0.4 V. The MZI output shows slow fluctuation before the current pulse and a slight disturbance due to Lorentz force during the current pulse, before transitioning to oscillatory amplitude variations in response to heating in the sample. In the zoomed in plot in Fig. 53, it can be seen that the voltage begins to rise at the 80 ms mark and between 90ms to 100 ms clear oscillations can be observed in the MZI output.



**Figure 54. MZI response to high heating in TPL5121 sample**

Fig. 54 shows the MZI response to high heating in the TPL5121 sample. 790 A is pulsed through the sample and voltage is observed in all parts of the sample with the overall voltage reaching 6 V. The zoomed in plot for Fig. 54 shows that the MZI transitions within 10 ms of the quench to an oscillatory response, the frequency of which can be seen to increase as the rate of temperature change in the sample increases. Once the current pulse has ended, lower frequency oscillations can be observed in the MZI output in response to sample cool down.

### 5.2.3 Discussion for the 65 cm TPL5121 sample

This sample had a much higher critical current than the SCS4050-AP sample, which meant higher currents had to be pulsed in the sample to achieve heating in the sample. This subjected the MZI to higher Lorentz force and acoustic noise disturbances leading to noisier measurements. While the MZI managed to detect a single

hotspot as well as multiple hotspots, the quality of the oscillations degraded and the oscillations were non-uniform. The MZI response to the single hotspot was not strong because of the low voltage (0.1 V) and hence very low temperature change in the hotspot. The phase shift introduced due to the heating therefore was unable to dominate the phase shift introduced due to fluctuation in the ambient factors (the high Lorentz force in this case). These points will be further addressed later on in this chapter, in the section highlighting challenges with the MZI technique. Overall, the MZI did manage to detect low and high heating in the sample within 10 ms. Due to the pulsed current measurement technique the MZI response to a single hotspot was not ideal, however for longer pulse duration this hotspot would have evolved into higher heating fault and would have been detected by the MZI.

### 5.3 30 cm OFE-HTS sample with soldered optical fibre

#### 5.3.1 Sample specifications

Table 7. OFE-HTS sample details

<b>Manufacturer</b>	Shanghai Jiao Tong University (SJTU), Shanghai (Sample name: OFE-HTS tape)
<b>HTS tape length</b>	30 cm
<b>HTS tape width</b>	12 mm
<b>HTS tape thickness</b>	0.3 mm
<b>Stabilization</b>	3 $\mu\text{m}$ all around silver + indirect stabilization through stainless steel encasing
<b>Substrate thickness</b>	50 $\mu\text{m}$ Hastelloy
<b>Critical current</b>	410 A (at 77 K and self-field conditions)
<b>Fibre integration</b>	Soldered at the edge
<b>Fibre diameter</b>	170 $\mu\text{m}$
<b>Magnet</b>	10 mm diameter placed at the center of the sample
<b>Sample holder</b>	“Caged” linear sample holder with the sample subject to zero Lorentz force during current pulse

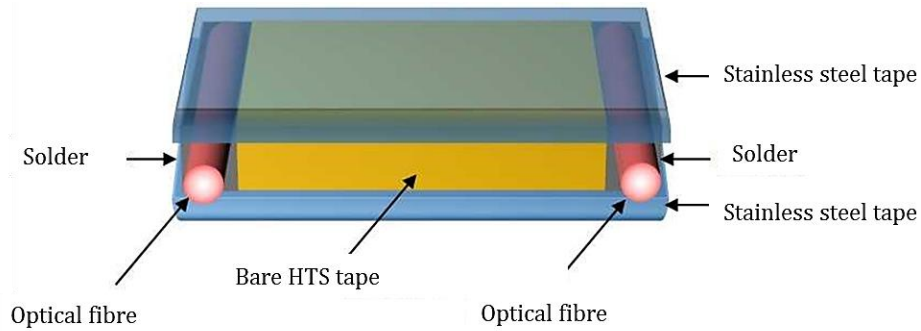
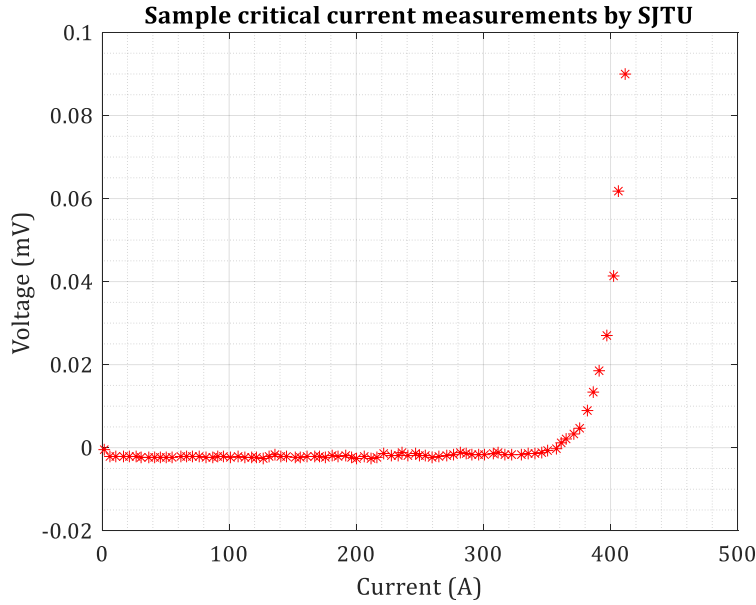


Figure 55. Structure of the encapsulated HTS tape (OFE-HTS tape) with soldered optical fibre[88]

This sample is manufactured at SJTU and is called the optical fibre encapsulated (OFE)-HTS tape [88]. It was kindly provided by SJTU to EPFL to test with the MZI setup. The motivation behind the OFE-HTS tape structure is to integrate optical fibre with the HTS tape to facilitate distributed sensing method for health monitoring in HTS applications. The objective is to integrate the fibre with the HTS conductor in such a way that the thermal conduction path between the optical fibre and HTS tape is reduced so distributed optical fibre sensors can more accurately detect heating in the HTS tapes during a quench. The OFE-HTS tape structure is shown in Fig. 55, whereby two optical fibres are placed on each side of a HTS tape along the entire conductor length. Two stainless steel tapes encase the HTS tape and the optical fibres. The optical fibres are fixed in place by means of solder. Integrating the optical fibre in this way enables faster thermal conduction of heat to the optical fibre and facilitates easier winding of HTS coils.



**Figure 56. Critical current of the OFE-HTS tape sample measured at SJTU**

The sample provided to EPFL was 30 cm long, with a critical current of 410 A as shown in Fig. 56. A 10 mm magnet was placed in the center of the sample to create a weak point of a known location. Voltage taps were placed to measure voltage around the magnet (hotspot voltage) in the adjacent segments on either side of the magnet (segment 1 and segment 2) and also to measure the total voltage in the sample (overall voltage). One of the two optical fibres broke while splicing, leaving insufficient length for splicing therefore only one fibre on the sample was spliced and connected to the MZI setup. The sample was mounted on a linear sample holder which was mentioned in Section 4.4.6 which ensured the sample experienced zero Lorentz force and hence did not move during the current pulse. The sample was placed in the cryostat at 77 K and current was pulsed in the sample for 50 ms every time. Data is acquired 50 ms before the current is pulsed as well to properly observe the MZI response variation in the event of heating in the HTS tape. MZI voltage has been normalized and scaled to vary between 0 and 1 for plotting purposes.

### 5.3.2 Experiment results

Fig. 57 shows the MZI response to no heating in the OFE-HTS tape. 290 A of current is pulsed in the sample. The overall voltage in the sample is zero, indicating no heating in the sample. The MZI output shows slow fluctuations with no pattern, in response to changes in the ambient environmental temperature for example.

Fig. 58 shows the MZI response to a single hotspot in the OFE-HTS tape sample. 470 A of current is pulsed in the sample. A very low voltage of 0.05 V (peak value) is observed around the hotspot and total sample length indicating a single point heating in the sample. The voltage and hence the heating in the sample is very low to sustain a strong MZI response but a slight disturbance is visible in the MZI output almost immediately as the hotspot voltage reaches peak value as apparent in the plot in Fig. 58.

Fig. 59 shows the MZI output to multiple hotspots in the sample. A current of 670 A is pulsed in the sample. A peak voltage of 0.6 V is observed in the sample, and a non-zero voltage is observed in the hotspot as well as the adjacent segments signifying either a propagation of the normal zone or multiple hotspots. The MZI output is slowly fluctuating before the heating event but transitions to a continuous high frequency oscillatory response within 10 ms of voltage rise in the sample.

Fig. 60 shows a high heating fault in the OFE-HTS tape. 690 A of current is pulsed in the sample and an overall voltage of 1 V is measured in the sample. A non-zero voltage is measured in the weak point as well as the adjacent segment indicating heating in multiple locations of the sample. The MZI output transitions from a slowly varying voltage to continuous rapid oscillations within 10 ms of voltage rise in the sample.

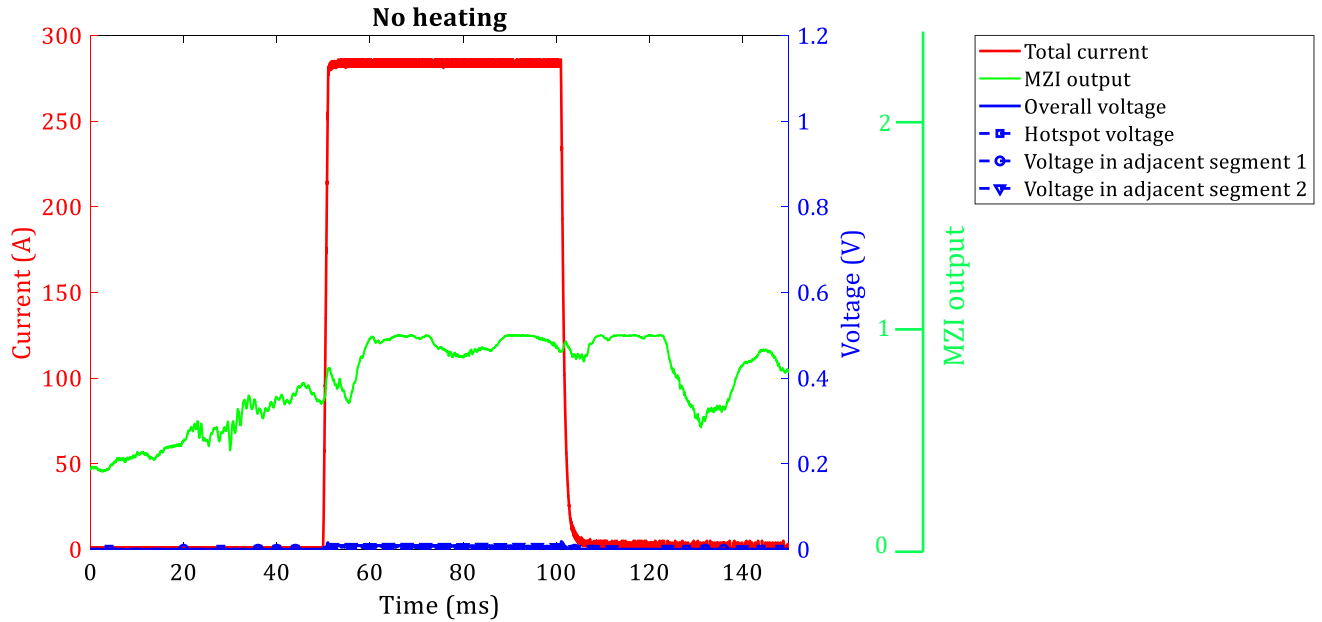


Figure 57. MZI response for no heating in OFE-HTS tape

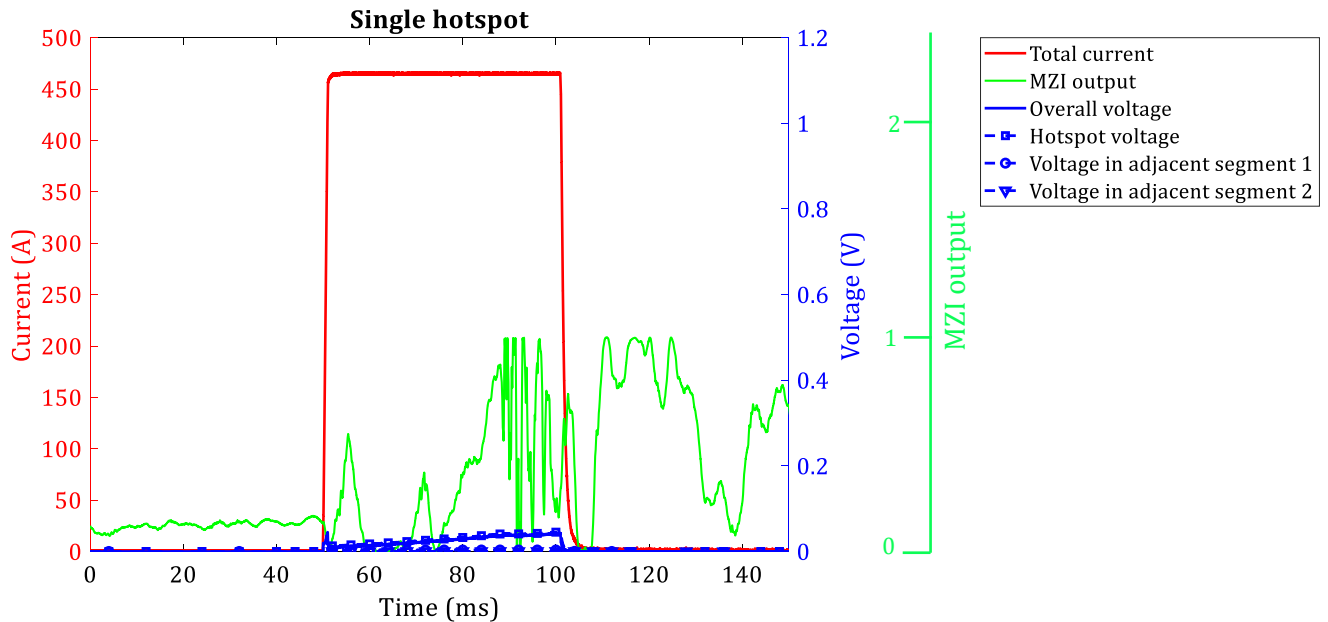


Figure 58. MZI response for a single hotspot in the OFE-HTS tape

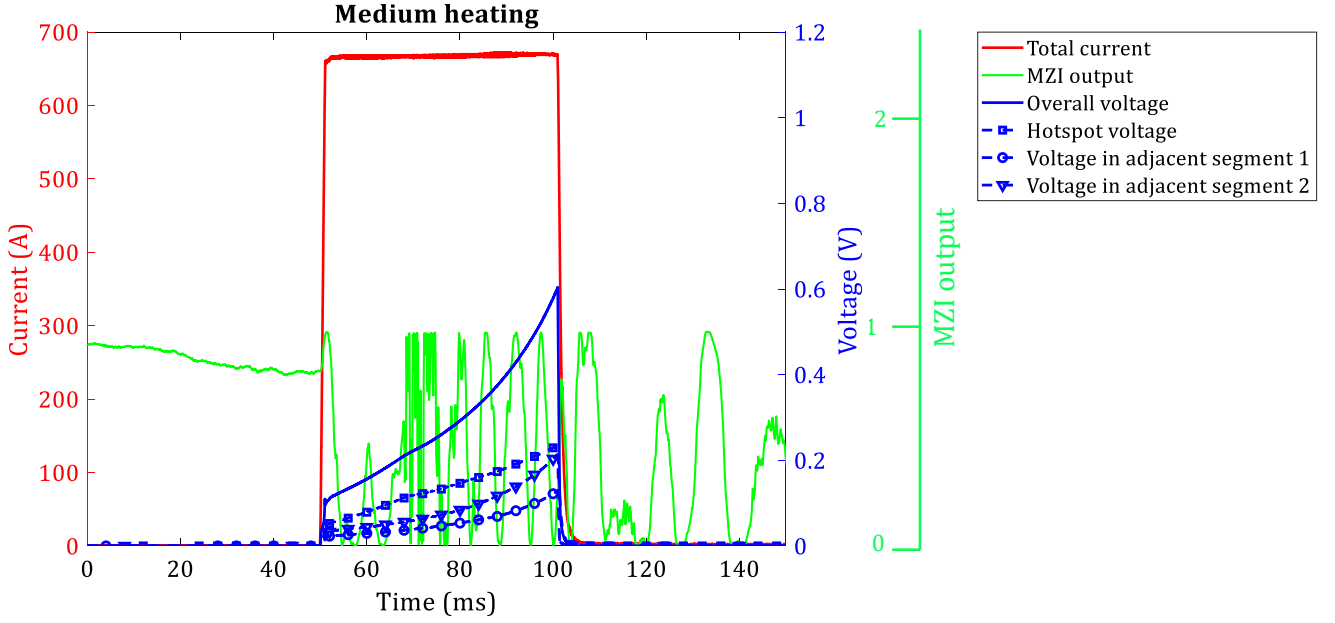


Figure 59. MZI response for medium heating in the OFE-HTS tape

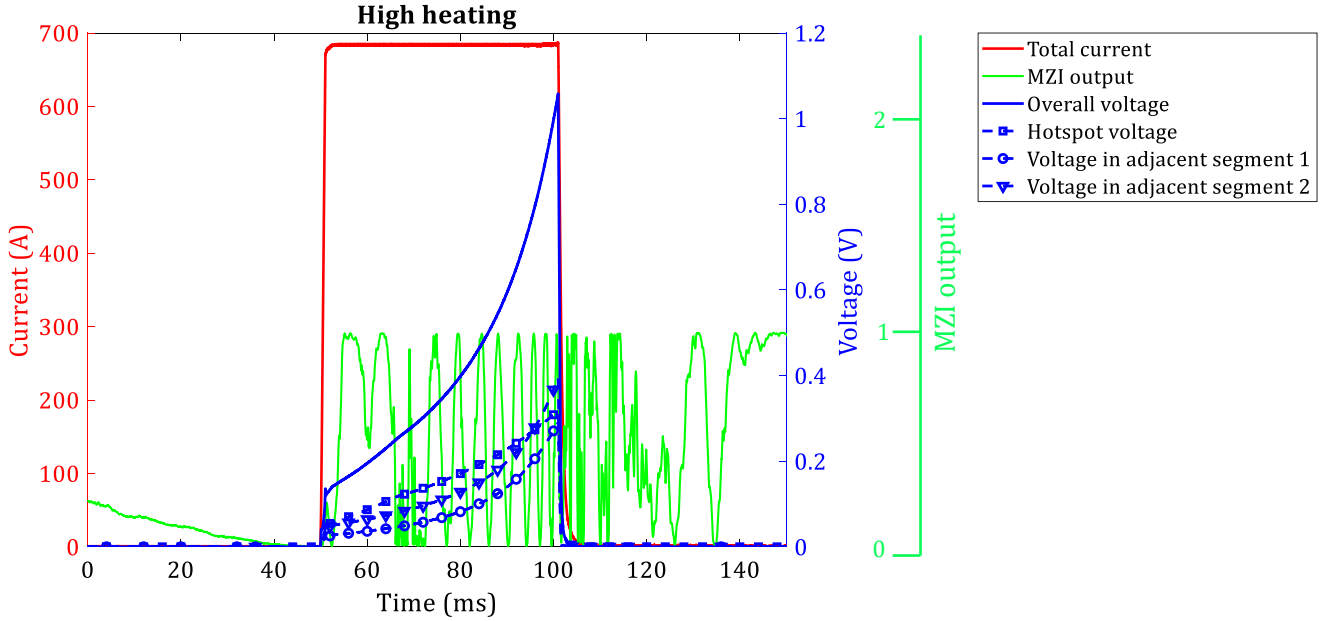


Figure 60. MZI response to high heating in the OFE-HTS tape

### 5.3.3 Discussion for the 30 cm OFE-HTS sample

The MZI technique was able to detect heating in the OFE-HTS sample within 10 ms. The MZI output was easily identifiable, with good quality oscillations. The response to a single hotspot was weak due to very low heating and the case of pulsed current measurement which does not allow the fault to evolve into high heating scenarios. Even though the critical current was 410 A and a magnet was placed on the sample, the hotspot was not observed until 490 A. This could be due to the thermal stabilization provided by the stainless steel encasing, which does not allow the sample to heat up easily. Even though higher currents had to be pulsed, the Lorentz force disturbance, did not cause noisy measurements as was the case with the TPL5121 sample. This shows

that the “caged” sample holder works well to eliminate perturbations that can be introduced in the MZI signal due to Lorentz force. The disturbance is lower overall in the MZI output for this sample which could be mainly because of the special sample holder but also because of the shorter length of the OFE-HTS tape, lower heating and less bubbling in the cryostat. With regards to optical fibre integration in this sample, it can be concluded that the soldered optical fibre does not hinder fast detection with the MZI. The MZI manages to detect heating in the sample within 10 ms. The solder ensures good mechanical coupling of the optical fibre with the sample, ensuring good temperature and strain transfer to the optical fibre from the conductor

## 5.4 Petite SFCL Pancake

### 5.4.1 Sample specifications

Table 8. Petite SFCL Pancake details

<b>Manufacturer</b>	HTS tape provided by Theva and wound by SuperGrid Institute Lyon (SGI)
<b>HTS tape length</b>	2x6 = 12 m
<b>HTS tape width</b>	12 mm
<b>HTS tape thickness</b>	0.1 mm
<b>Stabilization</b>	2 $\mu\text{m}$ all around silver
<b>Substrate</b>	50 $\mu\text{m}$ Hastelloy
<b>Pancake diameter</b>	570 mm
<b>Critical current</b>	330 A (at 77 K and self-field conditions)
<b>Fibre integration</b>	Three optical fibres per conductor taped along the length by means of Kapton
<b>Fibre diameter</b>	250 $\mu\text{m}$
<b>Magnet</b>	Not used

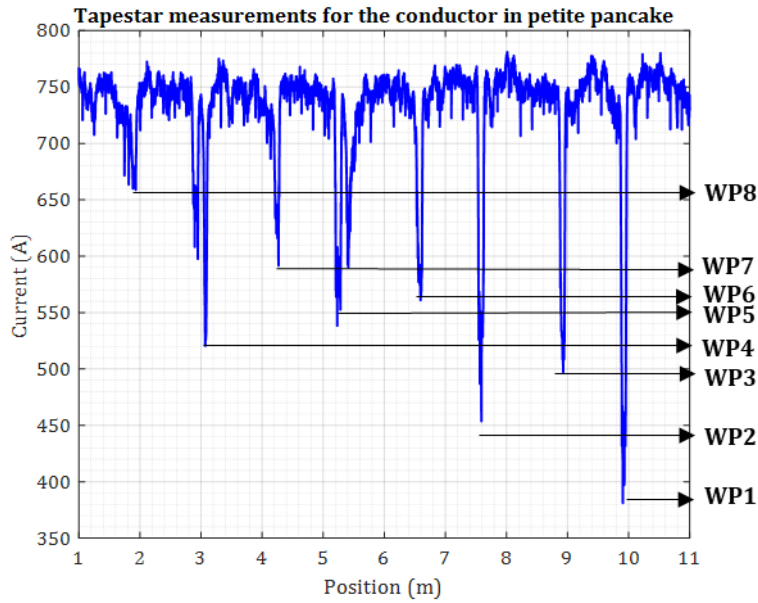


Figure 61. TapeStar plot for the Theva bare HTS tape used to wind the Petite SFCL Pancake

The Petite SFCL Pancake comprised two conductors, each with three optical fibres. Three optical fibres were integrated to introduce redundancy in case any fibre broke during the winding process or transport. 50 cm of optical fibres were left at the ends outside of the pancake for splicing. One fibre on each conductor was spliced and the two fibres were connected together in series to monitor the full length of conductor in the pancake (12 m). The conductor was manufactured by Theva without stabilizer and had a specified critical current of 330 A at 77 K and in self-field conditions. The TapeStar measurements for this conductor are shown in Fig.



61 [49] where it can be seen that while the highest critical current is 770 A there are numerous weak points with low critical current values marked on Fig. 61 from WP1 to WP8, numbered in order of increasing critical current values. This makes the pancake a good tool for testing the MZI technique as increasing the pulsed current value in a stepwise manner, from the weak point with lowest critical current (WP1 at 380 A), it can be determined which weak points are heating and study the MZI response to it. The pancake was cooled to 77 K. The plots for the experiment show the current pulsed in the pancake, voltages in the two conductors (voltage A and B), the overall voltage in the pancake, and the MZI output normalized by the maximum voltage. Data is acquired 50 ms before the pulse and 30 ms after in order to better observe the MZI response variation.

### 5.4.2 Experiment results

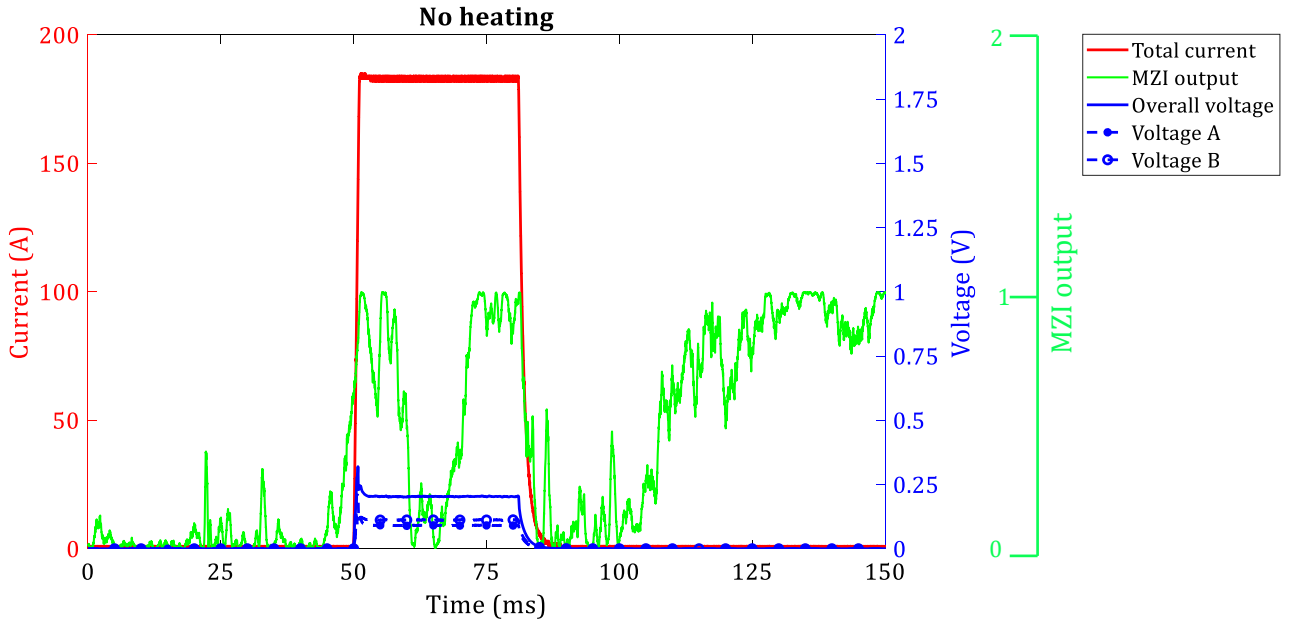


Figure 62. MZI response to no heating in the Petite SFCL Pancake

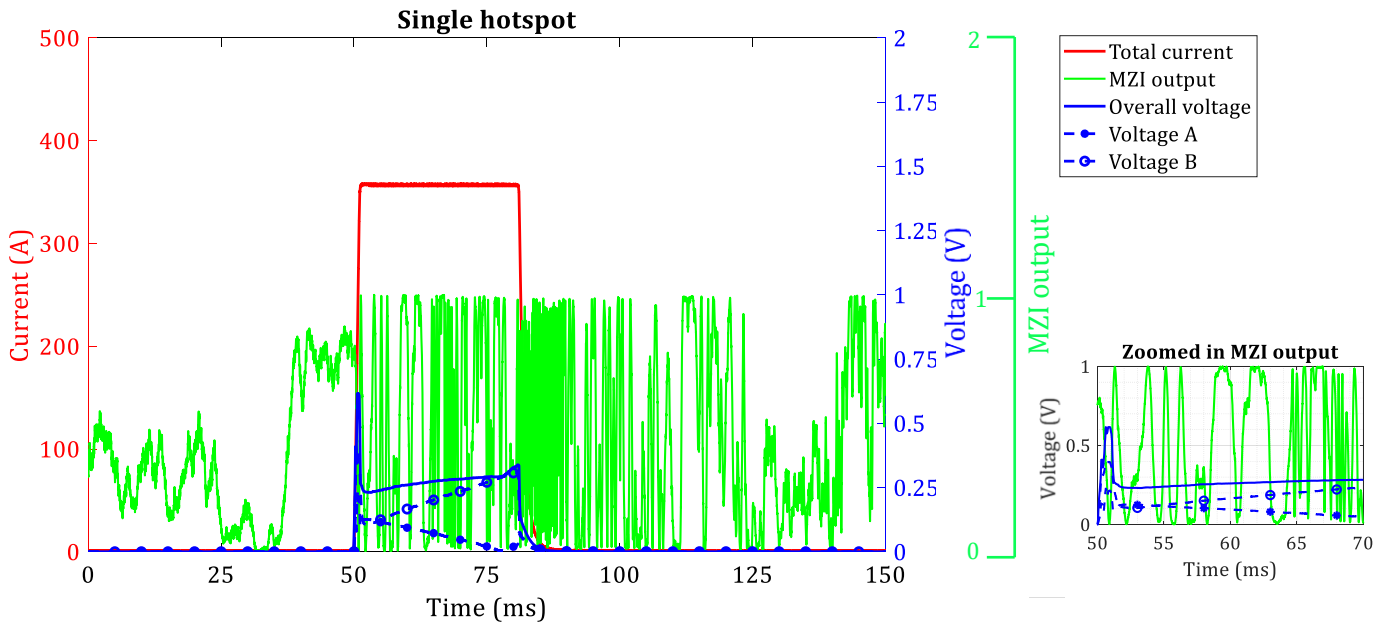


Figure 63. Single hotspot detection by the MZI in the Petite SFCL Pancake

Fig. 62 shows the experiment results for no heating in the Petite SFCL Pancake. 200 A of current is pulsed in the pancake for 30 ms and there is no voltage in the conductors. The constant voltage observed is simply the contact resistance. The MZI output shows no oscillatory response but a slight noise is observed which could be due to Lorentz force or bubbling in the cryostat.

Fig. 63 shows the results for a single point heating in the pancake. 340 A of current is pulsed in the pancake for 30 ms and voltage is observed in conductor B reaching a peak value of 0.25 V. The initial spike in the voltage measurement is due to the circuit inductance. Analyzing the result by means of the TapeStar measurements in Fig. 61, it can be deduced that in this case WP1 is the point that is transitioning and hence the MZI is detecting a single hotspot in the pancake. The MZI output can be seen to switch from slow fluctuations with no pattern to rapid oscillations almost immediately, in response to the hotspot.

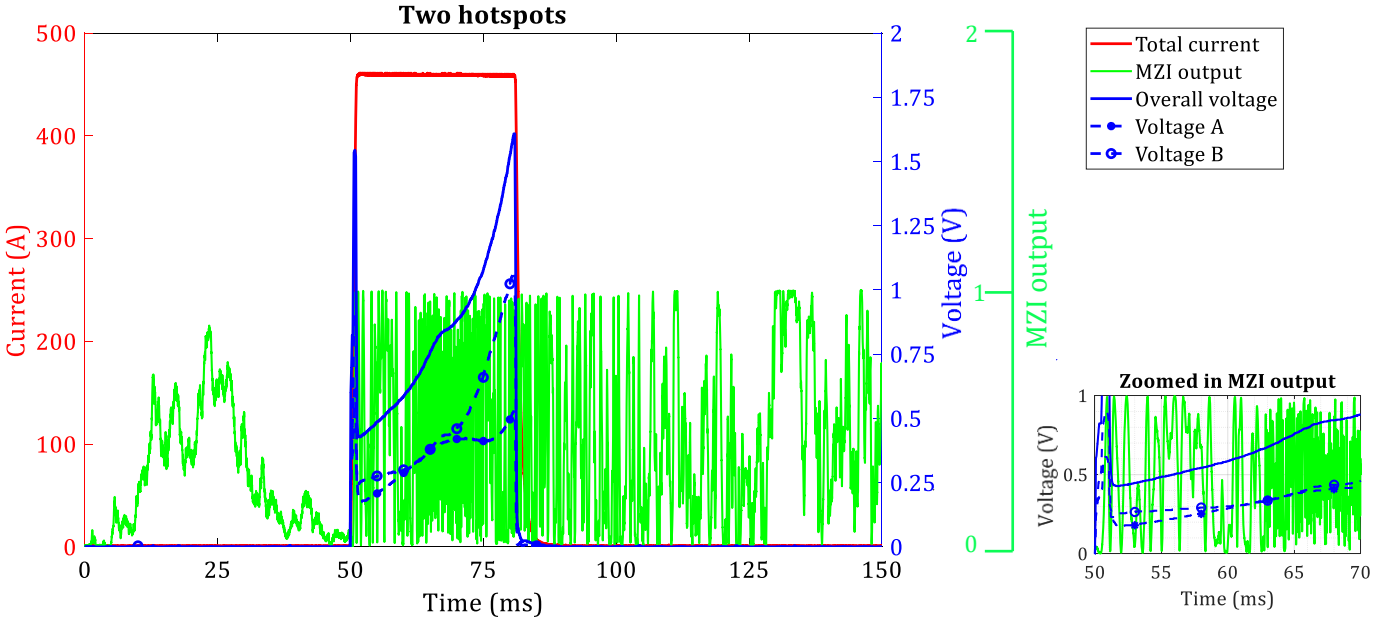


Figure 64. MZI response to two hotspots in the Petite SFCL Pancake

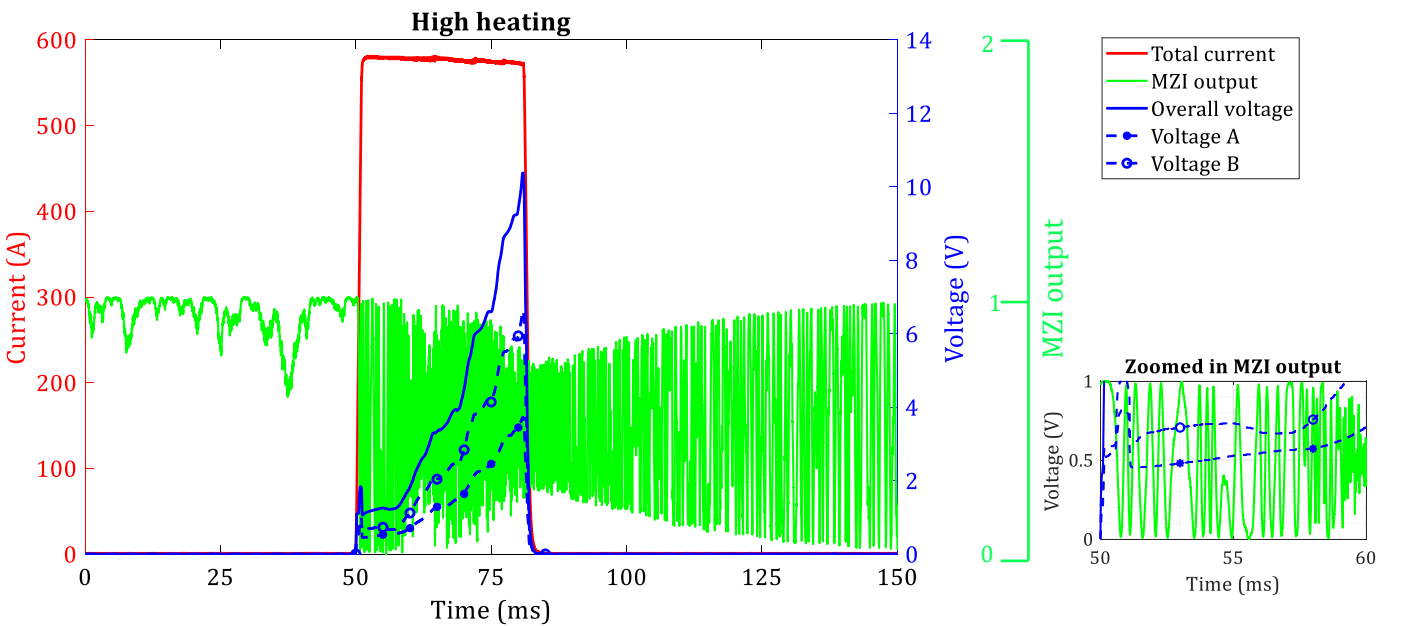


Figure 65. MZI response to multiple hotspots in the Petite SFCL Pancake

Fig. 64 shows the results for two points heating in the sample. 460 A is pulsed in the pancake for 30 ms and according to the TapeStar plot in Fig. 61, two weak points (WP1 and WP2) should transition. In Fig. 64 it can be seen that voltage rises in both conductors. Voltage B is greater than voltage A, from which it can be deduced that WP1 which was detected previously in conductor B is heating more and WP2 is located and heating in conductor A. A total voltage of 1.7 V (peak value) is observed in the full pancake. The MZI output can be seen to show continuous high frequency amplitude variations almost immediately in response to heating in the sample. These oscillations are easily identifiable in the first 5 ms of the event as visible in the zoomed in plot of Fig. 64 and then after 5 ms they degrade in quality.

Fig. 65 shows the results for high heating in the sample. 590 A of current is pulsed in the sample for 30 ms and maximum voltage of 10.5 V is observed in the pancake. From the TapeStar measurements in Fig. 65, at this current value WP1 to WP7 should transition and heat in the sample. The MZI in this case is therefore detecting multiple hotspots in the pancake. The MZI output can be seen to immediately detect the heating in the sample by transitioning to rapid and continuous amplitude variations the uniformity of which deteriorates 10 ms later. In the main plot in Fig. 65, there is some modulation visible in the outer envelope of the MZI output signaling a rotation in the polarization due to thermal and mechanical stresses causing the peak to peak amplitude of the MZI output to vary.

### 5.4.3 Discussion for the Petite SFCL Pancake

MZI performed extremely well for monitoring heating in 12 m of conductor in the petite pancake. The MZI technique was able to detect a single hotspot, two hotspots and multiple hotspots within 5 ms of the event. These results show the potential of MZI for fast hotspot detection in HTS applications. However, the MZI response quality degrades after 5 to 15 ms. This could be due to external disturbances like acoustic noise, bubbling in the cryostat, Lorentz force which are manifesting in the interference pattern in addition to the heating. It can also be due to a phenomenon called birefringence, which will be discussed later on in this chapter. In the absence of heating in the sample, the MZI output was noisier as compared to linear setups for shorter samples. This is because in the large cryostat, the MZI is subject to more perturbations while the long length of conductor in a winding configuration subjects the setup to higher Lorentz force.

## 5.5 The FastGrid pancake

### 5.5.1 Sample specifications

Table 9. The FastGrid pancake details

<b>Manufacturer</b>	HTS tape provided by Theva and wound by SuperGrid Institute Lyon (SGI)
<b>HTS tape length</b>	4x17=68 m (17 m was monitored using MZI)
<b>HTS tape width</b>	12 mm
<b>HTS tape thickness</b>	0.1 mm
<b>Stabilization</b>	2 $\mu\text{m}$ all around silver + 500 $\mu\text{m}$ Hastelloy
<b>Substrate thickness</b>	50 $\mu\text{m}$ Hastelloy
<b>Pancake diameter</b>	880 mm
<b>Critical current</b>	600 A (at 77 K and self-field conditions)
<b>Fibre integration</b>	Three optical fibres per conductor taped along the length by means of Kapton
<b>Fibre diameter</b>	170 $\mu\text{m}$
<b>Magnet</b>	Not used

The FastGrid pancake had two conductors, conductor A comprising A1 in parallel with A2 in series with conductor B comprising B1 in parallel with B2. Each conductor was 17 m in length with three optical fibres integrated along the full length by means of Kapton. Some of the optical fibres broke during transportation of the pancake to EPFL, hence only the optical fibre on conductor A2 could be spliced and tested. These results therefore only show the MZI monitoring heating in 17 m of conductor A2. Current however was pulsed in the full pancake and voltages and currents in all conductors are plotted along with the total current in the pancake and the MZI output. The MZI output voltage is normalized by the maximum for plotting purposes. The pancake was tested at 77 K.

### 5.5.2 Experiment results

Fig. 66 shows the experiment result for no heating in the FastGrid pancake. 390 A of current is pulsed in the sample for 30 ms and the voltage in all conductors is zero. Current in A2 is around 200 A. The MZI output only shows slow variations before the current pulse with no observable pattern. However during the current pulse the MZI is noisy for 10 ms, after the pulse in response to other perturbations arising due to Lorentz force or bubbling in the cryostat. The current sharing can be observed between A1 and A2 and B1 and B2 respectively (sum of currents in A1 and A2 equal the total current and likewise for B1 and B2).

Fig. 67 shows the results for the first heating event detected by MZI in the FastGrid pancake. 490 A is pulsed in the sample for 30 ms (current in A2 is around 250 A). There is a peak voltage of 0.7 V in A2 and the MZI can be seen to show a few oscillations when the voltage in A2 begins to rise and then because the heating is so low, the oscillations are unable to sustain. A few oscillations are observed again when the voltage in A2 reaches the value of 0.5 V.

Fig. 68 shows experiment results for a peak voltage of 4.3 V in A2. In this case 740 A is pulsed in the sample for 30 ms (Current in A2 is around 300 A and peak voltage of 4.3 V is observed in A2). The MZI output begins to show continuous oscillations immediately after the voltage begins to rise in A2.

Fig. 69 shows results for high heating in A2. 1000 A is pulsed in the pancake for 30 ms (current in A2 is around 400 A) and A2 reaches a peak voltage of 13 V. The MZI output switches from slow variations to high frequency continuous amplitude variations immediately in response to the quench as is visible in the zoomed in plot in Fig. 68. The oscillations are uniform for the first 5 ms in both Fig. 68 and Fig. 69 and after 5 ms they become non-uniform.

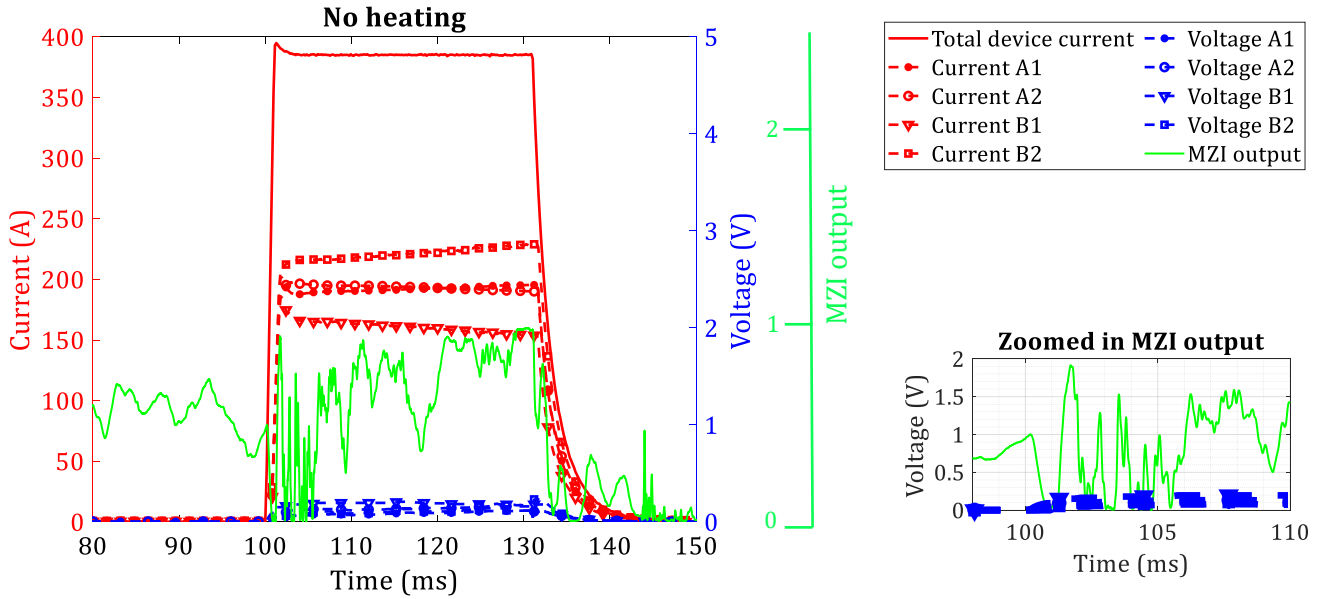


Figure 66 . MZI response to no heating in the FastGrid pancake

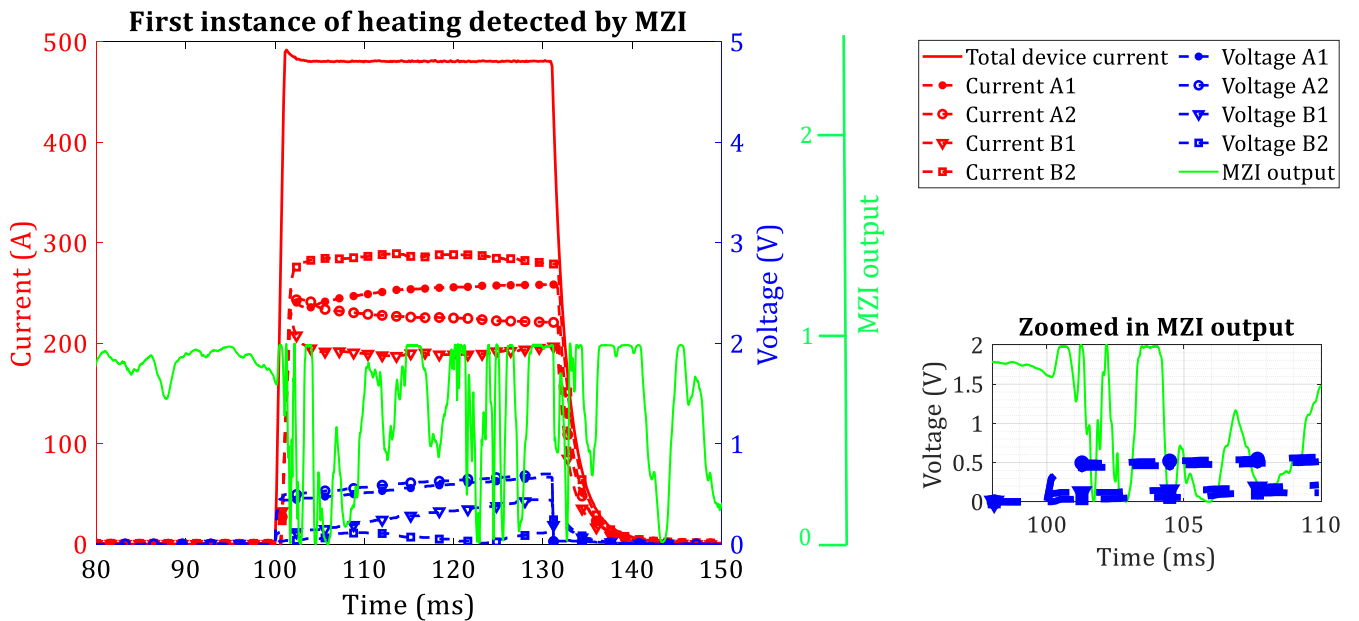


Figure 67. Lowest heating detected by MZI in the FastGrid pancake

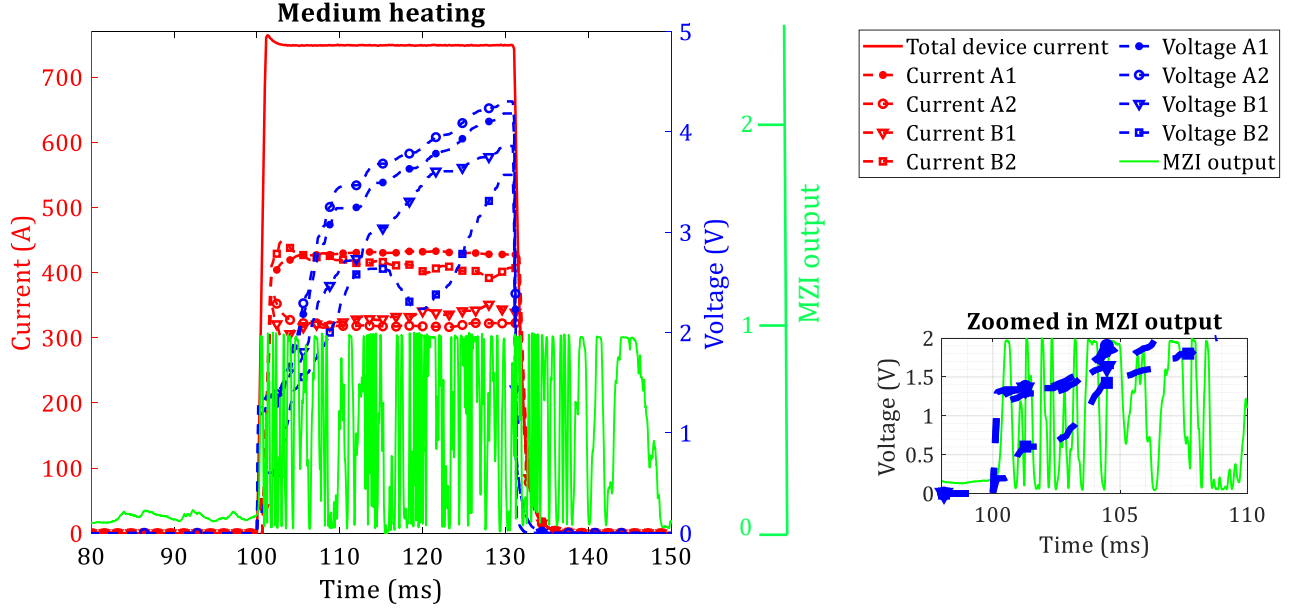


Figure 68. MZI response to medium heating in the FastGrid pancake

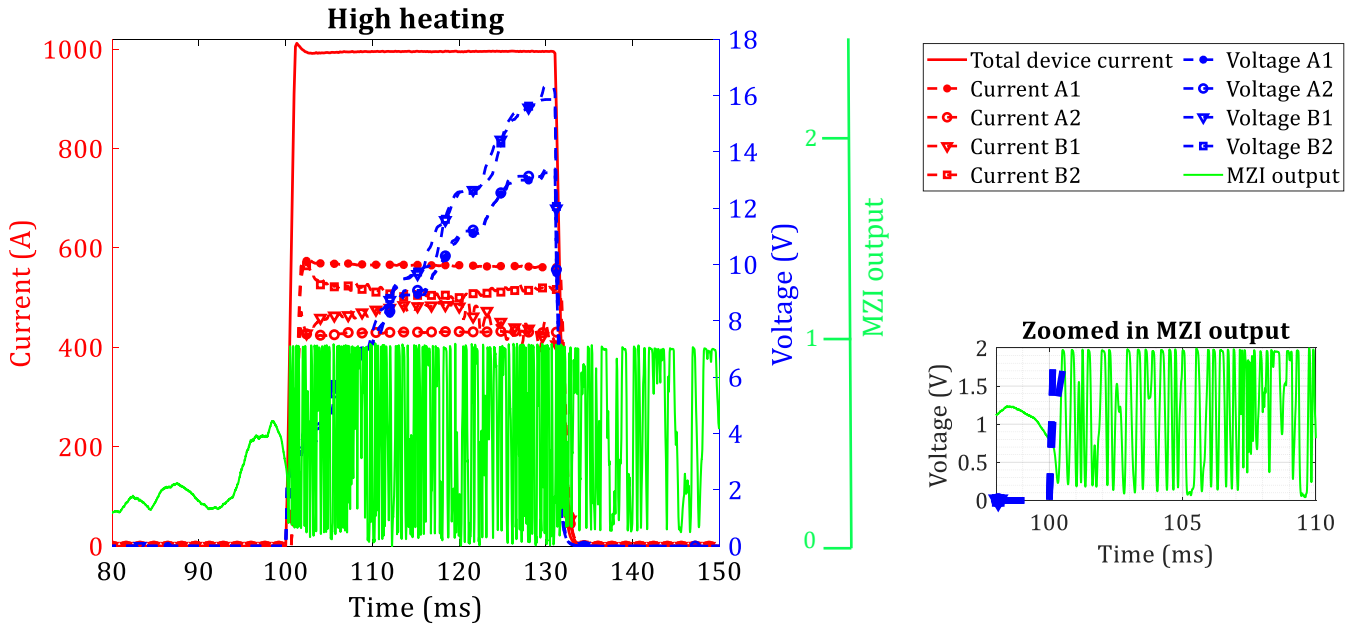


Figure 69. MZI response to high heating in the FastGrid pancake

### 5.5.3 Discussions for the FastGrid pancake

The MZI technique managed to detect heating in 17 m of conductor A2 in the FastGrid pancake almost immediately. In the case of the lowest heating detected by MZI the temperature change was not enough to dominate the other perturbations introducing a phase shift in the MZI output. The MZI was subject to higher disturbance in the case of this experiment setup, due to longer conductor length, bubbling in the big cryostat and Lorentz force which led to noisy MZI measurements in the absence of heating. However, in the event of medium to high heating, the temperature change in the conductor was able to dominate the other

perturbations and clear oscillations were observed in the MZI output immediately in response to the heating. However, similar to the case in the Petite SFCL Pancake, the oscillation quality degraded 5 to 10 ms after the event. This will be addressed in the following section on challenges with the MZI method.

## 5.6 Challenges faced with the MZI method

### 5.6.1 High sensitivity to noise

While the high sensitivity of the MZI plays in the favour of fast hotspot detection it also brings with it the challenge of distortions and non-uniformity in the interference pattern, as the MZI picks up the external perturbations in addition to the hotspot. These perturbations can arise due to vibration of the experimental equipment, bubbling in the cryostat, mechanical movements due to Lorentz force, as well as external temperature changes. These disturbances can also modulate the phase shift of the MZI and manifest in the interference pattern along with heating in the sample. In case of no heating in the sample, these disturbances may lead to false alarms while in the case of heating events these disturbances may deteriorate the interference pattern in the MZI output making it challenging to identify a quench. Fig. 51(b) and Fig. 66 are experiment results that show external perturbations leading to a noisy MZI output in the absence of heating in the sample. While Fig. 52 and Fig. 67 are examples of how in low heating scenarios, external perturbations do not allow the heating in the sample to dominate and modulate the phase shift in the MZI. The extent of this noise is not fixed and varies from perturbation to perturbation and setup to setup, which means it is non-quantifiable.

### 5.6.2 Birefringence

In the experiment results shown, while the MZI detected heating in the sample within 10 ms, the response quality deteriorated after the first 5 to 15 ms, particularly for the longer conductor lengths with higher critical current (Theva 65 cm TPL5121 sample) and the bigger experiment setups (Petite SFCL Pancake and FastGrid pancake). This inconsistency in the MZI response arises due to a phenomena called birefringence [89]. In an ideal case, the phase and group velocities of the polarization state within the optical fibre are not dependent upon the polarization. However, in reality the shape of the fibre core, inherent stresses and external stresses causes the polarization states to propagate with varying velocities developing a phase shift; this causes the polarization to vary along the length of the optical fibre which is called birefringence [90]. Studies have been performed to quantify the changes in refractive index and polarization due to external stresses in optical waveguides and in the MZI [91,92]. It has been shown that the inherent stresses arising due to the non-uniformity of fibre doping or core shape can be ignored [90,93]. It is the external stresses like tensile forces, bending forces and thermal stresses that mainly contribute to birefringence; however, it is very difficult to characterize these macroscopic disturbances and determine how the polarization is changing during experimentation [90]. The polarization changes manifest in the MZI output as the phase shift in the polarization states causes loss of coherence and imperfect interference at the coupler, deteriorating the response quality which was observed in the results for TPL5121 and the two SFCL pancakes. The optical fibre is subject to higher stresses in these setups due to higher Lorentz force in the case of both TPL5121 and the pancakes and bigger noisier setup in the case of the pancakes, therefore birefringence is more problematic for these measurements. Plotting the MZI output only from the petite pancake results in Fig. 65 in Fig. 70 we can see how the peak to peak voltage of the MZI output changes after the event of high heating in the sample. The polarization is adjusted before the experiment to give a maximum peak to peak voltage of 1 V (normalized),

initially the MZI shows this peak to peak value but then the polarization rotates after the heating event due to birefringence caused by thermo-mechanical stresses leading to amplitude and phase modulation causing the interference pattern to deteriorate due to loss of coherence as visible in Fig. 70.

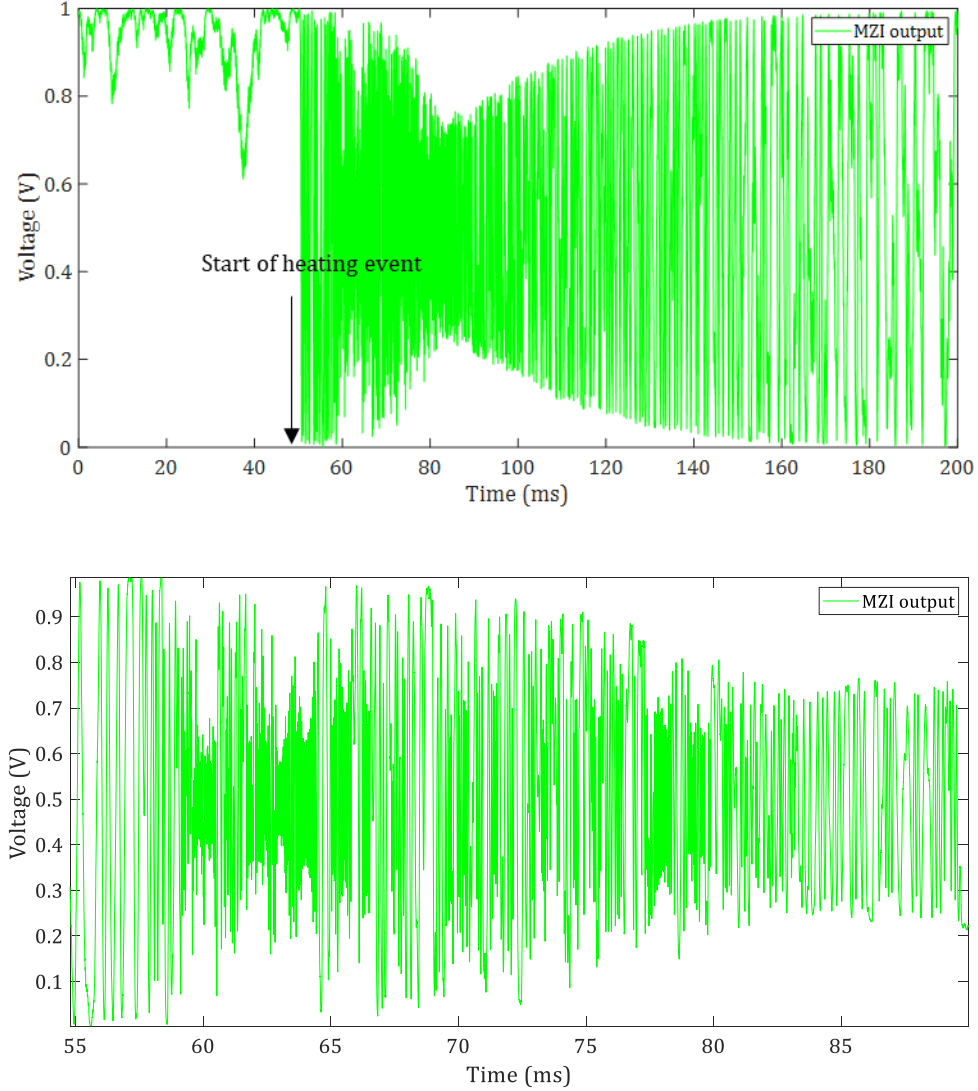


**Figure 70. Polarization rotation in the MZI during experimentation leads to amplitude modulation (top) and loss of coherence visible in the zoomed in plot (bottom)**

## Summary

This chapter showcased experiment results for five samples 30 cm, 65 cm and 100 cm in length in addition to two SFCL pancakes with 12 m and 17 m length of conductor which were monitored using MZI. The MZI managed to detect heating in all samples within 10 ms signifying its potential to detect hotspots in HTS applications quickly and economically. The results for the OFE-HTS tape were the least noisy overall because the sample holder used made sure that the sample did not move due to Lorentz force when current was pulsed in the sample, highlighting the importance of taking care to minimize the perturbations the MZI is subjected to (if possible). Single hotspots were also clearly detected in the case of the 1 m long SCS4050-AP sample, 30 cm long OFE-HTS sample and the Petite SFCL Pancake. However, the chapter also touched upon the challenges faced with the MZI method, using the experiment results as an example to show that the MZI



output is extremely sensitive to external disturbances and polarization changes. This causes the MZI output quality to deteriorate after the first 5 to 15 ms of good quality response, making data analysis difficult. These disturbances are variable for each experiment and difficult to quantify making it impossible to model the MZI system with mathematical equations. With this level of complexity, the MZI presents a “black-box” problem where we know the inputs, we can observe the outputs but the complete inner working of the system is not fully known. This sets the premise of Chapter 8, by highlighting the extreme need of a good data processing technique to supplement the MZI method. If the MZI is to be deployed in large scale HTS applications, there needs to be a way to work around the imperfect MZI output in the case of high disturbances for quench identification.





# 6

## Using finite element modelling to understand the Mach-Zehnder Sensitivity

The work showcased in this chapter has been published in:

A. Akbar, N. Riva, Z. Yang, L. Thevenaz, B. Dutoit, Fast Hotspot Detection in SFCLs by Exploiting Strain Response in Optical Fibre Sensing, IEEE Transactions on Applied Superconductivity 31 (2021). ([Link to publication](#))

Experiment results showed that the MZI technique is capable of detecting heating in the HTS samples within 10 ms. However, as the MZI output is a composite of strain and temperature sensitive contributions, it is important to understand whether the strain or temperature sensitivity of the fibre leads to the immediate response of the MZI technique to hotspots. A deeper understanding of this is important, because the thermal and strain sensitivities of optical fibres reduce to varying extents at cryogenic temperatures. It is therefore important to identify the sensitivity that leads to the fast reaction time of MZI, as it can enable a better handling of the optical fibre integration process which is crucial for optimal strain and temperature transfer to the fibre.

### 6.1 Optical fibre sensitivity in cryogenic temperatures

It was highlighted in Chapter 3, that the composite optical fibre response comprises of a strain response and a thermal response. The optical fibre's thermal sensitivity is defined by two key parameters: the thermo-optic coefficient and the coefficient of thermal expansion (CTE), which contribute to the temperature dependent term in the MZI principle equation (equation (6), Chapter 3). The sum of these coefficients determine the magnitude of the thermal sensitivity of the optical fibre. CTE of fused silica (the material of the optical fibre) is one order of magnitude lower than the thermo-optic coefficient of silica, therefore, in the thermal response, thermo-optic coefficient plays a more significant role as compared to the CTE. The plots of the variation in the two coefficients (thermo-optic and CTE) with temperature have been plotted in Fig. 71 and Fig. 72 respectively. In the plot in Fig. 71 it can be seen that at cryogenic temperatures there is a sharp decrease in the thermo-optic coefficient: the value of this coefficient is  $9 \times 10^{-6} \text{ K}^{-1}$  at room temperature which decreases by three times to  $3 \times 10^{-6} \text{ K}^{-1}$  at 77 K. This dramatic decrease in the thermo-optic coefficient causes the thermal sensitivity of the optical fibre to reduce at cryogenic temperatures, even though the absolute value of the CTE is higher at 77 K than at room temperature (shown in Fig. 72). For improving thermal sensitivity, approaches of recoating optical fibre with metallic or polymer coatings to enhance the CTE have been studied for

techniques like FBG [65]. It has also been discovered in studies that the overall decrease in the temperature sensitive contribution makes it possible to perform strain dominated measurements at cryogenic temperatures [94].

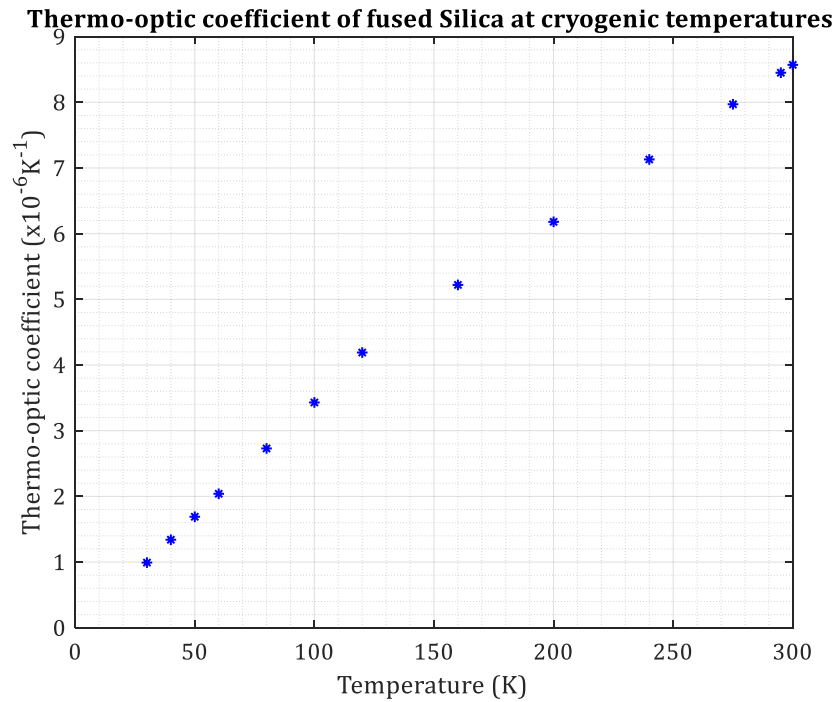


Figure 71. Temperature dependence of the thermo-optic coefficient of the optical fibre plotted from data obtained in [95]

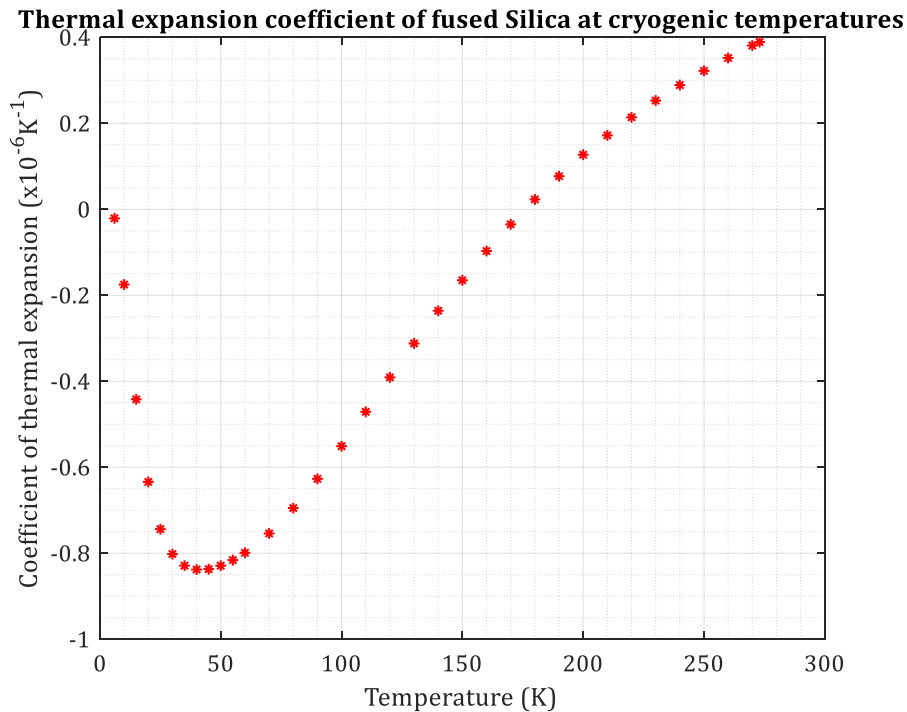


Figure 72. Temperature dependence of the coefficient of thermal expansion of the optical fibre plotted from data obtained in [96]

The strain sensitive contribution depends on the photo-elastic constant of the optical fibre, the value of which at cryogenic temperatures could not be found in literature. The strain sensitive contribution in the case of

optical fibre sensing for HTS arises due to the strain imposed on the optical fibre because of the thermal contraction or expansion of the host material, in this case the Hastelloy (substrate). For high strain sensitivity the integration of the optical fibre to the superconductor needs to be appropriate in order to maximize strain transfer from the host material to the optical fibre.

In order, to validate the dominant strain sensitive contribution of the MZI at 77 K, finite element modelling (FEM) was used. A 2-D thermal model was built, which used the experimental data of current and voltage in the sample to study the heat transfer from the HTS tape to the core of the optical fibre. In order to investigate how the thermal transfer varied with the integration medium, two thermal models were tested: one with Kapton as an adhesive and the other one with Stycast®, both with different thermal conductivities (The thermal conductivity of Stycast® is 0.9 W/(m · K) at 77 K and that of Kapton is 0.12 W/(m · K)).

## 6.2 Building a thermal model

Simulation results were used to demonstrate that the thermal transfer is much slower than the response of the optical fibre observed in the experiments. Since the purpose was to evaluate the thermal transfer from a hotspot in the conductor to the optical fibre, an electrothermal model was not necessary at this stage. Therefore, a 2-D thermal model simulating the cross section of the tape as shown in Fig. 73 was implemented. It was assumed that the thermal and geometrical properties of the conductor do not vary significantly along the length. The HTS tape simulated was the SCS4050-AP by SuperPower (the experiment results of which were showcased in the previous chapter). The voltage and current measurements from the experiment results for this sample, were taken and used to form the heat source in the model. The heat generated during a current pulse in the sample originates from the joule losses which are given by equation (9), where  $E$  is the electric field applied on the tape, and  $J$  is the current density. If the current density (and electric field) is assumed to be uniform on the cross-section of the conductor, we can write equation (9) in the form given in equation (10) where  $V$  is the voltage measured in the sample during the experiment,  $I$  is the measured current pulsed in the sample and  $Volume_{TAPE}$  is the volume of the HTS tape which includes copper stabilizer with a thickness of 10  $\mu\text{m}$ , 1  $\mu\text{m}$  of REBCO, 1  $\mu\text{m}$  of silver, and 50  $\mu\text{m}$  of Hastelloy. The heat source is applied on the conductor volume which is given by equation (11) where  $L_{TAPE}$  is the length of the HTS tape and  $C_{TAPE}$  is the cross section of the tape (marked with a dashed line enclosing the tape in Fig. 73). The Kapton/Stycast® do not contribute to the joule heating since no current can flow in them (due to their high resistivity with respect to the rest of the HTS tape), and thus they were not considered in the heat-source equation.

$$heat\ source = E \cdot J \quad (9)$$

$$heat\ source = \frac{V \cdot I}{Volume_{TAPE}} \quad (10)$$

$$Volume_{TAPE} = L_{TAPE} \cdot C_{TAPE} \quad (11)$$

The model was developed in COMSOL Multiphysics using the Heat Transfer Module (ht) [97]. The temperature dependence of all the material properties were considered and input to the model. The material properties utilized in the model can be found in [97–101]. The heat equation is solved on a 2-D domain and can be written as follows:

$$\rho_{mass}(T)C_p(T)\frac{\partial T}{\partial t} - \nabla \cdot (k\nabla T) = heat\ source - h_{LN2} \cdot (T - T_0) \quad (12)$$

where the left side of equation (12) has the mass density  $\rho_{\text{mass}}(T)$ , the specific heat capacity  $C_p(T)$  and the thermal conductivity  $k$ . On the right side of equation (12), is the heat source term and a cooling term.

The heat exchange with the liquid nitrogen was considered by applying a boundary condition as indicated in Fig. 73. The heat transfer coefficient  $h_{\text{LN}_2} \cdot (T - T_0)$  is a function of the temperature [102], but for a better readability it is written as  $h_{\text{LN}_2}$ .

The temperature profiles in time were then calculated for the REBCO and the optical fibre core, by taking an average over the respective volumes.

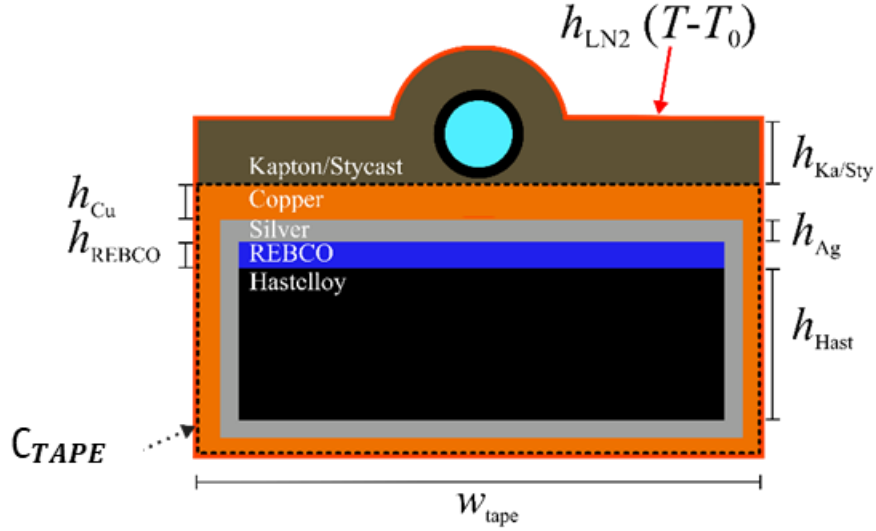
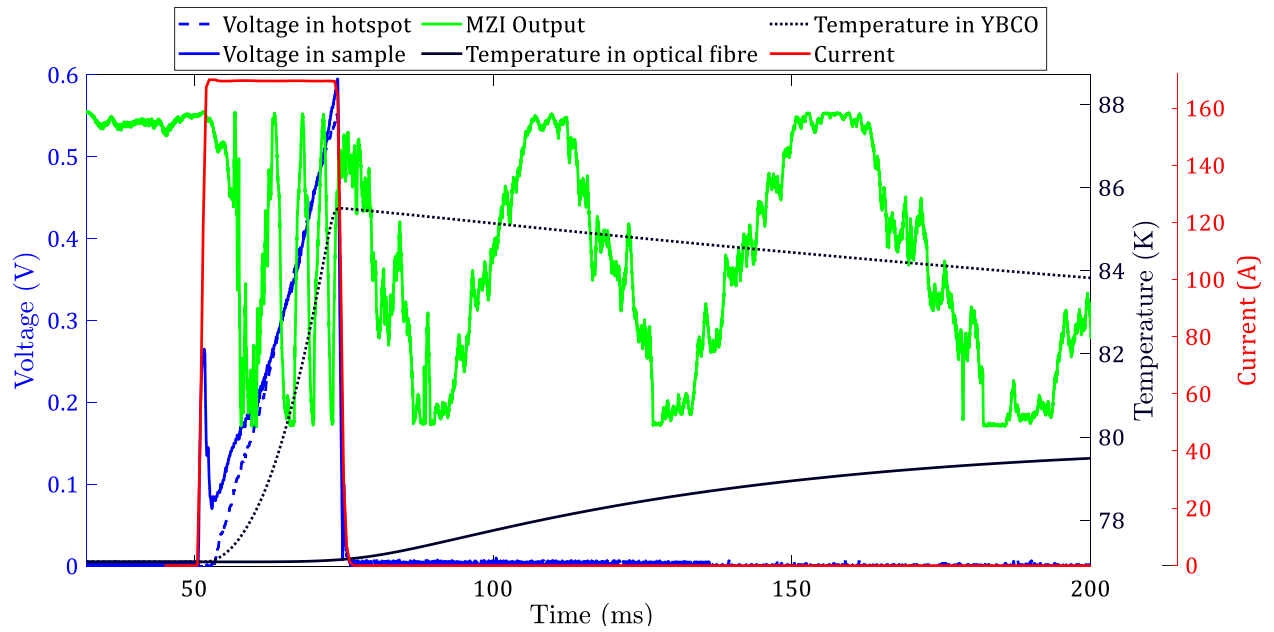


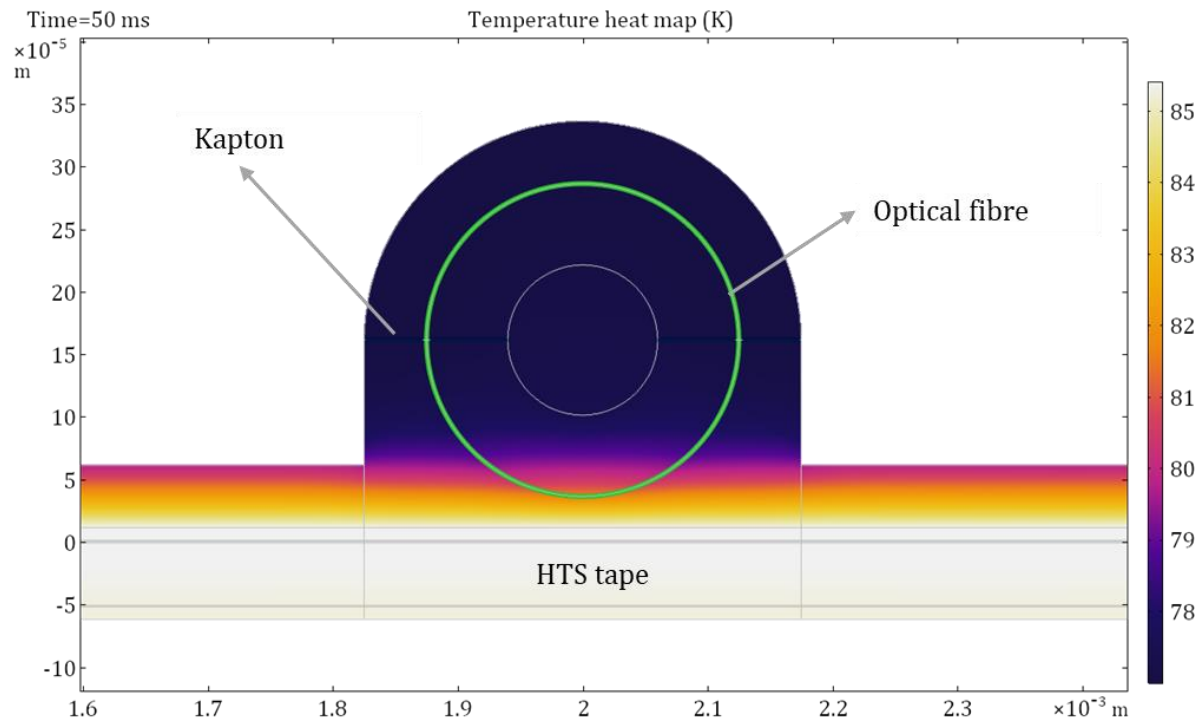
Figure 73. A schematic representation (not in scale) of the 2-D thermal model showing the cross-section of the superconductor tape and the boundary condition applied to account for convective heat transfer in liquid nitrogen bath. The quantity  $C_{\text{TAPE}}$  indicates the surface on which the heat source was applied.

### 6.3 Simulation results and discussion

The results for both Kapton and Stycast® are plotted in Fig. 74(a) and Fig. 75(a) respectively. The graphs show the experiment results for the SCS4050-AP sample as well as the simulated evolution of temperature with time in the REBCO (dashed black) and optical fibre (continuous black) domains. For the experiment results the graphs show the injected current in the sample (in red), the two voltages measured on the sample length (continuous blue), as well as around the magnet (dotted blue). In both cases in Fig. 74(a) and Fig. 75(a), it can be seen that the maximum voltage reached in the sample is similar to the maximum voltage in the hotspot; this signifies a single point heating (in the region of the magnet) in the superconductor sample. The MZI output (in green) shows no observable pattern before the event of the hotspot (voltage rise in the sample), and as the voltage in the sample rises, the MZI output switches to rapid amplitude variations, signaling a hotspot. Given that, it is necessary to explain here that the frequency of oscillations in Fig. 74(a) is lower than the frequency of the oscillations in Fig. 75(a) because of the lower power dissipated, hence smaller temperature change, in the sample for the case in Fig. 74(a). The MZI response for both cases, Fig. 74(a) and Fig. 75(a), however, is quick and within 10 ms. In order to understand the fast MZI response, it is interesting to look at the temperature curves obtained from the implemented 2-D thermal model, in Fig. 74(a) and Fig. 75(a).

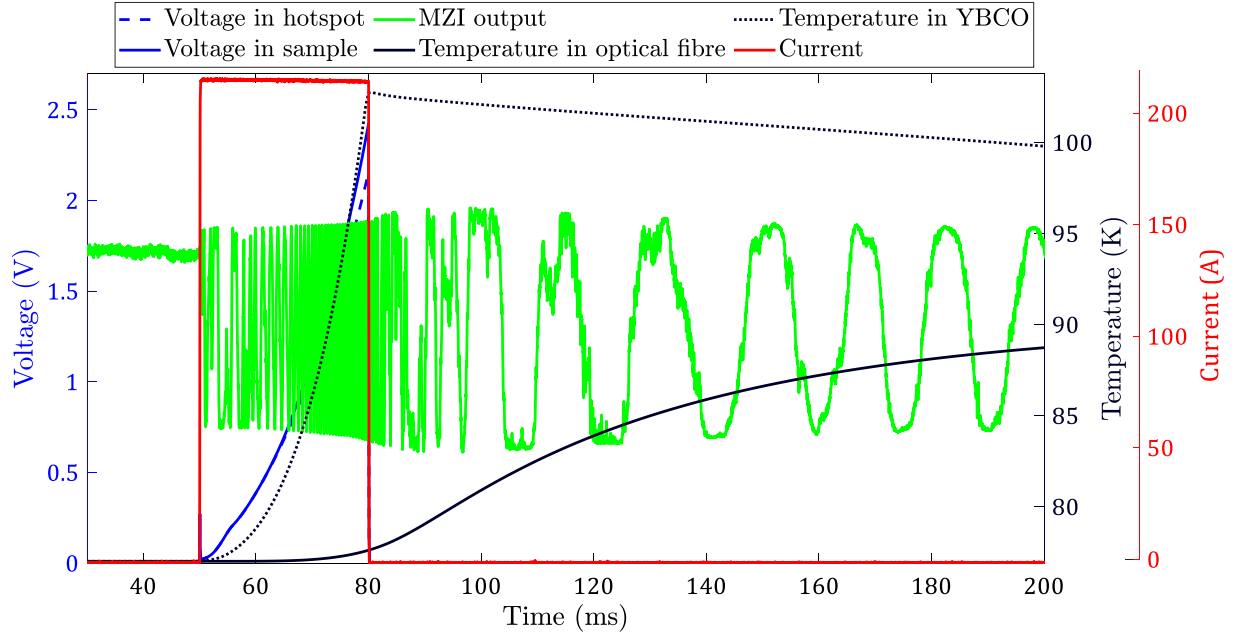


(a)

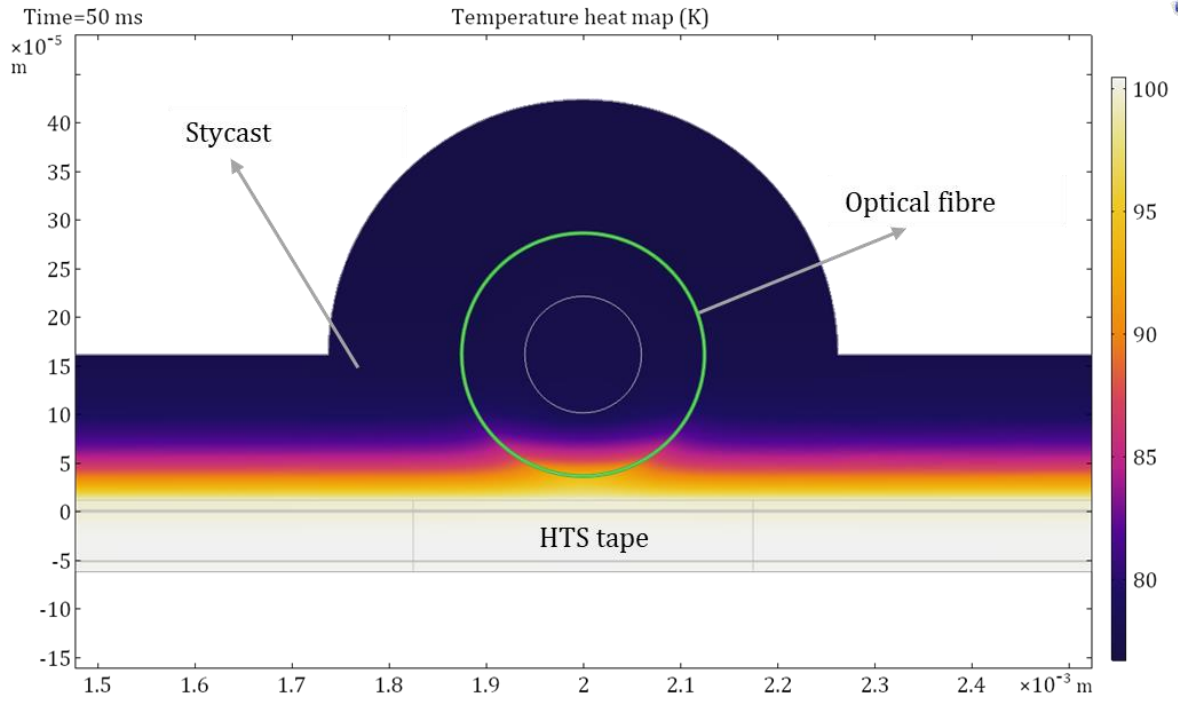


(b)

Figure 74. (a) Simulation results for temperature in REBCO and optical fibre (in black) for optical fibre integrated with Kapton plotted along with the experimental measurements and showing the observed MZI response before the temperature rise in the optical fibre (b) The heatmap obtained from the thermal model with Kapton shows the temperature gradient along the cross-section of the HTS tape, Kapton and the optical fibre



(a)



(b)

**Figure 75. (a) Simulation results for temperature in REBCO and optical fibre (in black) for optical fibre integrated with Stycast® plotted along with the experimental measurements and showing the observed MZI response before the temperature rise in the optical fibre (b) The heatmap obtained from the thermal model with Stycast® shows the temperature gradient along the cross-section of the HTS tape, Kapton and the optical fibre**

These simulation results show that the temperature change in the optical fibre, for both the cases shown, is negligible (almost zero) during the event of the hotspot and peaks much later. However, the MZI response is observed even in the absence of a temperature change experienced by the optical fibre. With this result, it can be deduced that the instantaneous MZI response arises because of the strain experienced by the optical fibre during the event of the hotspot due to the thermal expansion of the Hastelloy. The optical fibre therefore,



experiences the change in strain earlier than the temperature change. Another interesting result to note is that, even though Stycast® presents a higher thermal conductivity than Kapton, the temperature change in the optical fibre is still not fast enough to influence the MZI response within 10 ms.

The temperature change in the optical fibre is also impacted by the heat exchange with liquid nitrogen. Fig. 74(b) and Fig. 75(b) shows the heatmap for the case of integration by means of Kapton and Stycast® respectively. The heatmap was obtained for the thermal model at the end of the current pulse. Since the heat source was applied only on the conductor volume, the heat flux moves towards the upper part of the tape, generating a temperature gradient visible in both Fig. 74(b) and Fig. 75(b): for Kapton the temperature ranges from 86 K in the bottom part of the tape down to 77 K in the upper part of the tape, while for Stycast® the temperature ranges from 100 K in the bottom part of the tape down to 80 K in the upper part of the tape. The time-delay observed between the temperature curves for REBCO and the optical fibre therefore, is explained by both heat conduction across the tape and the cooling properties of the liquid nitrogen.

## 6.4 The importance of optical fibre integration quality with the superconducting power devices

The validation of the understanding, that at cryogenic temperatures the strain sensitive element leads to the high-speed detection of hotspots by the MZI, necessitates that the optical fibre be well coupled (mechanically) to the HTS sample.

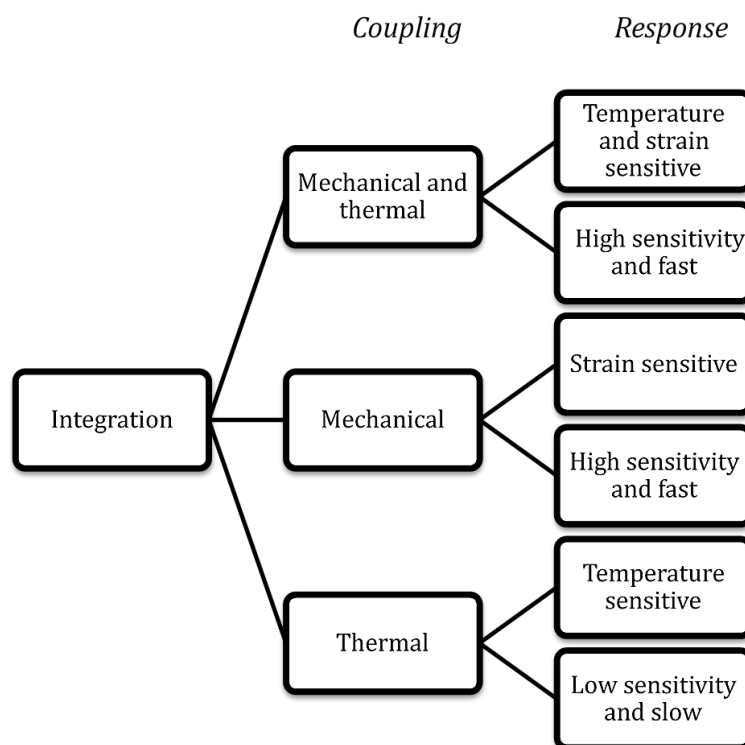


**Figure 76. Dependence of the MZI response on quality of integration of the optical fibre**

For high strain sensitivity the integration of the optical fibre to the superconductor needs to be appropriate to maximize strain transfer from the host material to the optical fibre. Proper mechanical coupling between the optical fibre and the superconductor can enhance the sensitivity of the setup to thermally-induced strains,

leading to a more instantaneous strain-dominated response while a weak mechanical coupling of the fibre to the HTS sample can lead to much slower temperature sensitive response which is not feasible for hotspot detection in HTS applications. This dependence of the MZI response time on the coupling of the optical fibre is shown in the flow chart in Fig. 76.

## Summary

The chapter discussed how the temperature sensitivity of the optical fibre decreases dramatically at cryogenic temperatures due to a significant decrease of the thermo-optic coefficient of the fibre. The only way to use fibre sensing at cryogenic temperatures is either to enhance the temperature sensitivity of the optical fibre by recoating it with high CTE materials or to perform strain sensitive measurements. For the MZI method, the mathematical analysis showed that due to the reduced temperature sensitivity of the fibre at 77 K the fast MZI response was arising due to the strain sensitive contribution. A 2-D thermal FEM model therefore was made, to study the heat transfer from the HTS tape to the optical fibre. The model was input with values of voltage and current obtained from the experimental measurements on the SCS4050-AP sample. Two models were simulated, one with the fibre integrated by means of Stycast® and the other with Kapton. The simulation results showed that even though Stycast® presents a higher thermal conductivity than Kapton, the temperature change in the optical fibre is still not fast enough to influence the MZI response within 10 ms. The 2-D FEM thermal model developed also validated the deduction that strain experienced by the optical fibre leads to the fast response of the MZI to hotspots, by showing that the MZI response to a hotspot occurs almost instantaneously and before a temperature change is experienced by the optical fibre. Therefore, in order to achieve the speedy response with the MZI setup proper coupling of the optical fibre with the HTS sample is crucial for rigidity to ensure optimal strain transfer from the Hastelloy to the fibre core. These results are also important to explain why the measurements for the FastGrid project were performed at 77 K and not 65 K (the target operating temperature of the FastGrid device): since the MZI is relying on the strain sensitivity, the decrease in temperature sensitivity at 65 K, will not significantly impact the technique performance.

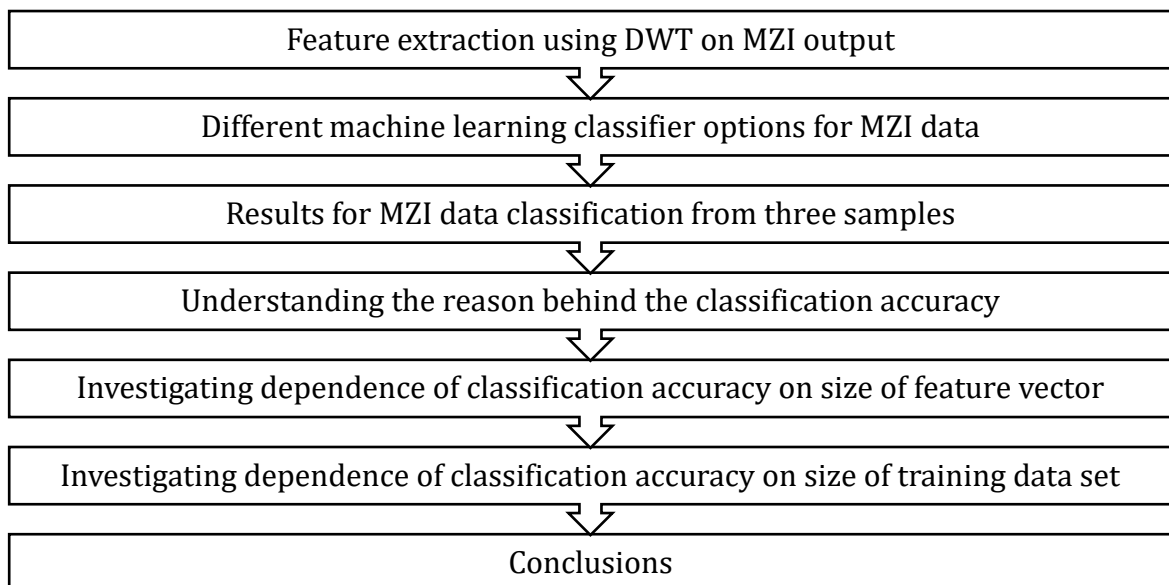
# 7

## Using Machine Learning with the Mach-Zehnder Method

The machine learning approach for MZI outlined in this chapter has been published in:

A. Akbar, N. Riva, B. Dutoit, Optical fibre based quench detection in HTS applications using machine learning classifiers, Physica C: Superconductivity and its applications 593 (2022) 1354007. ([Link to publication](#))

The experiment results in Chapter 5 established the working of the MZI setup as a black-box problem due to the non-quantifiable nature of the disturbances that may manifest in the MZI output. These perturbations not only vary with the experiment setup and sample configuration but also vary from one experiment measurement to another. This makes it difficult to analyze the experiment data. This is why machine learning becomes necessary for the MZI technique; with machine learning it is possible to use the output data and learn the relationship that exists in the black box between the inputs and outputs. However, before machine learning can be used, the MZI experimental data needs to be transformed into a suitable input for the machine learning classifiers. Giving the raw unprocessed MZI signal to the machine learning classifier is not the ideal way to go forth due to the large amount of data and high computation time. The data processing needs to be quick if the MZI method has to be used in real time with HTS applications. This chapter will use feature extraction to transform this big data to small data, that will be input into machine learning classifiers. The following flow chart shows the organization of this chapter:



## 7.1 Feature extraction using discrete wavelet transform

A feature is a distinctive or characteristic measurement or transform extracted from a signal or segment of a signal [103]. Features enable pattern recognition and representation. Through feature extraction the dimensional space needed to represent a pattern is greatly minimized; as a simple feature vector storing the set of features replaces the pattern which can be described as a large number of very small changes, which in this case is the many fluctuations of the MZI output. Feature extraction and its advantage of dimensionality reduction favours the engineering constraints of hardware and software, storage and data processing costs, and the need for compressed information [103]. The MZI output needs to be converted to a set of features that are stored in a condensed feature vector containing only the salient information. In order to extract this salient information from the MZI output Discrete Wavelet Transform (DWT) is used.

For a non-stationary signal like the MZI output, signal processing using Fourier Transform (FT) is not very useful because of loss of information in the time domain as the signal is transformed to the frequency domain. While one may suggest windowing with Short-time Fourier Transform (STFT), it is also not so effective due to the constant window size for all frequencies [104]. Discrete Wavelet Transform (DWT) has been used in many applications as a tool to extract information from signals as they provide localization in time as well as frequency [103,105]. Since in the MZI output, the response to heating is a localized part of the entire signal, DWT is ideal for analyzing frequency and spatial information at the same time for quench detection. It is important to stress here that, in the previous section the problem of degrading oscillation quality was presented in the experiment measurements; in those measurements while the MZI output quality degraded, it always had an initial good quality signal in response to a quench. This good quality signal has been observed to last for a duration of 5 to 10 ms as was discussed in the previous chapter. This makes DWT very useful to identify this highly localized response to heating in the sample.

DWT is a domain transform technique for hierarchical decomposition of finite energy signals given by equation (13) where  $\psi(t)$  is the mother wavelet and  $j, k$  are scaling parameters of dilation and translation respectively.

$$W(j, k) = \sum_j \sum_k x(k) 2^{-\frac{j}{2}} \psi(2^{-j}n - k) \quad (13)$$

The dilation parameter determines the wavelet length and oscillatory frequency while the translation parameter determines the position shift of the wavelet. The scale space stores an approximation of the outline of the signal in approximation coefficients ( $A_1, A_2, \dots, A_L$ ), where  $L$  is the levels of decomposition done using DWT. The wavelet space meanwhile, stores the detail of the signal which include localized changes in detail coefficients ( $D_1, D_2, \dots, D_L$ ). For the MZI output, detail coefficients are of immense interest as they store information for the localized signal that corresponds to the quench and hence will be utilized in the method presented in this thesis. DWT is performed on the normalized MZI voltage to ensure uniformity of maxima and minima across the data set. Fig. 77 shows the hierarchical decomposition of the MZI output using DWT with four levels. A 4-level decomposition was used for the analysis presented in this thesis. At each level, the detail coefficients are extracted to compute statistical features (formulas of which are presented in Table 10) which form the feature vector for the MZI output. These features are selected based on best representation of classes and on best distinction between classes for optimized classification. This is one way of selecting the input features for the classification models. There are other standard ways of selecting features using step-wise regression or Winston's best-first search [106].

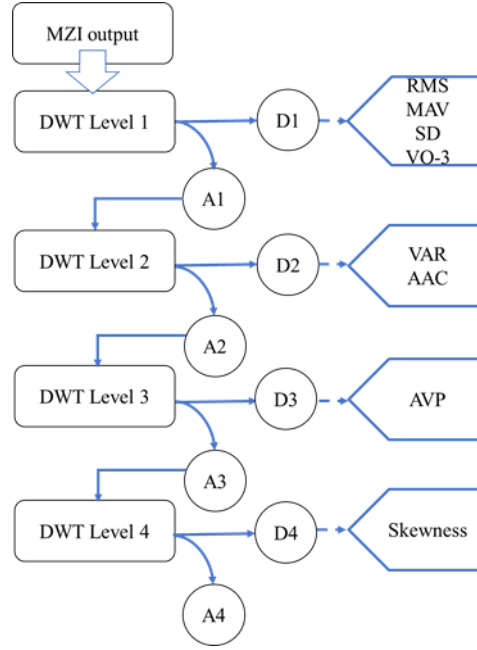


Figure 77. Hierarchical DWT decomposition of MZI output from experimental data and statistical feature extraction from detail coefficients at each level.

Table 10. Formulae for statistical features extracted from the MZI output

Statistical feature	Formula
Mean absolute value (MAV)	$\text{MAV} = \frac{1}{N} \sum_{n=1}^N  x_n $
Root mean square (RMS)	$\text{RMS} = \sqrt{\frac{1}{N} \sum_{n=1}^N x^2}$
Standard deviation (SD)	$\text{SD} = \sqrt{\frac{1}{N-1} \sum_{n=1}^N (x_n - \mu)^2}$
Variance third order (VO-3)	$\text{VO} - 3 = \left( \frac{1}{N} \sum_{n=1}^{N-1}  x_n ^3 \right)^{\frac{1}{3}}$
Average amplitude change (AAC)	$\text{AAC} = \frac{1}{N} \sum_{n=1}^{N-1}  x_{n+1} - x_n ^2$
Average power (AVP)	$\text{AVP} = \frac{1}{N} \sum_{n=1}^N  x_n ^2$
Skewness	$\text{Skewness} = \frac{\sum_{n=1}^N (x_n - \mu)^3}{N \cdot \text{SD}^3}$

A wavelet can be explained to be a smooth and quickly disappearing oscillating function with good localization properties in both frequency and time domains [107]. Different wavelets are suitable for different applications depending on their frequency components [108]. For the data analysis presented in this thesis, 51 wavelets were tested for the decomposition of the MZI output from experimental data to select the optimal wavelet choices. The wavelets tested belonged to the Haar, Coiflets, Daubechies, Symlet Biorthogonal and Meyer families presented in Table 11.

**Table 11. Wavelet families investigated for MZI where the number in the wavelet name represents the order**

<b>Wavelet family</b>	<b>Wavelets type investigated for MZI</b>
<b>Daubechies (db)</b>	db1, db2, db3, db4, db5, db6, db7, db8, db9, db10
<b>Symlets (sym)</b>	sym2, sym3, sym4, sym5, sym6, sym7, sym8
<b>Coiflets (coif)</b>	coif1, coif2, coif3, coif4, coif5
<b>Biorthogonal (bior)</b>	bior1.1, bior1.3, bior1.5, bior2.4, bior3.1, bior3.3, bior3.7, bior3.9, bior4.4, bior5.5, bior6.8, bior2.2, bior2.6, bior2.8
<b>Reverse Biorthogonal (rbior)</b>	rbior1.1, rbior1.3, rbior1.5, rbior2.2, rbior2.4, rbior2.6, rbior3.1, rbior3.3, rbior3.7, rbior3.9, rbior4.4, rbior5.5
<b>Discrete Meyer (dmey)</b>	dmey
<b>Haar</b>	Haar

## 7.2 Machine learning based classification

The features outlined in the previous section form the feature vector for the MZI output and will act as inputs for the classification models for quench identification. Machine learning is being used and documented in different spheres like medicine, power systems as well as in HTS, as a classification mechanism [109–112]. This chapter will present a comparative study of three machine learning based classifiers for the MZI output: k-Nearest Neighbours (KNN), Artificial Neural Networks (ANN) and Support-Vector Machine (SVM). Fig. 78 shows a step-wise illustration of how the MZI data is classified by means of machine learning classifiers. The experimental data is first input for DWT, the DWT coefficients are then used to extract statistical features and form the feature vector. The feature vector obtained is used as a training data set for the KNN, ANN and SVM models. Labels are assigned to the training data to one of the two classes: heating or no heating which are programmed as binary labels in the model. The trained models are then used to classify a new test dataset also obtained from experimental measurements. The measurements in the test data set is also converted into a feature vector by means of DWT before being classified by the trained models. In this chapter results for machine learning classification are shown on experiment dataset obtained from three samples (OFE-HTS tape, TPL5121 and the Petite SFCL Pancake). Care was taken to keep the datasets all-encompassing for each sample: containing heating cases and no heating cases. A range of MZI outputs, like weak responses, noisy responses and good responses was part of the training dataset for optimal training. The KNN, ANN and SVM models were tested for features extracted from the DWT using 24 different wavelets in the case of OFE-HTS tape and TPL5121, while 51 wavelets were tested in the case of the Petite SFCL Pancake. The classification accuracy

was then calculated for each run as a percentage shown in equation (14) where  $N$  is the size of the test dataset and  $L_m$  is the number of misclassified labels.

$$\eta = \left( \frac{N - L_m}{N} \right) \cdot 100 \quad (14)$$

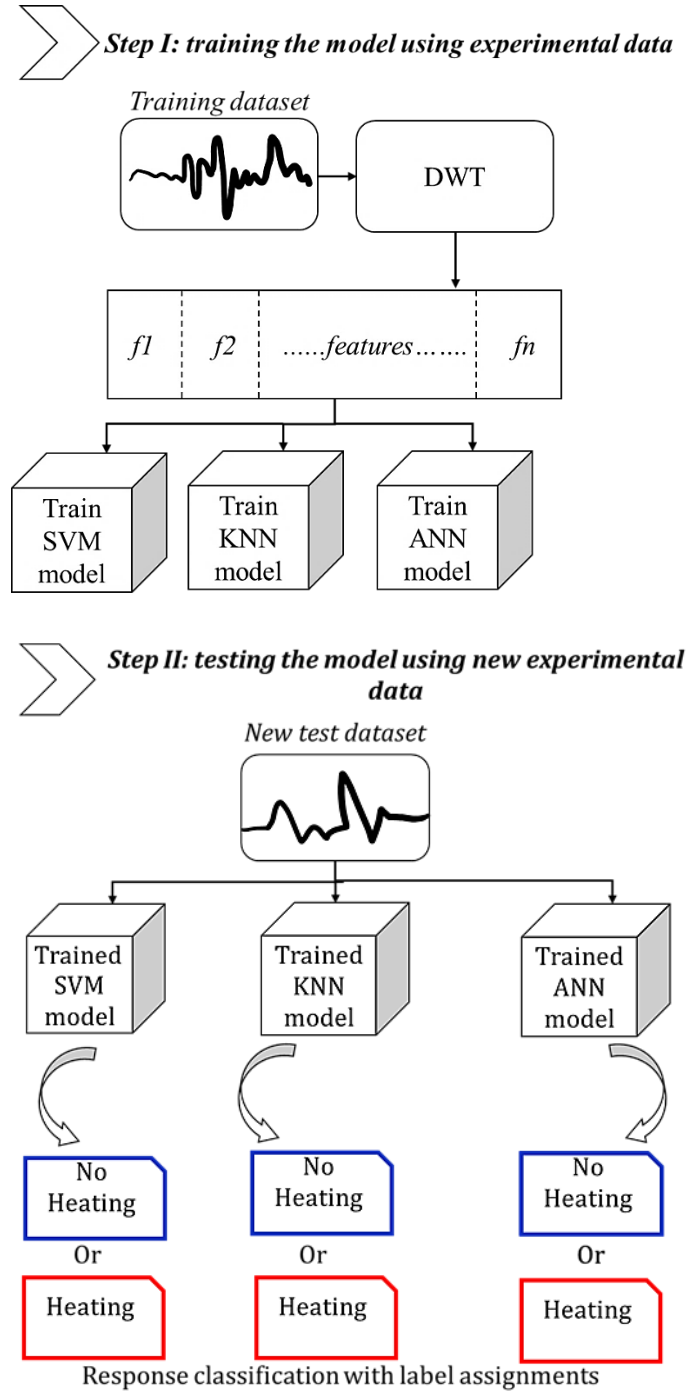


Figure 78. Stepwise illustration of training and testing machine learning models for MZI response classification

### 7.2.1 k-Nearest Neighbours – KNN

KNN is a lazy learning algorithm for instance-based learning used to classify objects based on their closest training examples in the feature space [113]. This is the most efficient classifier in terms of time complexity and simplicity and hence is most commonly used. The test object is classified into the class in which its  $k$ -nearest neighbours belong. To identify the nearest neighbours different distance metric can be used for example, Chebyshev, Chi-square, Euclidian etc. For the case presented in this thesis an optimized fitted KNN was implemented using the standardized Euclidian distance which is given by the equation (15), where  $N$  is the number of features and  $x_n$  is a feature value in the feature category  $n$  while  $y_n$  is the input query feature. The Euclidian distance is multiplied by a weight  $w_n$  which is the corresponding standard deviation computed from  $x_n$ . Fig. 79 shows how KNN works in assigning the data the class label. The value of  $k$  determines the radius in which the algorithm studies the neighbours of the data point to be classified. Choosing a large value of  $k$  can lead to high computation times and an overly generalized model, while a very small  $k$  value can lead to the noise in the dataset influencing the classification. Therefore the  $k$  value has to be carefully picked for each classification problem. The value of  $k$  can be chosen according to the size of the training dataset or simply using an optimized value [114]. For the data analysis in the case of MZI an optimized value of  $k = 4$  was selected.

$$d(x, y) = w_n \sum_{n=1}^N \sqrt{(x_n^2 - y_n^2)} \quad (15)$$

KNN is a convenient, simple to understand machine learning classifier and its memory-based approach allows it to easily adapt to new training data which makes it suitable for real time analysis.

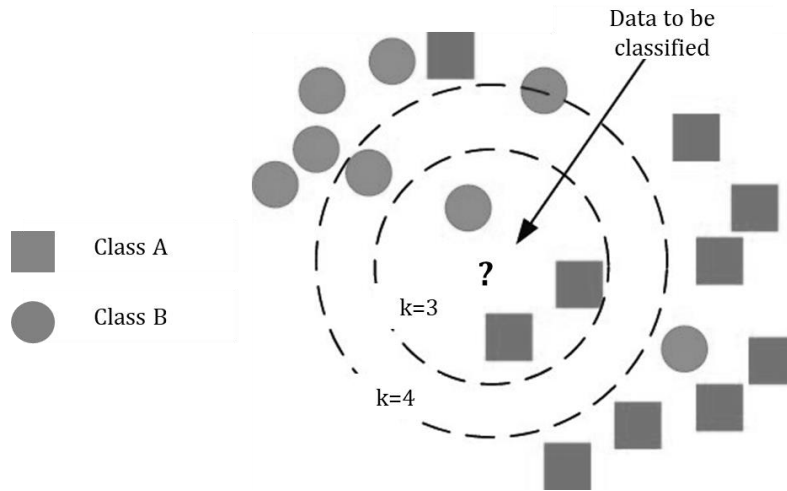


Figure 79. KNN assigns the data point a class based on its neighbours [115]

### 7.2.2 Artificial Neural Networks – ANN

ANN is a powerful machine learning classifier which is inspired by the working of the human nervous system [114]. Unlike KNN which was memorizing the training data for classification, ANN learns a discriminative function from the training data. Neural network models are low bias and a high variance classifier. They have a low bias because they make few assumptions about the mathematical functional form of the mapping function. They have a high variance because they are sensitive to the training data set. Differences in the training examples can result in a very different model. ANNs are composed of multiple



nodes, which imitate biological neurons of the human brain. Like neurons receive and transmit data, the nodes in ANN can take input data and perform simple operations on the data before passing them onto the other node. Each link is also associated with a weight, the value of which is altered as the ANN learns from the training dataset in a supervised learning strategy. In the case presented here a Feed Forward ANN model is used. A feed forward network is an essential deep learning strategy where the goal is to learn the best possible approximation of the function  $y = f(x, \theta)$  by learning  $\theta$  where  $y$ ,  $x$  are the outputs (predicted labels) and inputs (statistical features) respectively and  $\theta$  is the process that relates the two. ANN is best for applications where the inputs and outputs are well-understood but the relation  $\theta$  is complex forming a “black-box problem” [114]. This is the case for the MZI technique as was established earlier in the thesis, where multiple external perturbations are impacting the overall response hence forming a complex relationship between the input and output. The Feed Forward ANN topology comprises an input layer, an output layer and the hidden layer which is sandwiched between the two as shown in Fig. 80 and the information flow is unidirectional from inputs to the outputs. Fig. 80 shows how the input layer takes the input  $x$  and transforms it via a linear operation that weights ( $w_i$ ) the relative importance of the various inputs. This is followed by a non-linear transformation  $\sigma(z)$  called the activation function which is housed in the hidden layer. This is usually repeated several times until one transformed input reaches the output layer. The output layer is usually a simple classifier of the form of a logistic regression or soft-max function in the case of categorical data (with discrete labels) [116].

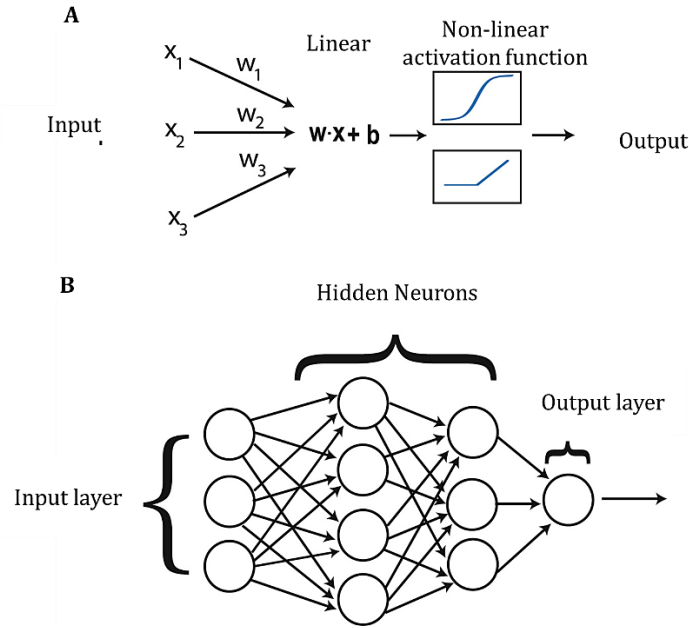


**Figure 80.** Topology of a feed forward ANN with the input layer, hidden layer and the output layer [116]

Traditionally, in the neural network literature, the activation function of choice are usually step-functions (perceptrons), sigmoids (Fermi functions), and the hyperbolic tangent [116]. Nowadays, rectified linear units (ReLU), leaky rectified linear units (leaky ReLUs), and exponential linear units (ELUs) are also being used. Different choices of non-linearities lead to different computational and training benefits for neurons [116]. The activation function chosen for MZI classification by means of ANN is the sigmoid function defined by equation (16) [114].

$$\sigma(z) = \frac{1}{1 + e^{-z}} \quad (16)$$

The sigmoid function is strongly sensitive to the input  $z$  when its near zero. This facilitates the learning of small variations by the ANN which is essential for pattern recognition. In order to train the ANN, Mean Squared Error (MSE) criterion is used to ensure that difference between ANN output and desired output has been minimized [114]. The inputs in the case of MZI output classification are the statistical features extracted from the signal and the output is the class label (heating or no heating).

### 7.2.3 Support Vector Machines – SVM

“Support Vector Machine” (SVM) is a supervised machine learning algorithm that can be used for both classification or regression challenges [117]. However, it is mostly used in classification problems. In the SVM algorithm, each data item is plotted as a point in a  $n$ -dimensional space (where  $n$  is a number of features you have) with the value of each feature being the value of a particular coordinate. Then, classification is performed by finding the hyper-plane that differentiates the two classes very well. SVM is used when the data has exactly two classes. The best hyperplane for an SVM is the one with the largest margin between the two classes. Margin in SVM is defined as the maximal width of the slab parallel to the hyperplane that has no interior data points. The support vectors are the data points that are closest to the separating hyperplane; these points are on the boundary of the slab. Fig. 81 illustrates these definitions by means of two classes (A and B).

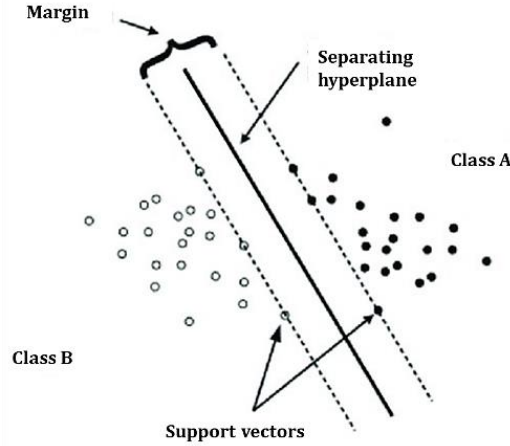


Figure 81. SVM binary classification using the optimal hyperplane [118]

The SVM kernel is a function that takes low dimensional input space and transforms it to a higher dimensional space i.e. it converts a non-separable problem to a separable problem. A kernel function is of the form of equation (17) where  $\psi$  is a function that projects vector  $x$  into a new vector space  $x'$ . The kernel function computes the inner-product between two projected vectors [119].

$$K(x, x') = \langle \psi(x), \psi(x') \rangle \quad (17)$$

It is mostly useful in non-linear separation problem. The kernel does some extremely complex data transformations, then finds out the process to separate the data based on the labels or outputs that have been set [120]. Selecting the kernel function parameter is one of the important parts of SVM modeling. The kernel function used for MZI response classification is the Radial basis function kernel, also called the RBF kernel, or Gaussian kernel. RBF is the most commonly used kernel for SVM that is in the form of a radial basis function (more specifically, a Gaussian function) which computes by means of equation (18) for two points  $x_1$  and  $x_2$

how close they are to each other, where  $\sigma$  is the variance and  $\|x_1 - x_2\|^2$  is the Euclidian distance between the two points [121].

$$K_{RBF}(x_1, x_2) = \exp\left(-\frac{\|x_1 - x_2\|^2}{2\sigma^2}\right) \quad (18)$$

The variance parameter determines the width of the bell-shaped gaussian curve. The smaller the variance parameter, the narrower the width and hence points that are extremely close together are assigned the same class and vice versa. An example is shown in Fig. 82 for a variance value of 2 where it can be seen that at distance of 0, the similarity calculated by the kernel is a maximum value of one, while for distances greater than 4 the similarity is zero. Having a large variance can lead to a high bias while a small variance can cause over fitting in SVM. Therefore, the optimized value of variance needs to be set for the best Bias-Variance Trade off.

SVM offers benefits of robustness against outliers, biased training data sets or irregularly distributed training datasets. Since SVMs are not bound to the original feature space in which the input is defined, they can increase the dimensionality of the problem up to a space until a solution is found. This ensures that SVMs ultimately always find a solution to a classification problem.

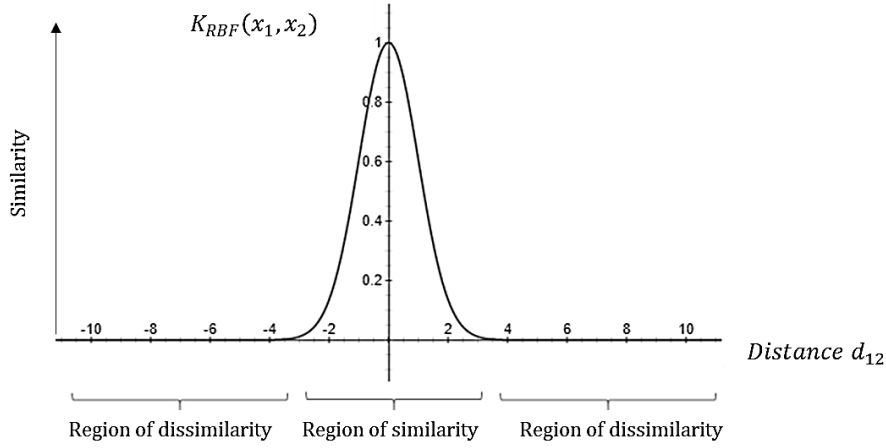


Figure 82. RBF kernel for a variance value of 2 [121]

## 7.2.4 Goals of the machine learning analysis

Feature extract with machine learning was the approach chosen for analyzing the MZI data due to the difficulty in understanding how various disturbances were affecting the MZI response. In this chapter three machine learning classifiers along with 51 different wavelets have been investigated for three different setups with the following goals:

- To figure out the optimum wavelet choice for feature extraction for MZI along with the optimum choice of the machine learning classifier.
- To understand how different experiment setups used with MZI impacts the optimal classifier choice.
- To understand the training dataset size requirements and feature vector size requirements for MZI response classification.

## 7.3 Results and Discussion

This section will showcase the classification results for the experimental data for three samples:

- 30 cm long HTS-OFE tape
- 65 cm long TPL5121 tape
- 12 m of conductor in the Petite SFCL Pancake

Experiment results for these samples were previously shown in Chapter 5. Now machine learning will be used to process that MZI data for identifying if there is heating in the sample or not. The results will discuss for each sample:

- The distribution of the training and test data set.
- The classification accuracy dependence on features extracted using different wavelets.
- The performance analysis of KNN, ANN and SVM.
- The nature of the misclassified measurements.

Before the results for the machine learning classification of MZI are discussed, it is important to stress here that assigning labels to low heating faults in the experiment measurements from the training dataset is extremely difficult due to the poor voltage resolution at low voltages. The experiment setup is able to measure voltage in the 0.1 V resolution range, hence assigning labels in the lower heating measurements leads to erroneous label assignments, bad training for those categories of measurements and lower overall classification accuracy.

### 7.3.1 Classification results for OFE-HTS tape 30 cm

#### Distribution of OFE-HTS tape dataset

Size of training dataset	88
Size of test dataset	63

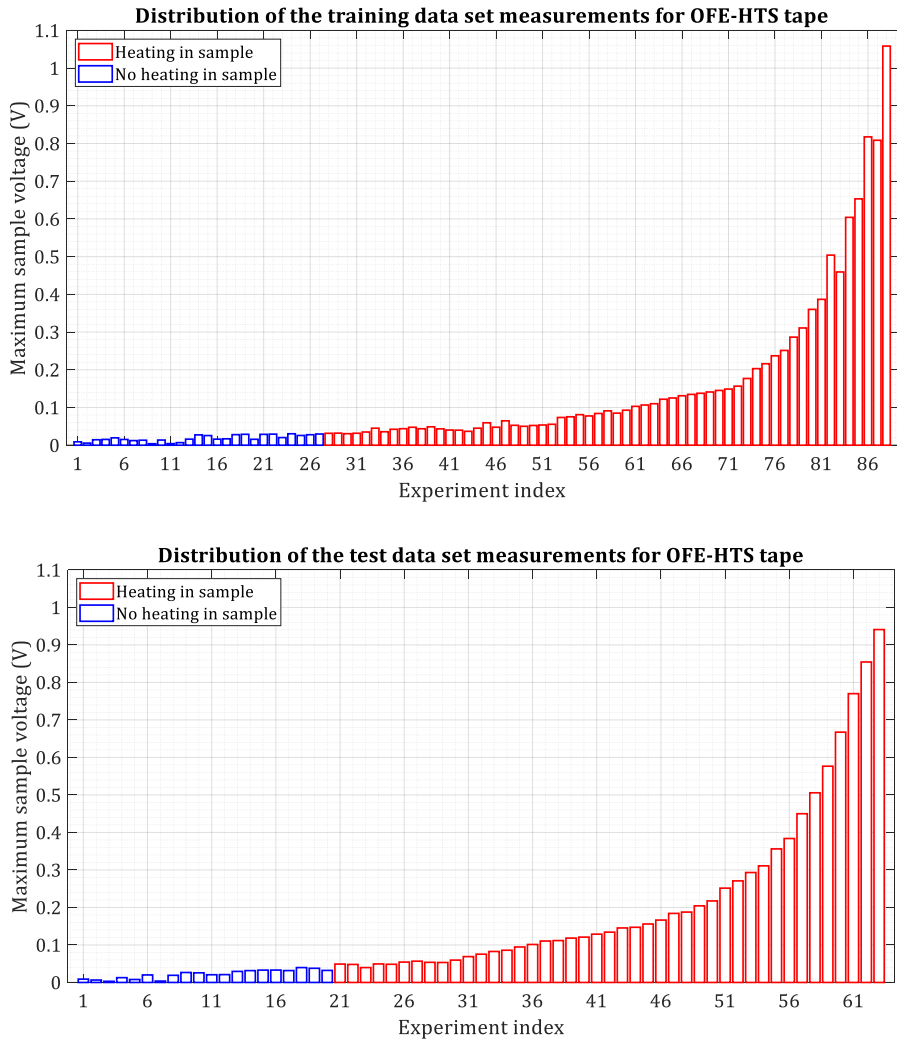


**Figure 83. Distribution of the training and test data set for OFE-HTS tape**

For the OFE-HTS tape a training data set of 88 experiment measurements was used. The MZI output was normalized by the maximum voltage value to ensure uniformity across both datasets. The plots in Fig. 83 show the distribution of both datasets. In these plots the experiments have been ordered in terms of increasing voltage in the total sample length. Care was taken to ensure the training dataset encompassed: no heating cases, heating cases and noisy cases.

## Classification performance for different wavelets

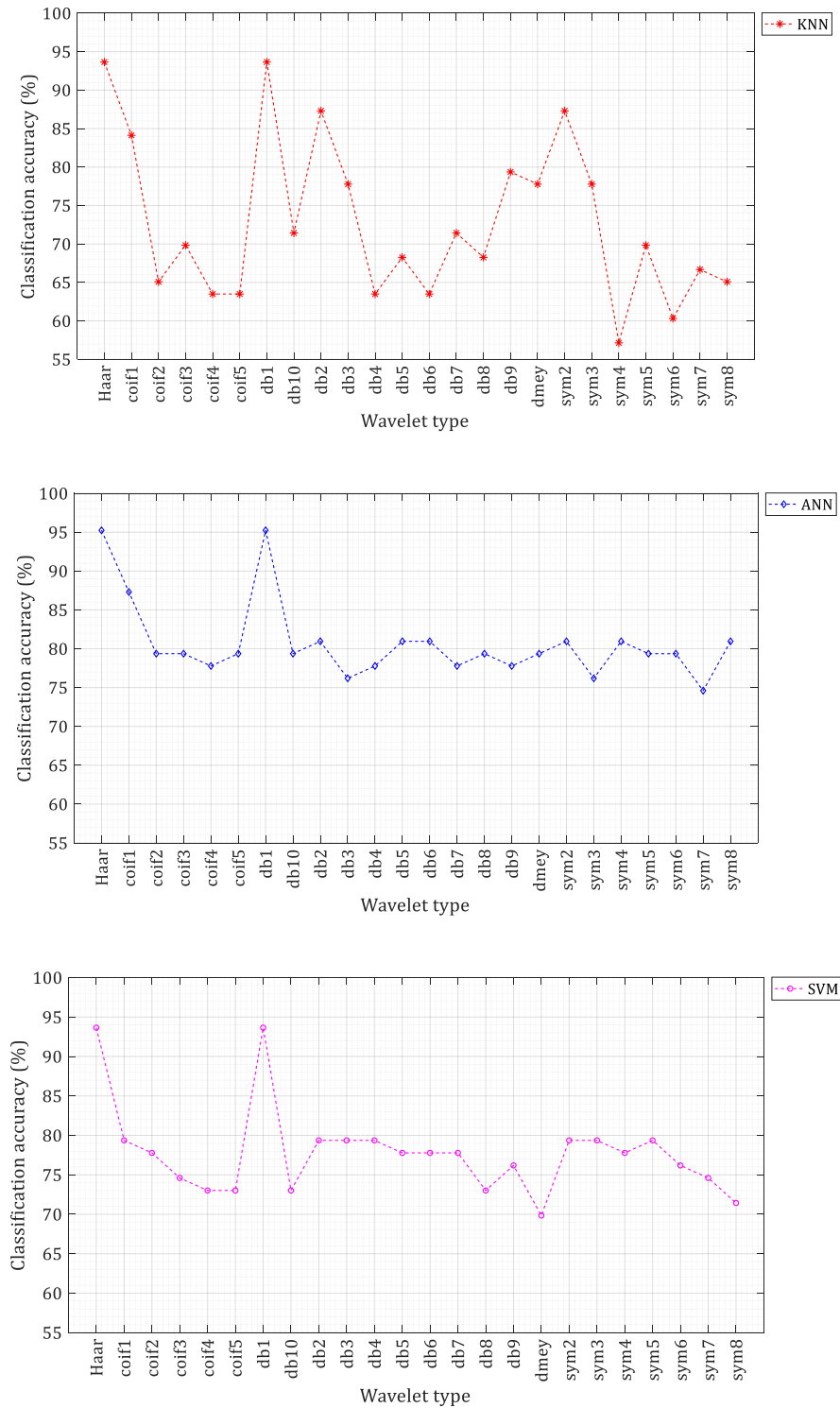


**Figure 84.** A performance analysis plot showing the accuracy of MZI response classification for KNN, ANN and SVM classifiers using feature vector extracted from 24 different wavelets for OFE-HTS tape

The training data set was used to form the feature vector for training the KNN, ANN and SVM models. The feature vector was extracted 24 times using a different wavelet for DWT in order to identify the best wavelet for the sample. The training and testing of the machine learning models was done 24 times each, for each

feature vector, and the classification accuracy was determined. Fig. 84 shows the classification accuracy for KNN, ANN and SVM models for the 24 wavelets. It can be seen that the classification accuracy is dependent on the wavelet used to extract the feature vector. Choosing the wrong wavelet for feature extraction for this sample can cause a 40% drop in classification accuracy in the case of KNN, a 30% drop for ANN and 25% drop for SVM. The worst performing wavelets belonged to the symlet family for KNN and ANN while for SVM it was the discrete meyer wavelet. The highest classification achieved for the OFE-HTS tape was with ANN (95%) when the Haar and db1 wavelets were used to extract the feature vector from the MZI experimental data. KNN and SVM performed the best with Haar and db1 wavelets as well, giving a classification accuracy of 94%.

### **Misclassified data for highest performing classifier**

If we look at the case of the highest classification accuracy achieved, which is ANN with Haar wavelet, and investigate the misclassified measurements, we find that the misclassified data points lie in bin numbers 15, 29 and 47 of the test dataset distribution in Fig. 83. Measurement 15 is a no heating case, the misclassification of which counts as a false alarm; this misclassification occurs due to the human error in label assignments at low sample voltages, mentioned earlier on this section. Measurements 29 and 47 however, are low heating low risk scenarios which would evolve into high heating faults in a real-life situation and would ultimately be classified correctly by the classifier.

### 7.3.2 Classification results for TPL5121 65 cm sample

#### Distribution of TPL5121 dataset

Size of training dataset	26
Size of test dataset	26

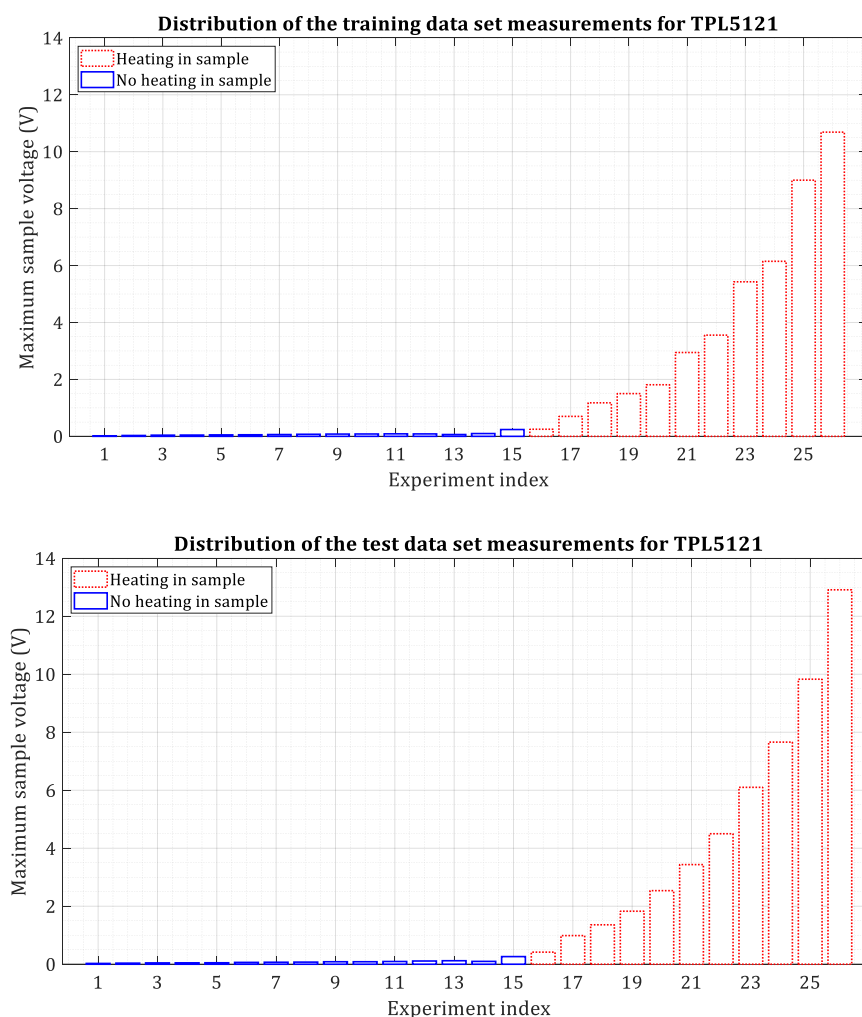


**Figure 85. Distribution of the training and test data set for TPL5121 sample**

For the TPL5121 sample a training data set of 26 experiment measurements was used. The MZI output was normalized by the maximum voltage value to ensure uniformity across both datasets. The plots in Fig. 85 show the distribution of both datasets. In these plots the experiments have been ordered in terms of increasing voltage in the total sample length. Care was taken to ensure the training dataset encompassed: no heating cases, heating cases and noisy cases.

TPL5121 was the sample that showed noisier measurements compared to OFE-HTS tape, as was discussed in Chapter 5. The MZI response showed disturbance in response to Lorentz force and mechanical perturbations in the experiment setup leading to noisy MZI measurements in the absence of heating in the sample. Classification results of measurements from this sample are interesting in order to determine if machine learning can help avoid such false alarms in noisy MZI measurements. The small training dataset was also



important to determine the feasibility of the machine learning classifiers for the situations where limited data is available to train the classifier.

## Classification results

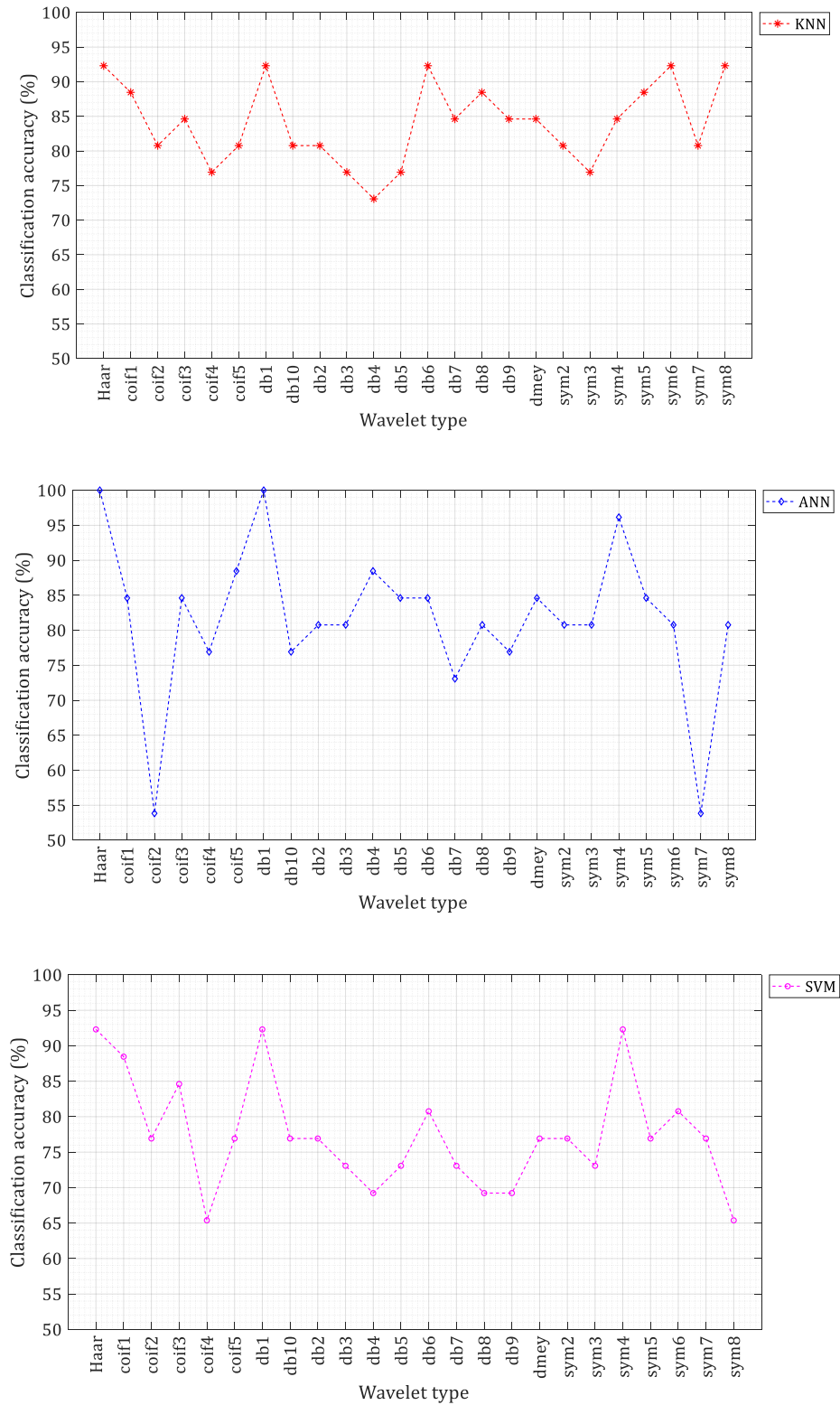


**Figure 86. A performance analysis plot showing the accuracy of MZI response classification for KNN, ANN and SVM classifiers using feature vector extracted from 24 different wavelets for TPL5121**

Fig. 86 shows the performance of all three classifiers for feature vectors extracted from 24 different wavelets from the TLP5121 test data set. The highest accuracy achieved is 100% with ANN when Haar and db1 wavelets are used. KNN gives a maximum accuracy of 93% when Haar, db1, db6, sym6 and sym8 wavelets are used while SVM gives the highest accuracy of 93% with the Haar, db1 and sym4 wavelets. For this sample as well, classification accuracy for all classifiers depends significantly on choosing the right wavelet for feature extraction. Choosing the worst wavelet can lead to a classification accuracy which is 20% lower than the maximum achieved accuracy for KNN, this drop is 50% for ANN and 27% for SVM. The worst performing wavelet was db4 for KNN, coif2 and sym7 for ANN and coif4 and sym8 for SVM.

### **Misclassified data for highest performing classifier**

Since the best performing classifier for TPL5121 was ANN with an accuracy of 100% there was no misclassified data to investigate. However, looking at the second-best classification pair of ANN and sym4 wavelet which gave an accuracy of 96%, the misclassified measurement lies in bin 16 of the test dataset distribution in Fig. 85. This measurement 16 is the lowest heating case in the test data set distribution with a sample voltage reaching 0.5 V (length 65 cm). This is a low risk measurement that has been misclassified while all the high heating cases have been correctly classified. All the no heating cases have been correctly classified as well for TLP5121, even though this sample had noise in the MZI output due to mechanical perturbations which manifested in the interference pattern even in the absence of heating in the sample, avoiding the risk of false alarms. Machine learning classifiers have therefore, given a satisfactory performance with this sample even with a smaller training data set.

### 7.3.3 Classification results for the Petite SFCL Pancake

#### Distribution of Petite Pancake dataset

Size of training dataset	103
Size of test dataset	100

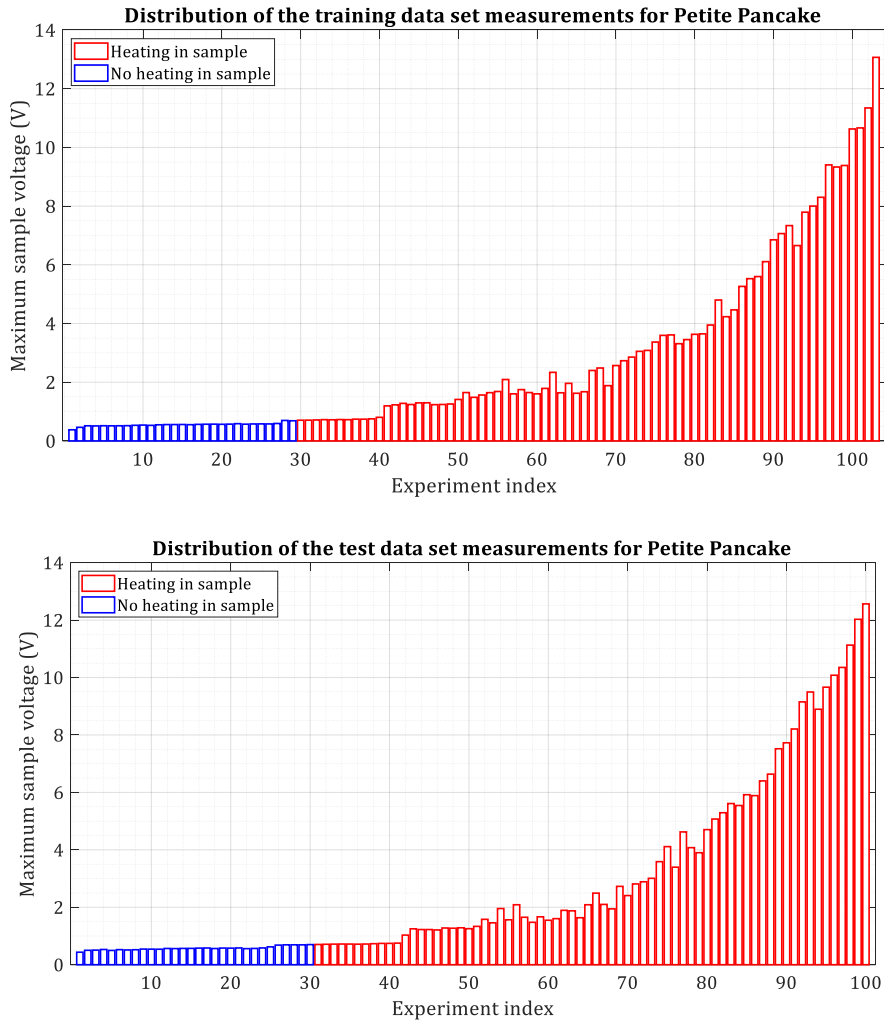


**Figure 87. A performance analysis plot showing the accuracy of MZI response classification for KNN, ANN and SVM classifiers using feature vector extracted from 24 different wavelets for Petite SFCL Pancake**

Experiment data from the Petite SFCL Pancake with 12 m of conductor, was used to form a training data set of 103 measurements and test dataset of 100 measurements. Results from this sample are of interest because of the complicated sample configuration with co-wound optical fibre and a bigger noisier setup. The MZI was subject a wider range of perturbations which led to slightly noisier measurements as compared to shorter sample lengths. In addition, the measurements also showed deteriorating quality of oscillations in the MZI output to a greater extent due to birefringence. For this sample 51 wavelets were investigated for feature extraction in order to determine if there are more possibilities to optimize the classifier's performance. The KNN, ANN and SVM models were trained and tested 51 times, each time with a different feature vector formed after feature extraction using a different wavelet for DWT.

## Classification results

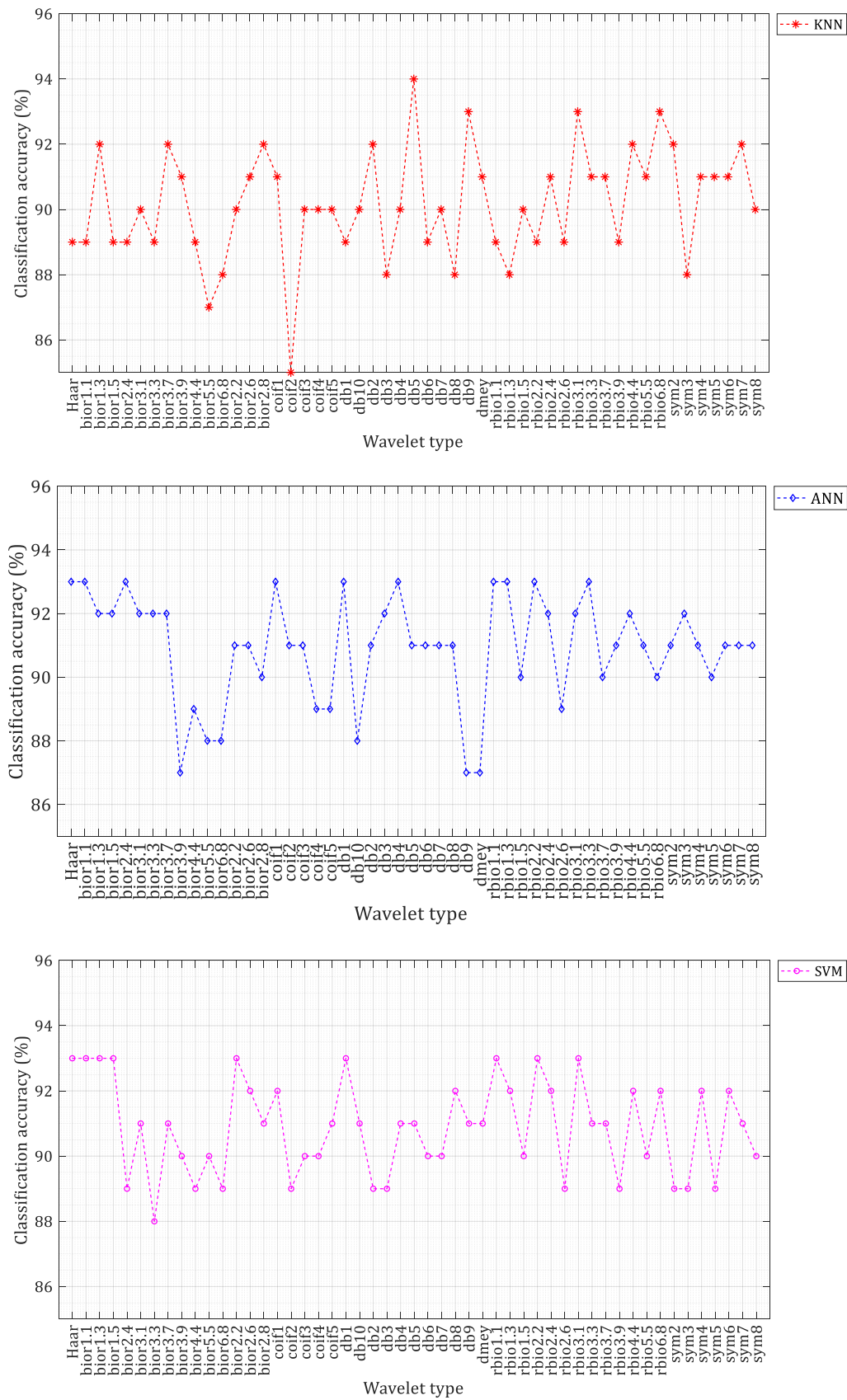


Figure 88. A performance analysis plot showing the accuracy of MZI response classification for KNN, ANN and SVM classifiers using feature vector extracted from 51 different wavelets for Petite SFCL Pancake

Fig. 88 shows the performance of all three classifiers for feature vectors extracted from 51 different wavelets from the Petite Pancake dataset. The highest accuracy achieved is 94% with KNN when db5 are used. ANN gives a maximum accuracy of 93% when Haar, bior1.1, bior2.4, coif1, db1, db4, rbio1.1, rbio1.3, rbio2.2, and rbio3.3 wavelets are used while SVM gives the highest accuracy of 93% with Haar, bior1.1, bior1.3, bior1.5, bior2.4, bior2.2, db1, rbio1.1, rbio2.2 and rbio3.1 wavelet. For this sample as well, classification accuracy for all classifiers depends on choosing the right wavelet for feature extraction. Choosing the worst wavelet can lead to a classification accuracy which is 10% lower than the maximum achieved accuracy for KNN, this drop is 6% for ANN and 5% for SVM. However, the classification performance for this sample was not as severely impacted with the worst wavelet, as was the case with previous samples. This could be due to the larger training dataset size or a better representation of classes in the training dataset.

### **Misclassified data for highest performing classifier**

This highest classification accuracy achieved was with the KNN classifier (94%) when db5 wavelet is used for feature extraction. Looking at the misclassified data, the measurements were found to lie in bins 20, 23, 30, 32, 34 and 36 of the test dataset distribution plotted in Fig. 87. Misclassified data in bins 20 and 23 are wrongly classified no heating case while bins 30, 32, 34 and 36 are on the lowest end of the spectrum of heating scenarios. This error arises due to human error in label assignment during training (which was addressed in the start of the section) as it is harder to assign labels at low voltage measurements due to poor voltage resolution. Nevertheless, these misclassified measurements would pose no risk to the SFCL device as the voltage is only 0.4 V in 12 m of HTS tape. In a real-life scenario, most fault cases would lie on the high heating side of the spectrum where the classification accuracy is 100 %. Therefore, overall the machine learning classifiers can be said to have given a satisfactory result for MZI classification in the Petite SFCL Pancake.

## 7.4 Understanding classification results based on class separability

The classification results for all three samples yielded satisfactory performance. The reason behind the high classification accuracy can be understood in terms of the features which were input to the classifier. In most classification problems, numerous features can be extracted, but only a select few are really discriminative. Therefore, feature selection becomes critical and leads to many benefits. Good features embed objects of the same class close together for all classes in the dataset (i.e., small interclass distance) and good features also embed objects of different classes far away from each other (i.e., large intraclass distance) [122]. This leads to higher class separability. It should be stressed, that higher separability can be achieved by selecting those features that have large interclass means yet small within class variance. The feature vector in the case of MZI was composed of statistical metrics which were explained earlier and if we plot the feature pairs from all three samples as scatter plots we can see the extent of class separability between the two classes for the MZI data (heating and no heating). The following scatter plots in Fig. 89, Fig. 90 and Fig.91 show two-dimensional representations of the features to showcase class separability for the Petite SFCL Pancake, OFE-HTS tape and TPL5121 sample respectively. The features were extracted using the top performing wavelet for each sample: db5 for the Petite SFCL Pancake and Haar wavelet for the OFE-HTS tape and TPL5121 sample. The scatter plots show two feature pairs each time from the feature vector to signify that the right feature selection for MZI helps achieve better classification accuracy. It can be seen for the scatter plots in Fig. 89 to Fig. 91 that while the heating and no heating classes can easily be discriminated for all samples by means of the selected features, it may be possible to further reduce the class variance by exploring additional features for the MZI data. Nevertheless, the feature pairs plotted in the scatterplots for all samples show how they enable discrimination between the two classes.

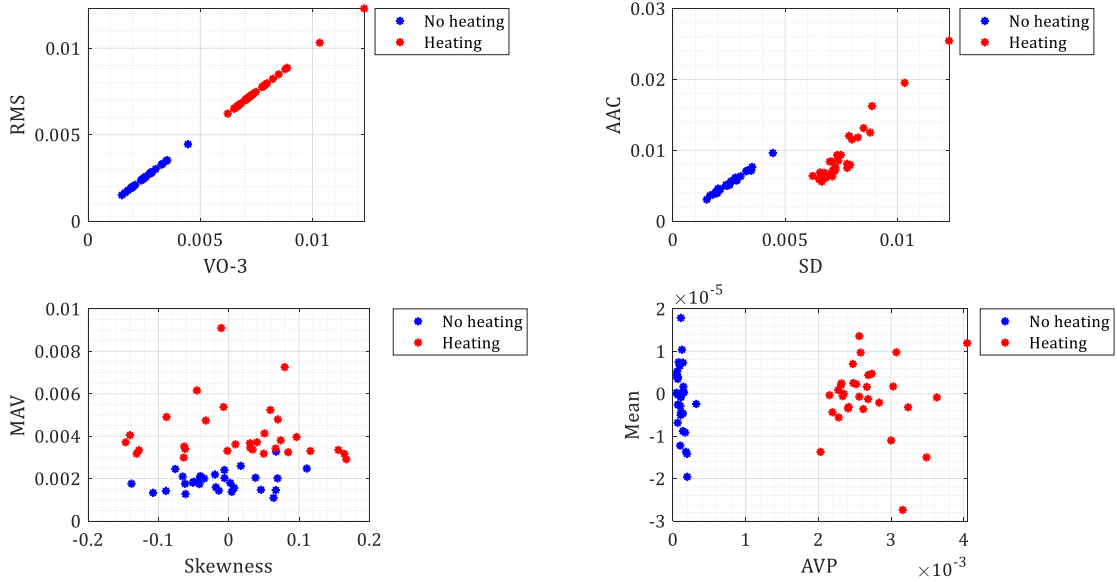


**Figure 89.** Scatter plots showing class separability of two-dimensional feature pairs extracted using db5 wavelet from the Petite SFCL Pancake MZI dataset

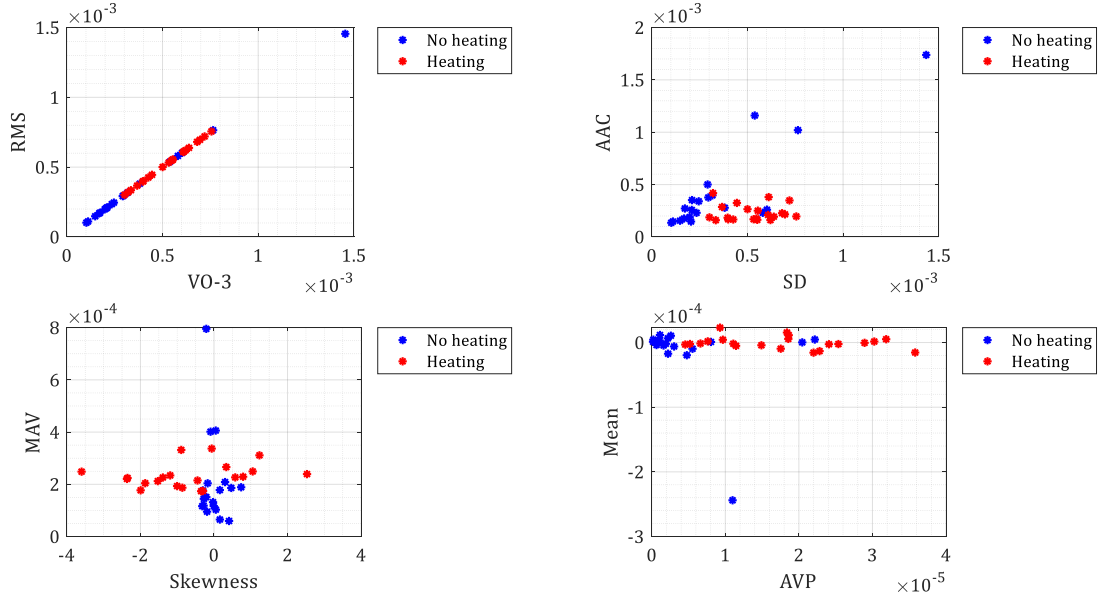


Figure 90. Scatter plots showing class separability of two-dimensional feature pairs extracted using Haar wavelet from the OFE-HTS tape MZI dataset

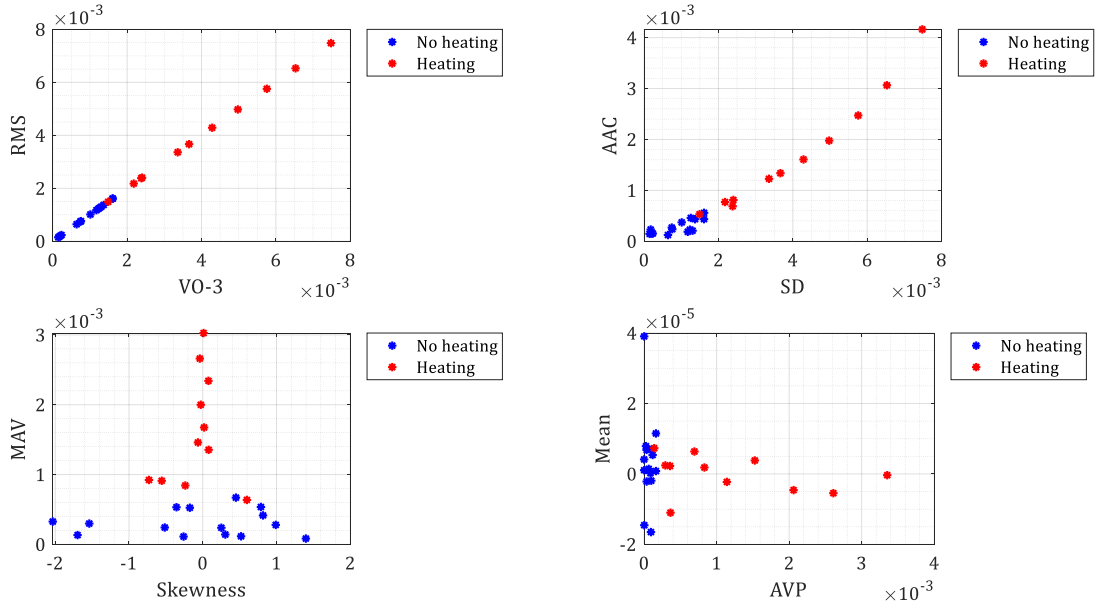
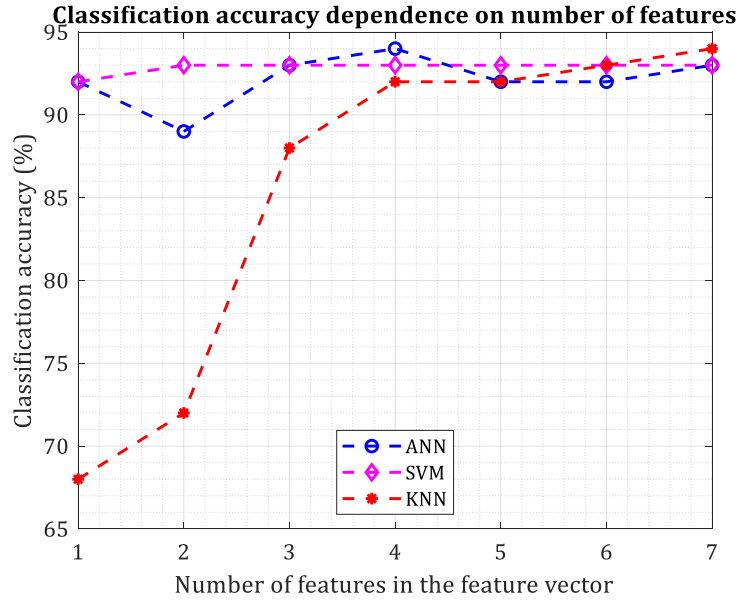


Figure 91. Scatter plots showing class separability of two-dimensional feature pairs extracted using Haar wavelet from the TLP5121 MZI dataset

## 7.5 Dependence of classifiers performance on size of the feature vector

The number of features selected for the feature vector can also influence the classification accuracy. All the classification results presented above are for a feature vector with seven features. In order to investigate how the classifiers performed with a smaller number of features in the feature vector, the classification was done with reduced feature vector sizes (but the same training dataset size) using the optimum wavelet choices for the Petite Pancake (db5 for KNN and Haar for ANN and SVM). The plot in Fig. 92 shows the classification accuracy varied for each classifier with different sizes of the input feature vector. It can be seen that for a feature

vector of size two to seven does not cause the SVM performance to vary however it drops by one percent from 93% to 92% when only one feature is used. KNN performance on the other hand is influenced greatly by the number of features input to the classifier giving a lower accuracy when only one or two features are used (68% and 72% respectively). For ANN, however, which gave a classification accuracy of 93% with the Petite Pancake when seven features were part of the feature vector, a one percent classification accuracy increase can be achieved by using four instead of seven features. For ANN therefore, an optimal lower number of features can be selected to achieve faster computation speeds for the Petite SFCL Pancake data. The same applies also for SVM which shows a high classification accuracy even with a lower number of features. This is important because if the MZI method is implemented for real time quench detection in HTS applications, choosing the right classifier can help reduce the optimum number of features required and hence decrease computation time and increase quench detection speed.



**Figure 92. Classification performance for KNN, ANN and SVM for different sizes of feature vectors extracted from the MZI output from the Petite SFCL Pancake**

## 7.6 Classification accuracy dependence on training dataset size

If the machine learning classification is used to supplement MZI for the health monitoring of HTS applications, it comes with the need to train the machine learning classifier. For every application the classifier has to be trained with a dataset from that particular setup. Obtaining a dataset from real life HTS applications to train a machine learning classifier would be challenging, because the superconductor needs to be heated to different extents to produce an all-encompassing data set that can train the machine learning classifier.

It is therefore important to investigate what the optimal data size is for the training dataset in the case of MZI response classification. Since the Petite SFCL Pancake is the longest conductor length and most complicated configuration tested with MZI and machine learning, an investigative study was performed on how changing the training dataset size affected the classification accuracy for the three classifiers (KNN, ANN, SVM). Care was taken to keep the reduced training dataset representative of all cases so that the results would be in response to the dataset size and not due to imbalance in the dataset itself.



Fig. 93 shows the results for varying the training dataset size from 25 experimental measurements to 100 obtained from the Petite SFCL Pancake. The plot shows that SVM is robust to changes in the training dataset size while KNN is impacted significantly by the training dataset size reduction, giving an 11 % decrease in the accuracy as the training dataset is decreased from 100 to 25 measurements. ANN however shows an optimal performance at a dataset size of 50 to 60 measurements, giving a higher accuracy than was previously achieved with a training dataset of 103 measurements. With a training dataset of 50 to 60 measurements ANN, the classification accuracy increases by 1%.

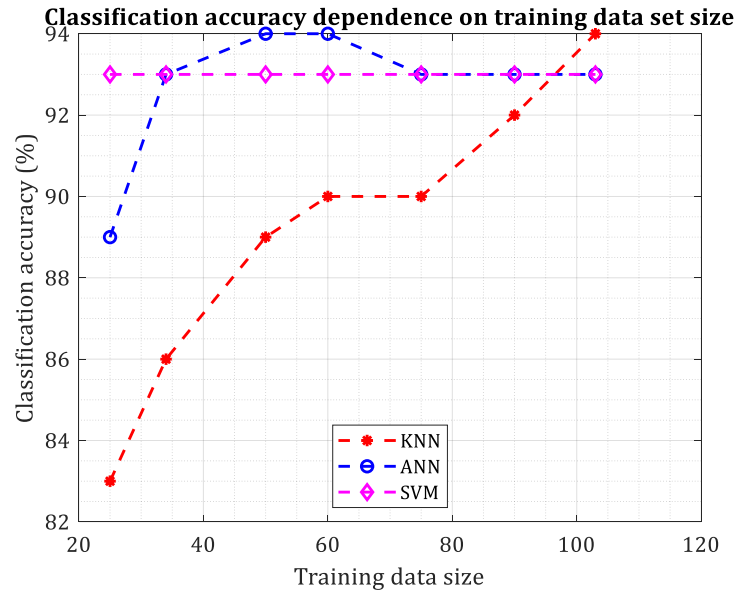


**Figure 93. Dependence of classifier performance on training dataset size**

This is an important and interesting result as it can make MZI more feasible for large scale HTS applications, as it shows that using the right classifier can help minimize the training dataset requirement.

## Concluding remarks

Before the concluding remarks, the summary of the classification results is presented in Table 12 and Table 13 which show the highest classification accuracies achieved for the three HTS-samples which were monitored using MZI (OFE-HTS tape, TLP5121 and Petite SFCL Pancake). Table 12 shows the optimal classifier-wavelet pair for each sample while Table 13 shows the highest classification accuracy achieved from the three classifiers (KNN, ANN and SVM) for the three samples.

**Table 12. Best performing machine learning classifier and wavelet pair for MZI response classification for the three HTS samples investigated**

Sample	Highest classification accuracy achieved	Wavelet	Classifier
OFE-HTS tape	95%	Haar, db1	ANN
TLP5121	100%	Haar, db1	ANN
Petite pancake	94%	db5	KNN

**Table 13. Highest classification accuracy achieved with ANN, KNN and SVM for the three HTS samples investigated**

	<b>ANN</b>	<b>KNN</b>	<b>SVM</b>
<b>OFE-HTS tape</b>	95%	94%	94%
<b>TLP5121</b>	100%	92%	92%
<b>Petite pancake</b>	94%	94%	93%

The classification technique worked well with all three samples, giving a highest accuracy greater than or equal to 94%. 100% accuracy was achieved for the 65 cm long TLP5121 sample which had the noisiest MZI measurements and smallest training dataset size which shows the potential of this data processing technique to work well with HTS applications in noisy setups that will be monitored for hotspots using the MZI technique.

Daubechies wavelet, which belongs to the family of orthogonal wavelets, is widely used in solving a broad range of problems because of its orthogonality and potential for localization and classification of disturbances, hence is an optimal wavelet choice for classifying the MZI output which is also validated by the high classification accuracy when it is used for feature extraction. These results highlight the significance of choosing a suitable wavelet to extract the feature vector.

The misclassified quench measurements were found to lie in measurements with low heating in the sample. This is an important observation which shows that the classifier fails to identify quench cases only in low heat low risk scenarios which pose no danger to the HTS device but never misses high heat high risk scenarios. It should be noted that these low energy cases exist in the test set because pulsed current measurements (limited in time) were performed for the experiment; in a real situation such faults would evolve to higher energy ones and will be detected by the classifier.

The classification accuracy depends on many factors including the size of training set, the selected features and the number of features input to the ANN, KNN and SVM models. With a larger training dataset, the accuracy can be further enhanced in the case of KNN but for SVM and ANN smaller training datasets also gave satisfactory performance when classifying data in the Petite SFCL Pancake measurements. In these cases, however, care was taken to ensure a representative training dataset even when reduced training datasets were used. Therefore, choosing the correct classifier and a training dataset that covers all possible cases can help minimize the required optimal size of the training dataset.

Also, feature selection can be further advanced by exploring different combinations and varieties of features and also varying the size of the feature vector to find the optimal set of parameters. The study presented for the feature vector size and classification accuracy for the Petite SFCL Pancake showed that SVM and ANN are capable of working well with a lower number of features in the feature vector. This is important in order to use the minimum possible but optimum number of features to reduce the computation time to facilitate faster real time classification of the MZI output.

The level of decomposition using DWT can also be further investigated on the MZI output data to see if more detail coefficients can improve discrimination. It should be noted that these aspects will need to be adjusted according to the system utilizing the MZI for quench detection. This brings us to the limitations of using machine learning to supplement MZI for quench detection.

1. Every application utilizing the MZI will require a different training dataset because the external perturbations and hence MZI output quality will vary according to the system properties like mechanical design, acoustic noise and vibrations. These perturbations need to be learnt by the machine learning models. It is not always feasible to obtain a training dataset from large scale HTS applications as it would require heating the superconductor to induce artificial quenches to gather training data.
2. Assigning labels in supervised machine learning models leads to human error which can impact the classification accuracy. For the specific cases presented in this chapter, misclassified values were found in low heat scenarios and no heat scenarios because it is difficult to assign labels in these cases as the voltage resolution is not good enough for an accurate idea.

However, despite these limitations, it has been shown in the results presented that machine learning for MZI gives a high classification accuracy and there is a possibility to use smaller datasets and a smaller number of features to train the classifiers, which can make MZI response classification in real time even more feasible.

The comparative study of the three machine learning classifiers presented in this chapter shows that all three machine learning classifiers are capable of overcoming the challenges of MZI response sensitivity to unwanted disturbances and a weak response to low temperature hotspots. However, the optimal choice of classifier will be determined according to computational speed requirements which makes ANN and SVM more suitable for MZI.

This is an important development for the MZI technique as it significantly impacts and improves the MZI reliability and practicality for HTS applications. Additionally, this is also of substantial importance to the progress of HTS applications in the industry, especially the power sector which continues to evolve with the shift towards renewables and will rely more on HTS applications like SFCLs and HTS cables. With a reliable hotspot detection technique like the MZI, we can facilitate mass adoption of such HTS applications.





# 8

## Milestones and future outlook

At the beginning of this thesis in 2019, the following roadmap was planned and presented for the candidacy exam, with a starting point of testing the MZI method on short sample lengths and an ending point of commercializing a full MZI module complete with the optical setup and a real time data processing of the MZI signal to raise an alarm within 30 ms of heating in a HTS sample.

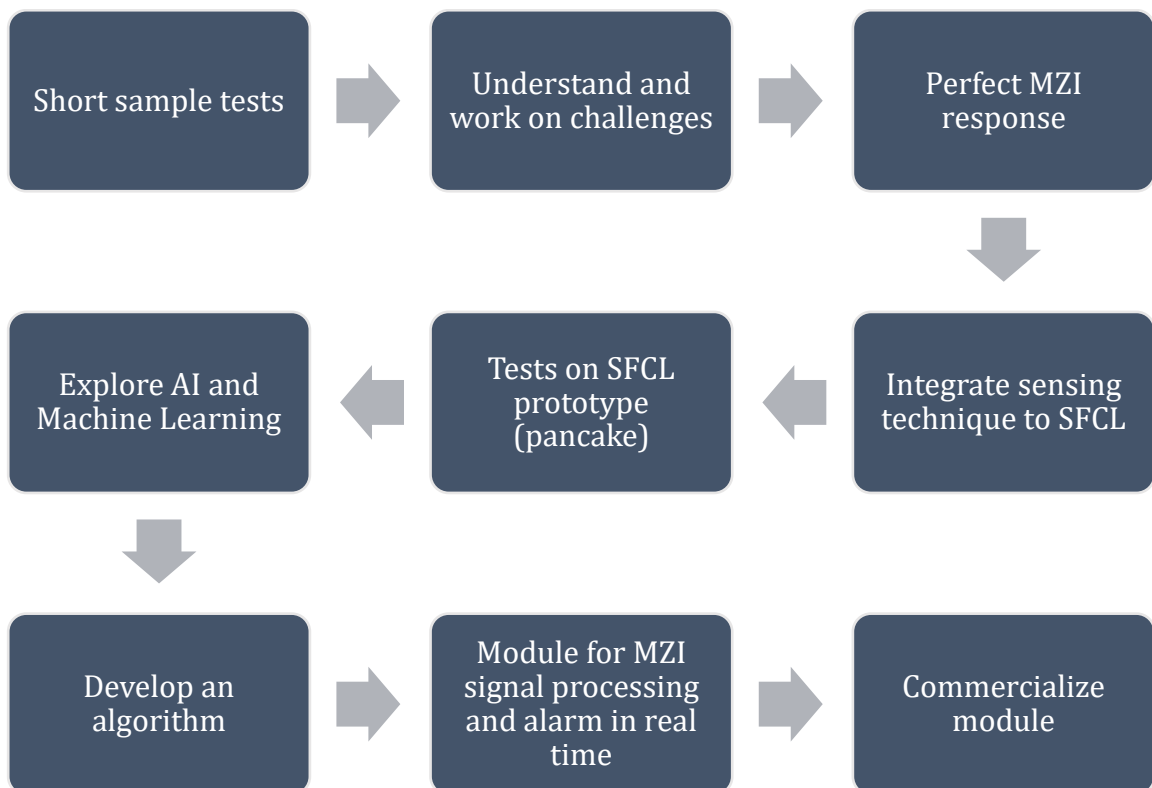


Figure 94. The proposed roadmap for the thesis presented in 2019

## Milestones

The major part of the road map was understanding the MZI response, optimizing the response quality, testing MZI with longer conductor lengths and using machine learning for data processing.

Within the course of this thesis the following milestones have been achieved:

### **Milestone: The fastest non-electrical detection of singular hotspots in HTS applications**

The feasibility and high-speed response of the MZI method has been successfully demonstrated experimentally on a range of samples, with varying lengths and configuration. The MZI was tested with 30 cm to 1 m long HTS samples and demonstrated on 12 m and 17 m of conductor lengths in SFCL pancakes. Singular hotspots within the entire conductor length, can be detected in a few milli-seconds (shown in experimental results), which is the fastest and most sensitive non-electrical demonstration to the best of our knowledge for hotspot detection.

### **Milestone: Demonstration of hotspot detection in a SFCL pancake**

MZI showed promising results for all sample lengths and was capable of detecting single hotspots even in 12 m of conductor length in a SFCL pancake. By help of Tapestar measurements for the pancake conductor, it was possible to increment the current pulsed in the sample and detect singular, double and multiple hotspots in the SFCL pancake by means of MZI within 5 ms.

### **Milestone: Patent**

Given the unmatched ability of MZI to detect hotspots within 5 ms to 10 ms, an international patent was filed and accepted for an original hotspot detection technique that caters to the fast hotspot detection requirements for HTS applications.

### **Milestone: Finite element modelling for MZI response understanding and optimization**

The MZI response is a composite of temperature sensitive and strain sensitive contributions. In order to understand whether strain or temperature is responsible for the fast response of the MZI, a FEM thermal model was built and run with experimental data. The simulation results showed that the temperature rise in the optical fibre is zero during the instantaneous detection of heating by the MZI, and does not peak until much later. The simulation results proved that the thermal transfer to the optical fibre was too slow to cause the speedy MZI response to heating in HTS samples and therefore the strain sensitivity of the optical fibre is useful for high speed hotspot detection in cryogenic temperatures. This allowed the optimization of the MZI method, by ensuring that proper steps were taken to enhance the strain transfer to the optical fibre by means of strong mechanical coupling between the HTS sample and the fibre.

### **Milestone: Machine learning based classification**

While the MZI brings high speed detection at a low cost to the table, its high sensitivity makes it extremely sensitive to external perturbations. These disturbances are difficult to quantify and vary from experiment to experiment. The external disturbances can manifest in the interference pattern in the MZI output in the same way as a hotspot, making it difficult to analyze the MZI data. A machine learning based classification was implemented to supplement the MZI method with a classification accuracy of greater than 94%. This analysis

was also successfully implemented with the SFCL pancake with 94% classification accuracy. The misclassified data was found to lie in low heating faults which arise due to the pulsed nature of measurements. In large scale setups, the classification accuracy would be higher because the faults will evolve to high heating scenarios which are easy to classify.

Therefore, from the road map in Fig. 94 the following targets were achieved:

1. Experimental demonstration of the MZI method for hotspot detection on short HTS sample lengths.
2. An investigation into the MZI response sensitivity for a better understanding of the optical fibre integration requirements.
3. Experimental demonstration of the MZI method for hotspot detection with long HTS sample lengths up to 1 m.
4. Experimental demonstration of the MZI method for hotspot detection with SFCL pancakes with 12 m and 17 m of conductor respectively.
5. A machine learning based high accuracy classification of the MZI response to deal with noisy and hard to understand interference patterns.

The following targets from the road map were not achieved:

1. A comprehensive hotspot detection module complete with the MZI setup along with the real time response classification by means of machine learning.
2. Commercializing this module for a range of HTS applications.

This brings us to the future outlook for this thesis.

## Future work

### **Future work: Real time implementation of MZI response classification for hotspot detection**

Work needs to be done to implement the machine learning based response classification of the MZI output in real time. The work has already been started and will hopefully be done in the coming months. The real time implementation will involve windowing the incoming MZI output in 15 ms timeframes with 5 ms overlap on either ends of the window. The machine learning classifier will be trained on multiple 15 ms files of MZI output which will form the training dataset. The incoming MZI signal from the HTS sample will be first converted into a feature vector and then be input to the trained classifier for response identification. This data processing will ultimately be programmed on a Field Programmable Gate Array (FPGA) and has to be quick enough to raise the alarm of heating in the sample within 30 ms. Preliminary testing of the real-time detection has been done in LabVIEW and the results show that this 30 ms target of quench detection complete with the data processing in real time is achievable. The classifier is trained before-hand, hence the real-time data processing needs to compute the feature vector with the statistical features which takes the most computation time, while the subsequent classification of the measurement (in the form of a feature vector) by means of the trained model is very fast.

### **Future work: Implementation of MZI method in largescale setups and lower temperatures**

Due to the high sensitivity of MZI to perturbations, it would be interesting to integrate and test the feasibility of the MZI method with large scale setups that will subject the MZI to real-life noisy situations of HTS

applications. Similarly, due to the decreasing sensitivity of the optical fibre at lower temperatures, it would be interesting to study the impact of lower temperatures on the hotspot detection speed of the MZI. Work is currently underway in collaboration with Paul Scherrer Institute (PSI) to integrate and test the MZI method with large scale HTS fusion conductors at 4 K. MZI will be used to monitor 2 m of conductor length at PSI, alongside other another quench detection technique being used at PSI by means of a superconducting wire [123]. The results and performance of MZI will be compared to this technique and will be made public in due time.

### **Future work: Implementation of compressed sensing for optimized feature selection**

Improving the number and type of features input to the feature vector can improve classification accuracy and increase computation speed. More discriminative features increase the ability of the machine learning classifier to make better predictions. Feature selection methods are still being investigated to optimize feature selection. A novel approach that has been documented in literature is feature selection by means of compressed sensing. Compressed sensors are common in signal processing whereby they enable signal reconstruction with minimal number of basis. Researchers are adapting this approach to feature selection by using compressed sensing algorithm to find the most informative features [124]. The compressed sensing model can give the few important coefficients which represent most of the data to be classified. This approach can be useful for MZI and should be tested for better classifier performance.

## **Thesis impact**

The motivation of this thesis had roots in climate change, renewable energy, evolving grid infrastructure and the role of superconductivity. The work done in this thesis impacts everything in the aforementioned list. Climate change necessitates renewable energy, renewable energy entails HVDC grids. In addition, the looming shortage of copper necessitates HVDC cables as they are much lighter than a conventional cable and hence can save copper resources. There will be (is) an unavoidable shift to HVDC systems due to these reasons. These HVDC systems will rely greatly on HTS applications for numerous protection and energy needs. HTS applications in turn require a reliable, and economical, health monitoring system before they can play their part in this crucial era of energy transformation. It was mentioned in the beginning of this thesis that superconductivity has to overcome the following challenges: cost, reliability and acceptance. With the recent progress in the fusion domain, superconductivity has garnered renewed enthusiasm and amplified interest. It is now time to break the other barriers. The work done for this thesis is useful for making HTS applications reliable, which together with acceptance, can lead to higher demand and hence lower manufacturing cost of superconductors.

The economic and functional feasibility of the MZI method for the health monitoring of HTS applications, can help overcome the reliability issue that stands in the way of the deployment of HTS applications. With a reliable hotspot detection technique like the one presented in this thesis, we can facilitate mass adoption of such HTS applications. The MZI method is low-cost and requires a simple setup. Even though the technique presents the challenge of high sensitivity to disturbances, the thesis showed that this problem can be overcome by means of machine learning based classification. With this development we can make quench detection even more reliable with MZI. If a real time application is developed using these data processing techniques, it can run alongside the MZI setup to build a valuable health monitoring system for HTS applications, paving way for the solutions to the problems in future grids.





# Appendix

## A.1 Working of the digital current pulser

The current source developed by SCI-consulting can deliver 400 A of currents per module. There are currently two groups with a total of eight modules in the current pulser at EPFL (capable of providing up to 3200 A) as the current source was in its early testing phase. The specifications of the current pulser used at EPFL are mentioned in Table 14 [85].

The ripple amplitude of the output current depends on the number of active modules, the PWM duty cycle for each module, the supply voltage as well as the load's impedance as shown in Fig. 95. Fig. 96 shows how the current ripple reduces with the addition of modules powered with phase shifted PWM control signals. Fig. 96 also explains why filtering of the noise from the current source is needed. This frequency of the noise introduced by the current source increases as more modules are added as seen in Fig. 96 hence for the eight modules at EPFL the current source operating frequency to be filtered is 500 kHz (62.5 kHz per module).

**Table 14. Specifications of the digital current pulser developed by SCI-consulting for low impedance loads [85]**

<b>General information</b>	
Supported supply voltage	4 to 40 V DC
Peak output current	3200 A
Maximum pulse duration at peak output current	170 ms
Pulse rise time	Down to 100 $\mu$ s
Number of modules	8
<b>Module information</b>	
Peak output current (per module)	400 A
Sustained output current (per phase)	50 A
PWM frequency for a module	62.5 kHz

For feedback purposes, the source measures the current output using Hall Effect Sensor(s) with a bandwidth of 200 kHz. The system is also able to detect imbalance between two groups of modules and returns an alarm if this occurs. Since the PWM frequency is 62.5 kHz, it is important to sample voltage measurements in the DAQ at the device frequency or multiples of the device frequency to prevent noisy measurements to avoid noise in the voltage measurements. For noise rejection, the same clock is used for controlling the current source and for data acquisition.

Fig. 97 shows the complete schematic of this purpose-built current source. The schematic shows the two groups of four modules, which are powered by an external high voltage source (two 165 F 48 V capacitors at the EPFL laboratory) and driven by separate PWM control signals. The sum of output current from the four modules in each group is measured using the current transducers. Current from both groups is fed back to the ADC of the control unit to check for any current imbalance between the two groups, for device safety. The total current from the two groups goes to the sample.

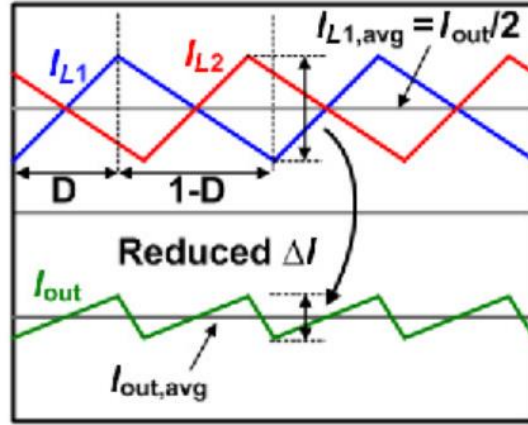


Figure 95. The generation of current pulse by means of phase shifted PWMs for reduced current ripple

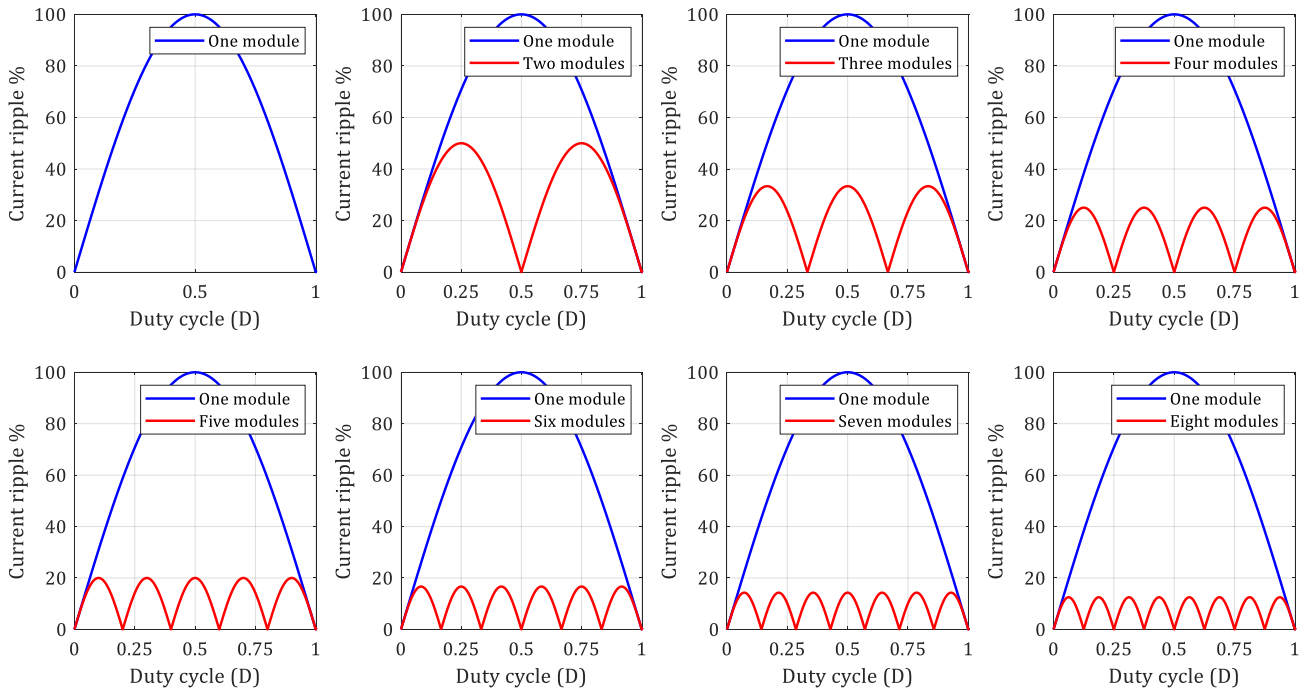


Figure 96. Ripple reduction in the current pulse by the addition of more modules driven with phase shifted control signals

Fig. 98 shows the control signals for each module which are phase shifted PWM signals. The duty cycle and hence the pulse width for the PWM is determined by the current setpoint which is required (input) by the user. The regulation loop compares this setpoint current to the current feedback from the transducers to control the pulse width.

Fig. 99 shows the schematic for the module that builds up this current pulser. The module comprises a high side and low side FET with gate drivers that receive the PWM control signals shown in Fig. 98. At the output of each module there is a smoothing inductor of  $10\ \mu\text{H}$  present.

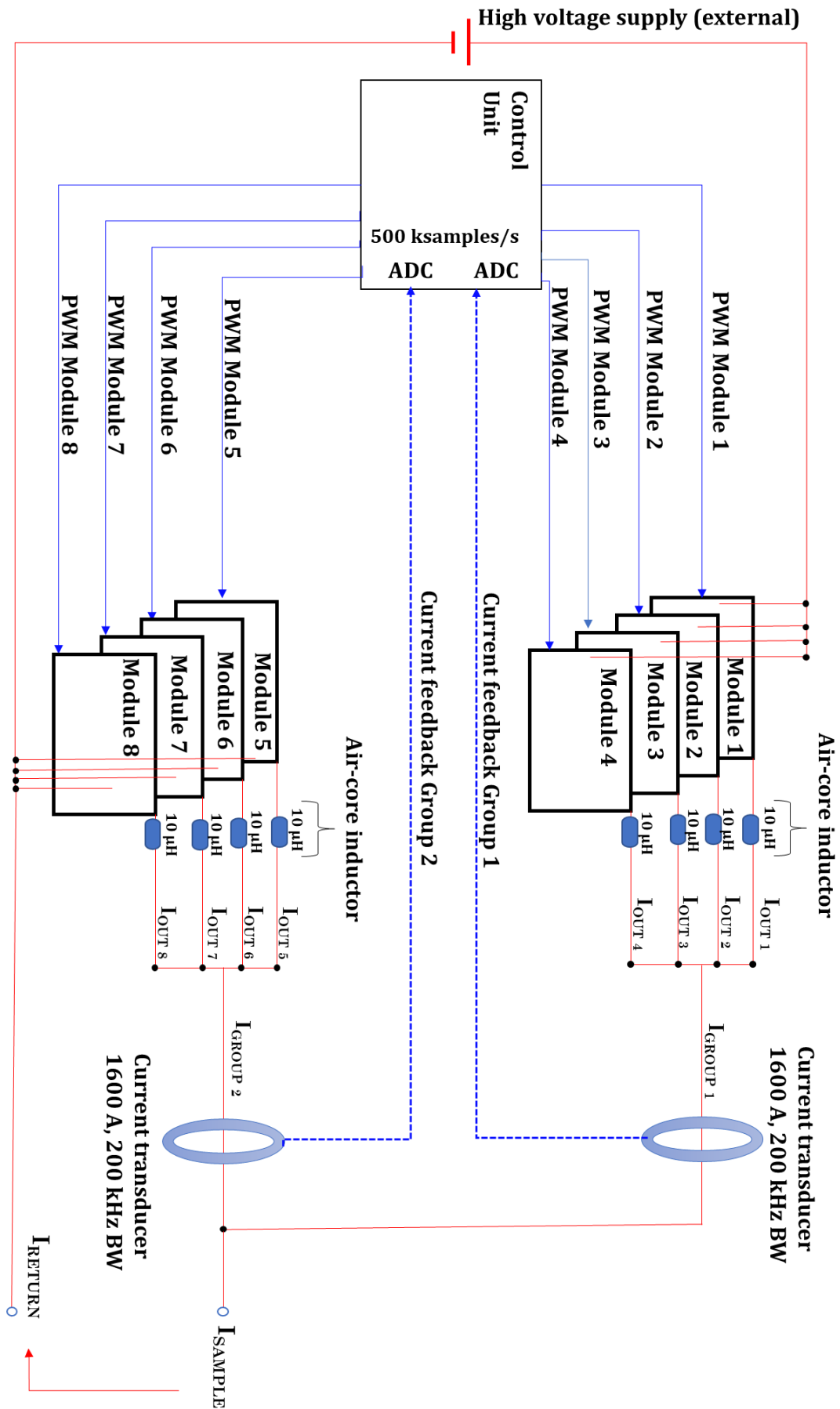


Figure 97. The schematic of the digital current pulser developed by SCI-consulting for EPFL

### PWM control signals with phase-shifts

Variable pulse width controlled by regulation loop by comparing setpoint current (programmed by the user) to the current feedback from the current transducers

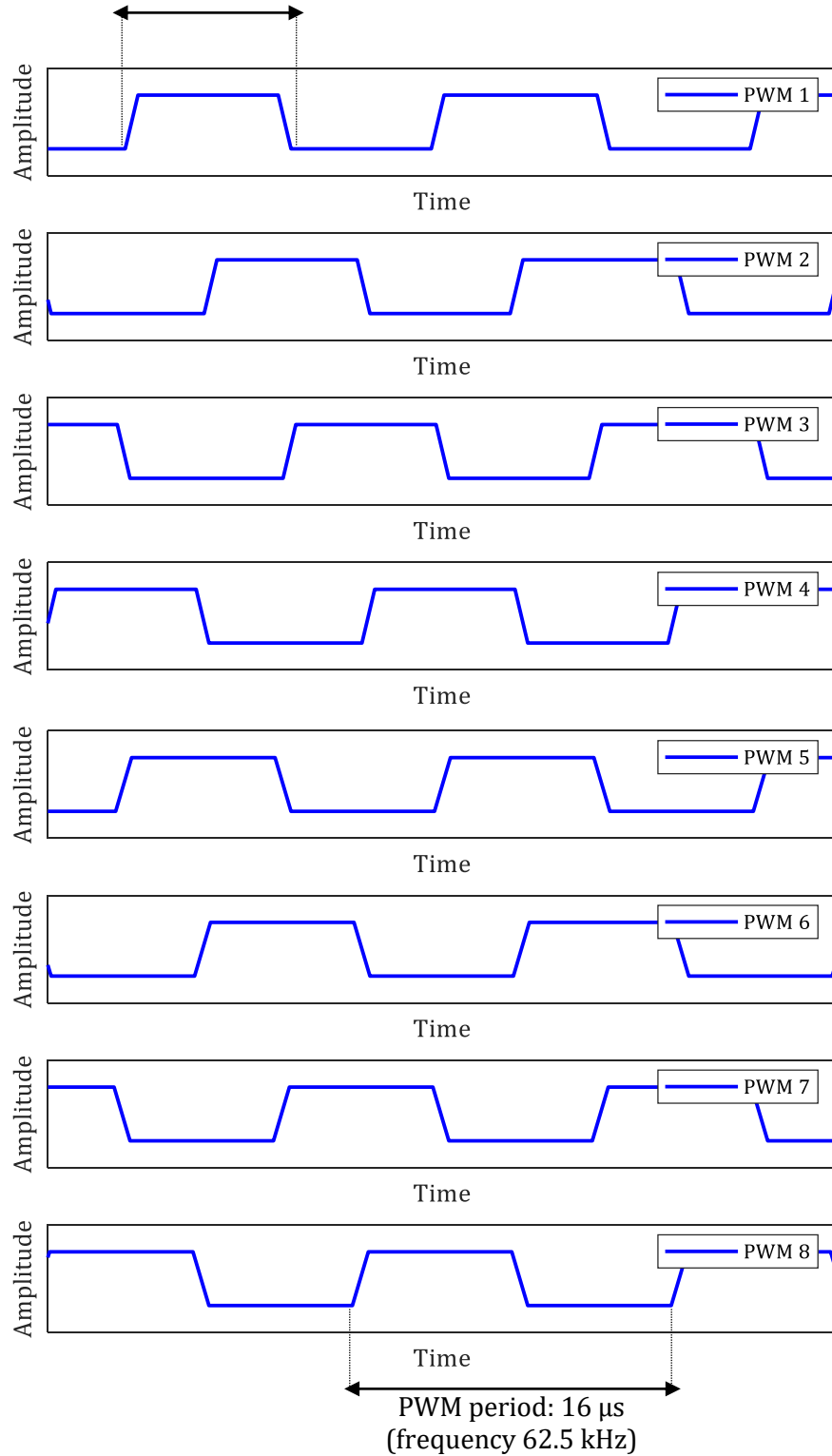


Figure 98. The phase shifted PWM control signals for each module

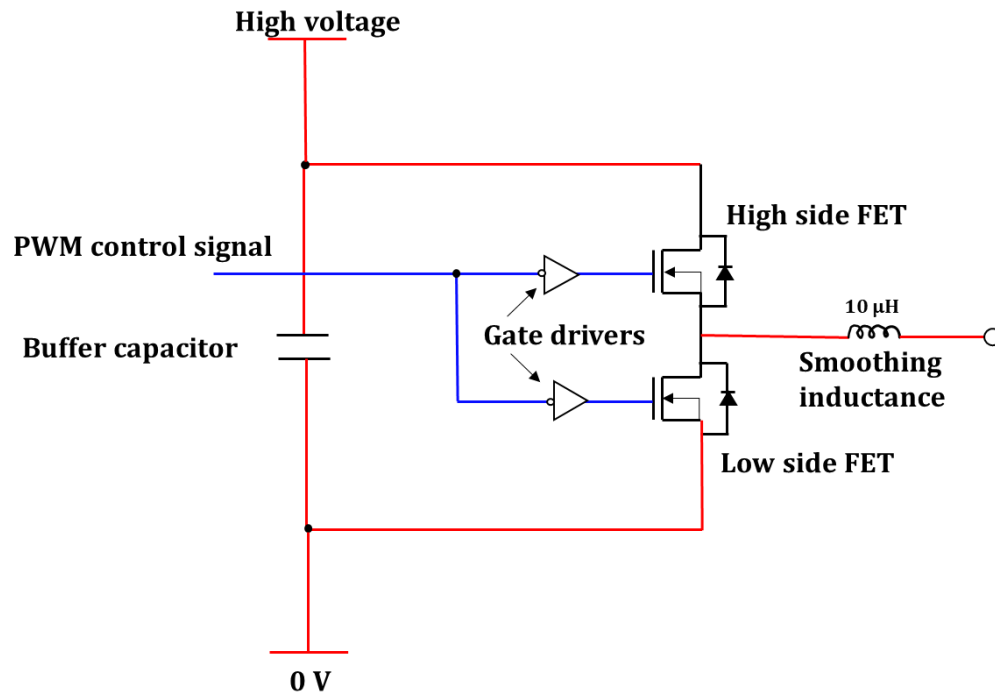


Figure 99. The schematic for the modules present in the digital current pulser

The current pulser can be operated by an easy to use file in LabVIEW. The user has to simply input the time and current values of the desired current pulse. The user can input various current pulse shapes, for example a ramp and can also control the rise and fall time of the current by defining trapezoidal current pulses.

## A.2 Differential amplifier to interface voltage measurement to DAQ

LT1997-2 (by Analog Devices, formerly Linear Technology) was used to get a gain of 0.25. This amplifier was selected due to its low noise level (40nV/√Hz RTO or 160nV/√Hz RTI) and good common mode rejection. The LT1997-2 circuit was configured as shown in Fig. 100 and circuitry to filter radio frequency interference (RFI) was added as per Fig. 100. The RFI disturbance can introduce a small dc offset voltage. These high frequency signals can be filtered by means of a low-pass RC network placed at the input of the instrumentation amplifier [125].

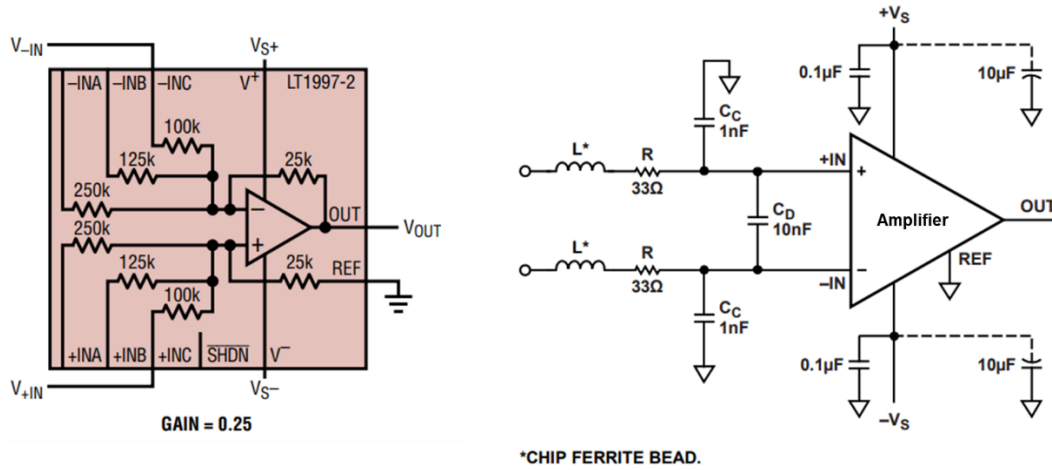


Figure 100. Configuration of the LT1997-2 for a gain of 0.25 (left) [125], RFI suppression circuitry added to LT1997-2 (right) [124]

In order to achieve a gain 9 LT1997-3 by Analog Devices, formerly Linear Technology was used in the configuration shown in Fig. 101 with the same RFI suppression circuit added to its inputs as shown in Fig. 101.

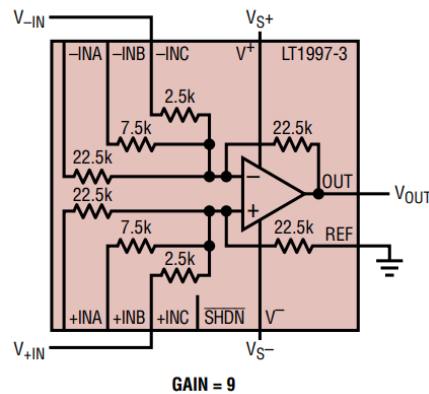


Figure 101. Gain 9 amplifier using LT1997-3 [126]

Both amplifiers take differential inputs of the voltage signal coming from the ethernet cable connected to the HTS sample. The ethernet cable connects to the amplifier PCB by means of an RJ-45 connector as shown in Fig. 102.

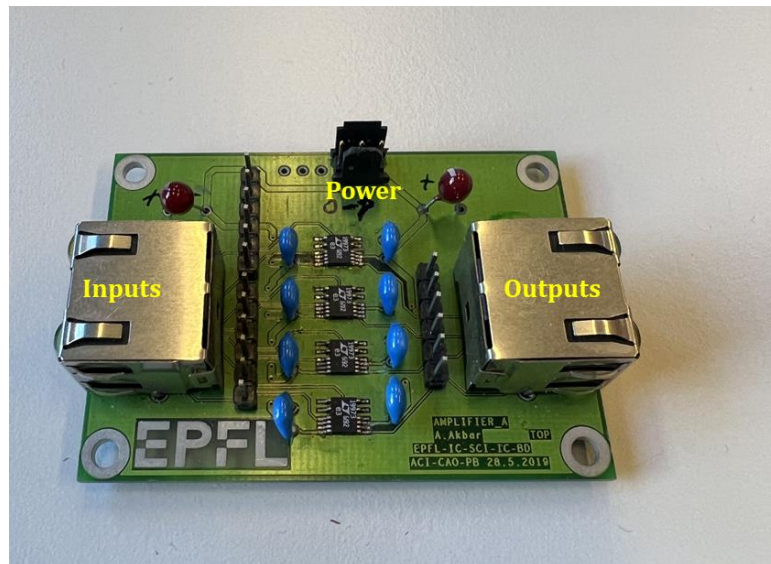
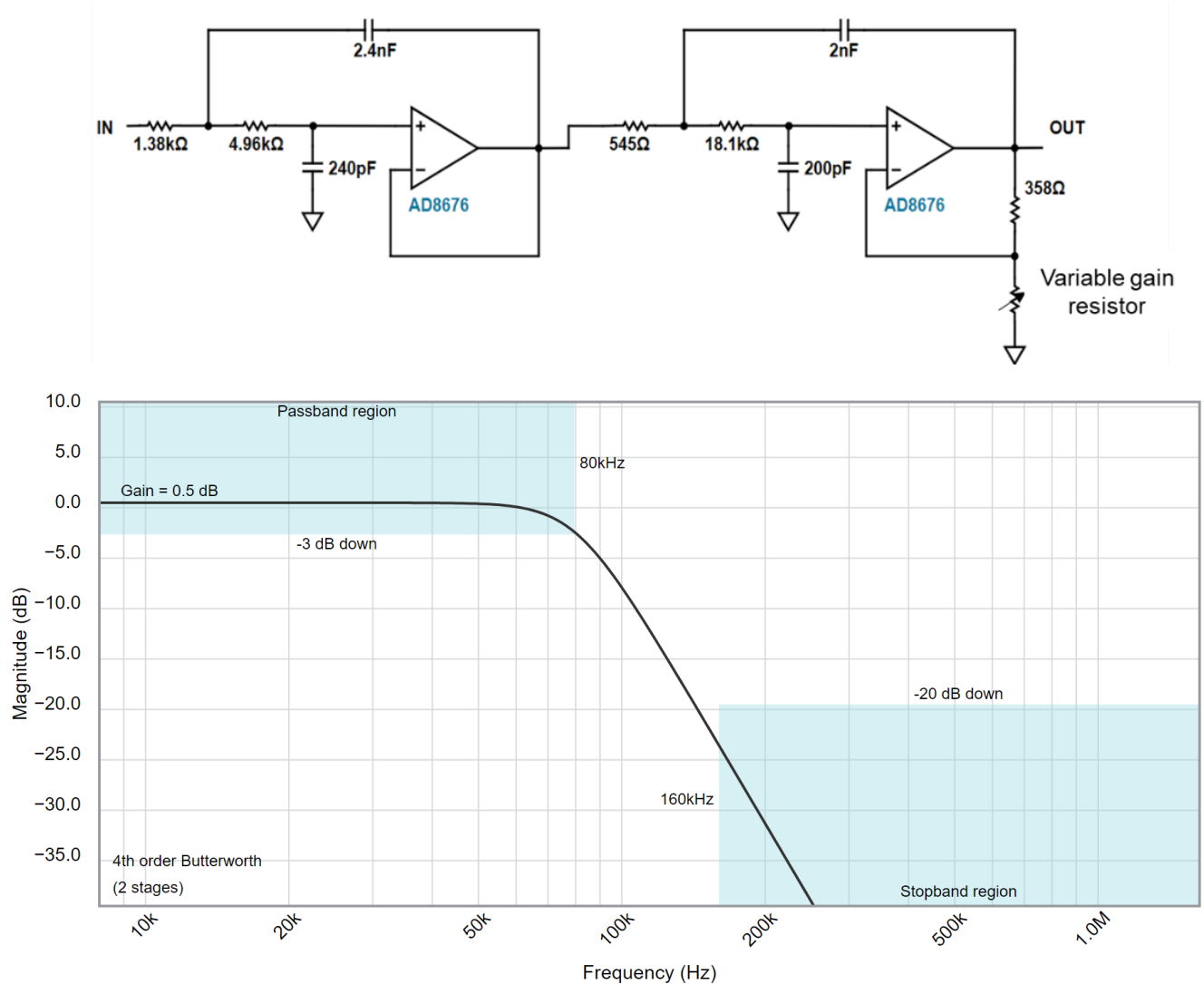


Figure 102. The prepared PCB board of the amplifiers for four channel inputs



### A.3 Low pass filter design for low noise DAQ measurements

The output of the voltage amplifier is connected to a fourth order low pass Butterworth filter which was designed for each voltage input channel of the Data Acquisition. Butterworth filter was chosen because it has a maximally flat amplitude response and hence offers the flattest gain response with frequency in the passband with moderate roll-off in the transition region. The cutoff was kept at 80 kHz which is lower than the BW of the DAQ (250 kHz) to avoid aliasing in the measurements. This cutoff frequency also allowed the filtering of the noise introduced due to the current source operating frequency of 500 kHz (62.5 kHz per module). A variable resistor was added in place of one of the gain resistors in case the gain of voltage measurements had to be adjusted before being input to the DAQ. Fig. 103 shows the design of the filter with its pass band and stop band while Fig. 104 shows the fully assembled PCB which caters to four channels.



**Figure 103.** The anti-aliasing filter designed using Analogue Devices Filter Wizard [127] to interface the voltage signals to the DAQ inputs

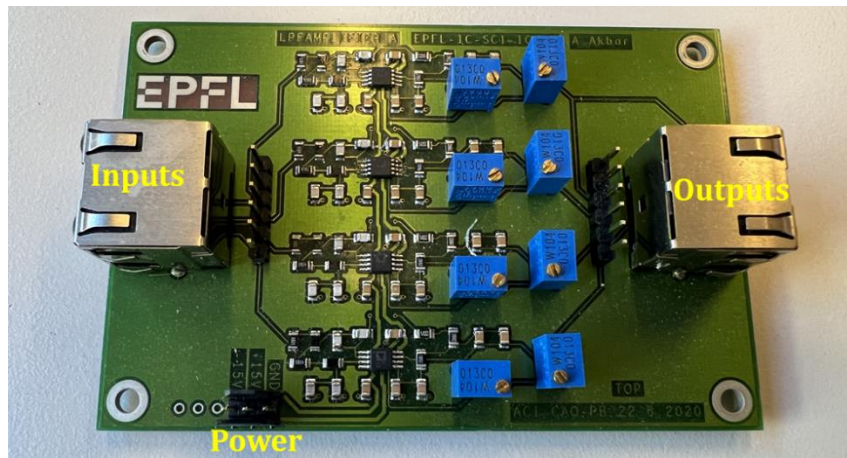


Figure 104. The PCB for the LPF which takes four inputs for filtering



## A C R O N Y M S

AAC	Average Amplitude Change
ACR	Air Coil Reactor
ANN	Artificial Neural Networks
AVP	Average Power
BW	Bandwidth
CESI	Centro Elettrotecnico Sperimentale Italiano
CFD	Current Flow Diverter
CFS	Commonwealth Fusion Systems
CTE	Coefficient of Thermal Expansion
DAQ	Data Acquisition
DC	Direct Current
DFB	Distributed Feedback
DWT	Discrete Wavelet Transform
ELU	Exponential Linear Units
EMI	Electromagnetic Interference
FBG	Fibre Bragg Grating
FC/APC	Fibre Connector/ Angled Physical Contact
FEM	Finite Element Modelling
FET	Field Effect Transistor
FPGA	Field Programmable Gate Array
HTS	High Temperature Superconductors
HV	High Voltage
HVAC	High Voltage Alternating Current
HVDC	High Voltage Direct Current
IEA	International Energy Agency
ITER	International Thermonuclear Experimental Reactor
KEPCO	Korea Electric Power Corporation
KNN	K-Nearest Neighbours
LTS	Low Temperature Superconductors
MAV	Mean Absolute Value
MOSFET	Metaloxide Semiconductor Field Effect Transistor
MTDC	Multi-terminal Direct Current
MZI	Mach-Zehnder Interferometer
NZPV	Normal Zone Propagation Velocity
OFDR	Optical Frequency Domain Reflectometry
PCB	Printed Circuit Board
PCM	Pulsed Current Measurement
PSI	Paul Scherrer Institute
PWM	Pulse-Width Modulation
QUELL	Quench Experiment on Long Length
RBF	Radial Basis Function
REBCO	Rare-earth Barium Copper Oxide
RELU	Rectified Linear Units

RFI	Radio Frequency Interference
RMS	Root Mean Square
RTI	Referred To The Input
RTO	Referred To The Output
SD	Standard Deviation
SDG	Sustainable Development Goals
SFCL	Superconducting Fault Current Limiters
SGI	SuperGrid Institute
SJTU	Shanghai Jiao Tong University
SVM	Support Vector Machine

## LIST OF FIGURES

### Chapter 1

Figure 1. Projected trends for renewable energy contribution by the International Energy Agency [2] .....	2
Figure 2. Schematic of a resistive SFCL showing the superconductor as a variable resistance adapted from [18] .....	4
Figure 3. The first resistive SFCL installed in a thermal power plant by Nexans in Germany in 2009: A picture of the drawing and complete 3-phase system after installation with the three cryostats [19].....	5
Figure 4. Front (left) and top view (right) of the 220 kV SFCL installed at the substation in Moscow [24] ....	5
Figure 5. Comparison of HTS power transmission with conventional systems, taken from C. E. Bruzek, “Introduction to superconducting power cable systems“, ESAS Summer School, 2017 .....	6
Figure 6. A comparison of the normal zone propagation in HTS and LTS conductors.....	8
Figure 7. Demonstration of the transient solution of a 4 cm normal zone development inside of a ReBCO coated conductor at 35 K and 90% $I_c$ shows how the temperature can reach almost 200 K within 0.4 s [39] ..	9

### Chapter 2

Figure 8. The architecture of a thermally stabilized 2G HTS tape with all its layers .....	11
Figure 9. The projected costs of 2G HTS tapes compiled by the CEO of SuperOX from [45–47].....	12
Figure 10. A break down of the work packages for the FastGrid project and the relevance of this thesis in the scheme outlined in red .....	12
Figure 11. An illustration of the non-inductive bi-filar winding (left) for the winding of the pancake [21], a pancake, the building block of the SFCL device (center) and the illustration of the FastGrid device with ten pancakes each wound with a bifilar winding (right) courtesy SuperGrid Institute, Lyon .....	14
Figure 12. A Tapestar plot for 10 m long Theva tape (TPL5121).....	14
Figure 13. A break down of the FastGrid tasks to deal with critical current inhomogeneity in superconductors and the role of EPFL and this thesis in the project .....	15
Figure 14. A schematic of protecting the SFCL using current thresholds with a circuit breaker in series (left) and a hypothetical scenario of grid operating current variation and the inefficient opening of the circuit breaker even in the absence of hotspots (right).....	16
Figure 15. An illustration of the hotspot cases a SFCL device may experience ranging from a one point quench (hardest to detect) to many points quenching (easiest to detect) in a SFCL device .....	17
Figure 16. The requirements this thesis had to meet while developing and testing a hotspot detection technique for HTS power applications .....	17

### Chapter 3

Figure 17. Cross section of an optical fibre .....	21
--	----

Figure 18. Basic components of a optical fibre based sensor system .....	22
Figure 19. The Mach-Zehnder Interferometer Schematic .....	25
Figure 20. A decision tree showing the comparison between Rayleigh backscattering, MZI and FBG to show the reasoning behind selecting MZI .....	26
<b>Chapter 4</b>	
Figure 21. The DFB laser used to build the MZI (top left) and its wavelength spectrum (top right ) [74], the laser driver used to power the laser diode with constant current (bottom) [76] .....	30
Figure 22. The manual three paddle polarization controller placed on the reference arm of the MZI [78] ....	31
Figure 23. How the waveplates in the polarization controller change the polarization states by means of quarter-wave plate (a) and half-wave plate (b) [79] .....	31
Figure 24. The InGaAs Photodiode (PD) used to build the photo-detector for the MZI (left), and the circuit used to build the photo-detector (right) [80].....	32
Figure 25. Wideband Fibre Optic Splitter/Coupler [81] .....	32
Figure 26. Variable attenuator used to balance the light intensity in in the two optical paths of the MZI (left) and its working principle (right) [82] .....	33
Figure 27. A schematic of the assembly of the MZI interferometer in the lab with the mentioned components .....	34
Figure 28. The inside of the MZI plug and play box (top) in a compact 20 cm x 20 cm x 12 box where the optical fibres from the HTS sample can simply be connected via FC/APC connectors (bottom) .....	35
Figure 29. The digital current pulser designed by SCI-consulting for low impedance loads with a built in DAQ board .....	36
Figure 30. Sample holder used to mount linear samples of HTS tapes (not drawn to scale).....	37
Figure 31. Illustration of how the optical fibre is integrated with the HTS sample and fixed along the sample holder and making its way out of the cryostat to the optical setup (not drawn to scale).....	38
Figure 32. Optical fibre lengths outside of the HTS sample are encased in teflon tubes to avoid fibre breakage (not drawn to scale).....	39
Figure 33. Voltage measurement contacts are placed on the HTS sample (top), voltage is acquired by means of a shielded signal cable (bottom) [86] .....	39
Figure 34. Placing the HTS sample in the cryostat and sealing the lid .....	40
Figure 35. Making the optical, electrical and data acquisition connections after the sample is placed in the cryostat.....	41
Figure 36. The process of splicing the optical fibres coming from the HTS sample .....	41
Figure 37. The purpose built device at SGI for integrating three optical fibres on the surface of the HTS tape which was used to wind the FastGrid SFCL pancakes (left), the stepwise integration of the three optical fibres to the HTS tape by means of Kapton using this device.....	43

Figure 38. Three optical fibres integrated with the HTS tape in the pancake by means of Kapton using the SGI device.....	44
Figure 39. The CAD drawing of the FastGrid FCL pancake (left) and a picture of the grooved current contacts for safe passage of the optical fibre (right), both pictures are courtesy of SuperGrid Institute Lyon .....	44
Figure 40. A custom-made cryostat for the FastGrid pancake .....	45
Figure 41. Connecting the FastGrid pancake to the current source and making the optical connections from fibres on conductor A2 .....	46
Figure 42. Acquired voltages for the FastGrid pancake measurements .....	46
Figure 43. A picture of the Petite SFCL Pancake with the four spliced optical fibres visible in red and blue. ....	47
Figure 44. The connections for the Petite SFCL Pancake.....	48
Figure 45. Acquired voltages for the Petite SFCL Pancake.....	48
<b>Chapter 5</b>	
Figure 46. MZI response to no heating in the SCS4050-AP sample .....	53
Figure 47. MZI response to single hotspot in the SCS4050-AP sample.....	53
Figure 48. MZI response to multiple hotspots in the SCS4050-AP sample.....	54
Figure 49. MZI response to high heating in the SCS4050-AP sample.....	54
Figure 50. TapeStar measurements and voltage tap locations for the portion (27.202 m to 27.8502 m) of the Theva TPL5121 tape which was tested with the MZI .....	56
Figure 51. MZI response to no heating in TPL5121 sample with low current (a), with high current (b).....	57
Figure 52. MZI response to single hotspot in TPL5121 sample.....	58
Figure 53. MZI response to low heating in TPL5121 sample.....	58
Figure 54. MZI response to high heating in TPL5121 sample.....	59
Figure 55. Structure of the encapsulated HTS tape (OFE-HTS tape) with soldered optical fibre[88] .....	61
Figure 56. Critical current of the OFE-HTS tape sample measured at SJTU .....	62
Figure 57. MZI response for no heating in OFE-HTS tape .....	63
Figure 58. MZI response for a single hotspot in the OFE-HTS tape.....	63
Figure 59. MZI response for medium heating in the OFE-HTS tape .....	64
Figure 60. MZI response to high heating in the OFE-HTS tape .....	64
Figure 61. TapeStar plot for the Theva bare HTS tape used to wind the Petite SFCL Pancake .....	66
Figure 62. MZI response to no heating in the Petite SFCL Pancake .....	67
Figure 63. Single hotspot detection by the MZI in the Petite SFCL Pancake .....	67
Figure 64. MZI response to two hotspots in the Petite SFCL Pancake .....	68
Figure 65. MZI response to multiple hotspots in the Petite SFCL Pancake .....	68



Figure 66 . MZI response to no heating in the FastGrid pancake .....	71
Figure 67. Lowest heating detected by MZI in the FastGrid pancake .....	71
Figure 68. MZI response to medium heating in the FastGrid pancake .....	72
Figure 69. MZI response to high heating in the FastGrid pancake .....	72
Figure 70. Polarization rotation in the MZI during experimentation leads to amplitude modulation (top) and loss of coherence visible in the zoomed in plot (bottom) .....	74

## Chapter 6

Figure 71. Temperature dependence of the thermo-optic coefficient of the optical fibre plotted from data obtained in [95] .....	78
Figure 72. Temperature dependence of the coefficient of thermal expansion of the optical fibre plotted from data obtained in [96] .....	78
Figure 73. A schematic representation (not in scale) of the 2-D thermal model showing the cross-section of the superconductor tape and the boundary condition applied to account for convective heat transfer in liquid nitrogen bath. The quantity <b>CTAPE</b> indicates the surface on which the heat source was applied. ....	80
Figure 74. (a) Simulation results for temperature in REBCO and optical fibre (in black) for optical fibre integrated with Kapton plotted along with the experimental measurements and showing the observed MZI response before the temperature peaks in the optical fibre (b) The heatmap obtained from the thermal model with Kapton shows the temperature gradient along the cross-section of the HTS tape, Kapton and the optical fibre .....	81
Figure 75. (a) Simulation results for temperature in REBCO and optical fibre (in black) for optical fibre integrated with Stycast® plotted along with the experimental measurements and showing the observed MZI response before the temperature rise in the optical fibre (b) The heatmap obtained from the thermal model with Stycast® shows the temperature gradient along the cross-section of the HTS tape, Kapton and the optical fibre .....	82
Figure 76. Dependence of the MZI response on quality of integration of the optical fibre .....	83

## Chapter 7

Figure 77. Hierarchical DWT decomposition of MZI output from experimental data and statistical feature extraction from detail coefficients at each level .....	87
Figure 78. Stepwise illustration of training and testing machine learning models for MZI response classification .....	89
Figure 79. KNN assigns the data point a class based on its neighbours [115] .....	90
Figure 80. Topology of a feed forward ANN with the input layer, hidden layer and the output layer [116] .	91
Figure 81. SVM binary classification using the optimal hyperplane [118] .....	92
Figure 82. RBF kernel for a variance value of 2 [121] .....	93
Figure 83. Distribution of the training and test data set for OFE-HTS tape .....	95

Figure 84. A performance analysis plot showing the accuracy of MZI response classification for KNN, ANN and SVM classifiers using feature vector extracted from 24 different wavelets for OFE-HTS tape .....	96
Figure 85. Distribution of the training and test data set for TPL5121 sample .....	98
Figure 86. A performance analysis plot showing the accuracy of MZI response classification for KNN, ANN and SVM classifiers using feature vector extracted from 24 different wavelets for TPL5121 .....	99
Figure 87. A performance analysis plot showing the accuracy of MZI response classification for KNN, ANN and SVM classifiers using feature vector extracted from 24 different wavelets for Petite SFCL Pancake .....	101
Figure 88. A performance analysis plot showing the accuracy of MZI response classification for KNN, ANN and SVM classifiers using feature vector extracted from 51 different wavelets for Petite SFCL Pancake .....	102
Figure 89. Scatter plots showing class separability of two-dimensional feature pairs extracted using db5 wavelet from the Petite SFCL Pancake MZI dataset .....	104
Figure 90. Scatter plots showing class separability of two-dimensional feature pairs extracted using Haar wavelet from the OFE-HTS tape MZI dataset .....	105
Figure 91. Scatter plots showing class separability of two-dimensional feature pairs extracted using Haar wavelet from the TLP5121 MZI dataset.....	105
Figure 92. Classification performance for KNN, ANN and SVM for different sizes of feature vectors extracted from the MZI output from the Petite SFCL Pancake.....	106
Figure 93. Dependence of classifier performance on training dataset size.....	107
<b>Chapter 8</b>	
Figure 94. The proposed roadmap for the thesis presented in 2019.....	111
<b>Appendix</b>	
Figure 95. The generation of current pulse by means of phase shifted PWMs for reduced current ripple ...	117
Figure 96. Ripple reduction in the current pulse by the addition of more modules driven with phase shifted control signals.....	117
Figure 97. The schematic of the digital current pulser developed by SCI-consulting for EPFL.....	118
Figure 98. The phase shifted PWM control signals for each module .....	119
Figure 99. The schematic for the modules present in the digital current pulser .....	120
Figure 100. Configuration of the LT1997-2 for a gain of 0.25 (left) [125], RFI suppression circuitry added to LT1997-2 (right) [124] .....	121
Figure 101. Gain 9 amplifier using LT1997-3 [126] .....	121
Figure 102. The prepared PCB board of the amplifiers for four channel inputs.....	122
Figure 103. The anti-aliasing filter designed using Analogue Devices Filter Wizard [127] to interface the voltage signals to the DAQ inputs .....	123
Figure 104. The PCB for the LPF which takes four inputs for filtering .....	124



## LIST OF TABLES

### Chapter 1

Table 1 Losses in HTS cables adapted from C. E. Bruzek, “Introduction to superconducting power cable systems“, ESAS Summer School, 2017.....	6
--	---

### Chapter 2

Table 2. The specifications of the FastGrid SFCL device .....	13
---	----

### Chapter 3

Table 3. Fibre optic sensors for health monitoring.....	22
---	----

### Chapter 4

Table 4. Cost break down of the MZI plug and play box .....	34
---	----

### Chapter 5

Table 5. SCS4050-AP sample details.....	52
---	----

Table 6. Theva TPL5121 details .....	56
--------------------------------------	----

Table 7. OFE-HTS sample details .....	61
---------------------------------------	----

Table 8. Petite SFCL Pancake details .....	66
--	----

Table 9. The FastGrid pancake details .....	70
---	----

### Chapter 7

Table 10. Formulae for statistical features extracted from the MZI output.....	87
--	----

Table 11. Wavelet families investigated for MZI where the number in the wavelet name represents the order .....	88
---	----

Table 12. Best performing machine learning classifier and wavelet pair for MZI response classification for the three HTS samples investigated.....	107
--	-----

Table 13. Highest classification accuracy achieved with ANN, KNN and SVM for the three HTS samples investigated .....	108
---	-----

### Appendix

Table 14. Specifications of the digital current pulser developed by SCI-consulting for low impedance loads [85].....	116
--	-----

## BIBLIOGRAPHY

- [1] U.S.E.P. Agency, Sources of Greenhouse Gas Emissions, (n.d.). <https://www.epa.gov/ghgemissions/sources-greenhouse-gas-emissions>.
- [2] IEA, Net Zero by 2050, 2021. <https://doi.org/10.1787/c8328405-en>.
- [3] IRENA, Innovation landscape brief: Supergrids, 2019.
- [4] G. Watson, Large-Scale Electricity Supergrids and the Transition to Electricity From Renewable Sources, *Renew. Energy Law Policy Rev.* 3 (2012) 87–99. <http://www.jstor.org/stable/24324737>.
- [5] M.J. Pérez-Molina, D.M. Larruskain, P. Eguía López, G. Buigues, Challenges for Protection of Future HVDC Grids, *Front. Energy Res.* 8 (2020) 33. <https://doi.org/10.3389/fenrg.2020.00033>.
- [6] J. Häfner, B. Jacobson, Proactive Hybrid HVDC Breakers - A key Innovation for Reliable HVDC Grids, in: 2011.
- [7] IEA, Clean energy investment in the net zero pathway, 2016-2050, (n.d.). <https://www.iea.org/data-and-statistics/charts/clean-energy-investment-in-the-net-zero-pathway-2016-2050>.
- [8] M. Larruskain, O. Abarrategui, I. Zamora, G. Buigues, V. Valverde, A. Iturregi, Requirements for Fault Protection in HVDC Grids, *Renew. Energy Power Qual. J.* (2015) 322–326. <https://doi.org/10.24084/repqj13.317>.
- [9] W. Leterme, D. Van Hertem, Classification of Fault Clearing Strategies for HVDC Grids, in: 2015.
- [10] D. Van Hertem, M. Ghandhari, J.-B. Curis, O. Despuys, A. Marzin, Protection requirements for a multi-terminal meshed DC grid, in: 2011.
- [11] M. Abedrabbo, M. Wang, P. Tielens, F.Z. Dejene, W. Leterme, J. Beerten, D. Van Hertem, Impact of DC grid contingencies on AC system stability, in: 13th IET Int. Conf. AC DC Power Transm. (ACDC 2017), 2017: pp. 1–7. <https://doi.org/10.1049/cp.2017.0025>.
- [12] E. Koldby, M. Hyttinen, Challenges on the Road to an Offshore HVDC Grid, in: 2009.
- [13] ABB, ABB reinvents the circuit breaker - breakthrough digital technology for renewables and next-gen power grids, 01-04-2019. (n.d.). <https://new.abb.com/news/detail/18527/abb-reinvents-the-circuit-breaker-breakthrough-digital-technology-for-renewables-and-next-gen-power-grids>.
- [14] M. Muniappan, A comprehensive review of DC fault protection methods in HVDC transmission systems, *Prot. Control Mod. Power Syst.* 6 (2021) 1. <https://doi.org/10.1186/s41601-020-00173-9>.
- [15] X. Pei, A.C. Smith, M. Barnes, Superconducting fault current limiters for HVDC systems, Elsevier B.V., 2015. <https://doi.org/10.1016/j.egypro.2015.11.405>.
- [16] G. Didier, C.H. Bonnard, T. Lubin, J. Lévêque, Comparison between inductive and resistive SFCL in terms of current limitation and power system transient stability, *Electr. Power Syst. Res.* 125 (2015) 150–158. <https://doi.org/https://doi.org/10.1016/j.epsr.2015.04.002>.
- [17] H. ten Kate, Superconducting Magnets Quench Propagation and Protection, (n.d.). <https://indico.cern.ch/event/194284/contributions/1472819/attachments/281522/393603/TenKat>

e\_-\_CAS\_-Handout-Quench-Erice-2103.pdf.

- [18] W. Hassenzahl, 8 - Superconducting fault current limiters and power cables, in: Z. Melhem (Ed.), *High Temp. Supercond. Energy Appl.*, Woodhead Publishing, 2012: pp. 259–293. <https://doi.org/https://doi.org/10.1533/9780857095299.2.259>.
- [19] J. Bock, M. Bludau, R. Dommerque, A. Hobl, S. Kraemer, M.O. Rikel, S. Elschner, HTS Fault Current Limiters—First Commercial Devices for Distribution Level Grids in Europe, *IEEE Trans. Appl. Supercond.* 21 (2011) 1202–1205. <https://doi.org/10.1109/TASC.2010.2099636>.
- [20] J. Bock, A. Hobl, J. Schramm, Superconducting Fault Current Limiters - a new device for future smart grids, in: 2012 China Int. Conf. Electr. Distrib., 2012: pp. 1–4. <https://doi.org/10.1109/CICED.2012.6508729>.
- [21] H.-P. Kraemer, W. Schmidt, H. Cai, B. Gamble, D. Madura, T. MacDonald, J. McNamara, W. Romanosky, G. Snitchler, N. Lallouet, F. Schmidt, S. Ahmed, Superconducting Fault Current Limiter for Transmission Voltage, *Phys. Procedia.* 36 (2012) 921–926. <https://doi.org/https://doi.org/10.1016/j.phpro.2012.06.230>.
- [22] S.R. Lee, J.-J. Lee, J. Yoon, Y.-W. Kang, J. Hur, Protection Scheme of a 154-kV SFCL Test Transmission Line at the KEPCO Power Testing Center, *IEEE Trans. Appl. Supercond.* 27 (2017) 1–5. <https://doi.org/10.1109/TASC.2017.2669159>.
- [23] Y.-H. Han, S. Yang, H. Kim, B.-J. Park, J. Yu, H.-R. Kim, S. In, Y.-J. Hong, H. Yeom, Development and Long-Term Test of a Compact 154-kV SFCL, *IEEE Trans. Appl. Supercond.* 29 (2019) 1–6. <https://doi.org/10.1109/TASC.2018.2880325>.
- [24] M. Moyzykh, D. Gorbunova, P. Ustyuzhanin, D. Sotnikov, K. Baburin, A. Maklakov, E. Magommedov, A. Shumkov, A. Telnova, V. Shcherbakov, D. Kumarov, L. Sabirov, M. Medovik, A. Kadyrbaev, S. Alexandrov, I. Mikoyan, S. Samoilnikov, A. Vavilov, First Russian 220 kV Superconducting Fault Current Limiter (SFCL) For Application in City Grid, *IEEE Trans. Appl. Supercond.* 31 (2021) 1–7. <https://doi.org/10.1109/TASC.2021.3066324>.
- [25] Y. Morishita, T. Ishikawa, I. Yamaguchi, S. Okabe, G. Ueta, S. Yanabu, Applications of DC Breakers and Concepts for Superconducting Fault-Current Limiter for a DC Distribution Network, *IEEE Trans. Appl. Supercond.* 19 (2009) 3658–3664. <https://doi.org/10.1109/TASC.2009.2018294>.
- [26] B. Xiang, Z. Liu, Y. Geng, S. Yanabu, DC Circuit Breaker Using Superconductor for Current Limiting, *IEEE Trans. Appl. Supercond.* 25 (2015) 1–7. <https://doi.org/10.1109/TASC.2014.2363058>.
- [27] S.I. Schlachter, W. Goldacker, 3 - High temperature superconductor (HTS) cables, in: Z. Melhem (Ed.), *High Temp. Supercond. Energy Appl.*, Woodhead Publishing, 2012: pp. 69–100. <https://doi.org/https://doi.org/10.1533/9780857095299.1.69>.
- [28] P.M. Noe, Table of Content Benefits of Superconducting Cables AC Cables DC Cables and Busbars, (2017). [https://indico.cern.ch/event/626654/attachments/1523851/2381785/Superconducting\\_Cables\\_-\\_Dr.\\_Mathias\\_Noel.pdf](https://indico.cern.ch/event/626654/attachments/1523851/2381785/Superconducting_Cables_-_Dr._Mathias_Noel.pdf).

- [29] D. Willén, F. Hansen, M. Däumling, C.N. Rasmussen, J. Østergaard, C. Træholt, E. Veje, O. Tønnesen, K.H. Jensen, S.K. Olsen, C. Rasmussen, E. Hansen, O. Schuppach, T. Visler, S. Kvorning, J. Schuzster, J. Mortensen, J. Christiansen, S.D. Mikkelsen, First operation experiences from a 30 kV, 104 MVA HTS power cable installed in a utility substation, *Phys. C Supercond. Its Appl.* 372–376 (2002) 1571–1579. [https://doi.org/10.1016/S0921-4534\(02\)01066-3](https://doi.org/10.1016/S0921-4534(02)01066-3).
- [30] M. Stemmle, F. Merschel, M. Noe, AmpaCity Project — World's First Superconducting Cable and Fault Current Limiter Installation in a German City Center, in: *Res. Fabr. Appl. Bi-2223 HTS Wires*, n.d.: pp. 263–278. [https://doi.org/10.1142/9789814749268\\_0019](https://doi.org/10.1142/9789814749268_0019).
- [31] M.C. Lee, H. Son, C. Ryu, Shingal Project; The 1st Commercial Application of 23 kV HTS Power Cable System in Korea, in: 2020: p. 2020.
- [32] F. Schmidt, J. Maguire, T. Welsh, S. Bratt, Operation Experience and further Development of a High-Temperature Superconducting Power Cable in the Long Island Power Authority Grid, *Phys. Procedia.* 36 (2012) 1137–1144. <https://doi.org/https://doi.org/10.1016/j.phpro.2012.06.190>.
- [33] D. Chandler, MIT-designed project achieves major advance toward fusion energy, (2021). <https://news.mit.edu/2021/MIT-CFS-major-advance-toward-fusion-energy-0908>.
- [34] J.-L. Duchateau, 11 - High temperature superconductors (HTS) in fusion technologies, in: Z. Melhem (Ed.), *High Temp. Supercond. Energy Appl.*, Woodhead Publishing, 2012: pp. 345–368. <https://doi.org/https://doi.org/10.1533/9780857095299.2.345>.
- [35] P. Bruzzone, W.H. Fietz, J. V Minervini, M. Novikov, N. Yanagi, Y. Zhai, J. Zheng, High temperature superconductors for fusion magnets, *Nucl. Fusion.* 58 (2018) 103001. <https://doi.org/10.1088/1741-4326/aad835>.
- [36] M. Marchevsky, Quench Detection and Protection for High-Temperature Superconductor Accelerator Magnets, *Instruments.* 5 (2021). <https://doi.org/10.3390/instruments5030027>.
- [37] H.P. Kraemer, W. Schmidt, B. Utz, H.W. Neumueller, Switching behavior of YBCO thin film conductors in resistive fault current limiters, *IEEE Trans. Appl. Supercond.* 13 (2003) 2044–2047. <https://doi.org/10.1109/TASC.2003.812980>.
- [38] C. Lacroix, J.H. Fournier-Lupien, K. McMeekin, F. Sirois, Normal zone propagation velocity in 2g hts coated conductor with high interfacial resistance, *IEEE Trans. Appl. Supercond.* 23 (2013) 3–7. <https://doi.org/10.1109/TASC.2013.2239696>.
- [39] J. van Nugteren, M. Dhallé, S. Wessel, E. Krooshoop, A. Nijhuis, H. ten Kate, Measurement and Analysis of Normal Zone Propagation in a ReBCO Coated Conductor at Temperatures Below 50K, *Phys. Procedia.* 67 (2015) 945–951. <https://doi.org/https://doi.org/10.1016/j.phpro.2015.06.159>.
- [40] and B.D. Mathias Noe, Achim Hobl, Pascal Tixador, Luciano Martini, Conceptual Design of a 24 kV, 1 kA Resistive Superconducting Fault Current Limiter, *IEEE Trans. Appl. Supercond.* 22 (2012) 64–65. <https://doi.org/10.1109/TASC.2011.2181284>.
- [41] P. Tixador, M. Bauer, C.E. Bruzek, A. Calleja, G. Deutscher, B. Dutoit, F. Gomory, L. Martini, M. Noe, X. Obradors, M. Pekarcikova, F. Sirois, Status of the european union project FASTGRID, *IEEE*

- Trans. Appl. Supercond. 29 (2019). <https://doi.org/10.1109/TASC.2019.2908586>.
- [42] A.P. Malozemoff, 1 - The power grid and the impact of high-temperature superconductor technology: An overview, in: C. Rey (Ed.), *Supercond. Power Grid*, Woodhead Publishing, 2015: pp. 3–28. <https://doi.org/https://doi.org/10.1016/B978-1-78242-029-3.00001-7>.
- [43] X. Pei, A.C. Smith, M. Barnes, Superconducting Fault Current Limiters for HVDC Systems, *Energy Procedia*. 80 (2015) 47–55. <https://doi.org/https://doi.org/10.1016/j.egypro.2015.11.405>.
- [44] S. Samoilenkov, Superconducting fault current limiters for grid protection, (n.d.). <https://hrcak.srce.hr/file/383300>.
- [45] S. Hyun Moon, HTS development and industrialization at Sunam, (n.d.). <https://indico.cern.ch/event/308828/contributions/1680708/>.
- [46] V. Matias, R.H. Hammond, YBCO Superconductor Wire based on IBAD-Textured Templates and RCE of YBCO: Process Economics, *Phys. Procedia*. 36 (2012) 1440–1444. <https://doi.org/https://doi.org/10.1016/j.phpro.2012.06.239>.
- [47] P.M. Grant, T.P.S. Epri, P. Alto, Ca, Saic, Gaithersburg, Md., Cost Projections for High Temperature Superconductors, *ArXiv Supercond.* (2002).
- [48] P.J. Tixador, A. Akbar, M. Bauer, M. Bocchi, A. Calleja, C. Creusot, G. Deutscher, F. Gomory, M. Noe, X. Obradors, M. Pekarcikova, F. Sirois, Some results of the EC project FASTGRID, *IEEE Trans. Appl. Supercond.* (2022) 1. <https://doi.org/10.1109/TASC.2022.3151318>.
- [49] THEVA, (n.d.). <https://www.theva.com/products/>.
- [50] J. Bock, A. Hobl, S. Krämer, M. Bludau, J. Schramm, C. Jänke, M. Rikel, S. Elschner, NEXANS' SUPERCONDUCTING FAULT CURRENT LIMITERS FOR MEDIUM VOLTAGE APPLICATIONS – STATUS AND PROSPECTS, in: 2011.
- [51] J. Chesnoy, Preface, in: J. Chesnoy (Ed.), *Undersea Fiber Commun. Syst.*, Academic Press, San Diego, 2002: pp. xxv–xxvi. <https://doi.org/https://doi.org/10.1016/B978-012171408-6/50002-7>.
- [52] Y. Yincan, J. Xinmin, P. Guofu, J. Wei, eds., Chapter 1 - Introduction, in: *Submar. Opt. Cable Eng.*, Academic Press, 2018: pp. 1–27. <https://doi.org/https://doi.org/10.1016/B978-0-12-813475-7.00001-1>.
- [53] OFS, Fiber Coatings, Buffering and Cabling Materials, (n.d.). <https://www.ofsoptics.com/optical-fiber-coatings/>.
- [54] B. Lee, Review of the present status of optical fiber sensors, *Opt. Fiber Technol.* 9 (2003) 57–79. [https://doi.org/https://doi.org/10.1016/S1068-5200\(02\)00527-8](https://doi.org/https://doi.org/10.1016/S1068-5200(02)00527-8).
- [55] H.-N. Li, D.-S. Li, G.-B. Song, Recent applications of fiber optic sensors to health monitoring in civil engineering, *Eng. Struct.* 26 (2004) 1647–1657. <https://doi.org/https://doi.org/10.1016/j.engstruct.2004.05.018>.
- [56] M. Turenne, R. Johnson, F. Hunte, J. Schwartz, H. Song, Multi-purpose fiber optic sensors for high



- temperature superconducting magnets, (2009). <https://doi.org/10.1109/FUSION.2009.5226397>.
- [57] S. Gupta, T. Mizunami, T. Yamao, T. Shimomura, Fiber Bragg grating cryogenic temperature sensors, *Appl. Opt.* 35 (1996) 5202–5205. <https://doi.org/10.1364/AO.35.005202>.
  - [58] A. Chiuchiolo, M. Bajko, J.C. Perez, H. Bajas, M. Consales, M. Giordano, G. Breglio, A. Cusano, Fiber bragg grating cryosensors for superconducting accelerator magnets, *IEEE Photonics J.* 6 (2014) 1–10. <https://doi.org/10.1109/JPHOT.2014.2343994>.
  - [59] A. Chiuchiolo, M. Bajko, J. Perez, H. Bajas, M. Guinchard, M. Giordano, G. Breglio, M. Consales, A. Cusano, Structural Health Monitoring of Superconducting Magnets at CERN Using Fiber Bragg Grating Sensors, in: 2014.
  - [60] E.E. Salazar, R.A. Badcock, M. Bajko, B. Castaldo, M. Davies, J. Estrada, V. Fry, J.T. Gonzales, P.C. Michael, M. Segal, R.F. Vieira, Z.S. Hartwig, Fiber optic quench detection for large-scale {HTS} magnets demonstrated on {VIPER} cable during high-fidelity testing at the {SULTAN} facility, *Supercond. Sci. Technol.* 34 (2021) 35027. <https://doi.org/10.1088/1361-6668/abdba8>.
  - [61] C.W.K. Schwartz Justin, Scurti Federico, Rogers Samuel, United States Patent Application Publication Schwartz et al., US 20170179364, 2017.
  - [62] F. Scurti, S. Ishmael, G. Flanagan, J. Schwartz, Quench detection for high temperature superconductor magnets: a novel technique based on Rayleigh-backscattering interrogated optical fibers, *Supercond. Sci. Technol.* 29 (2016) 03LT01. <https://doi.org/10.1088/0953-2048/29/3/03lt01>.
  - [63] F. Scurti, J. Schwartz, Optical fiber distributed sensing for high temperature superconductor magnets, in: 2017 25th Opt. Fiber Sensors Conf., 2017: pp. 1–4. <https://doi.org/10.1117/12.2265947>.
  - [64] J. Jiang, Z. Wu, B. Liu, J. Sheng, L. Wang, Z. Li, Z. Jin, Z. Hong, Thermal Stability Study of a Solder-Impregnated No-Insulation HTS Coil Via a Raman-Based Distributed Optical Fiber Sensor System, *IEEE Trans. Appl. Supercond.* 29 (2019) 1–4. <https://doi.org/10.1109/TASC.2018.2890384>.
  - [65] F. Scurti, J. McGarrahan, J. Schwartz, Effects of metallic coatings on the thermal sensitivity of optical fiber sensors at cryogenic temperatures, *Opt. Mater. Express.* 7 (2017) 1754. <https://doi.org/10.1364/ome.7.001754>.
  - [66] O. Tsukamoto, K. Kawai, Y. Kokubun, Quench detection of superconducting magnet by dual-core optical fiber, *IEEE Trans. Magn.* 23 (1987) 1572–1575. <https://doi.org/10.1109/TMAG.1987.1065015>.
  - [67] S. Pourrahimi, W.C. Guss, J. V Minervini, D.B. Montgomery, N.T. Pierce, J.H. Schultz, S.P. Smith, S. Ezekiel, US contributions to the development and calibration of quench detectors for the ITER QUELL, *IEEE Trans. Appl. Supercond.* 5 (1995) 491–494. <https://doi.org/10.1109/77.402573>.
  - [68] S. Pourrahimi, S.P. Smith, J.H. Schultz, J. V Minervini, S. Ezekiel, A. Anghel, G. Vecsey, Y. Takahashi, Performance of the US quench detection systems in the QUELL experiments, *IEEE Trans. Appl. Supercond.* 7 (1997) 447–450. <https://doi.org/10.1109/77.614530>.
  - [69] Y. Xie, M. Zhang, D. Dai, Design Rule of Mach-Zehnder Interferometer Sensors for Ultra-High Sensitivity, *Sensors.* 20 (2020). <https://doi.org/10.3390/s20092640>.

- [70] J.A. Flores-Bravo, J. Madrigal, J. Zubia, S. Sales, J. Villatoro, Coupled-core fiber Bragg gratings for low-cost sensing, *Sci. Rep.* 12 (2022) 1280. <https://doi.org/10.1038/s41598-022-05313-9>.
- [71] Z. Ding, C. Wang, K. Liu, J. Jiang, D. Yang, G. Pan, Z. Pu, T. Liu, Distributed Optical Fiber Sensors Based on Optical Frequency Domain Reflectometry: A review, *Sensors*. 18 (2018). <https://doi.org/10.3390/s18041072>.
- [72] D. Tosi, S. Poeggel, I. Iordachita, E. Schena, 11 - Fiber Optic Sensors for Biomedical Applications, in: H. Alemohammad (Ed.), *Opto-Mechanical Fiber Opt. Sensors*, Butterworth-Heinemann, 2018: pp. 301–333. <https://doi.org/https://doi.org/10.1016/B978-0-12-803131-5.00011-8>.
- [73] V. Toccafondo, C.J. Oton, Robust and low-cost interrogation technique for integrated photonic biochemical sensors based on Mach-Zehnder interferometers, *Photon. Res.* 4 (2016) 57–60. <https://doi.org/10.1364/PRJ.4.000057>.
- [74] THORLABS, Pigtailed, Distributed Feedback (DFB) Single-Frequency Lasers with Internal Isolator, (n.d.). [https://www.thorlabs.com/newgrouppage9.cfm?objectgroup\\_id=7928](https://www.thorlabs.com/newgrouppage9.cfm?objectgroup_id=7928).
- [75] L.V.T. Nguyen, Distributed-feedback (DFB) laser coherence and linewidth broadening, Edinburgh, S. Aust. : DSTO Systems Sciences Laboratory, Edinburgh, S. Aust., 2003.
- [76] THORLABS, LD1255R - 250 mA Precision Constant Current Laser Driver, RoHS Compliant, (n.d.). <https://www.thorlabs.com/thorproduct.cfm?partnumber=LD1255R>.
- [77] P. Purdue University, Basics of coherence theory, (n.d.). [https://www.physics.purdue.edu/webapps/index.php/course\\_document/index/phys322/1460/25/11076](https://www.physics.purdue.edu/webapps/index.php/course_document/index/phys322/1460/25/11076).
- [78] THORLABS, Manual Fiber Polarization Controllers, (n.d.). [https://www.thorlabs.com/newgrouppage9.cfm?objectgroup\\_id=343](https://www.thorlabs.com/newgrouppage9.cfm?objectgroup_id=343).
- [79] Meadowlark Optics, Principles of retarders, n.d. <https://www.meadowlark.com/store/PDFs/Retarders.pdf>.
- [80] THORLABS, InGaAs High Speed Photodiode with FC/PC Bulkhead, (n.d.). <https://www.thorlabs.com/drawings/c6448bee009b2bd0-5A68A996-99E0-22C3-CD005AACF8530E5D/FGA01FC-SpecSheet.pdf>.
- [81] THORLABS, 1550 nm 1x2 Single Mode Fused Fiber Optic Couplers / TapS, (n.d.). [https://www.thorlabs.com/newgrouppage9.cfm?objectgroup\\_id=9567](https://www.thorlabs.com/newgrouppage9.cfm?objectgroup_id=9567).
- [82] THORLABS, VOA50-APC - SM Variable Attenuator, 1310/1550 nm, 50 dB, In-Line, FC/APC Connectors, (n.d.). <https://www.thorlabs.com/thorproduct.cfm?partnumber=VOA50-APC>.
- [83] THORLABS, FC/APC Fiber Connectors: Single Mode, (n.d.). [https://www.thorlabs.com/newgrouppage9.cfm?objectgroup\\_id=6246](https://www.thorlabs.com/newgrouppage9.cfm?objectgroup_id=6246).
- [84] F. Sirois, J. Coulombe, A. Bernier, Characterization of the Superconducting to Normal Transition of HTS Coated Conductors by Fast Pulsed Current Measurements, *IEEE Trans. Appl. Supercond.* 19 (2009) 3585–3590. <https://doi.org/10.1109/TASC.2009.2018304>.

- [85] SCI-Consulting, (n.d.). <http://www.sci-consulting.ch/>.
- [86] AD-net, Intro to Screened Twisted-Pair (ScTP) and Screened Shielded Twisted-Pair (S/STP or S/FTP), (n.d.). <https://www.ad-net.com.tw/intro-screened-twisted-pair-sctp-screened-shielded-twisted-pair-sstp-sftp/>.
- [87] Measurement Computing, Data Acquisition Fundamentals: Improving Measurement Quality with Signal Conditioning, 2013. <https://www.mccdaq.com/pdfs/anpdf/Signal-Conditioning-White-Paper.pdf>.
- [88] J. Jiang, Z. Jin, Z. Li, Z. Hong, M. Song, X. Duan, Quench recovery time of an optical fiber encapsulated resistance-type {DC} superconducting fault current limiter coil determined by a Raman-based distributed temperature sensing system, *Supercond. Sci. Technol.* 34 (2021) 85014. <https://doi.org/10.1088/1361-6668/abee9b>.
- [89] N. Imoto, N. Yoshizawa, J. Sakai, H. Tsuchiya, Birefringence in single-mode optical fiber due to elliptical core deformation and stress anisotropy, *IEEE J. Quantum Electron.* 16 (1980) 1267–1271. <https://doi.org/10.1109/JQE.1980.1070382>.
- [90] G.W. Day, Birefringence Measurements In Single Mode Optical Fiber, *Single Mode Opt. Fibers.* 0425 (1983) 72–81. <https://doi.org/10.1117/12.936216>.
- [91] Y. Inoue, K. Katoh, M. Kawachi, Polarization Sensitivity of a Silica Waveguide Thermo-optic Phase Shifter for Planar Lightwave Circuits, *IEEE Photonics Technol. Lett.* 4 (1992) 36–38. <https://doi.org/10.1109/68.124868>.
- [92] G. Heise, R. Narevich, Simple model for polarization sensitivity of silica waveguide Mach-Zehnder interferometer, *IEEE Photonics Technol. Lett.* 17 (2005) 2116–2118. <https://doi.org/10.1109/LPT.2005.854342>.
- [93] K. Nagano, S. Kawakami, S. Nishida, Change of the refractive index in an optical fiber due to external forces, *Appl. Opt.* 17 (1978) 2080. <https://doi.org/10.1364/ao.17.002080>.
- [94] R. Rajini-Kumar, M. Suesser, K.G. Narayankhedkar, G. Krieg, M.D. Atrey, Performance evaluation of metal-coated fiber Bragg grating sensors for sensing cryogenic temperature, *Cryogenics (Guildf.)* 48 (2008) 142–147. <https://doi.org/10.1016/j.cryogenics.2008.02.007>.
- [95] D.B. Leviton, B.J. Frey, Temperature-dependent absolute refractive index measurements of synthetic fused silica, *Optomech. Technol. Astron.* 6273 (2006) 62732K. <https://doi.org/10.1117/12.672853>.
- [96] M. Okaji, N. Yamada, K. Nara, H. Kato, Laser interferometric dilatometer at low temperatures : application to fused silica SRM 739, *Cryogenics (Guildf.)* 35 (1995) 887–891.
- [97] COMSOL Multiphysics®, (n.d.). <https://www.comsol.ch/>.
- [98] S. Zou, V.M.R. Zermeno, F. Grilli, Simulation of Stacks of High-Temperature Superconducting Coated Conductors Magnetized by Pulsed Field Magnetization Using Controlled Magnetic Density Distribution Coils, *IEEE Trans. Appl. Supercond.* 26 (2016) 1–5. <https://doi.org/10.1109/TASC.2016.2520210>.

- [99] N. Bagrets, S. Otten, K.-P. Weiss, A. Kario, W. Goldacker, Thermal and mechanical properties of advanced impregnation materials for {HTS} cables and coils, {IOP} Conf. Ser. Mater. Sci. Eng. 102 (2015) 12021. <https://doi.org/10.1088/1757-899x/102/1/012021>.
- [100] National Institute of Standards and Technology, Material Properties: Polyimide (Kapton), (n.d.). [https://trc.nist.gov/cryogenics/materials/Polyimide Kapton/PolyimideKapton\\_rev.htm](https://trc.nist.gov/cryogenics/materials/Polyimide Kapton/PolyimideKapton_rev.htm).
- [101] National Institute of Standards and Technology, Material Properties: Copper, (n.d.). [https://trc.nist.gov/cryogenics/materials/OFHC Copper/OFHC\\_Copper\\_rev1.htm](https://trc.nist.gov/cryogenics/materials/OFHC Copper/OFHC_Copper_rev1.htm).
- [102] F. Roy, Modeling and Characterization of Coated Conductors Applied to the Design of Superconducting Fault Current Limiters, (2010) 98. <https://doi.org/10.5075/epfl-thesis-4721>.
- [103] D. Cvetkovic, E.D. Übeyli, I. Cosic, Wavelet transform feature extraction from human PPG, ECG, and EEG signal responses to ELF PEMF exposures: A pilot study, Digit. Signal Process. A Rev. J. 18 (2008) 861–874. <https://doi.org/10.1016/j.dsp.2007.05.009>.
- [104] S.G. Mallat, A theory for multiresolution signal decomposition: The wavelet representation, Fundam. Pap. Wavelet Theory. I (2009) 494–513. <https://doi.org/10.1515/9781400827268.494>.
- [105] P.P.S. Saputra, Misbah, Eliyani, R. Firmansyah, D. Lastomo, Haar and Symlet Discrete Wavelete Transform for Identification Misalignment on Three Phase Induction Motor Using Energy Level and Feature Extraction, J. Phys. Conf. Ser. 1179 (2019). <https://doi.org/10.1088/1742-6596/1179/1/012093>.
- [106] N. Kwak, C.H. Choi, Input feature selection for classification problems, IEEE Trans. Neural Networks. 13 (2002) 143–159. <https://doi.org/10.1109/72.977291>.
- [107] J. Kim, Discrete Wavelet Transform-Based Feature Extraction of Experimental Voltage Signal for Li-Ion Cell Consistency, IEEE Trans. Veh. Technol. 65 (2016) 1150–1161. <https://doi.org/10.1109/TVT.2015.2414936>.
- [108] O. Rashid, A. Amin, M.R. Lone, Performance analysis of DWT families, Proc. 3rd Int. Conf. Intell. Sustain. Syst. ICISS 2020. (2020) 1457–1463. <https://doi.org/10.1109/ICISS49785.2020.9315960>.
- [109] M. Yazdani-Asrami, M. Taghipour-Gorjikolaie, S. Mohammad Razavi, S. Asghar Gholamian, A novel intelligent protection system for power transformers considering possible electrical faults, inrush current, CT saturation and over-excitation, Int. J. Electr. Power Energy Syst. 64 (2015) 1129–1140. <https://doi.org/10.1016/j.ijepes.2014.08.008>.
- [110] G.H.S. Dreiman, M. Bictash, P. V. Fish, L. Griffin, F. Svensson, Changing the HTS Paradigm: AI-Driven Iterative Screening for Hit Finding, SLAS Discov. 26 (2021) 257–262. <https://doi.org/10.1177/2472555220949495>.
- [111] D.C. Neagu, G. Guo, P.R. Trundle, M.T.D. Cronin, A comparative study of machine learning algorithms applied to predictive toxicology data mining, ATLA Altern. to Lab. Anim. 35 (2007) 25–32. <https://doi.org/10.1177/026119290703500119>.
- [112] A. al-Qerem, F. Kharbat, S. Nashwan, S. Ashraf, khairi blaou, General model for best feature extraction of EEG using discrete wavelet transform wavelet family and differential evolution, Int. J. Distrib. Sens.

- Networks. 16 (2020). <https://doi.org/10.1177/1550147720911009>.
- [113] I.M. Galván, J.M. Valls, N. Lecomte, P. Isasi, A lazy approach for machine learning algorithms, *IFIP Int. Fed. Inf. Process.* 296 (2009) 517–522. [https://doi.org/10.1007/978-1-4419-0221-4\\_60](https://doi.org/10.1007/978-1-4419-0221-4_60).
- [114] K.A. Gaurav, L. Patel, *Machine Learning With R*, 2020. <https://doi.org/10.4018/978-1-7998-2718-4.ch015>.
- [115] R. Ye, L. Zhang, P. Suganthan, K-nearest neighbor based bagging SVM pruning, in: 2013: pp. 25–30. <https://doi.org/10.1109/CIEL.2013.6613136>.
- [116] P. Mehta, M. Bukov, C.-H. Wang, A.G.R. Day, C. Richardson, C.K. Fisher, D.J. Schwab, A high-bias, low-variance introduction to Machine Learning for physicists, *Phys. Rep.* 810 (2019) 1–124. <https://doi.org/https://doi.org/10.1016/j.physrep.2019.03.001>.
- [117] MATLAB, Support Vector Machines for Binary Classification, (n.d.). <https://ch.mathworks.com/help/stats/support-vector-machines-for-binary-classification.html>.
- [118] E.H. Rady, A. Anwar, Prediction of kidney disease stages using data mining algorithms, *Informatics Med. Unlocked.* 15 (2019) 100178. <https://doi.org/10.1016/j.imu.2019.100178>.
- [119] U. of Wisconsin–Madison, The Radial Basis Function Kernel, (n.d.). <https://pages.cs.wisc.edu/~matthewb/pages/notes/pdf/svms/RBFKernel.pdf>.
- [120] Analytics Vidhya, Understanding Support Vector Machine(SVM) algorithm, (n.d.). <https://www.analyticsvidhya.com/blog/2017/09/understaing-support-vector-machine-example-code/>.
- [121] S. Sreenivasa, Radial Basis Function (RBF) Kernel: The Go-To Kernel, (n.d.). <https://towardsdatascience.com/radial-basis-function-rbf-kernel-the-go-to-kernel-acf0d22c798a>.
- [122] B. Rajoub, Chapter 2 - Characterization of biomedical signals: Feature engineering and extraction, in: W. Zgallai (Ed.), *Biomed. Signal Process. Artif. Intell. Healthc.*, Academic Press, 2020: pp. 29–50. <https://doi.org/https://doi.org/10.1016/B978-0-12-818946-7.00002-0>.
- [123] N. Bykovskiy, D. Uglietti, P. Bruzzone, K. Sedlak, Co-Wound Superconducting Wire for Quench Detection in Fusion Magnets, *IEEE Trans. Appl. Supercond.* 32 (2022) 1–5. <https://doi.org/10.1109/TASC.2022.3140706>.
- [124] J. Yang, J. Ma, Compressive sensing-enhanced feature selection and its application in travel mode choice prediction, *Appl. Soft Comput.* 75 (2019) 537–547. <https://doi.org/https://doi.org/10.1016/j.asoc.2018.10.048>.
- [125] A. Devices, Low Noise Instrumentation Amplifier, AD8429 Datasheet, (n.d.). <https://www.analog.com/media/en/technical-documentation/data-sheets/ad8429.pdf>

**Name:** Arooj Akbar  
**Address:** BC 216, Station 14, CH-1015 Lausanne  
**Phone:** +41 78 334 00 78  
**Email:** [aroor.akbar@outlook.com](mailto:aroor.akbar@outlook.com)  
**Date of birth:** 19-06-1993  
[LinkedIn](#), [Google Scholar](#)

---

## EDUCATION

---

- École polytechnique fédérale de Lausanne (EPFL), Switzerland** **02.2019 – Present**  
Doctoral Assistant Electrical Engineering in the Applied Superconductivity Group  
*Thesis:* A Fibre Optic and Machine Learning Based Health Monitoring System for Superconducting Power Applications in Modern Supergrids  
*Thesis director:* Dr. Bertrand Dutoit, *Co-director:* Prof. Mario Paolone
- University of Nottingham (UoN), United Kingdom** **09.2016 – 12.2017**  
Master of Science in Power Electronics and Drives  
*Thesis:* Control Design of Starter/Generator Systems for More Electric Aircrafts
- Lahore University of Management Sciences (LUMS), Pakistan** **08.2012 – 06.2016**  
Bachelor of Science in Electrical Engineering  
*Final Year Project:* Grid-Tied Solar Micro-Inverter with Inverse Power Factor Correction

---

## PATENTS, PUBLICATIONS AND POSTER PRESENTATIONS

---

### Patent

*Title:* Hotspot Monitoring System for Superconducting Device **2021**  
*Patent number:* WO2021038505 (A1)  
Z. Yang, A. Akbar, Patent number: WO2021038505 (A1), **Hotspot Monitoring System for Superconducting Device**, (2021). ([Link to patent](#))

### Publications

- A. Akbar, N. Riva, B. Dutoit, **Optical Fibre Based Quench Detection in HTS Applications Using Machine Learning Classifiers**, Physica C: Superconductivity and its Applications 593 (2022) 1354007. ([Link to publication](#))
- A. Akbar, Z. Yang, S. Wang, L. Thévenaz, B. Dutoit, **Optical Fibre Sensing for Fast Hotspot Detection in SFCLs**, Superconductor Science and Technology journal 33 (2020) 115003. ([Link to publication](#))
- A. Akbar, B. Dutoit, **Fast Quench Detection in SFCL Pancake Using Optical Fibre Sensing and Machine Learning**, IEEE Transactions on Applied Superconductivity (2022) 1. ([Link to publication](#))
- A. Akbar, N. Riva, Z. Yang, L. Thevenaz, B. Dutoit, **Fast Hotspot Detection in SFCLs by Exploiting Strain Response in Optical Fibre Sensing**, IEEE Transactions on Applied Superconductivity 31 (2021). ([Link to publication](#))
- P.J. Tixador, A. Akbar, M. Bauer, M. Bocchi, A. Calleja, C. Creusot, G. Deutscher, F. Gomory, M. Noe, X. Obradors, M. Pekarcikova, F. Sirois, **Some Results of the EU Project FASTGRID**, IEEE Transactions on Applied Superconductivity (2022) 1. ([Link to publication](#))
- N. Ramzan, A. Akbar, Z.J. Khan, P. Naseer, N. Zaffar, **Reactive Power Compensation Through Synchronization of Networked VFDs**, Power Systems Conference PSC (2016). ([Link to publication](#))
- N. Riva, F. Grilli, F. Sirois, C. Lacroix, A. Akbar, B. Dutoit, **Optimization Method for Extracting Stabilizer Geometry and Properties of REBCO Tapes**, IEEE Transactions on Applied Superconductivity 31 (2021) 1–5. ([Link to publication](#))

- N. Ramzan, Z.J. Khan, P. Naseer, A. Akbar, N. Zaffar, **Grid Tied Solar Micro-Converter with Optimizer-Mode Operation for Weak-Grid Operation**, IEEE Applied Power Electronics Conference Expo. APEC (2017). ([Link to publication](#))

#### Invited Poster

Finite Element Modelling of Optical Fibre Sensing for Hotspot Detection in SFCL, at European Conference on Applied Superconductivity, 2019

---

#### RESEARCH PRESENTATIONS

- Oral presentation at the 27th International Conference on Magnet Technology, 2021
- Oral presentation at the Applied Superconductivity Conference, 2020
- Presentation for the International Energy Agency (IEA) Meeting, EPFL, 2019
- Talk at CERN TE-MS Seminar, 2019

---

#### TECHNICAL SKILLS

Power Electronics | Power Systems | Fibre Optic Sensors | Signal Processing | Technical Writing | Project Management | Schematic Capture | PCB Design | Altium | Machine Learning | Neural Networks | Data Acquisition | MATLAB/Simulink | COMSOL | FEM | C++ | Python |

---

#### WORK EXPERIENCE

##### **Lahore University of Management Sciences**

Research Assistant, Electrical Engineering Department

**06.2015–06.2016**

##### **Lahore University of Management Sciences**

Teaching Assistant, Mathematics Department

**08.2014 – 12.2014**

##### **Lahore University of Management Sciences**

Teaching Assistant, Physics Department

**08.2013 – 12.2013**

---

#### AWARDS

**École polytechnique fédérale de Lausanne:** Best Student Paper Award, Applied Superconductivity Conference 2020

**University of Nottingham:** Distinction Award | Full Developing Solutions Master's Scholarship Award

**Lahore University of Management Sciences:** Distinction Award | Dean's Honor List Award | Top Student Merit Scholarship

---

#### AFFILIATIONS

The European Society for Applied Superconductivity (ESAS) | The Institution of Engineering and Technology (IET) | Institute of Electrical and Electronics Engineers (IEEE)

